The Hashemite Kingdom of Jordan
Scientific Research Support Fund
The Hashemite University

JJEES

Jordan Journal of Earth and Environmental Sciences

Indexed by Scopus
ELSEVIER

Volume (14) Number (1)

Cover photo © Prof. Ahmad Al-Malabeh

JJEES is an International Peer-Reviewed Research Journal

ISSN 1995-6681 jjees.hu.edu.jo March 2023

Jordan Journal of Earth and Environmental Sciences (JJEES)

JJEES is an International Peer-Reviewed Research Journal, Issued by Deanship of Scientific Research, The Hashemite University, in corporation with, the Jordanian Scientific Research Support Fund, the Ministry of Higher Education and Scientific Research.

Editorial Board:

Associate Editorial Board: (Arranged Alphabetically)

International Advisory Board: (Arranged Alphabetically)

Editorial Board Support Team:

Submission address:

Manuscripts should be submitted electronically to the following e-mail:

jjees@hu.edu.jo

For more information and previous issues:

www.jjees.hu.edu.jo

Hashemite Kingdom of Jordan

Scientific Research Support Fund

Hashemite University

Jordan Journal of Earth and Environmental Sciences

JJEES

An International Peer-Reviewed Scientific Journal

Financed by the Scientific Research Support Fund

Volume 14 Number (1)

http:// jjees.hu.edu.jo/

ISSN 1995-6681

*Columnar jointing forms in lava flows from Wadi Al-Hidan, Jordan.
Photographed byProf. Ahmad Al-Malabeh

JJEES
Jordan Journal of Earth and Environmental Sciences

PAGES	PAPERS
1 - 8	Morphometric Characterization of Gelana Watershed, Awash River Basin, Ethiopia. *Tesfaye Wasihun Abro*
9 - 18	Geospatial Soil Suitability Assessment for Maize (Zea mays) Production in Derived Savanna of Agricultural Research and Training, OYO STATE, Nigeria *Anthony Tobore, Bolarinwa Senjobi, Ganiyu Oyerinde, Samuel Bamidele*
19 - 29	Utilization of Jordanian Bentonite Clay in Mortar and Concrete Mixtures *Ayoup M. Ghrair, Adi J. Said, Hussein Al-kroom, Naela Al Daoud, Bassel Hanayneh, Ahmad Mhanna, and Ahmed Gharaibeh*
30 - 49	Late Eocene (Priabonian) planktic foraminifera from Jabal Hafit, Al Ain area, United Arab Emirates *Haidar Salim Anan*
50 - 63	Anoxic Marine Conditions Recorded from the Middle Paleozoic Black Shales (Kaista and Ora formations), Northern Iraq: A multi-Proxy Approach *Ali I. Al-Juboury, Rahma S. Al-Auqadi, Safwan H. Al-Lhaebi, Harold D. Rowe and Salim H. Hussein*
64 - 69	2D Seismic Stratigraphic Analysis of Harthaand Kifl Formations in Balad Area– Center of Iraq *Ali M. Abed, Jassim M. Al-Halboosi, Amer S. Al-Jibouri, Salam O. Al-Hetty*
70 - 74	Chemical Effect on Soil Strength by adding Lime and Natural Pozzolana *Dr. Maiasa Mlhem*
75 - 82	Kinematic Analysis of Amman-Hallabat Structure, Northeast Dead Sea, Jordan *Masdouq Al-Taj*

JJEES

JJEES (2023) 14 (1): 1-8
ISSN 1995-6681

Jordan Journal of Earth and Environmental Sciences

Morphometric Characterization of Gelana Watershed, Awash River Basin, Ethiopia.

Tesfaye Wasihun Abro

Department of Geography and Environmental Studies, Dire Dawa University,Dire Dawa, Ethiopia

Received 28th September 2021; Accepted 18th May 2022

Abstract

Watershed resources analysis and development intervention at the catchment level requires primarily an understanding of the physical morphometry, but it has long been emphasized for hydrological analysis of soil and water conservation initiatives. This research was carried out to assess the morphometric characteristics of the sub-watersheds of Gelana using a geographic information system and remote sensing. The parameters considered were bifurcation ratio (Rb), stream frequency (Fs), drainage density (Dd), drainage texture (Dt), Length of overland flow (LoF), Constant of channel maintenance (CCM), infiltration number (If), elongation ratio (Re), circulatory ratio (Rc), form factor (Ff), compactness coefficient (Cc), basin relief (H), relief ratio (Rh), ruggedness number (Rn), stream power index (SPI), and sediment transport index (STI). Shuttle Radar Topographic Mission Digital Elevation Model 30 m resolution was used as input data to generate the value of these variables.

The results showed that linear parameters ranged from Rb = 1.4–5.0; Fs = 0.33–0.55; Dd = 0.54–0.851 while shape parameters revealed that the sub-watersheds (SWs) as being more elongated (Re = 0.46–0.71; Rc = 0.183–0.37; Cc = 1.62–2.33); LoF= 0.27–0.425; IF=0.19–0.46; CCM= 1.175–1.85. This reflects the dominance of dendric drainage patterns and high flooding susceptibility. In addition, the relief parameter also revealed that 75% of 262 km^2 of the seven sub-watersheds are relatively gentle relief (Rh<1.146). It can be concluded that sloppy terrain and high surface relief with relatively elongated shapes are observed in the northern and northeastern parts of the study sub-watersheds, implying high soil and water conservation priority, while the central and southern parts are characterized by a flat topography.

Keywords: *SRTM DEM; Areal parameters; Linear parameters; Shape parameters*

1. Introduction

Morphometry is the measurement and mathematical analysis of the configuration of the earth's surface and the shape and dimensions of its landforms, and it has various parameters like linear, areal, and relief aspects (Hlaing et al., 2008). These parameters describe the physical features of the watershed in terms of its ruggedness, overall shape, drainage qualities, and dissection (Horton, 1932).

Several studies have been carried out on the morphometric analysis of watersheds for different applications using the digital elevation model (DEM) in the GIS environment. For example, Chandniha, (2014) has applied watershed morphometric analysis to prioritize sub-watersheds for soil and water conservation measures. Sreedevi, et al. (2013), Aher et al. (2014), and Kumar et al. (2018) have also studied watershed morphometry to see its influence on hydrology. Moreover, Vittala et al. (2004) and Ayele et al. (2017) have evaluated drainage morphometry to better understand the watershed characteristics in general. Furthermore, the morphometric analysis also indicates the responsiveness of the watershed to rain events or its susceptibility to floods and erosion (Ayele et al., 2017). According to Das (2014), it is necessary to understand the topography and drainage patterns of an area for the preparation of a comprehensive watershed development plan, and therefore understanding the morphometry of the watershed has to be taken as a benchmark for the analysis of other characteristics of a watershed (Samal et al., 2015). To this purpose, a geographic information system is a powerful tool in terrain visualization, processing, and quantification of topographic attributes using DEM to morphometric studies.

In countries like Ethiopia, where a majority of the population depends on traditional agriculture for their livelihood and is dominated by rugged topography (Woldeamlak, 2003; Temesgen et al., 2017), studying the morphometry of the watershed is important for understanding the physical landscape and to soil and water conservation planning. Watershed hydrological behavior could be understood through the analysis of morphometry of a watershed, especially in data-scarce areas like the Gelana watershed, and this could be a good opportunity for conservation planners to visualize the nature of this area. However, a few research studies have been undertaken on morphometric characterization in Ethiopian watersheds (morphometry of a watershed as one cause of flood risk (Sitotaw and Hailu, 2018) the implication of drainage morphometry (Ayele et al, 2017) the implication of morphometry on soil and water conservation (Daniel and Getachew, 2019) morphometric analysis for prioritizing sub-watersheds and management planning and practices (Gadisa et al, 2020).

* Corresponding author e-mail: tesfayebecon@gmail.com

The purpose of this research is to characterize the morphometric features of Gelana sub-watersheds in Ethiopia's Awash River basin using Shuttle Radar Topographic Mission Digital Elevation Model (SRTM DEM) data on the GIS environment. The findings of this study could be utilized as a supplement in the preparation of a comprehensive watershed development plan, which necessitates a thorough understanding of the topography, erosion susceptibility, and drainage patterns of a given area.

2. Material and Methods

2.1 Description of the study area

The study area, the Gelana watershed, is part of the Awash River basin and administratively found in the North Wollo zone of Amhara National Regional State, Ethiopia. It is located between 11°31'30″ and 11°40'00″N, and 39°35'05″ and 39°45'50″E (Figure 1) covering an area of 262km^2 of land inhabited with a total population of 120,250. The elevation of the Galena watershed ranges from 1,363 to 3,474 m above sea level.

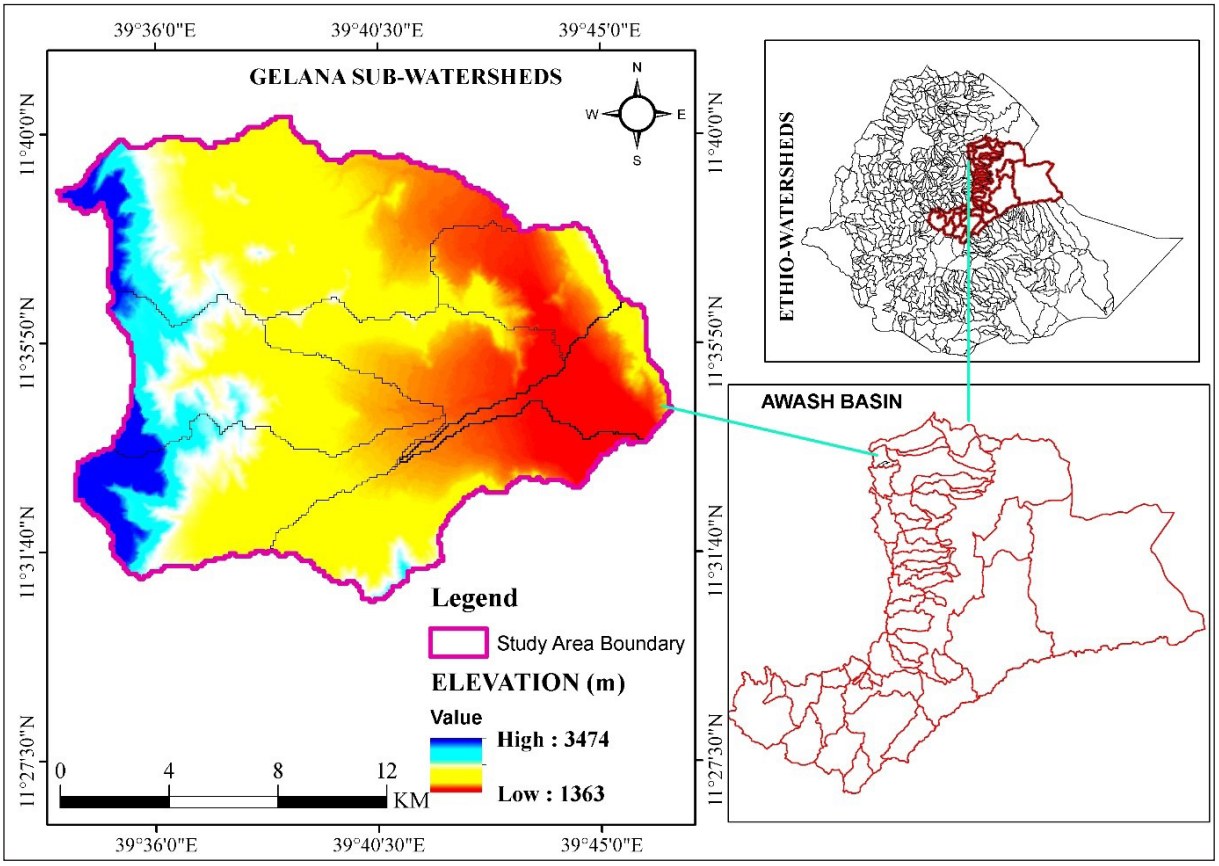

Figure 1. Map of the study area: left— Gelana sub-watershed with elevation (m.a.s.l.) information, top right—Ethiopia watersheds, bottom right—Awash basin

2.2 Input Data and Analytical approach

For the analysis of morphometry of the study watershed, SRTM DEM (https://EarthExplorer usgs.gov) 30 m resolution released on September 2014 was used to delineate and generate the numeric characteristics of different parameters. Identification of smaller geohydrological units is needed for more efficient and better-targeted resource management programs (Sharma and Thakur, 2016). Therefore, the Gelana sub-watershed has been classified into seven sub-watersheds (SWs) using ArcSWAT in ArcGIS 10.4. After creating a shape file of watersheds, the DEM of each catchment was masked. Then, sinks (areas of internal drainage, that is, areas that do not drain out anywhere), were filled to ensure proper delineation of basins and streams (Horton, 1932). If the sinks are not filled, a derived drainage network may be discontinuous. Moreover, a flow accumulation threshold value of 1000 was used and the result stream networks were cross-checked with a toposheet (1:50,000 scale) to have approachable results and generated streams of seven sub-watersheds (Figure 2). The analysis for individual sub-watersheds has been achieved through the calculation of linear, shape, and relief parameters using the formula indicated for each parameter in Table 1.

Table 1. Description of Morphometric Parameters used for this study

SN	Morphometri c Parameters	Definition/ Formula	Description	References
1	Bifurcation ratio (Rb)	Rb = Nu/Nu+1	It is the ratio of the number of streams of the given order u to the number of streams of the next higher order u+1. It shows the complexity and degree of dissection of a drainage watershed.	Schumm (1956); (Strahler, 1964)
2	Stream frequency (Fs)	Fs = Nu/A	It is the ratio of the total number of streams in a watershed to the watershed area.	Horton (1932)
3	Drainage density (Dd)	Dd= Lu/A	It is the ratio of the total length of streams of all orders of a watershed to the area of the watershed	Horton (1932)
4	Drainage texture (Dt)	Dt = Nu/P	It refers to the relative spacing of drainage lines. It is the total number of stream segments of all orders (Nu) per perimeter length of that watershed.	Horton (1945)
5	Compactness Coefficient (Cc)	$Cc = 0.2821P/A^{0.5}$	It is the ratio of the perimeter of the basin to the circumference of a circle with an equal area.	Horton (1945)
6	Form factor (Ff)	$Ff=A/Lb^2$	The form factor is the ratio of the watershed area (A) to the square of the maximum length of the watershed.	Horton (1932)
7	Elongation ratio (Re)	$Re=2/Lb*(A/\pi)^{0.5}$	It is the ratio between the diameters of a circle with the same area as that of the watershed to the maximum length of the watershed.	Schumm (1956)
8	Circulatory ratio (Rc)	$Rc = 4 * \pi * A/P^2$	It is the ratio of the basin area to the area of a circle having the same parameter as the basin.	Miller (1953)
9	Length of overland flow (LoF)	LoF=0.5*Dd	It is the length of water flow over the surface of the ground before it confines into definite stream channels.	Horton (1945)
10	Infiltration Number (IF)	IF=Dd*Fs	It helps to predict the permeability of the surface of the watershed and higher values of 'IF' indicates impermeable surface and resistance to soil loss	Faniran (1968)
11	Constant of Channel Maintenance	CCM=1/Dd	The lower value of CCM indicates higher flood potentiality and young geomorphological adjustment.	Schumm (1956)
12	Basin relief (H)		The difference between the lowest and highest point in a watershed	Hadley and Schumm (1961)
13	Relief ratio (Rh)	Rh = H/Lb	It is a measure of the overall steepness of the drainage area and is an indicator of the intensity of erosion processes operating on the slopes of the watershed.	Schumm (1956)
14	Ruggedness no. (Rn)	Rn = H * Dd	It is the product of the maximum watershed relief and its drainage density. Slope steepness and the length of the watershed affect it.	Melton (1957)
15	Sediment Transport Index (STI)	$(\text{Flow Acc.}/22.13)^{0.6} *(\text{Sin } \beta/0.0806)^{1.3}$	It characterizes the process of erosion and deposition and reflects the erosive power of overland flow.	
16	Stream Power Index (SPI)	(Flow Acc. + 1) * (tan β)	It is the product of catchment area and slope and could be used to describe potential flow erosion and related landscape processes.	Florinsky (2012)
17	Land use land cover (LU/LC)*	Landsat 8 image OLI–TRIS**–2018)	Land use indicates how people are using the land while land cover refers to the physical land type.	https://earthexplorer.usgs.gov/

**another parameter **OLI-TRIS-Operational land imager Thermal Infrared Sensor*

The parameters considered in this study are stream order, number of streams, stream length, bifurcation ratio (Rb), stream frequency (Fs), drainage density (Dd), drainage texture (Dt), length of overland flow (LoF), constant of channel maintenance (CCM), infiltration number (If), elongation ratio (Re), circulatory ratio (Rc), form factor (Ff), compactness coefficient (Cc), basin relief (H), relief ratio (Rh), ruggedness number (Rn), slope (S), stream power index (SPI), sediment transport index (STI) and land use land cover (LU/LC).

Landsat OLI images of 2018 have been downloaded from the US Geological Survey https://earthexplorer.usgs.gov/ Web site. A satellite image has been downloaded (website: https://earthexplorer.usgs.gov/) for the year 2018. Then, the supervised classification has been carried out for Land use land cover (LU/LC) by using the ERDAS IMAGINE 2014 software. The sub-watersheds have been classified into five distinct classes' built-up area, forestland, shrubs, cultivated land, and bare lands. The LU/LC processing will be undertaken to crosscheck its relation with the drainage density of catchments.

Moreover, the soil texture of the study sub-watersheds was obtained from the regional agriculture and rural development bureau and compared with the calculated drainage density of the study area. Here, the resulting soil texture vector map was converted into a raster map to better visualize the areal extent of each soil texture type (Figure 4).

3. Results and Discussion

3.1 Linear Morphometric Parameters

Aher et al. (2014) indicated that the classification of stream order is important to index the size and scale of the basin. Using Strahler's (1957) system of stream order, the Gelana watershed has five (5) main streams order, with each stream order in each sub-watershed having a varying number of streams (Table 2).

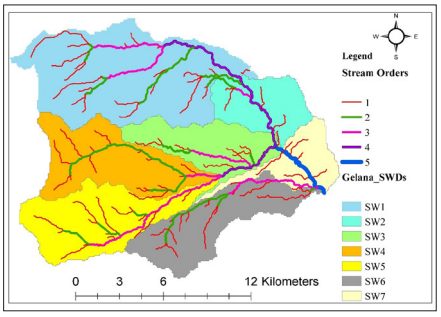

Figure 2. Stream orders of Gelana sub-watersheds.

The study watershed has an area of 261 km^2 with which 116 total streams with a total stream length of 200 km. This means that there are about 0.44 streams in a km^2 and an average of 0.76 km stream length per km^2 area. Considering the sub-watersheds, SW1 is the highest in terms of stream length at 64 km while SW7 has the lowest stream length with a total of 11 km (Table 2).

The result showed that five out of seven sub-watersheds have a bifurcation ratio (Rb) ranging from 3.25 up to 5.0 (Table 1) with a mean of 3.6 which fits with Horton's (1945) natural drainage characteristics (Rb=3.0–5.0). Lower-order streams have a higher bifurcation ratio that reflects the high dissection in the upland area. Lower bifurcation ratios (Rb<3.0) are the characteristics of structurally less disturbed watersheds (Ayele et al., 2017) which were observed in SW2 and SW1.

Horton (1945) noted that the value of stream frequency depends on the total number of streams and the corresponding basin area. In the present study, stream frequency varies from 0.33 to 0.55 (Table 2). In addition, the stream frequency of sub-watersheds showed a positive correlation with the drainage density values of the sub-watersheds indicating the increase in streams concerning an increase in drainage density.

Table 2. Linear morphometric parameters

SW	Parameters	Stream Order					Fs	Dd	Dt
		1st	2nd	3rd	4th	5th			
1	No. of streams	24	7	2	1	-	0.43	0.81	0.56
	Stream Length/km	34	12	11	7	-			
	Ave. length/km	1.4	0.9	2.2	2.33	-			
	Basin Length(km)	17.01							
	Bifurcation ratio	3.42	3.5	2					
	Mean Rb	**2.97**							
2	No. of streams	7	1	-	-		0.36	0.54	0.29
	Stream Length/km	7	5	-	-				
	Ave. length/km	1.0	1.0	-	-				
	Basin Length(km)	7.2							
	Bifurcation ratio	1.4							
	Mean Rb	**1.4**							
3	No. of streams	10	4	1	-		0.55	0.851	0.34
	Stream Length/km	10	5	8					
	Ave. length/km	1.0	1.25	1.6					
	Basin Length(km)	11.08							
	Bifurcation ratio	2.5	4						
	Mean Rb	**3.25**							
4	No. of streams	15	2	1			0.45	0.7	0.39
	Stream Length/km	14	12	2					
	Ave. length/km	0.93	1.0	1.0					
	Basin Length(km)	12.85							
	Bifurcation ratio	7.5	2	-					
	Mean Rb	**4.75**							
5	No. of streams	15	4	1	-	-	0.5	0.85	0.57
	Stream Length/km	18	5	11	-	-			
	Ave. length/km	1.2	0.83	1.37	-	-			
	Basin Length(km)	13.8							
	Bifurcation ratio	3.75	4		-	-			
	Mean Rb	**3.87**							
6	No. of streams	12	2	1	-	-	0.42	0.8	0.32
	Stream Length/km	19	7	2		-			
	Ave. length/km	1.58	1.0	1.0	-	-			
	Basin Length(km)	14.04							
	Bifurcation ratio	6	2		-	-			
	Mean Rb	**4**							
7	No. of streams	5	1	-	-		0.33	0.61	0.13
	Stream Length/km	7	4	-	-				
	Ave. length/km	1.4	1.0	-	-				
	Basin Length(km)	10.6							
	Bifurcation ratio	5	-	-	-	-			
	Mean Rb	**5**							

Drainage density (km/km^2) provides a clue about the density of vegetation cover, soil, and rock characteristics of a watershed. Therefore, the higher the drainage density the lesser density of vegetation cover and impermeable soil and rock surface which lets the movement of overland flow as runoff (Horton, 1945). He also noted that infiltration, controlled by permeability, might influence drainage density by determining at what distance from a divide there will be a sufficient surface flow of water to start gullying erosion. Based on this, the sub-watershed with higher drainage density (SW3 and SW5–0.85) (Table 2) have shown low forest coverage (Figure 3) and manifested with clay, clay loam, and sandy clay soil (Figure 4). Thus, these sub-watersheds are inherently slow soil permeability, which will have significant implications on soil erosion and runoff generation. Ayele et al. (2017) noted that an impermeable surface would generate high drainage density and efficiently carry away runoff, with high peak discharge but low base flow.

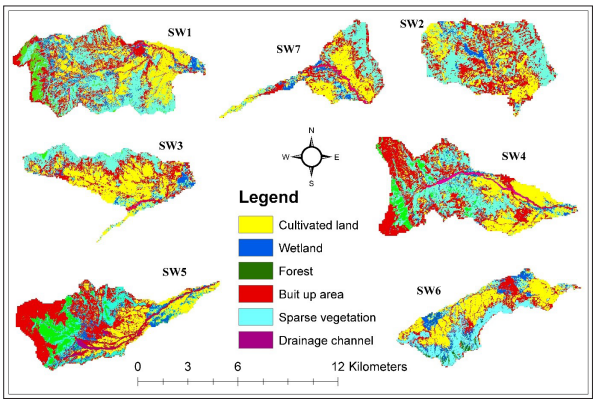

Figure 3. Land use/land cover of Gelana sub-watersheds.

Because drainage texture is the relative spacing of drainage lines, the lower its value means the far apart of drainage lines which are significantly affected by underlying lithology, vegetation, soil type, infiltration capacity, and relief aspect (Horton, 1945; Smith, 1950).

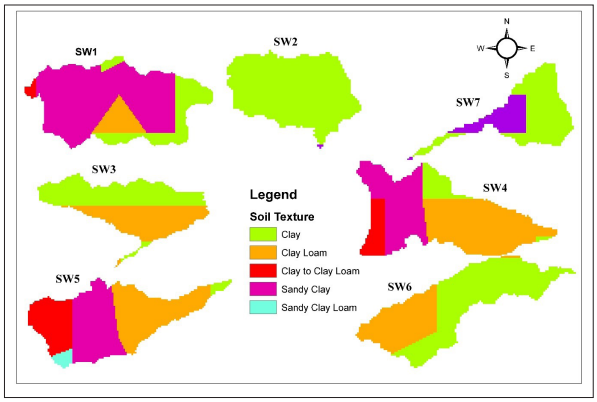

Figure 4. Soil textures of Gelana Sub-watersheds using regional agriculture and rural development bureau soil data.

Smith (1950) has classified a watershed with different drainage textures (very coarse (<2), coarse (2–4), moderate (4–6), fine (6–8), and very fine (>8). In the present study, drainage texture varies from 0.13 (SW7) to 0.57 (SW5) reflecting a very coarser drainage texture.

3.2 Areal Morphometric Parameters

Samal et al. (2015) have revealed that for a perfectly circular basin, the value of the form factor is greater than 0.78. Nevertheless, the highest Form factor in the present study is 0.42 for SW2 indicating the elongated shape of the sub-watersheds. On the other hand, the value of the form factor can also reveal the hydrological behavior of a watershed that is the lower the form factor value, the lesser the peak flow for a longer duration while the higher the form factor, the higher the peak flow for shorter duration (Hlaing et al., 2008). Therefore, the smaller numeric value of the form factor of Gelana sub-watersheds implies that they are relatively elongated and will have a flatter peak flow over an extended time that makes flooding less susceptible.

Table 3. Areal morphometric parameters of the Gelana watershed

SW	A(km^2)	P(Km)	Ff	Re	Rc	LoF	IF	CCM	Cc
1	79	60	0.273	0.551	0.27	0.405	0.348	1.23	1.9
2	22	27	0.42	0.71	0.37	0.27	0.19	1.85	1.62
3	27	43	0.21	0.527	0.183	0.425	0.468	1.175	2.33
4	40	46	0.24	0.553	0.237	0.35	0.31	1.42	2.05
5	40	46	0.2296	0.535	0.237	0.425	0.42	1.176	2.05
6	35	46	0.17	0.467	0.207	0.4	0.342	1.25	2.19
7	18	35	0.15873	1.07	0.184	0.305	0.20	1.63	2.32

A = Watershed Area; P = watershed Perimeter

Strahler (1964) classified Re value into four classes; <0.7– (elongated), 0.7–0.8 (less elongated), 0.8–0.9 (oval), >0.9 (circular). In the present study, the value of the elongation ratio is lower than 0.7 reflecting the elongated ness of Gelana SWs except for SW2–0.71 and SW7–1.07. Elongated watersheds are characterized by high spreading out runoff over time resulting in smaller peak floods. Strahler (1964) and Samal et al. (2015) noted that the Re value approaching 1 is indicative of very low relief, whereas values in the range of 0.6–0.8 are generally associated with strong relief and steep ground slopes.

The circularity ratio is the ratio of the basin area to the area of a circle having the same perimeter as the basin (Miller, 1953). The slope, relief geologic structure of the basin, and land use land cover, influences the circularity ratio. A low Rc value implies an elongated basin shape while a high Rc value indicates a near-circular. In the present study, relatively higher Rc was found at WS2 and WS1 with Rc of 0.37 and 0.27, respectively while the lowest Rc was observed at WS3 (0.183) and SW7 (0.184) (Table 3).

Infiltration number (IF) is a function of drainage density and stream frequency (Odiji et al., 2021). Faniran (1968) noted that areas with higher IF values are an indication of lower infiltration and higher surface runoff. Sub-watersheds with relatively higher IF values are SW3 and SW5 indicating that the amount of water entering into the soil is low and by implication, runoff is high (Table 3).

Length of overland flow (LoF) refers to the length at which rainfall runs over the surface before it drains into a stream channel (Horton 1945). The LoF ranges from 0.27km to 0.425km in the seven sub-watersheds (Table 3) with a mean of 0.36km which implies that the watershed has a short flow path. The values of the LoF are small in the entire sub-watershed which means that surface runoff will enter stream channels rapidly and therefore the areas are highly vulnerable to flooding due to reduced water percolation into the soil.

The constant of channel maintenance (CCM) is inversely related to drainage density (Schumn, 1956). It depends on the rock type, permeability, climatic regime, vegetation cover, and relief as well as the duration of erosion. It decreases with increasing erodibility (Schumn1956). According to Bhagwat et al. (2011), higher values of CCM suggest more area is required to produce surface flow, which implies that part of water may get lost by evaporation, percolation, etc while lower value indicates fewer chances of percolation/ infiltration and hence more surface runoff. The SW3 and SW5 have low CCM values of 1.175 km/km2 and 1.176 km/km2, respectively (Table 3) indicating that these sub-watersheds are under the influence of high structural disturbance, low permeability; steep to very steep slopes, and high surface runoff. On the other hand, SW2 and SW7 have the highest CCM values of 1.85km/km2 and 1.65km/km2, respectively, and are under very less structural disturbances and fewer runoff conditions (Table 3).

3.3 Relief Morphometric Parameters

Relief controls the rate of draining water through a watershed and run-off is generally faster in steeper terrain, producing discharges that are more peaked and greater erosive power (Schumn, 1956). In the present study, total relief varies from 602m in SW7 to 1992m SW1 and SW5 while the relief ratio ranges from 0.099 (SW2) to 0.15 (SW5) (Table 4) and that proves the relatively flat terrain of the sub-watersheds. Ruggedness number combines slope steepness and length. Its higher values occur when slopes are not only steep but long as well.

SW1 and SW5 showed higher values of ruggedness number than the other sub-watersheds, with SW5 slightly higher (1.69) than SW1 (1.61).

Table 4. Relief morphometric Parameters of the Gelana watershed

Items	Sub watersheds						
	1	2	3	4	5	6	7
Basin Relief (m)	1992	715	713	1877	1992	930	602
Relief ratio	0.116	0.099	0.064	0.146	0.15	0.66	0.056
Ruggedness number	1.61	0.386	0.606	1.313	1.69	0.744	0.367

3.4 Other Characteristics

The sediment Transport Index (STI) characterizes the process of erosion and deposition and reflects the erosive power of overland flow (Jaiswal et al, 2015). The STI value is higher in SW7—78.16. This may be due to sediments emanating from the whole sub-watershed meeting at this sub-watershed making higher sediment loads.

Table 5. Other characteristics of the Gelana watershed.

Items	Sub watersheds						
	1	2	3	4	5	6	7
STI	30.68	60.99	52.97	29.77	31.19	29.4	78.16
SPI	30.6	40.09	26.78	31.58	35.71	14.07	64.91
TWI	1.5715	1.758	1.81	1.54	1.66	1.74	1.8152

Concerning Stream Power Index (SPI), high stream power was observed in SW7 (64.9) which may be associated with the flow of higher amounts of water from the upper areas. The higher the power of stream water, the greater the probability of washing down vulnerable topsoil leading to land degradation through transporting soil material and sediment to the plain areas. Knighton (1999) noted that stream power may vary in the downstream direction and maximum power lies around the outlet because of the large increase in mid-watershed discharge associated with a series of large, closely spaced tributaries. In this regard, the prevailing variety of geomorphic setting downslope has a significant implication for the movement and storage of materials in the watershed. Therefore, high SPI values represent areas on the landscape where high slopes and flow accumulations exist and thus the flows can concentrate with higher erosive potential.

Table 6. Correlation coefficient between morphometric parameters.

	Rb	Fs	Dd	Dt	Ff	Re	Rc	LoF	IF	CCM	Cc	H	Rh	Rn	STI	SPI	TWI
Rb	1.00																
Fs	0.02	1.00															
Dd	0.20	0.83	1.00														
Dt	-0.19	0.58	0.66	1.00													
Ff	-0.86	-0.21	-0.49	0.17	1.00												
Re	0.23	-0.73	-0.70	-0.71	-0.08	1.00											
Rc	-0.80	-0.35	-0.52	0.19	0.97	-0.06	1.00										
LoF	0.20	0.83	1.00	0.66	-0.49	-0.70	-0.52	1.00									
IF	0.10	0.96	0.95	0.61	-0.37	-0.72	-0.47	0.95	1.00								
CCM	-0.30	-0.80	-0.99	-0.63	0.56	0.67	0.58	-0.99	-0.92	1.00							
Cc	0.75	0.31	0.43	-0.32	-0.93	0.14	-0.99	0.43	0.41	-0.48	1.00						
H	0.16	0.35	0.45	0.87	0.03	-0.49	0.10	0.46	0.37	-0.49	-0.26	1.00					
Rh	0.15	-0.04	0.27	-0.02	-0.33	-0.44	-0.18	0.27	0.11	-0.28	0.14	-0.07	1.00				
Rn	0.16	0.45	0.60	0.92	-0.05	-0.54	0.01	0.60	0.50	-0.62	-0.16	0.98	-0.02	1.00			
STI	-0.07	-0.52	-0.66	-0.80	0.07	0.87	-0.01	-0.66	-0.56	0.67	0.15	-0.78	-0.48	-0.80	1.00		
SPI	0.21	-0.58	-0.62	-0.49	0.01	0.95	0.00	-0.62	-0.61	0.60	0.06	-0.26	-0.64	-0.32	0.79	1.00	
TWI	-0.13	-0.17	-0.23	-0.71	-0.15	0.46	-0.23	-0.23	-0.15	0.28	0.37	-0.92	0.02	-0.84	0.75	0.30	1.00

The correlation matrix (Table 6) shows that a strong positive correlation exists between linear morphometric parameters (IF with LoF, Fs, and Dd; Dd with Fs; LoF with Fs and Dd).

Horton (1945) noted that high transmissibility (as evidenced by infiltration capacity) leads to low drainage density, high base flow, and a resultant low magnitude peak flow. Besides, in impermeable surfaces, runoff is usually accelerated by the development of a greater number of more closely spaced channels and thus higher Fs, Dd, and IF (Ayele et al., 2017). A positive correlation was also observed between Rc and Ff; H and Dt; Rn with Dt and H; STI and SPI with Re. Conversely, CCM with LoF and IF; Cc with Rc has shown a strong negative correlation. Areas with low CCM (i.e limited infiltration) tend to generate more overland flow (Steedevi et al., 2013).

4. Conclusions

The results of this study have demonstrated that the Gelana watershed has five (5) order streams with a mean Rb of 3.6; low drainage density (0.54–0.851 km/km^2) and coarser drainage texture (0.13–0.57) indicating that the sub-watersheds have relatively less dissected terrain features and permeable surfaces.

Results of shape parameters, on the other hand, showed Gelana watershed has an elongated shape (Ff = 0.15–0.42; Re = 0.467–0.71 except SW7 which has Re of 1.07; Rc = 0.183–0.37). The study watershed is characterized by relatively low relief demonstrating the dominance of flat terrain in the sub-watersheds. Moreover, higher LoF and IF have been observed in SW3 and SW5 manifesting a lower probability of runoff in these watersheds with a higher Dd–0.851 and 0.85, respectively while the lower level of CCM– 1.175 and 1.176 implying a higher soil erodibility, low vegetation cover, and low infiltration. The results of this study provide information on drainage morphometry of the Gelana watershed which could be a tool for strategic planning, implementation, and management of watershed resources. However, the morphometric analysis only detects the physical terrain and morphology which does not consider human aspects of the watershed resources, further research should be conducted embedding both natural and human factors-based modeling for conservation prioritization.

Acknowledgment

The author would like to express his gratitude to the United States Geological Survey (USGS) for their efforts in developing and disseminating remotely sensed satellite data and digital elevation model (DEM) products to the public free usage on the internet. The author also extends his gratitude to the anonymous reviewers for substantial comments on earlier versions of the manuscript.

References

Aher, P.D, Adinarayana J. and Gorantiwar S.D. (2014). Quantification of morphometric characterization and prioritization for management planning in semi-arid tropics of India: A remote sensing and GIS approach. Journal of Hydrology 511 (2014): 850–860.

Ayele, A., Hiroshi Y., Katsuyuki S., Nigussie, H., and Kifle W. (2017). Quantitative analysis and implications of drainage morphometry of the Agula watershed in the semi-arid northern Ethiopia. Applied Water Science, 7(7):3825–3840, Springer Berlin.

Bhagwat, T.N, Shetty, A, and Hegde, V.S (2011). Spatial variation in drainage characteristics and geomorphic instantaneous unit hydrograph (GIUH); implications for watershed management—a case study of the Varada River basin, Northern Karnataka. Catena 87:52–59

Chandniha, S.K, and Kansal, M.L (2014). Prioritization of sub-watersheds based on morphometric analysis using the geospatial technique in Piperiya watershed, India. Appl Water Sci (2017) 7:329–338.

Faniran, A. (1968). The index of drainage intensity—a provisional new drainage factor. Aust J Sci 31:328–330

Florinsky, I.V. (2012). Digital terrain analysis in soil science and geology. Academic Press is an imprint of Elsevier. The Boulevard, Langford Lane, Kidlington, Oxford OX5 1GB, UK, 379

Gadisa, C.A, Azene B.T, Abiyot L.T, and Getahun H.A. (2020). Morphometric analysis for prioritizing sub-watersheds and management planning and practices in Gidabo Basin, Southern Rift Valley of Ethiopia. Applied Water Science (2020) 10:158. Springer Nature. https://doi.org/10.1007/s13201-020-01239-7

Daniel, A. and Getachew, W. (2019). Quantitative analysis of morphometry on Ribb and Gumara watersheds: Implications for soil and water conservation. International Soil and Water Conservation Research 7 (2019) 150–157.

Hadley, R.F., and Schumm, S.A. (1961). Sediment sources and drainage basin characteristics in the upper Cheyenne River basin. Water Supply Paper 1531-B, U.S. Geological Survey.

Hlaing, K.T, Haru, Y.S., and Aye, M.M. (2008). Using GIS-based distributed soil loss modeling and morphometric analysis to prioritize watershed for soil conservation in Bago river basin of Lower Myanmar. Front. Earth Science, 2(4): 465–478. doi 10.1007/s11707-008-0048-3.

Horton, R.E. (1932). Drainage basin characteristics. Transactions, America Geophysical Union, 13: 350–361.

Horton, R.E. (1945). Erosional development of streams and their drainage basins; hydrological approach to quantitative morphology. Bulletin of Geological Society of America, 56 (3): 275–370.

Hurni, H. (1985). Erosion – productivity – conservation systems in Ethiopia in Proceedings of the 4th International Conference on Soil Conservation, Maracay, Venezuela, 654–674. January 1985.

Jaiswal, R.K, Ghosh, N.C, Galkate, R.V, and Thomas, T. (2015). Multi Criteria Decision Analysis (MCDA) for watershed Prioritization. International Conference on Water Resources, Coastal and Ocean Engineering (ICWRCOE 2015). Aquatic Procedia 4 (2015) 1553 – 1560.

Knighton, A. (1999). Downstream variation in stream power. Volume 29, Issue 3 3-4, pages 293-306.

Melton, M.A. (1957). An analysis of the relation among elements of climate, surface properties, and geomorphology. Technical Office of National Research, project NR Columbia University.

Miller, V.C. (1953). A quantitative geomorphic study of drainage basin characteristics in the Clinch Mountain area. Technical Report-3, Columbia. University Department of Geology, New York.

Odiji, C.A, Aderoju, O.M, Eta, J.B, Shehu, I., Mai-Bukar, A., and Onuoha, H. (2021). Morphometric analysis and prioritization of upper Benue River watershed, Northern Nigeria. Applied Water Science (2021) 11:41. https://doi.org/10.1007/s13201-021-01364-x.

Samal, D.R, Gedam, S.S, and Nagarajan, R. (2015). GIS-based drainage morphometry and its influence on hydrology in parts of Western Ghats region, Maharashtra, India. Geocarto International. Centre of Studies in Resources Engineering (CSRE), Indian Institute of Technology Bombay, Mumbai, India.

Schumn, S.A. (1956). Evolution of drainage systems and slopes in badlands at Perth Amboy, New Jersey. Geological Society of America Bulletin 67: 597-646.

Sharma, D.D, and Thakur, B.R. (2016). Prioritization of Micro Watersheds in Giri Catchment for Conservation and Planning. Transactions, 38 (2): 267-280.

Sitotaw, H., and Hailu, W. (2018). Flood risk analysis: causes and landscape based mitigation strategies in Dire Dawa city, Ethiopia. Geo-environmental Disasters (2018) 5:16 https://doi.org/10.1186/s40677-018-0110-8.

Smith, K.G. (1950). Standards for grading textures of erosional topography. American Journal of Science, 248 (9):655–668.

Soil Conservation Research Project (SCRP) (1996) Soil erosion hazard assessment for land evaluation. Research report. SCRP, Addis Ababa.

Sreedevi, P.D, Sreekanth, P.D, Khan H.H, and Ahmad S., (2013). Drainage Morphometry and its influence on hydrology in a semi-arid region: Using SRTM Data and GIS. Environmental Earth Sciences, 70:839–848.

Strahler, A.N. (1957). Quantitative analysis of watershed geomorphology. Transactions

American Geophysical Union, 38(6):913–920.

Strahler, A.N. (1964). Quantitative geomorphology of drainage basins and channel networks: In Chow V, (Ed.). Handbook of applied hydrology. Section 439-476, McGraw Hill Book Company, New York.

Temesgen, G. Taffa, T., and Mekuria, A. (2017). Erosion risk assessment for prioritization of conservation measures in Geleda watershed, Blue Nile basin, Ethiopia. Environmental System Research, 6: (1) https://doi.org/10.1186/s40068-016-0078-x. Accessed on 25 February 2020.

Vittala, S.S, Gavindaiah, S., and Gowda, H.H., (2004). Morphometric analysis of sub-watersheds in the Pavagada area of Tumkur district, South India using remote sensing and GIS techniques. Journal of Indian Society of Remote Sensing, 32: 351-362.

Woldeamlak B. (2003). Towards integrated watershed management for resource conservation in Chemoga watershed, Northwestern highlands of Ethiopia. Tropical Resource Management Papers, No. 44. ISBN 90-6754-708-5.

JJEES

JJEES (2023) 14 (1): 9-18
ISSN 1995-6681

Jordan Journal of Earth and Environmental Sciences

Geospatial Soil Suitability Assessment for Maize (Zea mays) Production in Derived Savanna of Agricultural Research and Training, OYO STATE, Nigeria

Anthony Tobore[1*], Bolarinwa Senjobi[1], Ganiyu Oyerinde[2], Samuel Bamidele[3]

[1]Department of Soil Science and Land Management, Federal University of Agriculture Abeokuta, Ogun State, Nigeria. P.M.B. 2240, Abeokuta, Ogun State, Nigeria.
[2]Department of Soil Science, Faculty of Agriculture, University of Abuja, Nigeria
[3]Department of Plant & Soil Sciences, University of Delaware, 531 S. College Avenue, Townsend Hall Rm. 152, Newark, DE 19716, USA

Received 21st September 2021; Accepted 19th May 2022

Abstract

The study focused on the geospatial assessment of the physicochemical properties of soils at the Institute of Agricultural Research and Training, Ilora, Oyo State, Nigeria. Using the random survey method, 100 surfaces (0 to 20 cm) samples were collected and subjected to standard soil laboratory analyses. The variability of soil nutrients was examined using descriptive statistics, while spatial investigation and interpolation were achieved using the Ordinary krigging (OK) method. Cross-validation accuracy with exponential and spherical models was used as a precision tool for the analyzed soil nutrients. Soil nutrient spatial trends were exponentially distributed across the area. Temporal predicted land surface temperature (LST), and soil-adjusted vegetation index (SAVI) were estimated through Landsat images of the years 2000 and 2020 using ArcGIS 10 software. The spectral variables – LST and SAVI were merged with soil nutrients to assess the maize suitability evaluation of the area. The LST and SAVI results revealed the qualitative differences in the studied area. The maize suitability showed that the studied soils ranged from moderately (85%), marginally (60%), and not suitable (< 40%). To increase the suitability of the soils for optimum maize production there is a need to enhance the limiting dominant factors such as undulating topography, rainfall, and erosion hazard. Hence, the study recommends the integration of geospatial techniques such as remote sensing covariate variables and exponential models as indispensable methods to assist farmers and policymakers in sustainable and precision agriculture.

Keywords: *Geospatial approaches: Maize suitability; Ordinary krigging; Soil nutrients: Derived savanna.*

1. Introduction

Variability assessment of the soil nutrients is considered a fundamental step required for sustainable precision farming (Ge et al., 2007). The major factor limiting food production in most developing countries can be traced to the inappropriate and abuse of soils (Ekeleme et al., 2014). For instance, in Nigeria, soil properties are faced with anthropogenic activities such as the illegal felling of trees, and abuse of pesticides and fertilizers, etc. (United Nations, 2017). Moreover, Adekiya and Agbede (2009) also stated that derived Savanna soils are prone to nutrient soil loss which led to crop failure, especially maize. Maize (Zea mays) is an agroecological staple crop cultivated worldwide (Liu et al., 2015). Nevertheless, attaining optimum yield of crop such as maize in ever-changing environments, require the need to assess the soil nutrients such as physical and chemical properties using geospatial approaches (Liu et al., 2015).

Moreover, Remote sensing techniques (RST) are becoming acceptable methods and decision-support techniques used for modeling and mapping the physical and chemical properties of soils especially when precision agriculture is desired (Carlson et al., 1994). Additionally, multi-criteria assessment using the Analytical hierarchy technique (AHT) has been used as a bottom-up approach to monitoring changes in soil properties (Marko et al., 2014). Besides, many researchers have utilized the Ordinary kriging (OK) method to interpolate and predict un-sampled points for site-specific studies (Zhang et al., 2010). For example, Martey et al., (2014) utilized Landsat imageries to map soil properties using spectral indices such as predicted land surface temperature (LST) and predicted soil-adjusted vegetation index (SAVI). The research concluded that LST and SAVI gave a better qualitative accuracy on soil nutrients.

Despite the widespread use of these geospatial approaches, studies on soil properties using multi-criteria evaluation coupled with remote sensing and geostatistical modeling are still lacking in implementation in Nigeria. Hence, the study seeks to integrate the AHT to evaluate spatial changes of soil nutrients at the Institute of Agricultural Research and Training (IAR&T), Ilora, Oyo State, Nigeria using LST, SAVI, and OK interpolation models such as exponential and spherical. More specifically, the study is targeted to map variability changes in soil nutrients for maize production using geospatial approaches. Therefore, the study objectives are:

1. To assess and interpolate the soil physical and chemical nutrients of the study area.
2. To produce a maize soil suitability map using PLST, PSAVI, and OK interpolation models.

* Corresponding author e-mail: toboreao@funaab.edu.ng

2. Methods

2.1 The study region

The study area lies at the transitionally derived savanna with mixed rolling topography in Nigeria within Northing $7^{0}48'5$ N and $7^{0}49'4$ N and Easting $3^{0}49'0$ E and $3^{0}44'5$ E (Fig. 1). The relative humidity mean within the study area falls between 60 % with 90 days cumulative rainfall (FDALR, 1990). The soils of the study area originated from basement complex parent material (USDA, 1999).

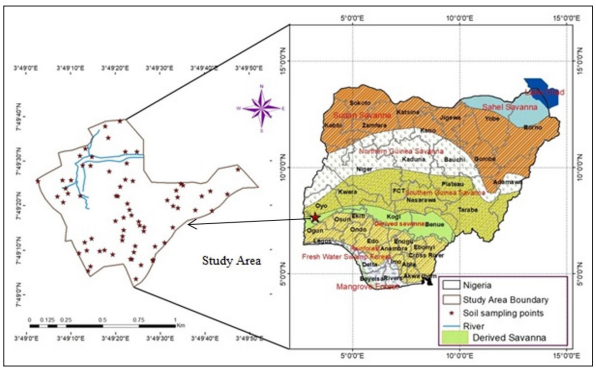

Figure 1. Agro-ecological (Nigeria) zones showing the soil sampling in the study area.

2.2 Assessment of soil properties using remote sensing variables

The dependent variables used in this study include existing roads, rivers, predicted soil-adjusted vegetation index (SAVI), and predicted land surface temperature (LST). The remote sensing variables – SAVI and LST were used to assess and monitor changes in soil properties through the acquired Landsat images of the years 2000 and 2020 (Gilabert et al., 2002). The Landsat images were obtained freely from the United States Geological Survey (USGS) repository website. The satellite images were downloaded using path 191 and row 055 and georeferenced with World Geographic System (WGS) 84 datum (Jiang et al., 2006; Jeevalakshmi, 2017). The images were downloaded during low cloud cover to avoid seasonal variation and mitigate disruption in data sets (Table 1).

Table 1. Spectral index used for the present study.

Landsat 7 ETM+	Landsat 8 OLI/TIR
B-3:Red (0.631 – 0.69um)	B-4: Red (0.636 – 0.673um)
B-4: Near-infrared (0.77 – 0.90um)	B-5: Near-infrared (0.77 – 0.90um)
B-6: Thermal (10.40 – 12.50 um)	B-10&11: Thermal infrared 1&2 (10.60 – 11.19um) & (11.50 – 12.51um)

B: denotes Bands, OLI: Operational land image

2.3 Predicted soil-adjusted vegetation index (SAVI)

To perform the SAVI, Dorigo et al., (2007) formula was used in ArcGIS 10 ESRI (Environmental software research Institute) in equation (1).

$$SAVI = \frac{(\mathrm{NIR} - \mathrm{RED})}{\mathrm{NIR} + \mathrm{RED} + \mathrm{L}}(1 + L) \quad \text{..... (1)}$$

Where NIR is the Near-infrared representation, RED is the visible red, and L is the constant or correction factor (Huete, 1988).

2.4 Predicted land surface temperature assessment

The Predicted land surface temperature (LST) variables were often used to monitor soil temperature changes and serve as an important spectral index that provides fundamental information for human survival (Cai et al., 2018). In this study, two steps were employed to assess the PLST. To perform the first step using Landsat 7, the spectral index of band 6 was used (Cai et al., 2018):

$$R\tau m^{6} = \frac{V}{255(R_{\max} - R_{\mathrm{mln}})} + R_{\mathrm{mln}} \quad \text{..... (2)}$$

The R_{TM6} denotes luminance of radiation; digital numbers of band 6 were used to represent the V. Rmaximum = 1.896: Rminimum = 1.896". Thereafter, equations (3) and (4) were used to convert the PLST (luminance radiation) into kelvin and degree Celsius.

$$T_{\mathrm{k}} = \frac{K_1}{ln\left\{\frac{K_2}{\mathrm{RTM6}\ /\mathrm{b}}\right\} + 1} \quad \text{..... (3)}$$

$K_1 = 1260.56$; $K_2 = 607.66$. The K_1 and K_2 are constant and 1.239 (µm) spectral ranges were used to represent b.

$$T^{0}c = T_{\mathrm{k}} - 273 \quad \text{..... (4)}$$

Thereafter, Vegetation proportion (VP) data derived from the year 2020 in equation (1) were used to support the estimation of the PLST for the year 2020. The PLST estimation was expressed in equation (5):

$$VP = \left(\frac{\mathrm{PSAVI} - \mathrm{PSAVI}_{\mathrm{min}}}{\mathrm{PSAVI}_{\mathrm{max}} - \mathrm{PSAVI}_{\mathrm{min}}}\right)^{2} \quad \text{..... (5)}$$

The PSAVI $_{\mathrm{min}}$ and $_{\mathrm{max}}$ was derived from the minimum and maximum value of PSAVI. The PSAVI value ranges from -1 and 1. Equation (6) was used to assess the VP of the study area.

$$VP = \left(\frac{\mathrm{SAVI} + 1}{2}\right)^{2} \quad \text{..... (6)}$$

The Landsat 8 Operational land images (OLI) were used to perform step 2. The digital numbers (DNs) of bands 10 and 11 were used to estimate the (spectral radiance, (LSE) Land surface emissivity, and (BT) Brightness temperature (Rasul et al., 2015). For the year 2020 PLST, the equations described by Jesus and Santana (2017) were used to assess the LSE, BT, and of the study area.

$$L\lambda = 0.03342 * \text{spectral band10} + 0.1 \text{ and spectral band11} + 0.1 \quad \text{..(7)}$$

$$LSE = 0.004 * PV + 0.986 \quad \text{..... (8)}$$

$$BT = \frac{K2}{ln\left\{\frac{K1}{L\lambda}\right\} + 1} - 273.15 \quad \text{..... (9)}$$

BT is measured in Celsius; K1 and K2 are the thermal calibrations constant and both are measured in Kelvin.

$$PLST = \frac{BT}{1(\frac{\lambda BT}{PV} * \ln LSE)} \quad \text{..... (10)}$$

2.5 Soil Analyses and Spatial mapping

Random and reconnaissance sampling method was employed using FAO (2007) soil survey manual. With the aid of a soil auger, 100 samples were collected at 0 to 20 cm soil depths and their coordinate points were tied to each sampling point and documented using a global positioning system (GPS) device. Afterward, the representative soil samples were further subjected to 2 mm diameter sieving and air-drying before being taken to routine soil laboratory analysis. Particle size distribution was examined using the hydrometer method (Bouyoucos, 1962). Soil pH was determined using a pH glass meter electrode in 1:2

suspensions of water (McLean et al., 1982). Organic carbon (OC) was examined by Walkley and Black, (1939) using the acid chromic oxidation method. Total nitrogen (TN) was examined using the Macro Kjeldahl method (Bremner and Mulvaney, 1982). Available phosphorus (P) was determined by the Bray-1 method (Nelson and Sommers, 1996). The potassium (K) was examined by a flame photometer (Kuo, 1996). Finally, effective cation exchange capacity (ECEC) was determined through the summation method using acidity and exchangeable cations (Chapman, 1965).

2.6 Data modeling and Analysis

In the last decades, ordinary krigging (OK) interpolation remains one of the unbiased and superior linear spatial prediction methods for precision agriculture (Radocaj et al., 2021). In this study, we subjected the analyzed soil properties to the OK method in ArcGIS v.10 extensions geostatistical analyst tool to assess the accuracy of the interpolation and spatial autocorrelation. The present study employed dependent (SAVI and LST) and independent (soil nutrients) variables to assess the soil suitability for maize production (Fig 2). Furthermore, descriptive and geo-statistics methods were used to generate possible correlations. Thereafter, the soil properties were spatially interpolated using the Ordinary Krigging (OK) method in ArcGIS v.10.5 extension analyst geostatistical tool. Accuracy and cross-validation of soil properties were examined by semi-variogram modeling including the isotropic detection (equations 11 and 12) (Wang, 1999; Western et al. 2004).

$$Z*=(x_0)=\sum_{i=1}^{N}\lambda^1 z(x_i) \quad \text{..... (11)}$$

Where Z* represents the unknown sample at (x_0) location, while (x_1) represents known soil sampling values, is the sampled weighting coefficient and n is the neighborhood interpolated locations.

$$\gamma^{(h)}=\frac{1}{2N(h)}\sum_{i=1}^{n^{(h)}}[z(x_i)\text{-}z(x_i+h)]^2 \quad \text{..... (12)}$$

Where z (xi) is the value of the variable, is the lag, and N(h) is the pairs of sample points separated by h.

Accuracies of the interpolated soil properties, such as mean error (ME), root mean square error (RMSE), nugget (C_0), sill ($C+C_0$), and range (a) were used as indicators (Schloeder et al., 2001). The basic spatial parameter used in this study enables easy classification and characterization of soil properties. The formula described by Schloeder et al., (2001) in equations (13) and (14) was used to assess the ME and RMSE:

$$ME=\frac{1}{N}\sum_{i=1}^{N}[z(x_i)\text{-}\check{Z}(x_i)] \quad \text{..... (13)}$$

$$RMSE=\frac{1}{N}\sum_{i=1}^{N}[z(x_i)\text{-}\check{Z}(x_i)]^2 \quad \text{..... (14)}$$

2.7 Multi-criteria evaluation

The utilized AHP and weighted overlay method were used as dependent and independent variables for maize soil suitability. The independent and dependent variables were selected based on the proposed FAO land criteria evaluation and supported by Oluwatosin and Ogunkunle (1991), for rainfed maize soil suitability (Table 2). Thereafter, the AHT and weighted method were performed in ArcGIS 10 software. The criteria were further subjected to the Random inconsistency index (RI) and the consistency ratio was then calculated using the principal eigenvalue (Saaty, 2008). Afterward, the AHP and the comparison matrix were used to classify the soils into suitability classes using the formula described by Saaty, (1977) in equations (15) and (16).

$$\text{Weighted}=\sum_{i=1}^{N}Ci*W_n \quad \text{..... (15)}$$

Where Ci is the reclassified criterion and Wn is the weighted number of data.

$$S=f(x,\ldots\ldots,x_n) \quad \text{..... (16)}$$

Where S is the suitability level for land criteria.

Table 2. Modified maize soil suitability ratings for rainfed.

Suitability ratings (%) classes	100 Highly (S1)	85 Moderately (S2)	60 Marginally (S3)	< 40 Not suitable (N1)
RST variables				
Slope (%)	2-4	4-8	8-16	16-20
Rainfall at growing season (mm)	700-800	600-700	500-600	<500
PLST index (°C)	22-25	20-22	18-20	16-18
drainage	Perfectly	Moderately	Imperfectly	poorly
PSAVI	0.37 – 0.79	0.22 – 0.37	0 – 0.218	-0.30 - 0
Soil variables (0-20cm)	I			
Total N (%)	0.08-0.15	0.08-0.04	0.02-0.04	<0.02
Avail P (mg/kg)	13-22	6-13	3-6	<3
Potassium (cmol kg $^{-1}$)	0.3-0.5	0.2-0.3	0.1-0.2	<0.1
Nutrient retention (n)				
ECEC (cmol kg $^{-1}$)	10-15	5-10	3-5	<3
Organic matter (g/kg)	3 - 4	2-3	1- 2	<1
Texture	Sandy clay loam	Sandy Loam,	Loamy sand	Sandy
(%)	15-40	40-60	60-75	75-90

S1: Highly (100%); S2: Moderately (85%); S3: Marginally (60%) and N1: Not suitable (<40%). Modified from Oluwatosin and Ogunkunle, (1991).

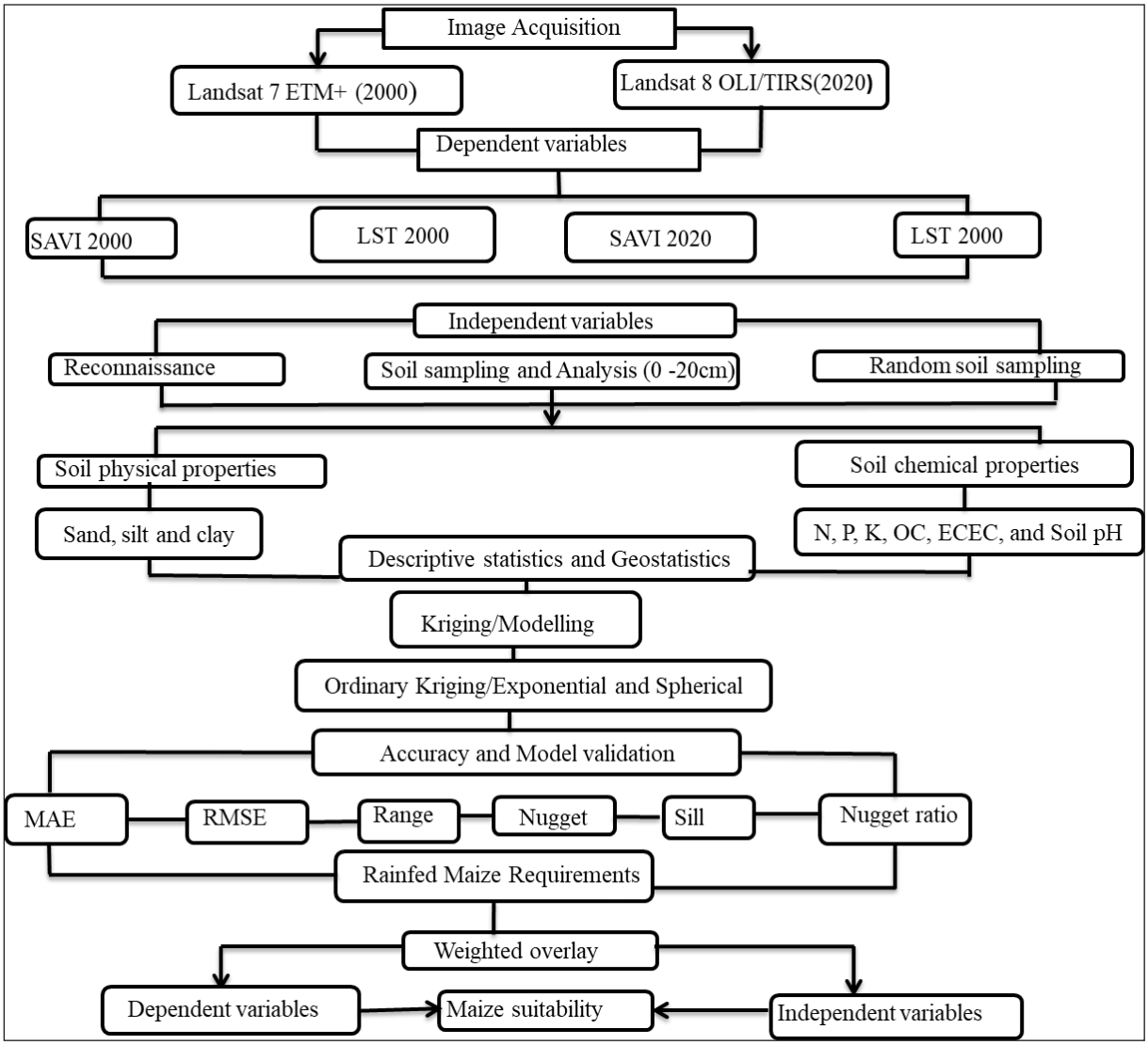

Figure 2. Workflow of the study.

3. Results and Discussion

3.1 Maize soils suitability using satellite-based covariates

Figures (3) and (4) showed that the SAVI and LST ranged from -1 (low) to 1 (high) in the study area. The observed low SAVI in the year 2020 suggests the presence of low vegetation cover and can therefore be traced to an increase in anthropogenic activities such as illegal tree felling and intensive cattle grazing. Moreover, deforestation and indiscriminate grazing are one of the threats faced by developing countries such as Nigeria (Nguetnkam and Dultz, 2011). Additionally, Staver et al., (2011) stated that pastoralism and deforestation tend to result in low soil nutrients, especially in the savanna region. Furthermore, Lie et al., (2013) pinpointed that SAVI techniques serve as one of the efficient spectral vegetation indices used for monitoring changes in soil properties, especially in an area with low vegetation cover. According to Frederiksen, (1993), SAVI is becoming an acceptable technique used in the support of crop nutrients assessment. The result of the present study can also be found in the study of Wu et al., (2018) who effectively correlate SAVI with soil pH and total nitrogen for a site-specific location using Landsat images.

The LST spatial variation of the study area ranged from 23.5^0 to 39.9^0 Celsius (See Fig 4). The sudden increase of the LST in the year 2020 could be a result of global climate change. It was also noticed that the study area is faced with consistent bush burning and deforestation. Moreover, according to Yao et al., (2004) sudden increase in surface temperature can lead to low crop yield. Besides, Wang et al. (2018) posit that a high increase in surface temperature can be regarded as a major environmental threat posed to crop farmers, especially in sub-Saharan Africa. The present study also coincides with the study carried out by Post et al., (1994) who utilized SAVI and LST as environmental covariates to study soil surface reflectance of soil properties for site-specific locations. Additionally, the spectral index random relationship observed in the present study is also by Sandholt et al., (2002).

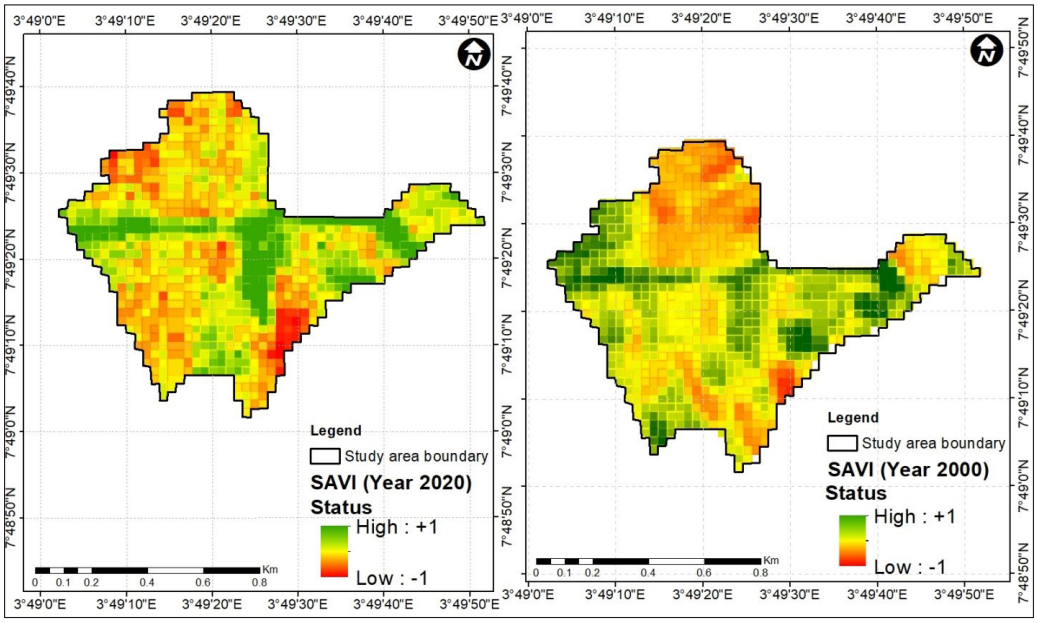

Figure 3. The predicted soil-adjusted vegetation index for the years 2020 and 2000.

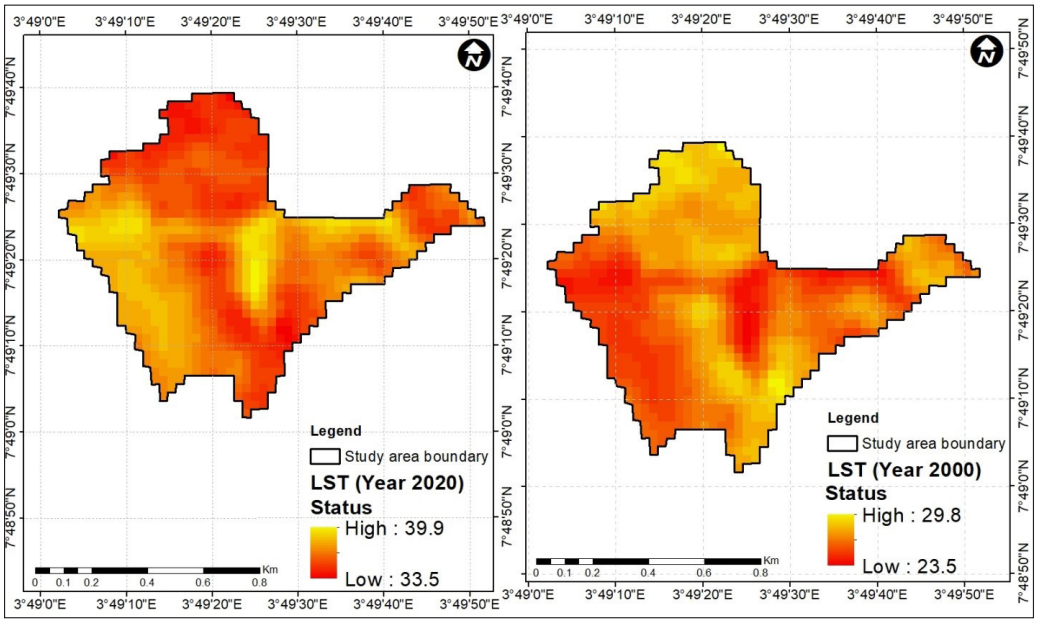

Figure 4. The predicted land surface temperature for the years 2020 and 2000.

3.2 Descriptive and correlation analysis of soil properties

Tables (3) and (4), show the description and correlation of the physical and chemical soil properties of the study area. The study reported by Carvalho et al., (2002) stated that when soil properties kurtosis and skewness values of soil properties are less than 3, such soil properties can be considered to have normal frequency distribution. From the results, it was observed that the majority of the soil properties had normal frequency distribution.

Table 3. Description of physical and chemical soil properties.

	Sand	Silt	Clay	OC	TN	Soil pH	ECEC	P	K
	(%)	(%)	(%)	(%)	(%)		mg kg^{-1}		cmol/kg
Min	85.8	3.0	4.1	1.2	1.1	3.0	3.8	2.0	1.2
Max	92.9	6.8	8.4	1.1	1.4	7.9	6.8	12.9	3.0
Median	88.4	5.4	5.7	1.0	1.3	3.9	7.1	5.8	1.2
Std. dev	3.0	1.6	1.8	1.1	1.8	2.0	1.0	4.9	1.5
Skewness	0.9	0.8	0.7	1.5	4.0	1.9	-2.0	0.4	2.0
Kurtosis	1.3	0.8	1.2	1.2	7.9	1.4	4.0	-0.4	3.2

Minimum (Min); Maximum (Max); Standard deviation (Std. dev)

Table 4. Soil correlation of the studied properties.

			OC	TN			Sand	Silt	Clay
	Soil pH	ECEC mg kg^{-1}	(%)		P mg kg^{-1}	K cmol/kg	(%)		
Soil pH	1								
ECEC	0.63	1							
OC	0.31	0.24	1						
TN	0.05	0.05	0.12	1					
P	0.15	-0.10	0.10	-0.17	1				
K	0.55	0.86	0.25	-0.10	-0.21	1			
Sand	0.02	0.03	0.00	0.01	0. 48	0.18	1		
Silt	0.09	0.02	0.01	0.06	0.29	0.89	-0.86	1	
Clay	0.08	0.00	0.01	0.04	0.30	0.88	-0.89	0.53	1

3.3 Spatial modeling of soil properties

In this study, the soil texture ranged from clay to sandy clay loam. Oluwatosin and Ogunkunle (2011) opined that soil texture within the range of sandy clay loam can be classified as suitable for maize production. The fertility soil distribution maps of the study area were produced using OK interpolated techniques. The soil TN ranged from (< 0.1%) very low to (0.2%) low. The low concentration of soil TN observed in the study area could be attributed to undulating topography or slope etc. Nevertheless, high P was observed with pockets of low concentration (Fig 5). The pH of the studied soils ranged from 5.6 (moderately acidic) and 7.3 (Neutral). The high soil OC distribution observed can be traced to litter or waste material decomposition in the study area (Fig 6). However, the inappropriate use of pesticides and fertilizers in the study area could be responsible for the soil to be acidic, and this interim with the result of Wang et al., (2018). In addition, the vicinities dumping of waste materials into seasonal rivers and streams which are sometimes used for irrigation could harbor toxic substances and therefore be responsible for the soils to moderately acidic. The spatial distribution concentration of K and ECEC concentration was also documented in the study soils (Fig 7).

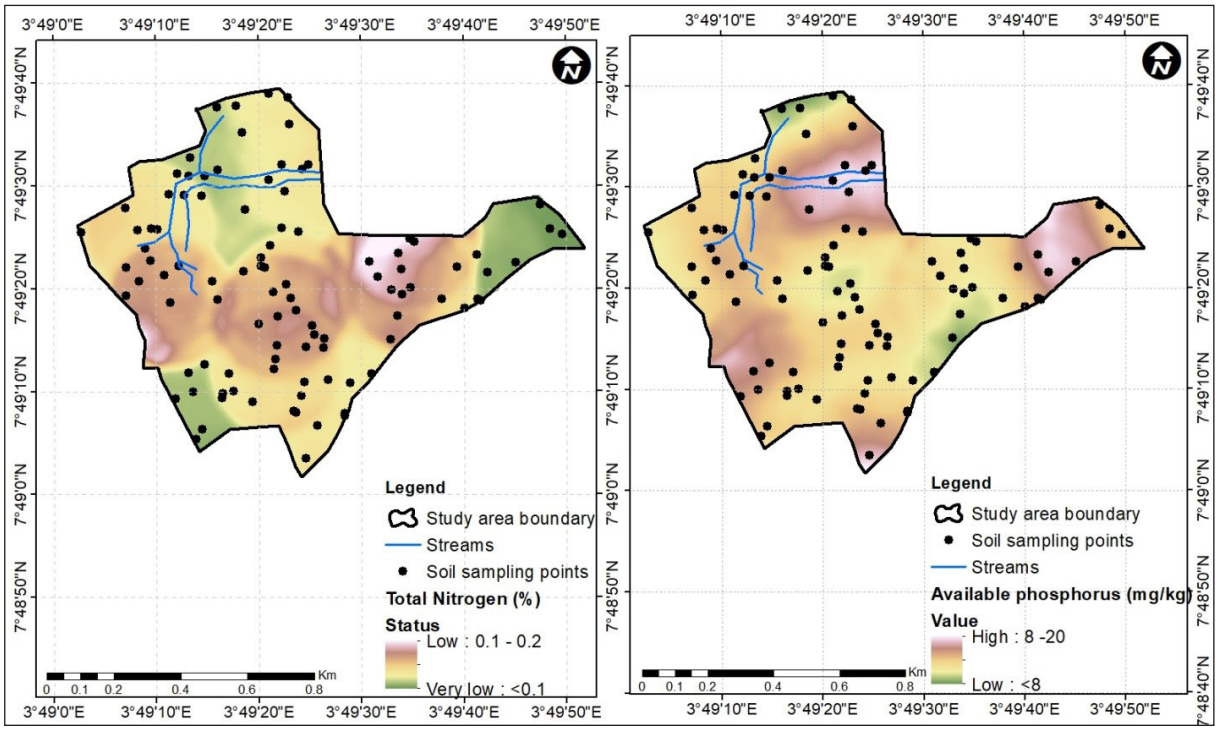

Figure 5. Distribution of total nitrogen and phosphorus.

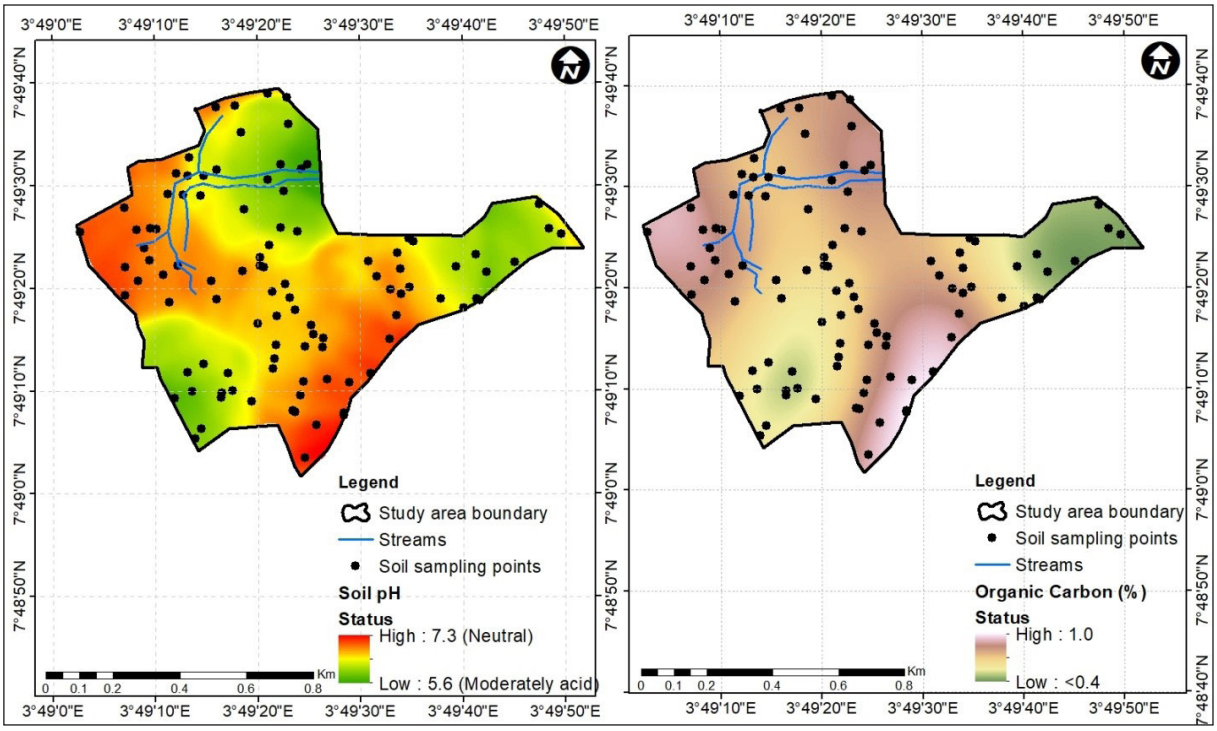

Figure 6. Distribution of soil pH and organic carbon.

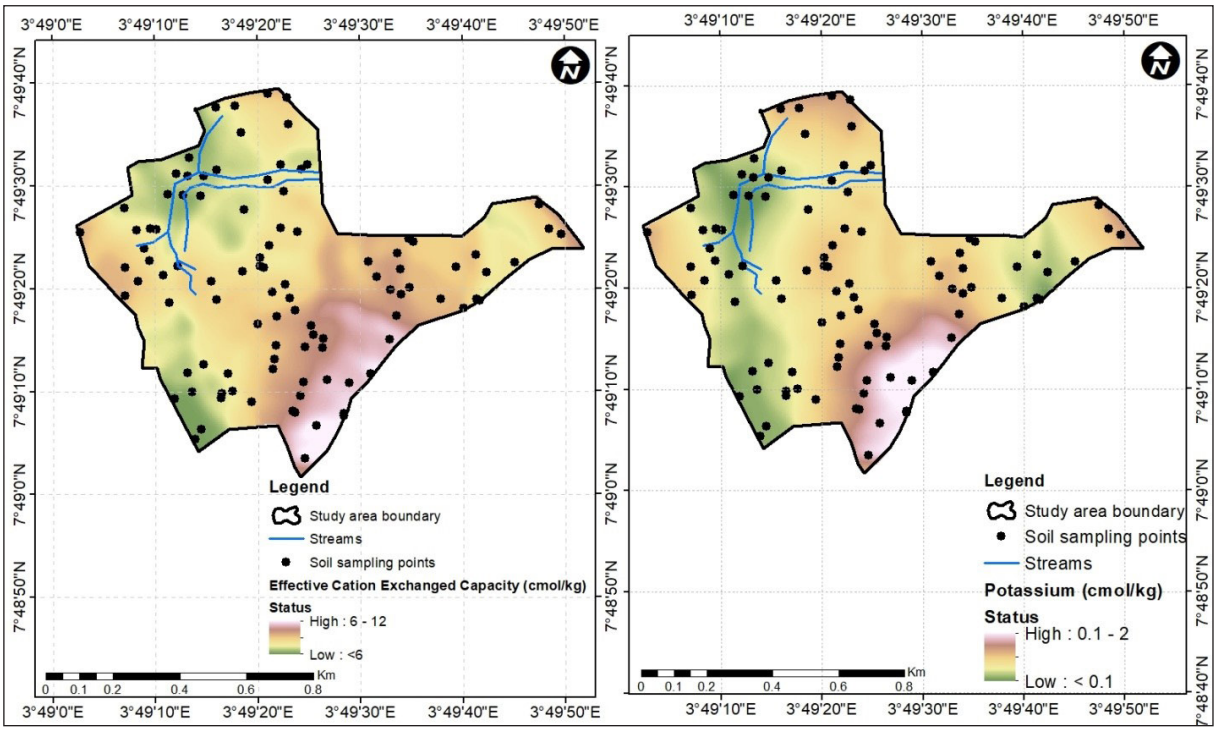

Figure 7. Distribution of effective cation exchanged capacity and potassium.

The ME and RMSE were used to identify the accuracy of the soil properties using OK interpolation (Table 5). The ME and RMSE values showed that the interpolated soil properties had lower nugget effects when a model with exponential. According to Robertson, (2008), soil properties with low nuggets have been widely used for site-specific agriculture. In the present study, a ratio less than 25% (percent) means strong spatial variance and those within the ratio of 25 % and 75 % means moderate distribution of soil properties, therefore, from the interpolated soil analysis, soil pH, K, OC, and silt soil texture gave the strong spatial dependency for an exponential model, while the spherical model provided moderate spatial dependency for TN, P, CEC, clay, and sand. However, the moderate spatial dependency can be traced to an increase in human activities such as erosion hazards, abuse of fertilizer, and global climate change (Cambardella et al. 1994). The results of the present study are also following the research conducted by Venteris et al., (2014).

Table 5. Accuracy and validation of soil properties.

	Model	ME	RMSE	Range (m)	Nugget (C0)	C0/(CO+C)	Nugget ratio (%)
Soil pH	EX	0.3	0.9	264	0.05	0.21	21
N (%)	SP	0.1	0.8	236	12.9	0.30	30
K (cmol/kg),	EX	0.2	0.5	269	16.1	0.16	16
P (mg kg^{-1})	SP	0.4	3.3	214	11.66	0.44	44
OC (%)	EX	0.4	0.1	267	0.03	0.13	13
CEC (cmol/kg)	SP	0.2	1.2	271	0.01	0.50	50
Sand (%)	SP	0.3	11	972	0.06	0.58	60
Silt (%)	EX	0.1	0.6	254	0.04	0.24	24
Clay (%)	SP	0.4	3.9	567	0.09	0.60	60

EX: Exponential, SP: Spherical

3.4 Maize soil suitability using AHP and weighted overlay

The dependent and independent layers based on the AHT and weighted techniques were used to assess the maize suitability using a pairwise comparison matrix (Table 6). The present study employed a scale of 0 to 100 % to itemize the procedure and a 7.5 % ratio was obtained for consistency. The soil fertility distribution and thematic map layers of the PLST, PSAVI, existing river, and soil map of the study area were coupled together and produced in a raster format. The results of the thematic layers were rated in the following order: 35 % (soil nutrients), 20 % (LST), 20 % (SAVI), 15 % (river), and 10 % (road) to produce the maize soil suitability of the area (Fig 8).

Table 6. Weights criteria using pairwise comparison.

	Soil nutrients	PLST	PSAVI	River	Road	Priority	Scale
Soil nutrients	2	1	1	0.5	1	35	1
PLST	1	0.5	2	1	0.5	20	2
PSAVI	0.5	1	0.5	1	1	20	3
River	0.5	1	1	0.5	0.5	15	4
Road	1	0.5	1	1	0.5	10	5

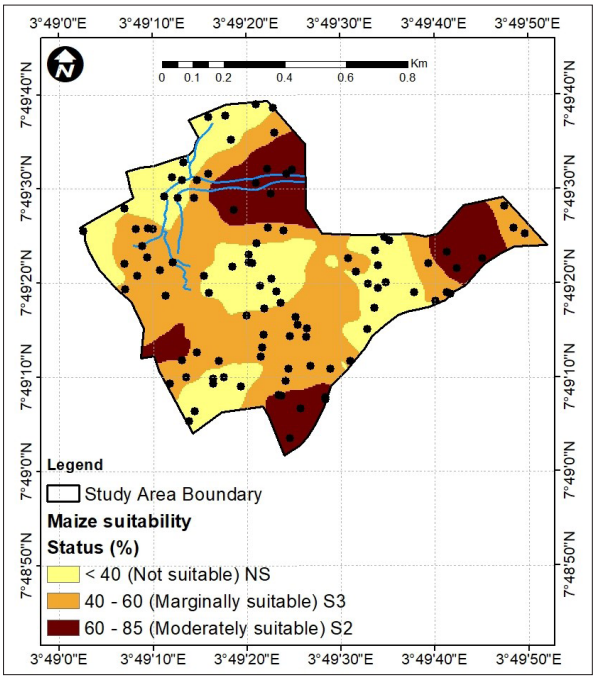

Figure 8. Maize soil suitability.

4. Conclusions

The study focused on the variability assessment of soil nutrients and its impacts on soil suitability for maize production using remote sensing (RS) and geographic information system (GIS) techniques. The increase and awareness of precision agriculture have necessitated the integration of GIS, RS, and geo-statistics methods, especially in the spatial environment of today. The combined GIS and RS techniques through multi-criteria have assisted in efficiently mapping the soil nutrients of the area in less time and with higher accuracy for maize production. The AHT shows that RS variables - LST, SAVI, and the interpolated soil properties can help individual or soil users, especially farmers to identify suitable land areas for precision farming and optimum crop production. The soil fertility distribution maps generated showed that the exponential model gave the lowest values of ME and RMSE than the spherical model. However, the weighted overlay and AHT used helped to partition the studied soils into moderately (85%), marginally (60%), and not suitable (40%) for maize production. The limiting factors were an increase in anthropogenic activities (such as abuse of pesticides or fertilizers), an undulating slope, an increase in surface temperature, and erosion hazard. The present study proved that integration of OK, AHT coupled with remotely sensed-based spectral indices such as LST and SAVI will help farmers and policy-makers for sustainable and precision agriculture.

5. Data availability statement

The data that support the findings of this study are not available but can be provided upon reasonable request.

Acknowledgment

The author wishes to thank the authorities of the Institute of Agricultural Research and Training Moor Plantation, Ibadan, Obafemi Awolowo University for their support and understanding.

References

Adekiya, A.O., Agbede T.M., (2009). Growth and yields of tomato (Lycopersicon esculentum Mill) as influenced by poultry manure and NPK fertilizer. Emirate Journal of Food Agriculture; 21(1): 10–20.

Bouyoucos, G.H., (1962). Hydrometer method for making particle size analysis of soils. Agronomy Journal 54: 464-465. DOI: 10.2134 /agronj1962.00021962005400050028x.

??Bremner, J. M., & Mulvaney, C. S. (1982). Nitrogen-Total.

Cambardella. C.A., Moorman. T.B.,Novak, J.M., Parkin, T.B., Karlen, D.L., Turco. R.F, and Konopka, A.E, (1994). Field–scale variability soil properties in central Iowa soils. Soil Science Society of American Journal 58:1501-1511. doi:10.2136/sssaj1 994.03615995005800050033x.

Chinese Journal of Applied Ecology. 2018; 29. https://doi.org/10.13287/j.1001-9332.201803.038

Carvalho, J. d., Silveira, P. d., & Vieira, S. R. 2002. Geoestatística na determinação da variabilidade espacial de características químicas do solo sob diferentes preparos. Pesquisa Agropecuária Brasileira, 37(8), 1151-1159.

Dorigo, W., Richter, R., Muller, A., (2005). A lookup table approach for biophysical parameter retrieval by radioactive transfer model inversion is applied to the wide field of view data. In: Proceedings of the Fourth EARSeL Workshop on Imaging Spectroscopy, Warsaw, Poland.

Ekeleme, F., Jibrin, J.M., Kamara, A.Y., Oluoch, M., Samndi, A.M., Fagge, A.A. Assessment of the relationship between soil properties, Striga hermonthica infestation and the on-farm yields of maize in the dry Savannas of Nigeria. Crop Prot. (2014) 66, 90–9

FAO. Guidelines for soil description. Rome: FAO; (2007). Page. 109.

FDALR. The Reconnaissance Soil Survey of Nigeria. 1990; volume. 2.

Frederiksen, P. (1993). Satellite-based assessment and monitoring of land degradation in semi-arid tropical Africa: aspects of the soil/vegetation complex.

Ge, F.L., Zhang, J.H., Su Z.G., Nie X.J., (2007) Response of changes in soil nutrients to soil erosion on a purple soil of cultivated sloping land. Acta Ecol Sin 27:459–463. doi: 10.1016/s1872-2032(07)60018-3

Jeevalakshmi, & Manikiam, B. (2017). Land Surface Temperature Retrieval from LANDSAT data using Emissivity Estimation.

Jesus, J. B., Santana, I. D. M., (2017). Estimation of land surface temperature in caatinga area using Landsat 8 data, 7, 150157. Retrieved from https//periodicos.ufpe.br/revistos/hrs/article/view/22766101 (3) , 366-378

Jiang, Z., Huete, A. R., Chen, J., Chen, Y., Li, J., Yan, G., 2006. Analysis of NDVI and scaled difference vegetation index retrievals of vegetation fraction. Remote Sensing of Environment,

Liu L, Wang H., Dai W, Lei X., Yang X, Li X (2015) Spatial variability of soil organic carbon in the forestlands of northeast China. J For Res 25 (4): 867–876.

Marko K., Elfeki A.M.M., Alamri N.S (2014). Geostatistical analysis using GIS for mapping groundwater quality: a case study in the recharge area of Wadi Usfan, western Saudi Arabia. Arab J Geosci 7:5239–5252

Martey, E., Wiredu, A. N., Etwire, P. M., Fosu, M., Buah, S. S. J., Bidzakin, J., Kusi, F. (2014). Fertilizer adoption and use intensity among smallholder farmers in Northern Ghana: A case study of the AGRA soil health project. Sustainable Agriculture Research, 3, 24–36. doi:0.5539/sar.v3n1p24.

McLean E.O. pH and lime requirements. In: Page ALE, editor. Methods of Soil Analysis. Madison, WI, USA: American Society of Agronomists Inc.; (1982)

Nelson, D.W., Sommers, L.E., (1996). Total carbon, organic carbon, and organic matter. In: Sparks et al. (Eds.), Methods of Soil Analysis. Part 3: Chemical methods. SSSA, Madison, WI, USA.

Oluwatosin, G. A., Ogunkunle, A. O., (1991). Suitability rating of some soils of the savanna zone of South-western Nigeria for rainfed Maize. Nigeria Journal of Soil Science 10: 1-24.

Nguetnkam, J.P., & Dultz, S. (2014). Clay dispersion in typical soils of north Cameroon as a function of ph and electrolyte concentration. Land Degradation & Development, 25.

Rasul, A., H., Balzter, C., Smith, 2015. Spatial Variation of the Daytime Surface Urban Cool The island during the Dry Season in Erbil, Iraqi Kurdistan, from Landsat 8." Urban Climate 14: 176–186.doi:10.1016/j.uclim.2015.09.001.

?Relationship between soil color and Landsat reflectance on semiarid rangelands. Soil Science Society of America Journal 58: 1809 ± 1826.

Radocaj, D., Juriši´c, M., and Antoni´c, O., (2021). Determination of Soil C:N Suitability Zones for Organic Farming Using an Unsupervised Classification in Eastern Croatia. Ecol. Indic. 123, 107382.

Robertson, G.P., (2008). In: GS+: Geostatistics for the Environmental Sciences. Gamma Design Software. Plainwell, Michigan, USA.

Saaty, T.L., (1977). The Analytic Hierarchy Process: Planning, Priority Setting. Resource Allocation. McGraw-Hill International, New York, NY, USA.

Saaty, T.L., (2008). Decision-making with the analytic hierarchy process. Int. J. Services Sciences, Vol. 1, pg 83–98.

Sandholt I., Rasmussen K., Andersen J (2002). A simple interpretation of the surface temperature/vegetation index space for assessment of surface moisture status. Remote Sens Environ 79:213–224.

Sys, I., E. Van-Ranst, and J. Debveye. (1991). Land evaluation. Part 1: principles in land evaluation and crop production calculations. General Administration for Development Cooperation, Brussels, Belgium (Agricultural Publications No. 7).

Staver, A. C., S. Archibald, and S. A. Levin. (2011). The global extent and determinants of savanna and forest as alternative biome states. Science 334:230–232.

Schloeder C.A., Zimmermen NE., Jacobs M.J (2001). Comparison of methods for interpolating soil properties using limited data. Soil Sci Soc Am J 65:470–479.

USDA Soil Taxonomy. Soil Survey Staff, Agriculture Handbook, No. 436, 2nd ed. Washington, DC: United States Department of Agriculture, Natural Resources Conservation Service; (1999). p. 869.

United Nations. (2017). World Urbanization Prospects: The Revision United Nations (Population Framework for decision support tools for integrated soil fertility management in sub-Saharan Africa (Draft). Paper presented at the African Soil Health Consortium inaugral workshop.

Venteris, E., Basta, N., Bigham, J., Rea, R., (2014). Modeling spatial patterns in soil arsenic to estimate natural baseline concentrations. J. Environ. Qual. 43 (3), 936–946.

Wu, B., Guo, S.H., Li, B.L., Zhang LY. Draft of soil environmental function regionalization of China.

Walkley, A., Black, I. A., (1939). An examination of Degtjareff method for determining soil 714 organic matter and a proposed modification of the chronic acid titration method.Soil Science, 71537, 29 – 38. DOI: 10.1097/00010694193401000-00003.

Wang, X., Ma, X., & Yan, Y. (2017). Effects of soil C: N:P stoichiometry on biomass allocation in the alpine and arid steppe systems. Ecology and Evolution, 7, 1354 - 1362.

Western, A. W., S.-L. Zhou, R. B. Grayson, T. A. McMahon, G. Blöschl and D. J. Wilson (2004) Spatial correlation of soil moisture in small catchments and its relationship to dominant spatial hydrological processes. Journal of Hydrology, 286 (1-4), pp. 113-134.

Warrick, A.W., (1998) Spatial variability. In Environmental soil physics, ed. D. Hillel, 655–675. San Diego, Calif.: Academic Press.

Wang, Z. Q., (1999), Geostatistics Applied in Ecology. Beijing: Science Press. 109-126 [in Chinese]

Yao, X., Fu, B., Lu, Y., Sun, F., Wang, S., Liu, M., (2004). Comparison of four spatial interpolation methods for estimating soil moisture in a complex terrain catchment. PLoS ONE 8 (1)

Zhang, Z., Yu, D., Shi, X., Weindorf, D.C., Sun, Y., Wang, H., Zhao, Y. (2010). Effects of prediction methods for detecting the temporal evolution of soil organic carbon in the Hilly Red Soil Region, China. Environ. Earth Sci., 64, 319–328.

JJEES

JJEES (2023) 14 (1): 19-29
ISSN 1995-6681

Jordan Journal of Earth and Environmental Sciences

Utilization of Jordanian Bentonite Clay in Mortar and Concrete Mixtures

Ayoup M. Ghrair[1*], Adi J. Said[2], Hussein Al-Kroom[3], Naela Al Daoud [2], Bassel Hanayneh[3], Ahmad Mhanna[4], and Ahmed Gharaibeh[5]

[1] Department of Water Resources and Environmental Management, Al-Balqa Applied University, Salt 19385, Jordan.
[2] Foundational Science Research Division, Research for Development Pillar, Royal Scientific Society, Amman 11941, Jordan
[3] Department of Civil Engineering, The University of Jordan, Amman 11942, Jordan
[4] Middle East /North Africa Region at American Concrete Institute, Dubai, United Arab Emirates
[5] Ministry of Energy and Mineral Resources, P.O Box 140027, Amman 11814, Jordan

Received 9th March 2022; Accepted 22nd May 2022

Abstract

The reduction of cement content in mortar and concrete mixtures reduces both the amount of CO_2 in the environment and the cost of production. Therefore, this research utilizes Jordanian bentonite as a pozzolanic material in both mortar and concrete sample mixtures. Three types of Jordanian bentonite samples were added to the mortar and concrete mixtures 1: natural bentonite 2: heated bentonite at 250 °C, 550 °C, and 750 °C, and 3: calcium-bentonite. Then, 21 mortar mixtures were prepared. Bentonite was added to the mortar mixtures in weight proportions of 0% (reference sample), 10%, 20%, 30%, 40%, and 50% by cement weight. On the other hand, 9 concrete mixtures were prepared from natural bentonite, heated bentonite, and ca-bentonite with proportions of 0% (reference sample), 10%, and 20% partial replacement of cement weight. The tested results show that heated bentonite at 750 °C achieved close results to the control sample. Moreover, both natural bentonite and Ca- bentonite reduce concrete shrinkage. Concrete permeability was highly reduced by using bentonite, especially Ca-treated, where permeability was reduced by 60%. Cost and environmental analyses were conducted to evaluate the utilization of bentonite.

Keywords: *Bentonite, Compressive strength, SEM-image, XRD-analysis, Thermal gravimetric analysis, Concrete, Cement)*

1. Introduction

Cement is known as an essential plastering material in construction in which it is the commonly used binder in a mortar and concrete mixtures. Many researchers have studied the strength of evolving and hydration process of cement along with its production costs [1-5]. Based on the understanding of the rheological behavior of cement, alternative low-CO_2 emission clinker materials were proposed [6, 7]. It is found that belite-rich cement gives promising results in comparison to Ordinary Portland Cement (OPC) as it has good flow properties and stability [8,9]. However, strength development at an early age is relatively slow. Weathered basalt (WB) was deployed in clinker manufacturing to evaluate its performance as an alternative binder material. The results indicate that WB has low silica, SO_3, and chlorine as well as high content of MgO and Fe_2O_3 which gives a better clinker ability and an environmental advantage [10]. Moreover, experimental investigations into the utilization of natural, waste, and by-product industrial materials as partial replacements for cement have been conducted. The investigations of these materials aimed to produce sustainable production at a low cost. For instance, research works on steel slag [11-13], silica fume [14,15], and fly ash [16,17] present very good results in comparison to the control mixtures i.e. concrete mix with 100% OPC.

Because of the aforementioned effort in finding an economical and environmental partial replacement for cement, Bentonite was introduced to the concrete and mortar mixtures [18-21]. Wilbur C. Knight as an absorbent and swelling material proposed the material and it has been mainly used for the development of oil and gas resources as drilling mud [22]. It is a natural pozzolana predominantly composed of montmorillonite. Bentonite is classified into three categories; sodium bentonite, calcium bentonite, and magnesium bentonite. Its influence on the mixtures is based on its chemical composition in which its effects on the strength of concrete and mortar are changeable. Ahmad S. et al. reported that the compressive strength of cement-bentonite concrete mixtures is lower than that of ordinary concrete mixtures [23]. On the other hand, the work of Memon S. et al. shows an increase in compressive strength in the mixtures containing bentonite compared to the control mixtures without bentonite [24]. Nevertheless, there is a consensus on the feasibility of bentonite's contribution to improving the workability and impermeability of mixtures [25, 26].

In most developing countries, like Jordan, natural resources are used in construction leading to a reduction in the cost and improvement of the quality of construction materials. This study is conducted to produce low-cost mortar and concrete by replacing the cement in mortar and concrete

* Corresponding author e-mail: ayoup.ghrair@bau.edu.jo

with local bentonite in various proportions. Incorporating bentonite in mortar and concrete as a substitute for cement can minimize the depletion of natural resources and materials used in cement and solve environmental problems related to its production process. An investigation of the Jordanian natural resource of bentonite was carried out. Three bentonite samples were collected from three different areas in Jordan to evaluate its potential use in mortar and concrete. The locations of the three areas are as follows in Table (1):

Table 1. The explored bentonite locations in Jordan

The areas	Coordinate system in the WGS 84			
Ein Al-Bayda area	31°	52’	35”	N
	36 °	49’	35”	E
Qa’ Al-Azraq area	31°	48’	22”	N
	36 °	47’	35”	E
Al-yamaniah – Aqaba	29 °	26’	58”	N
	34 °	58’	26”	E

Samples were taken from different three locations. The Ein Al Bayda bentonite and Q’a Al Azraq bentonite are located in the Azraq area and belonged to the same lithological consequence (Neogene-Quaternary basalt and volcanic tuff). However, Al Yamaniyya bentonite belongs to different lithological consequences. It is found within the Pleistocene sediments close to the shoreline [27]. Comprehensive chemical and mineralogical analyses were done for each sample. In addition, an analysis of the cost and CO_2 emissions of the proposed contribution of bentonite was conducted.

2. Methods & Materials:

An experimental program was carried out to create mortar and concrete mixtures with reduced cement content by using a substitution amount of Jordanian bentonite. The properties of each material in the study were extensively examined to assess their effect on performance in the mixtures. Both the materials and the test procedures are described below.

2.1 Materials

2.1.1 Bentonite:

The bentonite clay was collected from the southern area of Al-Azraq (Qa’ Al-Azraq). A comprehensive examination of the material was conducted. The raw bentonite sample was heat-treated at various temperatures 250 °C, 550 °C, and 750 °C utilizing Stackable Electric kilns (Olympic Kilns, Model - 2831HE/240, USA). Afterward, the heated bentonite sample was passed through a 150 µm sieve and then grinded and passed through an 80 µm sieve. Then the produced powder was submicron in size. The median particle size of the grinded sample was 0.51 µm using a laser diffractometer. Bentonite contains negatively charged particles that attract positively charged compounds and trap them in its porous structure. According to the classification scheme of Riddick [28], the stability of the bentonite particles is low at pH = 9.5. The zeta potential is less than 16.6 mV. The electrical conductivity is 79 µS/cm. Figure (1) shows particle size distribution and SEM-image of grinded bentonite. The SEM image shows the needle crystal of Illite.

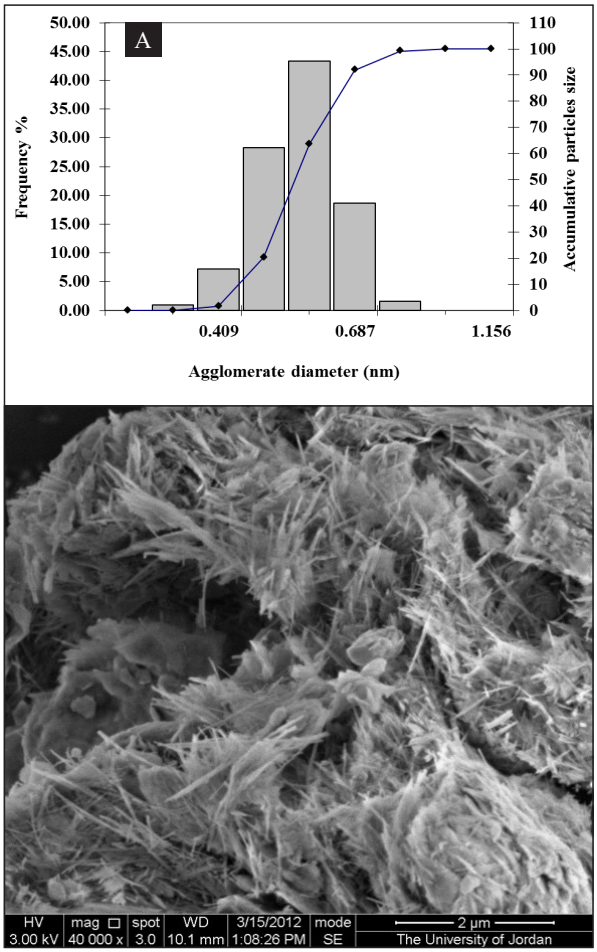

Figure 1. Particles size distribution and SEM-image of grinded bentonite sample. (it was conducted at the University of Jordan)

In addition, the X-ray diffraction (XRD) pattern of natural Jordanian bentonite is given in Figure (2). The spectra indicate that the clay is composed primarily of mixed layers of Illite, Montmorillonite, and Kaolinite. The other peaks are impurities corresponding to quartz. At 550 °C, Kaolinite peaks disappeared. This result is in harmony with the previous literature review. Deer et al [29] reported that Bentonite is a clay rock that consists of minerals mostly of montmorillonite. Moreover, it is found that the Jordanian Bentonite is composed of mixed layers of smectite/illite or Kaolinite with average silica and alumina 28-51 %, and 8.4-15 %, respectively [30]. The chemical composition of natural bentonite is shown in Table (2).

Table 2. Chemical composition of the natural bentonite was conducted by the XRF technique.

SiO_2	Al_2O_3	Fe_2O_3	CaO	MgO	K_2O	TiO_2	P_2O_5	LOI
49.30	14.50	7.46	2.03	3.63	3.O3	0.68	0.80	13.7

Thermal Gravimetric Analysis (TGA) was carried out to determine the sample losses at different temperatures (Isocratic and gradient) of raw Bentonite samples in the open atmosphere condition. The mass of the Bentonite sample used was 5 grams, Max. The heating range was from ambient to 1000°C, at stepwise (Max. Ramp Rate, from Ambient to 104°C the ramp rate was 15°C/min, and from 104°C to 1000°C was 50°C/min). Figure (3) shows the TGA of the air-dried bentonite sample.

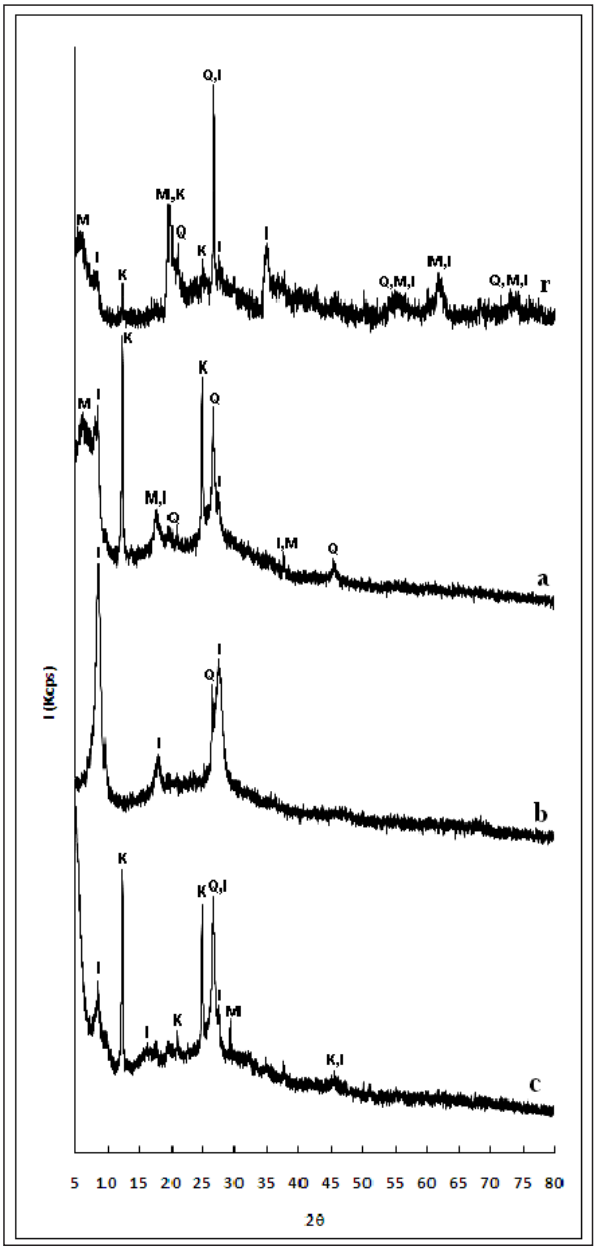

Figure 2. XRD spectra for the bentonite sample (r) randomly powder and oriented crystal distribution [(a) at 105ºC, (b) at 550 ºC, and (c) with ethylene glycol. (**I**: Illite, **K**: Kaolinite, **M**: Montmorillonite and **Q**: Quartz). (The XRD test was conducted at the Royal Scientific Society)

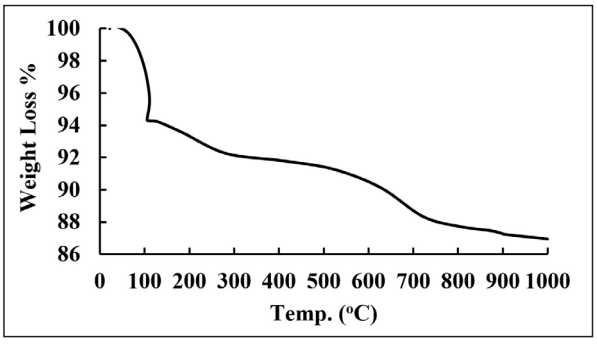

Figure 3. Thermal gravimetric analysis of bentonite (it was conducted at Natural Resources Authority (NRA), Jordan).

The TGA curve of the bentonite sample shows that up to 118 °C, there is a residual humidity (free water) of mass loss characterized by a drop in weight of 6.0%. There is a significant mass loss until 292°C by 2.0% in the second step. At this step, the loss was characterized by crystalline-bound water (dehydration) and some low-temperature organic volatiles. There is a minor mass loss until 500°C by 0.9%. During this step, the total combustion of any carbonaceous organic compounds almost occurs which mainly derives from plant and animal fossils in the bentonite sample, and partial de-hydroxylation occurs. This is followed by a second significant drop, which ends at 744°C, characterized by a mass loss of 3.1% due to mainly de-hydroxylation and combustion of any residual carbonaceous organic compounds as well as decomposition of the present bentonite sample and minerals such as kaolinite. Finally, a second minor drop, which ends at 1000°C, is characterized by mass loss of 0.7% due to residual de-hydroxylation, calcination, and decomposition of the clays and minerals where the actual clay structure (the hydroxyl groups) is destroyed and decomposition of carbonates with the formation of oxides and carbon dioxide occurs. The most notable metal oxide of all formed by these reactions is calcium oxide (*CaO*) which is formed from calcium minerals present in clay in the form of calcite ($CaCO_3$). The results are in harmony with the previous literature review [31].

To produce Ca-Bentonite, the exchangeable cations *Na, K, Ca, and Mg* in the raw bentonite were exchanged to *Ca* form following Sarikaya and Yildiz [32]. A composite sample of raw bentonite was crushed and sieved to pass 150 µm to be used to prepare the Ca-bentonite. The raw bentonite sample was treated with 3 grams $CaCl_2$ /100 g bentonite. The excess $CaCl_2$ was washed out with distilled water. Consequently, the obtained Ca-bentonite sample was dried in an oven at 105 ºC. The dried sample was crushed and passed through a 150µm sieve and kept to be used in the concrete mixtures. Finally, 4 grams of *Ca*-bentonite was taken and washed three times with ethanol until the supernatant liquid electrical conductivity become less than 40 µm. The adsorbed *Ca*-cations in bentonite were replaced by NH_4^+ (Ammonium Acetate solution, 1.0 N). Then, the amount of adsorbed *Ca*-cations was determined.

2.1.2 Cement

Ordinary Portland Cement (Type II) was used in preparing mortar and concrete mixtures. The chemical and physical properties of the cement used are shown in Table (3).

Table 3. The chemical and physical properties of Ordinary Portland Cement (Type II) cement.

Property	Test Result	Limitations	Test Method
% Chloride Content (*Cl*)	0.037	≤ 0.10	BS EN 196-2 [33]
% Sulfate Content (SO_3)	2.97	≤ 3.5	BS EN 196-2 [33]
Setting Time (min)	180	≥ 60	JS 1470-3 [34]
Expansion (mm)	1.00	≤ 10	JS 1470-3 [34]
Compressive strength at 2 days (MPa)	24.5	≥ 10	JS 1470-3 [34]
Compressive strength at 28 days (MPa)	50.3	≥ 42.5 ≤ 62.5	JS 1470-1[35]

2.1.3 Coarse and fine aggregate

For concrete mixtures, two sizes of coarse aggregates (coarse and medium-coarse) and two sizes of fine aggregate (medium-fine and fine) were used, while the latter size was used in the preparation of mortar. The physical properties of aggregates are shown in Table (4) while the combined gradations are shown in Figure (4). Curves indicate the upper and lower limits specified in ASTM C 33 [36] for coarse aggregate and fine aggregate. Weight aggregates should meet the requirements of ASTM C 33. These specifications limit the allowable amounts of substances and provide requests for aggregate characteristics.

Table 4. The physical properties of the aggregate.

Aggregate Type	Bulk Specific Gravity (SSD)	Absorption (%)	Fineness Modulus
Coarse Aggregate	2.68	1.0	---
Medium Coarse Aggregate	2.68	1.0	---
Medium Fine Aggregate	2.66	1.4	---
Fine Aggregate	2.64	0.34	2.5

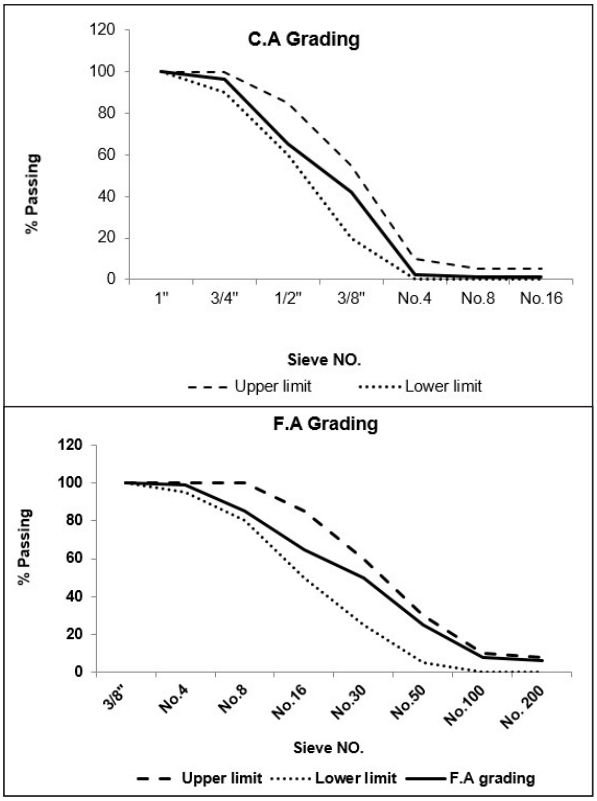

Figure 4. Coarse aggregate (C.A. Grading) and Fine aggregate (F.A. Grading) combined grading curve (

2.1.4 Chemical admixture

For concrete mixtures, a medium-range superplasticizer was used and it was suitable for the components of concrete mixture and greatly improve cement dispersion. The properties of both admixtures are listed in Table (5).

Table 5. The properties of plasticizer/superplasticizer used in the mixtures.

Property	Trowlit P	ADMIX CF 113
Color	Light brown liquid	Brown
Specific Gravity	1.02	1.06
Chloride content	Null	Null
Freezing point	0 °C	--

2.2 Experimental procedure

Twenty-one mixtures of mortar were prepared. The first mix is designated as a control mix where it is free of clay bentonite. The rest of the mixtures were prepared with different proportions of three types of bentonite (natural bentonite, heated bentonite, and Ca-bentonite). The addition of bentonite was introduced as a replacement of 10%, 20%, 30%, 40%, and 50% by the cement quantity. The bentonite was treated with different levels of heat. Three types of heated bentonite were introduced into the mixtures 250 ^{o}C, 550 ^{o}C, and 750 ^{o}C in addition to the natural bentonite. Table (6) shows the proportions of materials of the 21 mortar mixtures where they are considered according to proportion ranges suggested by Jordanian standards [32]. It is shown that the components of the mixtures were kept constant as those in the control one, except water, which was added for each mix to obtain the same workability as the control, mix. During the mortar mix design process, the flow table was used as a workability indicator for the whole mixture, and it was fixed at 70 cm. In this way, it was possible to determine the amount of water needed for each mix.

For each mortar mix, six prisms (40X40X160 mm) and six briquettes (25X25 mm central area) were prepared for sample casting, Figure (5). The samples were prepared to examine the compressive strength, tensile strength, and flexure strength of each mix. The mortar mixtures were performed according to BS EN 196-1 [33]. A standard mixer was used in the mixing process. Afterward, the mortar was filled in the molds and compacted by a Jolting table, and then covered with glass plates and kept in standard conditions (21±2 °C and 50±10% R.H.) to the next day. After 24 hours from casting, samples were taken out from the molds and stored for curing in a water tank under standard temperature (21±2) °C. For each test mix, samples of 6 molds were casted; three of them for the 7 days of age tests and the remaining three for the 28 days of age tests.

a. Compressive and flexural mold

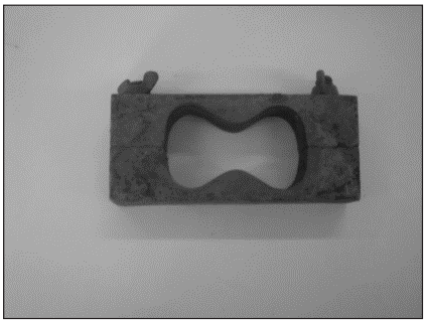

b. Tensile Mold

Figure 5. Molds shapes.

Table 6. Mortar-Bentonite Mixtures Proportions.

Mix Designation	Fine Aggregate (g)	Cement (g)	Water (g)	Bentonite (g)	Type of Bentonite
M1	1350	550	280	0	-
M2	1350	495	320	55	Natural Bentonite
M3	1350	440	360	110	Natural Bentonite
M4	1350	385	400	165	Natural Bentonite
M5	1350	330	440	220	Natural Bentonite
M6	1350	275	480	275	Natural Bentonite
A2	1350	495	320	55	Heated at 250 °C
A3	1350	440	360	110	Heated at 250 °C
A4	1350	385	400	165	Heated at 250 °C
A5	1350	330	440	220	Heated at 250 °C
A6	1350	275	440	275	Heated at 250 °C
B2	1350	495	290	55	Heated at 250 °C
B3	1350	440	320	110	Heated at 250 °C
B4	1350	385	330	165	Heated at 250 °C
B5	1350	330	345	220	Heated at 250 °C
B6	1350	275	360	275	Heated at 250 °C
C2	1350	495	280	55	Heated at 750 °C
C3	1350	440	290	110	Heated at 750 °C
C4	1350	385	320	165	Heated at 750 °C
C5	1350	330	340	220	Heated at 750 °C
C6	1350	275	360	275	Heated at 750 °C

On the other hand, five sets of concrete mixtures were prepared plus the control mix. Each set was developed with two proportions of bentonite, 10%, and 20% by the cement's mass as a partial replacement. One set was mixed with natural bentonite while another one was prepared with Ca-bentonite. The rest of the concrete mixtures were prepared with heated bentonite of 250 °C, 550 °C, and 750 °C, respectively. Table (7) shows the concrete mixture proportions. The mixtures were designed by the Jordanian standard JS 1652 parts 1&2 [34]. For each concrete mix and after the completion of mixing, concrete fresh properties including temperature, slump, density, air content, and setting time respectively were tested. Thereafter, each concrete mix was cast in six cubes (150X150X150 mm) for compressive strength, three cylinders (150X300 mm) for splitting tensile strength, three prisms (100X100X500 mm) for flexural strength, three prisms (70X70X250 mm) for shrinkage, and three molds (200X200X120 mm) for permeability tests according to EN 12390-8 [40]. Molds were covered with plastic sheets and kept in standard conditions (21±2 °C and 50±10% R.H.) to the next day. After 24 hours from casting, samples were taken out from molds and stored for curing in a water tank at standard temperature (21±2) °C until the testing date. The whole strength tests were performed according to JS 1652 parts 3, 5, and 6 [39].

Table 7. Concrete-Bentonite Mixtures Proportions.

Mix Designation	Type of Bentonite	Coarse Aggregate (kg/m^3)	Fine Aggregate (kg/m^3)	Cement (kg/m^3)	Water (kg/m^3)	Bentonite (kg/m^3)	Superplasticizer (L/100 kg cement)
AC	-	1230	589	315	200	0	0
BC	Natural Bentonite	1230	589	283	200	32	1.
CC	Natural Bentonite	1230	589	252	200	63	1.7
DC	Heated at 250 °C	1230	589	283	200	32	0.4
EC	Heated at 250 °C	1230	589	252	200	63	0.8
FC	Heated at 550 °C	1230	589	283	200	32	0
GC	Heated at 550 °C	1230	589	252	200	63	0.6
HC	Heated at 750 °C	1230	589	283	200	32	0
JC	Heated at 750 °C	1230	589	252	200	63	0.4
KC	*Ca*-bentonite	1230	589	283	200	32	1.2
LC	*Ca*-bentonite	1230	589	252	200	63	2

2.3 Statistical analysis

The normality test for the results of all tested hypotheses was conducted for both mortar and concrete mixtures. The normality test results of all measurements were found to be normally distributed, and therefore, the arithmetic mean and standard deviation were calculated.

3. Results and discussion

3.1 Tests of mortar mixtures

Figure (6) shows the mean value of the compressive strength of the mixtures at 7 days of age compared to the mixtures at 28 days of age which are found to be significantly different at $p<0.01$. That is consistent with the fact that compressive strength develops with time. In addition, Figure (6) shows the mean value of the compressive strength of the control mix (0 % of bentonite) compared to the mean value of various proportions of bentonite which are found to be significantly different at $p<0.01$. As it is explained, bentonite was added to the mix in an increment of 10%. Reducing cement content reduces compressive strength. In contrast, compressive strength develops with time. The reduction in strength is referred to as the increase in water content. This interpretation is in line with the finding of Jiang J. et al., whom they indicated that the water content of cement-bentonite mixtures becomes larger as the proportion of bentonite increases [41]. However, the water content does not influence the stability of the mixture. According to the results shown, the mean values of the compressive strength of the mixtures of heated bentonite compared to the natural bentonite mixtures are found to be significantly different at $p<0.01$ and exhibit relatively higher strength which points out to the efficiency of the heat treatment of bentonite [23].

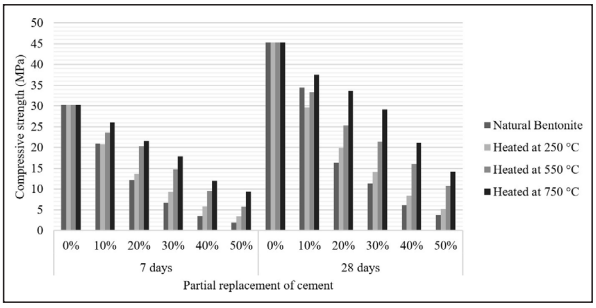

Figure 6. Compressive strength of mortar mixtures at 7 and 28 days.

In general, the results of flexural strength have the same behavior that was observed for the compressive strength of mortar mixtures at 7 and 28 days. Figure (7) shows the mean value of the flexural strength of the mixtures at 7 days of age compared to the mixtures at 28 days of age which are also found to be significantly different at $p<0.01$. That is consistent with the fact that flexural strength develops with time. Furthermore, Figure (7) shows the mean value of the flexural strength of the control mix (0% of bentonite) compared to the mean value of various proportions of 10% and 20% of heated bentonite at 550 and 750 °C which have not significantly found difference at $p<0.01$ with values between 87% to 95% of the control mix's flexural strength. These promising outcomes point out the effect of the heat treatment conducted on the material [23]. While the mean values of the flexural strength of the 30%, 40%, and 50% mixtures of natural and heated bentonite at 250 °C compared to the control mix are found to be significantly different at $p<0.01$, and exhibit relatively higher flexural strength.

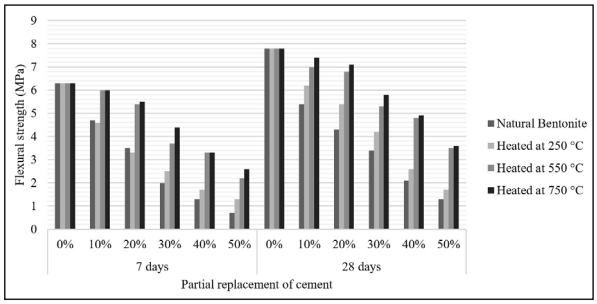

Figure 7. Flexural strength of mortar mixtures at 7 and 28 days

The results of tensile strength have the same behavior observed for the flexural strength of mortar mixtures at 7 and 28 days of age. Figure (8) shows the mean value of the tensile strength of the mixtures at 7 days of age compared to the mixtures at 28 days of age which are also found to be significantly different at $p<0.01$. And that is consistent with the fact that also the tensile strength develops with time. Furthermore, Figure (8) shows the mean value of the tensile strength of the control mix compared to the mean value of various proportions of 10% and 20% of heated bentonite at 550 and 750 °C which are found to be not significantly different at $p<0.01$. These promising outcomes point out the effect of the heat treatment conducted on the material [23]. While the mean values of the tensile strength of the 30%, 40%, and 50% mixtures of natural and heated bentonite at 250 °C compared to the control mix are found to be significantly different at $p<0.01$, and exhibit relatively higher tensile strength.

Herein, it is seen that treated bentonite has better results than natural. The development of the strength of the cement-bentonite mixtures is slower at an early age which is due to the slow gain of strength for the pozzolana materials in general [20]. Nevertheless, the mixtures with 10% and 20% of heated bentonite at 750 °C show development of tensile strength at 28 days by 27 and 32% of their strength at 7 days. In addition, their tensile strengths are 92 and 87% of the tensile strength of the control mixture.

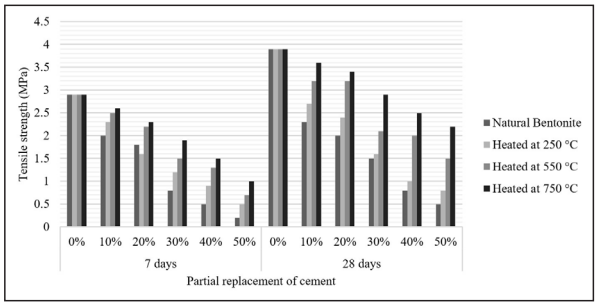

Figure 8. Tensile strength of mortar mixtures at 7 and 28 days

3.2 Tests of concrete mixtures

Results of the tests conducted to find the concrete fresh properties are shown in Table (8) where the mean values were calculated for each test. These results include immediate temperatures at the end of mixing, slump cone, fresh density, air content, and initial setting time. Table (8) includes the testing standard for each test. Temperature results were almost the same for all mixtures due to the standard condition in the lab and fresh densities also were the same. While for slump cone tests, values varied from 3

cm to 18 cm depending on the type and amount of bentonite used. For example, the lowest slump values were obtained for 20% replacement of cement by natural bentonite and *Ca*-bentonite. This is referred to a specific area of bentonite, that is higher than the specific surface area of cement. Thus, the workability of the cement-bentonite mixtures reduces as the bentonite content increases. This finding is in line with the study of [24]. However, the results show that the heat treatment of bentonite can improve workability. This is indicated in the results of mix HC and JC which have heated bentonite at 750 °C. Air content outcomes varied from 1.4% to a maximum of 2.4%, the highest values obtained at 20% replacement of cement with natural and *Ca*-bentonite. These results again point out the advantage of the heat treatment of bentonite, which gives very good results in comparison with the control mix. From the initial setting time, it can be seen that the initial setting time was increased in mixtures containing bentonite and superplasticizer in comparison with the control mix, which is expected out of the known behavior of pozzolana material [14, 20, and 21].

Table 8. Concrete Mixtures Fresh Properties

Mix Designation	Temperature (C)	Slump (mm)	Fresh Density (kg/m³)	Air Content (%)	Initial Setting Time (hr)
Standards	ASTM C 1064 [42]	JS 1651-2 [43]	JS 1651-6 [44]	JS 1651-7 [45]	ASTM C 403 [46]
AC	20.3	18	2380	1.5	4:00
BC	20.5	9	2360	2	5:00
CC	20.6	3	2340	2.4	5:30
DC	21.0	15	2380	1.7	4:30
EC	20.5	9	2390	1.6	5:00
FC	20.7	16	2390	1.6	4:30
GC	22.0	12	2380	1.5	5:00
HC	21.8	17	2370	1.6	4:30
JC	21.2	18	2390	1.4	5:00
KC	20.3	12	2390	1.5	5:30
LC	20.9	3	2400	2.3	5:30

As it is mentioned before, the mechanical properties of the mixtures were examined through different experiments. For the compressive strength test, specimens were tested at 7- and 28-days of age, Figure (9). While for flexure and splitting tensile strength tests, specimens were tested at 28 days of age, Figure (10). The mean of the three specimens of each test at each age was calculated.

Figure (9) shows the mean value of the compressive strength of the concrete mixtures at 7 days of age compared to the mixtures at 28 days of age are found to be significantly different at $p<0.01$. And that is consistent with the fact that compressive strength develops with time. Also, Figure (9) shows the mean value of the concrete compressive strength of the control mix compared to the mean value of 10% and 20% proportions of bentonite are found to be significantly different at $p<0.01$. Reducing cement content reduces compressive strength. In contrast, compressive strength develops with time. The mean values of the compressive strength of the mixtures with 10% and 20% of heated bentonite and *Ca*-bentonite are compared to the natural bentonite mixtures which are found to be not significantly different at $p<0.01$. Even though the results show that compressive strength is developed in all mixtures, it is developed for the mix with 10% of heated bentonite at 750 °C and *Ca*-bentonite by about 28%. On the other hand, it is almost developed by 25% of the mixture with 20% of heated bentonite at 750 °C and *Ca*-bentonite. This is in line with the previous conclusion, that increasing the bentonite affects the development of strength at an early age, which is due to the slow pozzolanic reaction. Thus, it is expected that the compressive strength of the cement-bentonite mixture will increase with time because of the continuous reactions.

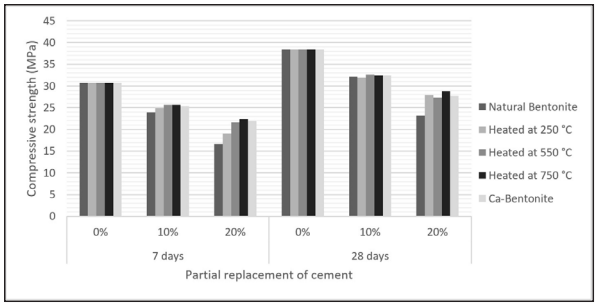

Figure 9. Compressive strength of concrete mixtures at 7 and 28 days.

According to the results shown in Figure (10), the mean value of the 10% and 20% proportions of natural bentonite, heated bentonite, and Ca-bentonite concrete flexural strength and splitting tensile strength compared to the mean value of the control mix which is found to be significantly different at $p<0.01$. Thief increases in the flexural and splitting tensile strength can be noticed in all tests of the mixtures with the heat-treated bentonite and *Ca*-bentonite. In contradiction, the replacement of natural bentonite reduces the strength compared to the control mixtures. This behavior can be attributed to the structure and the physicochemical properties that could be affected by thermal treatment [47,48]. The flexural strength increased up to 20% with an addition of 10% of heated bentonite at 750 °C. On the other hand, the maximum increase of splitting tensile strength is about 25% for the mix with 10% heated bentonite at 750 °C in comparison to the control mixture. The findings of these experiments are in line with the conclusion of Xianggyang Man et al. [49].

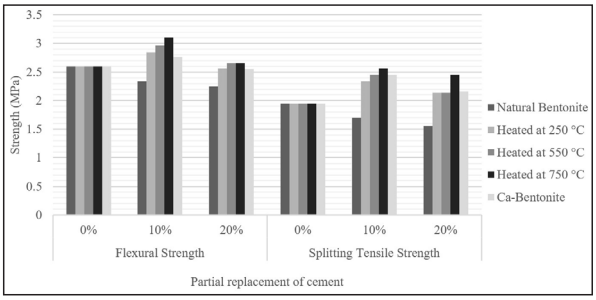

Figure 10. Flexural and splitting tensile strengths of concrete mixtures at 28 days

Figure (11) shows the results of the shrinkage and water permeability tests of concrete mixtures at 28 days of the age of the 10% and 20% proportions of natural bentonite, heated bentonite, and *Ca*-bentonite and the control mix. The mean values of the 10% and 20% proportions of natural bentonite, heated bentonite, and *Ca*-bentonite maintain shrinkage and impermeability compared to the mean value of the control mix which is found to be significantly different at $p<0.01$. The concrete shrinkage in all cement-bentonite mixtures is reduced especially for the mixtures with natural and *Ca*-bentonite. The recorded shrinkage of the control mixture at 28 days is 296-μ strain, whereas it drops to 226 and 206 μ strain for the mixture of 10% and 20% of the *Ca*-bentonite, respectively. However, the shrinkage of the heat-treated bentonite at 750 °C with replacement of 10% and 20% is 287 and 267 μ strain, respectively. The behavior of the heat-treated bentonite can be explained by the thermal gravimetric analysis, Figure (3). It is indicated that the weight losses of bentonite at 250 °C, 550 °C, and 750 °C are 92.6%, 91.2%, and 88.1%, respectively. Thus, the free water of the bentonite is reduced by increasing the heating of the bentonite and so the shrinkage increases. Nevertheless, the TGA tests and the mechanical experiments of the cement-bentonite mixtures point to the stability and durability of the heated bentonite at 750 °C. Salman Afzal et al. [50] examined the effect of the partial replacement of cement by bentonite on autogenous shrinkage. The findings of their work are in high agreement with the outcomes of the experiment that was attained in this study. They concluded that the presence of bentonite enhances the relative humidity and then improves concrete shrinkage.

The results of the permeability tests show an improvement where the maximum reduction is noticed in the mixture of 20% of the *Ca*-bentonite (24.4 mm). These results describe the characteristics of bentonite, which is known as a filling material. In addition, that improvement in impermeability is attributed to the chemical composition of the used bentonite, which is mainly composed of SiO_2 and Al_2O_3 (63.8%). That chemical characteristic helps increase the rate of the hydration process, and thus refine the pores, which lead to enhancing the impermeability [25, 26].

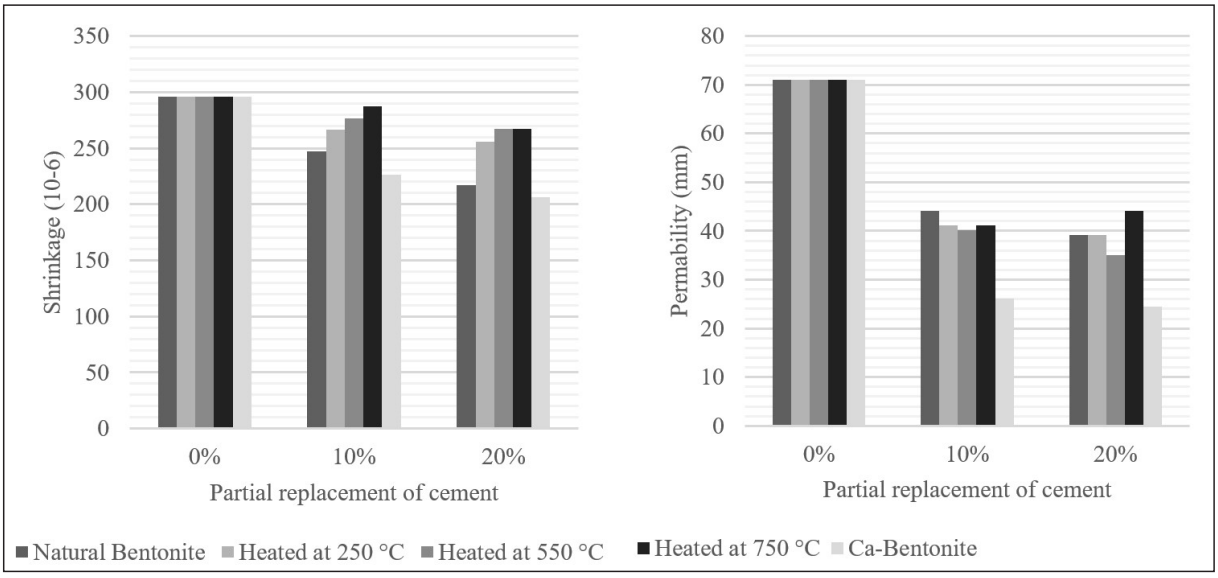

Figure 11. Shrinkage and permeability of concrete mixtures at 28 days

4. Cost analysis

The manufacturing of cement involves the sintering of blended ingredients (limestone, sand, and clay) at 1480 °C in a rotary kiln. The high temperature needed for the production process makes it an energy-intensive process. The production of one ton of cement requires 5-6 GJ of energy from fuel. This amount of energy is obtained from the burning of 175 m^3 of natural gas, 263 m^3 of LPG, or 6 tons of heavy fuel oil. In addition, the process requires 100-200 KW/ton of electricity for the motors that derive the rotary kiln and mills. On the other hand, calcination of bentonite requires firing at 550 °C, hence replacing part of the cement with bentonite in any proportion will lead to a great reduction in fuel and electricity consumption. Tables (9 and 10) show the effects of replacing the cement with bentonite. The calculations are based on data obtained from a cement factory, in Amman.

Table 9. Shows the effect of replacing cement with bentonite up to 50% on the consumption of heavy fuel oil and consumption of electricity.

	The Mixtures		Energy consumption		Energy reduction	
	Cement %	Bentonite %	HFO ton	Electricity KW	Fuel	Electricity
Case 1	100	0	6	130	-	-
Case 2	90	10	5.68	123	5%	5%
Case 3	80	20	5.36	116	11%	11%
Case 4	70	30	5.04	109	16%	16%
Case 5	60	40	4.72	102	21%	22%
Case 6	50	50	4.4	95	27%	27%

Table 10. Shows the effect of using bentonite as a substitute for part of the cement on liquid propane gas (LPG) consumption.

	The Mixtures		Energy consumption		Energy reduction	
	Cement %	Bentonite %	Fuel LPG	Electricity KW	Fuel	Electricity
Case 1	100	0	263	130	-	-
Case 2	90	10	249.7	123	5%	5%
Case 3	80	20	236.4	116	10%	11%
Case 4	70	30	223.1	109	15%	16%
Case 5	60	40	209.8	102	20%	22%
Case 6	50	50	196.5	95	25%	27%

It is evident from the data shown in Tables (9 and 10) that replacing cement with bentonite reduces the consumption of heavy fuel oil by 5% to 27%, and the LPG by 5% to 25% depending on the percentage quantity of bentonite. The percentage reduction in electrical power follows the same trend. The reduction in fuel quantity (whether it is heavy fuel oil, LPG, or any other fossil fuel) with a reduction in electric power consumption has a great reflection on the total cost of cement.

In addition, cement manufacturing releases CO_2 in the atmosphere both directly when calcium carbonate is heated, producing lime and carbon dioxide [51], and indirectly through the use of energy. The cement industry produces about 5% of global man-made CO_2 emissions of which 50% is from the chemical process and 40% from burning fuel [52]. The amount of CO_2 emitted by the cement industry is nearly 900 kg of CO_2 for every 1000 kg of cement produced [53]. In comparison with Ordinary Portland Cement (OPC), heat-treated bentonite at 550 ºC produces only 16% CO_2 from burning fuel instead of 40%. The heating of bentonite does not produce any CO_2 by itself. Therefore, the total amount of CO_2 emitted by 1000 kg of bentonite produced at 550 ºC is 144 kg, and at 750 ºC is 193 kg. Heat-treated bentonite partially applies for replacing cement in concrete mixtures to reduce CO_2. It also has consumed a lower energy requirement in production compared to OPC cement.

5. Conclusion

The following conclusions can be drawn from the experimental results obtained: Bentonite addition decreased mortar strength in comparison with the control mix without bentonite due to the increase in water need, but it still can be used for producing low-strength products with lower cost.

The mortar mixtures containing heated bentonite at 750 °C achieved good results close to those results achieved by OPC alone. The bentonite particles seem to act as a pore-reducing or filling material.

For concrete mixtures, natural and *Ca*-treated bentonite increase fresh concrete viscosity and as a result increase its cohesion and consistency. This property can be very useful in the field of self-compaction concrete instead of viscosity modifier admixtures where this is mandatory. Using natural bentonite instead of a viscosity modifier can reduce production costs.

Both flexural and compressive strength was increased by 20% and 25% respectively for most of the bentonite-concrete mixtures. These results can be used for producing products where these properties are more critical.

Both natural and *Ca*-treated bentonite reduce concrete shrinkage at an early age due to its expansion nature. *Ca*-bentonite behavior was slightly better than natural bentonite at the early ages of concrete.

Concrete permeability was highly reduced by using bentonite especially Ca treated where permeability was reduced by 60%. This is an excellent indication for using this material in producing more durable concrete structures or concrete components such as curbstone, concrete pipes, or even tiles and bricks.

In conclusion, Jordanian clay bentonite has the potential to become an alternative for producing more durable concrete structures or concrete components such as curbstone, concrete pipes, or even tiles and bricks. Furthermore, bentonite particles seem to act as a pore-reducing or filling material. Consequently, it decreases concrete permeability. More investigations shall be conducted on dry mortar products and applications using treated bentonite like cement plaster, grout, and repair mortar.

Acknowledgments

The Scientific Research Support Fund funded this study. The authors would like to express their gratitude to the Royal Scientific Society, The University of Jordan, Al-Balqa Applied University, and the Ministry of Energy and Mineral

Resources for their facilities and help to achieve this project. In addition, the authors would like to thank Kyle E. Cordova and Eng. Sarah Tabbalat for text editing and improving.

Author's Contributions:

Conceptualization, A. Ghrair & H. Al-kroom; Methodology, A. Ghrair; Investigation, A. Ghrair & H. Al-kroom, A. Gharaibeh, A. Said, and B. Hanayneh; Writing - original draft, H. Al-kroom & A. Ghrair; Writing - review & editing, H. Al-kroom, A. Ghrair; Funding acquisition, A. Ghrair; Resources, N. Al Daoud, A. Mhanna, and A. Said; Supervision, Ayoup M. Ghrair.

References

Abdel-Latief MA, El-Sayed MI, Shahien MG, Zayed AM. A new insight upon the use of weathered basalt as alternative raw material in Portland clinker production. Ain Shams Engineering Journal. 2020 Sep 22.

Afzal S, Shahzada K, Fahad M, Saeed S, Ashraf M. Assessment of early-age autogenous shrinkage strains in concrete using bentonite clay as internal curing technique. Construction and Building Materials. 2014 Sep 15; 66:403-9.

Ahmad S, Barbhuiya SA, Elahi A, Iqbal J. Effect of Pakistani bentonite on properties of mortar and concrete. Clay Minerals. 2011 Mar 1; 46(1):85-92.

Anantharaman N. Energy audit in cement industry (1500 tpd). International Journal of Science Technology & Engineering. 2017; 3(10):12-8.

ASTM C1064. Standard Test Method for Temperature of Freshly Mixed Hydraulic-Cement Concrete, ASTM International, West Conshohocken, PA, 2012, www.astm.org

ASTM C33 (2007). Standard Specification for Concrete Aggregates.

ASTM C403 / C403M-08, Standard Test Method for Time of Setting of Concrete Mixtures by Penetration Resistance, ASTM International, West Conshohocken, PA, 2008, www.astm.org

Bohac M, Kubatova D, Rybova A, Zezulova A, Stanek T. Rheological properties of belite-rich cement doped with sulfur. InIOP Conference Series: Materials Science and Engineering 2019 Jul 1 (Vol. 583, No. 1, p. 012027). IOP Publishing.

BS EN 196-1. Methods of testing cement. Determination of strength, 2016. https://doi.org/10.3403/30291447U

BS EN 196-2. Methods of testing cement. Chemical analysis of cement, 2005. https://shop.bsigroup.com/ProductDetail/?pid=000000000019983594

Bullard J. W., Jennings H. M., Livingston R. A., Nonat A., Scherer G. W., Schweitzer J. S., Scrivener K. L., Thomas J. J. Mechanisms of cement hydration, Cement and Concrete Research, 2011 Volume 41, Issue 12, Pages 1208-1223. https://doi.org/10.1016/j.cemconres.2010.09.011

Chen Z, Poon CS. Comparative studies on the effects of sewage sludge ash and fly ash on cement hydration and properties of cement mortars. Construction and Building Materials. 2017 Nov 15; 154:791-803.

Deer, W.A., Howie R.A., and Zussman J. (1985). An introduction to rock-forming minerals. 1985, London: Longmans.

Dellisanti, F., Minguzzi, V., Valdrè, G. Thermal and structural properties of Ca-rich montmorillonite mechanically deformed by compaction and shear. Applied Clay Science, 2006 vol. 31, pp. 282-289. http://dx.doi.org/10.1016/j.clay.2005.09.006

EIA – Emissions of Greenhouse Gases in the U.S. Carbon Dioxide Emissions 2006. https://www.eia.gov/environment/emissions/ghg_report/

EN 12390-8:2019. Testing hardened concrete - Part 8: Depth of penetration of water under pressure.

Fadaie MA, Nekooei M, Javadi P. Effect of dry and saturated bentonite on plastic concrete. KSCE Journal of Civil Engineering. 2019 Aug; 23(8):3431-42.

Gartner E, Sui T. Alternative cement clinkers. Cement and concrete research. 2018 Dec 1; 114:27-39.

He Z, Zhu X, Wang J, Mu M, Wang Y. Comparison of CO2 emissions from OPC and recycled cement production. Construction and Building Materials. 2019 Jun 30; 211:965-73.

Jalil A, Khitab A, Ishtiaq H, Bukhari SH, Arshad MT, Anwar W. Evaluation of steel industrial slag as partial replacement of cement in concrete. Civil Engineering Journal. 2019 Jan 27; 5(1):181-90.

Jiang J, Lu Z, Li J, Xie Y, Luo K, Niu Y. Preparation and properties of nanopore-rich lightweight cement paste based on swelled bentonite. Construction and Building Materials. 2019 Feb 28; 199:72-81.

JS 1470-1. Cement - Methods of testing cement Part 1: Determination of strength, 2005. http://www.jsmo.gov.jo/en/EServices/Standards/Pages/stdDetails.aspx?mfn=2459

JS 1470-3. Cement - Methods of testing cement -Part 3: Determination of setting time and soundness, 2005. http://www.jsmo.gov.jo/en/EServices/Standards/Pages/stdDetails.aspx?mfn=2461.

JS 1651-6. Concrete - Testing fresh concrete part 6: density, 2004. http://www.jsmo.gov.jo/en/EServices/Standards/Pages/stdDetails.aspx?mfn=2253

JS 1651-7. Concrete - Testing fresh concrete Part 7: Air content - Pressure methods, 2004. http://www.jsmo.gov.jo/en/EServices/Standards/Pages/stdDetails.aspx?mfn=2254

JS 1652- 1, 2, 3, 4, 5, and 6. Concrete – Testing hardened concrete Part 1: Shape, dimensions, and other requirements for specimens and molds. Part 2: Making and curing specimens for strength tests; Part 3- Compressive strength of test specimens, Part 4: compressive strength-specification for testing machines, Part 5: Flexural strength of test specimens, part 6: Testing splitting strength of test specimens. 2004. http://www.jsmo.gov.jo/en/EServices/Standards/Pages/StdLists.aspx?ICS=9110030

JS 2133-2. Admixtures for concrete, mortar, and grout Part 2- Concrete admixtures – Definitions, requirements, conformity, marking, and labeling. 2016. http://www.jsmo.gov.jo/en/EServices/Standards/Pages/stdDetails.aspx?mfn=5600

Liu M, Hu Y, Lai Z, Yan T, He X, Wu J, Lu Z, Lv S. Influence of various bentonites on the mechanical properties and impermeability of cement mortars. Construction and Building Materials. 2020 Apr 30; 241:118015.

Lu Z, Hou D, Hanif A, Hao W, Li Z, Sun G. Comparative evaluation on the dispersion and stability of graphene oxide in water and cement pore solution by incorporating silica fume. Cement and Concrete Composites. 2018 Nov 1; 94:33-42.

Mahasenan, N.; Steve S., Kenneth H., Kaya Y. The Cement Industry and Global Climate Change: Current and Potential Future Cement Industry CO2 Emissions, 2003. https://doi.org/10.1016/B978-008044276-1/50157-4

Mahasneh, M.A. and Saleh, S.K. (2012) Evaluation of Jordanian Bentonite Performance for Drilling Fluid Applications. Contemporary Engineering Sciences, 5, 149-170.

Man X, Haque MA, Chen B. Engineering properties and microstructure analysis of magnesium phosphate cement mortar containing bentonite clay. Construction and Building Materials. 2019 Dec 10; 227:116656.

Marchon D, Flatt RJ. Mechanisms of cement hydration. Science and technology of concrete admixtures 2016 Jan 1 (pp. 129-145). Woodhead Publishing.

Martin BO, Theodor ST, Anežka ZE, Alexandra RY, Dana KU, Radoslav NO. Early Hydration of Activated Belite-Rich Cement. Advanced Materials Research. 2019 Jan 1; 1151.

Memon SA, Arsalan R, Khan S, Lo TY. Utilization of Pakistani bentonite as partial replacement of cement in concrete. Construction and building materials. 2012 May 1; 30:237-42.

Mesboua N, Benyounes K, Benmounah A. Study of the impact of bentonite on the physicomechanical and flow properties of cement grout. Cogent Engineering. 2018 Jan 1; 5(1):1446252.

Morozov, I.; Zakusin, S.; Kozlov, P.; Zakusina, O.; Roshchin, M.; Chernov, M.; Boldyrev, K.; Zaitseva, T.; Tyupina, E.; Krupskaya, V. Bentonite–Concrete Interactions in Engineered Barrier Systems during the Isolation of Radioactive Waste Based on the Results of Short-Term Laboratory Experiments. Appl. Sci. 2022, 12, 3074. https://doi.org/10.3390/app12063074

Nawasreh M.K. and Al Omari Y. Bentonite. Ministry of Energy and Mineral Resources. Internal Report, 2014. Jordan, Amman. Available on line: https://emrc.gov.jo/EchoBusV3.0/SystemAssets/Awarnesstools/cdec7a2e-ebcc-4326-a5d6-6639d9a802d2_%D8%A7%D9%84%D8%A8%D9%86%D8%AA%D9%88%D9%86%D8%A7%D9%8A%D8%AA.pdf.

Parkar A, Sawant RS, Mandake MB. Energy audit of the cement industry: a review. ENERGY. 2019 Apr; 6(04).

Paya J, Monzo J, Peris-Mora E, Borrachero MV, Tercero R, Pinillos C. Early-strength development of Portland cement mortars containing air classified fly ashes. Cement and concrete research. 1995 Feb 1; 25(2):449-56.

Rao V., Reddy M. Utilization of Bentonite in Concrete: A Review. International Journal of Recent Technology and Engineering (IJRTE) Volume-7, Issue-6C2, April 2019:541-544.

Riddick, T. Control of colloid stability through zeta potential; with a closing chapter on its relationship to cardiovascular disease. Published for ZETA–METER, INC. by Livingston Publishing Company, Wynnewood, Pennsylvania. 1968, 372p.

S 1651-2. Concrete -Testing fresh concrete part 2: Slump test, 2004. http://www.jsmo.gov.jo/en/EServices/Standards/Pages/stdDetails.aspx?mfn=2237

Sarikaya, Y. and Yildiz, N. (1999). The characterization of Na2CO3 Activated K¨utahya Bentonite. Turk J Chem 23, 309 - 317.

Scrivener K, Ouzia A, Juilland P, Mohamed AK. Advances in understanding cement hydration mechanisms. Cement and Concrete Research. 2019 Oct 1; 124:105823.

Shannag MJ. High-strength concrete containing natural pozzolan and silica fume. Cement and concrete composites. 2000 Dec 1; 22(6):399-406.

Sutherland WM. Wyoming bentonite—Summary report (Doctoral dissertation, University of Wyoming. Libraries).

Tsakiridis PE, Papadimitriou GD, Tsivilis S, Koroneos C. Utilization of steel slag for Portland cement clinker production. Journal of Hazardous Materials. 2008 Apr 1; 152(2):805-11.

WBCSD: Getting the Numbers Right Project: reporting CO2, World Business Council for Sustainable Development, 2012. http://www.wbcsdcement.org/GNR-2012/index.html,

Xie Y, Li J, Lu Z, Jiang J, Niu Y. Effects of bentonite slurry on the air-void structure and properties of foamed concrete. Construction and Building Materials. 2018 Aug 10; 179:207-19.

Yang H, Long D, Zhenyu L, Yuanjin H, Tao Y, Xin H, Jie W, Zhongyuan L, Shuzhen L. Effects of bentonite on pore structure and permeability of cement mortar. Construction and Building Materials. 2019 Nov 10; 224:276-83.

Yüksel İ. A review of steel slag usage in the construction industry for sustainable development. Environment, Development, and Sustainability. 2017 Apr; 19(2):369-84.

Zuzana O, Annamária M, Silvia D, Jaroslav B. Effect of thermal treatment on the bentonite properties. Arhiv za tehnicke nauke. 2012 Dec 1;7(1):49-56.

JJEES

JJEES (2023) 14 (1): 30-49
ISSN 1995-6681

Jordan Journal of Earth and Environmental Sciences

Late Eocene (Priabonian) Planktic Foraminifera from Jabal Hafit, Al Ain area, United Arab Emirates

Haidar Salim Anan

Emeritus, former Professor of Stratigraphy and Micropaleontology of Ain Shams University (Egypt), United Arab Emirates University (UAE), and Vice President of Al Azhar University-Gaza (Palestine), P. O. Box 1126.

Received 11th October 2021; Accepted 30th May 2022

Abstract

Thirty two planktic foraminiferal species belonging to seven genera: *Catapsydrax* (two species), *Subbotina* (8 species), *Globigerinatheka* (4 species), *Cribrohantkenina* (1 species), *Hantkenina* (3 species), *Dentoglobigerina* (3 species), *Pseudohastigerina* (1 species), *Turborotalia* (9 species), *Chiloguembelina* (1 species) of the time interval corresponding to the Late Eocene (Priabonian) from the top part of Mazyad Member of the Dammam Formation from the eastern limb of Jabal Hafit anticline, Al Ain area, United Arab Emirates (UAE) are identified and twenty five of them are illustrated. The taxonomic consideration, biostratigraphic position, and probable phylogeny of these species are presented. The number of the Late Eocene planktic foraminifera species in the current study yields a higher number (32 species) than others in or outside the Al Ain area, UAE. Three planktic foraminiferal biozones (Tripartite) are recognized in the current study, according to the modern biozonation (after Berggren and Pearson, 2005, and Wade et al., 2011), from base to top: *Globigerinatheka semiinvoluta* Zone (E14), *G. index* Zone (E15), and *Hantkenina alabamensis* Zone (E16). The temporal distribution is also compared with the same stratigraphic horizon in the surrounding areas in Al Ain (UAE and Oman border), and some other Tethyan localities. The identified species are recognized in different localities in the Tethys: the Atlantic Ocean (USA, Mexico, Trinidad), the Northern Tethys (Spain, France, Italy, Caucasus), and the Southern Tethys (Tanzania, Libya, Egypt, Syria, UAE, Oman, Pakistan, India, Indian Ocean, Pacific Ocean, New Zealand, Australia).

Keywords: *Fiber in concrete, Plastic waste, Recycling, Concrete properties, Waste management.*

1. Introduction

The present paper is one of a series of studies of planktic and benthic foraminiferal assemblages from the Maastrichtian-Paleogene succession of the Al Ain area. The current work presents a review of the complete record of the foraminiferal content of the Late Eocene of the upper part of Mazyad Member of the Dammam Formation of the eastern limb of Jabal Hafit (the upper part of Tle5 of Hunting, 1979), in the Al Ain, UAE (Fig. 1). This succession is composed of different lithologies, from base to top: shale, marl, phosphatica limestone, shale, marl, glauconitic limestone, marl in the top, separated by a conglomeratic limestone as an unconformity (P15/P16). This late Eocene succession is compared with the synchronous outcrops in Al Ain-Al Buraimi area, west of the Northern Oman Mountains, which are located at the border line between the western limb of Jabal Malaqet, UAE (Anan, 1995) and J. Qatar, to the east of J. Malaqet in the Sultanate of Oman (Abdelghany, 2002). The previous studies of the planktic faunal content of the study area by Cherif and El Deeb (1984), Cherif et al. (1992), and Anan et al. (1992) are also pertinent to the present study.

2. Stratigraphy

Five marly samples (nos. 17, 19, 20-22, Fig. 2) were collected from about 100 m thick vertical succession of the Late Eocene sediments of the eastern limb of Jabal Hafit anticline (Lat. 24º 06' - 24º 09' N, Long. 55 º 46'-55 º 49' E) along Al Ain-Mazyad asphalted road, which consists mainly of marl, as a part of the Middle-Late Eocene Mazyad Member of the Dammam Formation, which consists of alternated lithologies of shales and marls. These rocks are intercalated by phosphatic limestone and glauconitic limestone beds (Fig. 3). Thirty two planktic foraminiferal species are identified and recorded from the Late Eocene (Priabonian) succession of the study area, and twenty-five species of them are illustrated in three Plates (1-3). Some differences in the definition of the Late Eocene biozonation from Al Ain area (around the border line between east UAE and west Oman) were made by Cherif and El Deeb (1984) as *Globorotalia c. cerroazulensis* Zone, followed by Cherif et al. (1992) as *Turborotalia c. cerroazulensis* Zone, Anan et al. (1992) as *Globigerinatheka semiinvoluta* and *Turborotalia c. cerroazulensis* Zones, Anan (1995) as *Cribrohantkenina inflata* Zone and *C. inflata* or younger, and Abdelghany (2002) as *Turborotalia cunialensis/Cribrohantkenina inflata* Concurrent-Range Zone. The disappearance of the spinose genera *Morozovella* and *Truncorotaloides* has been taken by many authors (Toumarkine and Luterbacher, 1985; Haggag, 1990; Anan et al., 1992) to mark the Middle/Upper Eocene boundary in the tropical and Mediterranean regions.

The Late Eocene planktic foraminiferal content was subdivided early into two zones (Bipartite) by some authors (Stainforth et al., 1975; Toumarkine and Luterbacher, 1985; Keller, 1985): the lower *Globigerinatheka semiinvoluta* Zone (P 15) and the upper *Turborotalia cerroazulensis*

* Corresponding author e-mail: profanan@gmail. Com

Zone (P16/17), while it was subdivided it into three zones (Tripartite) by others (Blow, 1969; Berggren and Miller, 1988; Coccioni et al, 1988; Anan, 1995): the lower *Globigerinatheka semiinvoluta* Zone (P15), the middle *Cribrohantkenina inflata* Zone (P16), and the upper *Turborotalia cerroazulensis* Zone (P17), which was based on the stratigraphic range of the *C. inflata* between *G. semiinvoluta* and *T. cunialensis.* The tripartite subdivisions are currently used by different authors (Fig. 4). On the other hand, Haggag (1990) introduced the *Globigerina pseudoampliapertura* Zone as an interval from the last occurrence of *Truncorotaloides rohri* to the first appearance of *Globigerinatheka semiinvoluta* and was assigned to the Late Eocene in the Egyptian stratigraphy. Three planktic foraminiferal conventional biozones are recognized in the studied section, from base to top: *Globigerinatheka semiinvoluta* Zone (E14), *Globigerinatheka index* Zone (E15) and *Hantkenina alabamensis* Zone (E16) of the worldwide standard zonation of Berggren and Pearson (2005), Pearson et al. (2006), Wade et al. (2011) and Molina (2015).

3. Systematic Paleontology

The taxonomy followed in this study is that of Pearson et al. (2006). Thirty two Late Eocene planktic foraminiferal species are identified from the upper part of Mazyad Member, Dammam Formation of Jabal Hafit, and twenty five of them are illustrated in Plates 1-3. The stratigraphic ranges of the identified species are presented in Fig. 3.

Order: Foraminifera Eichwald, 1830

Suborder: Globigerinina Delage and Hérouard, 1896

Superfamily: Globigerinacea Carpenter, Parker and Jones, 1862

Family: Globigerinidae Carpenter, Parker and Jones 1862

Genus: *Catapsydrax* Bolli, Loeblich and Tappan, 1957

Type species: *Globigerina dissimilis* Cushman and Bermúdez, 1937

***Catapsydrax dissimilis* (Cushman and Bermúdez, 1937)**

1937 *Globigerinita dissimilis* Cushman and Bermúdez, p. 25, pl. 3, figs. 4-6.

1957 *Catapsydrax dissimilis*; Bolli et al., 36, pl. 7, fig. 6.

1970 *Globigerinita dissimilis*; Samanta, p. 35, pl. 6, fig. 1.

1992 *Catapsydrax dissimilis*; Anan et al., p. 239, fig. 11.13.

1997 *Catapsydrax dissimilis*; Pearson and Chaisson, p. 57, pl. 2, fig. 12.

2000 *Catapsydrax dissimilis*; Sztràkos, p. 143, pl. 21, figs. 15,16.

2006 *Catapsydrax dissimilis*; Olsson et al., p. 71, pl. 5.3, figs. 18-20.

2021 *Catapsydrax dissimilis*; Salama et al., p. 12, fig. 7. K.

Remarks: This Middle-Late Eocene species is characterized by its obligate bulla with a uniform continuous lip bordering the infralaminal apertures. Olsson et al. (2006) suggested that this species probably evolved from the Early-Late Eocene *C. unicavus* in the Late Eocene. It is recorded in Al Ain area before (Anan et al., 1992). It was also recorded in the Atlantic Ocean, the Northern Tethys (Spain, France), and the Southern Tethys (Tanzania, Libya, Egypt, UAE, Pakistan, India, Indian Ocean, and Pacific Ocean (Table 1).

***Catapsydrax unicavus* Bolli, Loeblich and Tappan, 1957**

(Pl. 1, fig. 1)

1957 *Catapsydrax unicavus* Bolli et al., p. 37, pl. 7, fig. 9.

1969 *Globigerinita unicava*; Samanta, p. 332, pl. 1, fig. 4.

2006 *Catapsydrax unicavus*; Olsson et al., p. 75, pl. 5.3, figs. 1-17.

2006 *Catapsydrax unicavus*; Hernitz Kučenjak et al., p. 30, pl. 1, fig. 10.

2015 *Catapsydrax unicavus*; Molina, p. 172, fig. 5.

2015 *Catapsydrax unicavus*; Pearson and Wade, p. 8, fig. 4. 1-5.

2021 *Catapsydrax unicavus*; Salama et al., p. 12, fig. 7. M.

Remarks: This Eocene species has 4 globular chambers in the final whorl with slightly inflated bulla extending over the umbilicus. It is recorded and illustrated in Al Ain area herein, for the first time. It was recorded in the Atlantic Ocean, the Northern Tethys (Spain), and the Southern Tethys (Tanzania, Libya, Egypt, Syria, India, New Zealand, and in the Pacific Ocean).

Genus *Subbotina* Brotzen and Pozaryska, 1961

Type species *Globigerina triloculinoides* Plummer, 1926

Subbotina angiporoides (Hornibrook, 1965)

1965 *Globigerina angiporoides* Hornibrook, p. 835, figs. 1, 2.

1968 *Globigerina angiporoides*; Srinivasan, p. 147, pl. 15, fig. 9.

1969 *Globigerina angiporoides*; Samanta, pl. 330, pl. 3, fig. 1.

1975 *Globigerina angiporoides*; Toumarkine and Bolli, p. 182, pl. 5, figs. 5-7.

1971 *Globigerina (Subbotina) a. angiporoides*; Jenkins, pl. 20, figs. 588-594.

1992 *Subbotina angiporoides*; Anan et al., p. 239, fig. 10.10.

2006 *Subbotina angiporoides*; Olsson et al., p. 126, pl. 6.6, figs. 1-13.

2021*Subbotina angiporoides*; Salama et al., p. 14, fig. 8. D.

Remarks: This Middle-Late Eocene species have strongly embracing final chamber and a low slit-like aperture with a thick lip. Olsson et al. (2006) suggested that it evolved from the long-range Eocene *S. linaperta.* It is recorded in Al Ain area before (Anan et al., 1992; Anan, 1995). It was recorded in the Atlantic Ocean, the Northern Tethys (Spain, Italy, Caucasica), and the Southern Tethys (Egypt, New Zealand, Indian Ocean, and New Zealand, Fig. 5).

***Subbotina corpulenta* (Subbotina, 1953)**

1953 *Globigerina corpulenta* Subbotina, p. 101, pl. 9, figs. 5-7.

1970 *Globigerina corpulenta*; Samanta, p. 32, pl. 7, figs. 9,10.

1992 *Globigerina corpulenta*; Anan et al., p. 239, pl. 10, fig. 15.

1995 *Globigerina corpulenta*; Anan, p. 8, pl. 1, fig.11.

2006 *Subbotina corpulenta*; Olsson et al., p. 75, pl. 6.7, figs. 1-14.

2006 *Subbotina corpulenta*; Hernitz Kučenjak et al., p. 30, pl. 1, fig. 7.

2015 *Subbotina corpulenta*; Molina, p. 172, fig. 5.

2015 *Subbotina corpulenta*; Pearson and Wade, p. 13, fig. 10. 3, 4.

2021 *Subbotina corpulenta*; Salama et al., p. 14, fig. 8. G.

Remarks: The *Subbotina corpulenta* Middle-Late Eocene species has a larger-size test with 4 globular chambers in the final whorl. Stainforth et al. (1975) considered that *S. corpulenta* is a half way between *S. eocaena* and *S. gortanii,* while it may probably evolve from *S. eocaena* by Haggag and Luterbacher (1991), or from *S. hagni* by Olsson et al. (2006). It is recorded only in E14 in this study. It was recorded in the Atlantic Ocean, the Northern Tethys (Spain, France), and the Southern Tethys (Tanzania, Egypt, UAE, Oman, India, Indian Ocean, and Pacific Ocean).

***Subbotina eocaena* (Guembel, 1868)**

1868 *Globigerina eocaena* Guembel, p. 662, pl. 2, fig. 109.
1953 *Globigerina pseudoeocaena* var. *pseudoeocaena* Subbotina, p. 81, pl.5, figs.1, 2.
1953 *Globigerina pseudoeocaena* var. *compacta* Subbotina, p. 81, pl. 5, fig. 3.
1953 *Globigerina pseudoeocaena* var. *trilobata* Subbotina, p. 84, pl. 5, fig. 5.
1969 *Globigerina eocaena*; Samanta, pl. 330, text- fig. 1.
1975 *Globigerina eocaena*; Toumarkine and Bolli, p. 180, pl. 4, figs. 1, 2.
1992 *Globigerina eocaena*; Anan et al., p. 239, pl. 10, fig.11.
1992 *Globigerina eocaena*; Haggag, p. 106, pl. 2, figs. 5,6.
1992 *Subbotina eocaena*; Cherif et al., p. 46, pl. 1, fig. 36.
1995 *Globigerina eocaena*; Anan, p. 8, pl. 1, fig. 10.
2000 *Subbotina eocaena*; Sztràkos, p. 124, pl. 22, fig. 8.
2002 *Subbotina eocaena*; Abdelghany, p. 214, pl. 1, fig. 7.
2006 *Subbotina eocaena*; Olsson et al., p. 138, pl. 6.9, figs. 1-16.
2015 *Subbotina eocaena*; Molina, p. 172, fig. 5.
2015 *Subbotina eocaena*; Pearson and Wade, p. 13, fig. 10. 5-8.
2020 *Subbotina eocaena*; Anan, p. 497.
2021 *Subbotina eocaena*; Salama et al., p. 12, fig. 7. T.

Remarks: *Subbotina eocaena* recorded here from Middle-Late Eocene is characterized by its 3½-4 globular embracing chambers in the last whorl, with an embracing aperture bordered by a thin irregular lip. It is recorded from many localities in the Atlantic Ocean, the Northern Tethys (Spain, France, Italy, Caucasus) and the Southern Tethys (Tanzania, Libya, Egypt, UAE, Oman, India, Indian Ocean).

***Subbotina gortanii* (Borsetti, 1959)**

(Pl. 1, fig. 2)

1959 *Catapsydrax gortanii* Borsetti, p. 205, pl. 1, fig. 1.
1969 *Globigerina g. gortanii*; Blow, p. 320, pl. 17, fig. 1.
1970 *Globigerina gortanii*; Samanta, p. 32, pl. 7, figs. 11,12.
1995 *Globigerina gortanii*; Anan, p. 8, pl. 1, fig. 12.
2002 *Subbotina gortanii*; Abdelghany, p. 214, pl. 1, fig. 8.
2006 *Subbotina gortanii*; Olsson et al., p. 138, pl. 6.10, figs. 1-17.
2015 *Subbotina gortanii*; Molina, p. 172, fig. 5.
2015 *Subbotina gortanii*; Pearson & Wade, p. 8, fig. 11. 1-8.
2020 *Subbotina gortanii*; Anan, p. 498, pl. 1, fig. 2.

Remarks: The Middle-Late Eocene *Subbotina gortanii* species is characterized by its trochospiral loosely coiled test, 4 globular loosely embracing chambers in the final whorl with a large umbilicus enclosed by surrounding chambers. It was also recorded in the Atlantic Ocean, the Northern Tethys (Spain, France, Italy, Caucasus), and the Southern Tethys (Tanzania, Libya, Egypt, UAE, Oman, India, and Indian Ocean).

***Subbotina jacksonensis* (Bandy, 1949)**

(Pl. 1, fig. 3)

1949 *Globigerina rotundata jacksonensis* Bandy, p. 121, pl. 23, fig. 6.
2006 *Subbotina jacksonensis*; Olsson et al., p. 146, pl. 6.13, figs. 1-20.
2020 *Subbotina jacksonensis*; Anan, p. 498, pl. 1, fig. 4.

Remarks: The Middle-Late Eocene *Subbotina jacksonensis* specie is characterized by its much-embracing chambers, with a reduced final chamber projecting and covering the umbilicus. It was originally recorded from the USA, the Northern Tethys (Spain), and the Southern Tethys (Egypt). It is recorded and illustrated here, for the first time, from Al Ain area.g

***Subbotina linaperta* (Finlay, 1939)**

(Pl. 1, fig. 4)

1939 *Globigerina linaperta* Finlay, p. 125, pl. 23, figs. 54-57.
1968 *Subbotina linaperta*; Srinivasan, p. 149, pl. 16, figs. 7, 10, 11.
1970 *Globigerina linaperta*; Samanta, p. 33, pl. 6, figs. 19, 20.
1971 *Globigerina (Subbotina) linaperta;* Jenkins, p. 162, pl. 18, figs. 551-554.
1975 *Globigerina linaperta*; Toumarkine and Bolli, p. 182, pl. 5, figs. 1, 2.
1990 *Subbotina linaperta*; Premoli Silva and Spezzaferri, p. 312, pl. 2, fig. 2.
1992 *Globigerina linaperta*; Haggag, p. 106, pl. 2, fig. 4.
2000 *Subbotina linaperta*; Sztràkos, P. 143.
2002 *Subbotina linaperta*; Abdelghany, p. 214, pl. 1, figs. 10-11.
2006 *Subbotina linaperta*; Olsson et al., p. 149, pl. 6.14, figs. 1-16.
2015 *Subbotina linaperta*; Molina, p. 172, fig. 5.
2020 *Subbotina linaperta*; Anan, p. 498, pl. 1, fig. 5.
2021 *Subbotina linaperta*; Salama et al., p. 12, fig. 7. W.

Remarks: *Subbotina linaperta* from the Eocene was considered by several authors (e.g. Stainforth et al., 1975; Bolli and Saunders, 1985; Haggag and Luterbacher, 1991) as the basic stock, from which all Eocene *Globigerina* groups or lineage have been differentiated. Olsson et al. (2006) considered *S. linaperta* belongs to a group of tightly coiled subbotinids with a coarse, symmetrical cancellate wall texture which include *S. velascoensis*, *S. patagonica*, *S. angiporoides*, *S. utilisindex*. It appears that Early-Late Eocene *S. linaperta* is derived from Early-Middle Eocene *S. patagonica* by flattening of chambers and rotation of the aperture to a more extraumbilical position. This cosmopolitan species was recorded in Al Ain area, UAE as a part of the Southern Tethys (Tanzania, Libya, Egypt, Oman, Pakistan, India, Indian Ocean, New Zealand, Pacific Ocean), and recorded also in the Northern Tethys (Spain, France, Italy, and the Caucasus).

***Subbotina utilisindex* (Jenkins and Orr, 1973)**

(Pl. 1, fig. 5)

1973 *Globigerina utilisindex* Jenkins and Orr, p. 1089, pl. 10, figs. 6-8.

2000 *Subbotina linaperta utilisindex*; Sztràkos, p. 143.

2006 *Subbotina utilisindex*; Olsson et al., p. 161, pl. 6.6, figs. 14-20.

2021 *Subbotina utilisindex*; Salama et al., p. 14, fig. 8. P.

Remarks: This Late Eocene species is characterized by its trilobate test, spinose wall, final chamber comprising about half of the test, and umbilical-extraumbilical slit-like aperture. It is recorded and illustrated, for the first time, in the current study. It was recorded in the Northern Tethys (France) and also the Southern Tethys (Egypt, Indian Ocean, and Pacific Ocean).

***Subbotina yeguaensis* (Weinzierl and Applin, 1929)**

(Pl. 1, fig. 6)

1929 *Globigerina yeguaensis* Weinzierl and Applin, p. 409, pl. 43, fig. 1.

1968 *Subbotina yeguaensis*; Srinivasan, p. 149, pl. 16, figs. 1-4.

1969 *Globigerina yeguaensis*; Samanta, p. 332, pl. 3, fig. 7.

1992 *Globigerina yeguaensis*; Anan et al., p. 239, fig. 10.18.

1992 *Globigerina yeguaensis*; Haggag, p. 106, pl. 2, figs. 7, 8.

1995 *Globigerina yeguaensis*; Anan, p. 8, pl. 1, fig. 13.

2006 *Globigerina yeguaensis*; Olsson et al., p. 162, pl. 6.18, figs. 1-16.

2015 *Globigerina yeguaensis*; Molina, p. 172, fig. 5.

2021 *Globigerina yeguaensis*; Salama et al., p. 12, fig. 7. Y.

Remarks: The *Subbotina yeguaensis* Eocene species is characterized by its smaller ultimate chamber size than its penultimate chamber size. Haggag and Luterbacher (1991) considered *D. tripartita* (Koch) as being developed from *S. yeguaensis* with many transitional forms, while Olsson et al. (2006) noted that *S. yeguaensis* arose in the Early Eocene possibly from *S. eocaena* (Guembel). It was recorded in the Atlantic Ocean, the Northern Tethys (Spain, Caucasus), and the Southern Tethys (Tanzania, Libya, Egypt, UAE, Pakistan, India, Indian Ocean, New Zealand, and the Pacific Ocean).

Genus *Globigerinatheka* Brönnimann, 1952

Type species *Globigerinatheka barri* Brönnimann, 1952

***Globigerinatheka index* (Finlay, 1939)**

(Pl. 1, fig. 7)

1939 *Globigerinoides index* Finlay, p. 125, pl. 14, figs. 85-88.

1968 *Glopigerapsis index*; Srinivasan, p. 149, pl. 16, figs. 8,9,12.

1985 *Globigerinatheka index*; Keller, p. 886, fig. 4.15.

1988 *Globigerinatheka index*; Coccioni et al., p. 75, pl. 1, figs. 11, 12.

1990 *Globigerinatheka index*; Premoli Silva and Spezzaferri, p. 311, pl. 1, fig. 8.

1992 *Globigerinatheka i. index*; Anan et al., p. 239, fig. 10.6.

1992 *Globigerinatheka i. index*; Haggag, p. 108, pl. 3, fig. 12.

1995 *Globigerinatheka i. index*; Anan, p. 8, pl. 1, fig. 4.

2000 *Globigerinatheka i. index*; Sztràkos, p. 143, pl. 23, fig. 3.

2006 *Globigerinatheka index*; Premoli Silva et al., p. 183, pl. 7.5, figs. 1-20.

2013 *Globigerinatheka index*; Strougo, et al., p. 128, fig. 12. L.

2015 *Globigerinatheka index*; Molina, p. 172, fig. 5.9.

Remarks: The *Globigerinatheka index* species recorded from Middle-Late Eocene is characterized by its three inflated chambers in the last whorl and the last one making almost one-half of the test size, and secondary aperture at the base of the last chamber above the sutures of the previous chambers usually without bullae. *G. index* is one of the three members of the genus *Globigerinatheka* in the Late Eocene besides *G. luterbacheri* and *G. tropicalis.* It is evolved from the Middle Eocene *G. subconglobata* according to Premoli Silva et al. (2006). It was recorded in the Atlantic Ocean, the Northern Tethys (Spain, France, Italy, Caucasus), and also the Southern Tethys (Tanzania, Libya, Egypt, UAE, India, Indian Ocean, New Zealand, and the Pacific Ocean).

***Globigerinatheka luterbacheri* Bolli, 1972**

(Pl. 1, fig. 8)

1972 *Globigerinatheka subconglobata luterbacheri* Bolli, p. 132, pl. 7, fig. 13.

1988 *Globigerinatheka luterbacheri*; Coccioni et al., p. 75, pl. 1, fig. 13.

1990 *Globigerinatheka luterbacheri*; Premoli Silva and Spezzaferri, p. 312, pl. 2, fig. 7.

1992 *Globigerinatheka subconglobata luterbacheri*; Anan et al., p. 239, fig. 10.1.

2006 *Globigerinatheka luterbacheri*; Premoli Silva et al., p. 191, pl. 7.4, figs. 9,10,13.16.

2015 *Globigerinatheka luterbacheri*; Molina, p. 172, fig. 5.

Remarks: The Middle-Late Eocene species is characterized by its robust wall and nearly globular large test with numerous secondary apertures mostly without bullae. It is recorded only in E14 only. It was recorded in the Atlantic Ocean, the Northern Tethys (Spain, Italy), and also the Southern Tethys (Egypt, UAE, Indian Ocean and Pacific Ocean).

***Globigerinatheka semiinvoluta* (Keijzer, 1945)**

(Pl. 1, fig. 9)

1945, *Globigerinoides semi-involutus* Keijzer, p. 206, pl. 4, fig. 58.

1957 *Globigerapsis semiinvoluta*; Bolli et al., p. 34, pl. 6, fig. 7.

1975 *Globigerinatheka semiinvoluta*; Toumarkine and Bolli, p. 184, pl. 6, figs. 15-24.

1985 *Globigerinatheka semiinvoluta*; Keller, p. 886, fig. 4.16.-

1988 *Globigerinatheka semiinvoluta*; Coccioni et al., p. 75, pl. 1, fig. 10.-

1990 *Globigerinatheka semiinvoluta*; Premoli Silva and Spezzaferri, p. 312, pl. 2, fig. 4.

1992 *Globigerinatheka semiinvoluta*; Anan et al., p. 239, fig. 10.9.

1996 *Globigerinatheka semiinvoluta*; Haggag and Bolli, p. 368, fig. 3.15-22.

2000 *Globigerinatheka semiinvoluta*; Sztràkos, p. 144.

2006 *Globigerinatheka semiinvoluta*; Premoli Silva et al., p. 197, pl. 7.9, figs. 1-15.
2013 *Globigerinatheka semiinvoluta*; Strougo et al., p. 128, fig. 12. M.
2015 *Globigerinatheka semiinvoluta*; Molina, p. 172, fig. 5.10,11.
2021 *Globigerinatheka semiinvoluta*; Salama et al., p. 14, fig. 8. V1-V3.

Remarks: *Globigerinatheka semiinvoluta* early Late Eocene [E14] species is characterized by its globular test, inflated enveloping last chamber, and large circular height secondary apertures. It is recorded in the upper part of the Mazyad Member of the Dammam Formation. G. semiinvoluta was recorded in the Atlantic Ocean, the Northern Tethys (Spain, France, Italy, Caucasus) and in the Southern Tethys (Tanzania, Libya, Egypt, UAE, Indian and Pacific Oceans).

***Globigerinatheka tropicalis* (Blow and Banner, 1962)**
1962 *Globigerinoides tropicalis* Blow and Banner, p. 124, pl. 15, figs. D-F.
1970 *Globigerapsis tropicalis*; Samanta, p. 35, pl. 6, figs. 21-23.
1972 *Globigerinatheka index tropicalis*; Bolli, p. 127, text-figs. 58-59.
1990 *Globigerinatheka tropicalis*; Premoli Silva and Spezzaferri, p. 311, pl. 1, fig. 9.
1992 *Globigerinatheka index tropicalis*; Anan et al., p. 239, fig. 10.8.
2000 *Globigerinatheka index tropicalis*; Sztràkos, p. 143.
2006 *Globigerinoides tropicalis*; Premoli Silva et al., p. 204, pl. 7.3, figs. 9-16.
2015 *Globigerinatheka index tropicalis*; Molina, p. 172, fig. 5.
2013 *Globigerinatheka tropicalis*; Strougo et al., p. 128, fig. 12. I.
2020 *Globigerinatheka tropicalis*; Anan, p. 498, pl. 1, fig. 9.

Remarks: The Middle-Late Eocene *Globigerinatheka tropicalis* species is characterized mainly by its mainly sub-circular secondary apertures with rims. Blow (1969) considered it to be largely restricted to cooler water, but Bolli (1972) extends its distribution to mid-latitudes. Anan (1995) noted the presence of keels (*T. cunialensis*), accessory apertures (*Globigerinatheka* members), and tubular spines (*Hantkenina* members), which predominant in tropical warm-temperature regions. He suggested that in the Late Eocene time, the UAE had been in the tropical belt. This species was recorded in the Atlantic Ocean, the Northern Tethys (Spain, France, Italy, Caucasus), and the Southern Tethys (Tanzania, Libya, Egypt, UAE, India, Indian Ocean, New Zealand, and the Pacific Ocean).

Family Hantkeninidae Cushman, 1927
Genus *Cribrohantkenina* Thalmann, 1942
Type species *Hantkenina (Cribrohantkenina) bermudezi* Thalmann, 1942

Cribrohantkenina inflata (Howe, 1928)
(Pl. 2, fig. 10)
1928 *Hantkenina inflata* Howe, p. 14, pl. 14, fig. 2.
1969 *Cribrohantkenina inflata*; Samanta, p. 337, pl. 1, fig. 11.
1975 *Cribrohantkenina inflata*; Martinez-Gallego and Molina, p. 178, pl. 1, fig. 2.
1988 *Cribrohantkenina inflata*; Coccioni, p. 87, pl. 2, figs. 9-12; pl. 3, figs. 1-8 .
1990 *Cribrohantkenina inflata*; Premoli Silva and Spezzaferri, p. 311, pl. 1, fig. 7.
1992 *Cribrohantkenina inflata*; Anan et al., p. 236, fig. 8.8.
1992 *Cribrohantkenina inflata*; Cherif et al., p. 46, pl. 1, fig. 32.
1995 *Cribrohantkenina inflata*; Anan, p. 8, pl. 1, figs. 14, 15.
1997 *Cribrohantkenina inflata*; Pearson and Chaisson, p. 57, pl. 2, fig. 9.
2002 *Cribrohantkenina inflata*; Abdelghany, p. 215, pl. 2, figs. 3-6.
2006 *Cribrohantkenina inflata*; Coxall and Pearson, p. 226, pl. 8.3, figs. 1-14.
2006 *Cribrohantkenina inflata*; Hernitz Kučenjak et al., p. 32, pl. 2, fig. 7.
2015 *Cribrohantkenina inflata*; Molina, p. 173, fig. 6.2.
2015 *Cribrohantkenina inflata;* Pearson and Wade, p. 20, fig. 22. 1-3; fig. 23. 1-21.
2018 *Cribrohantkenina inflata*; Anan, p. 124, fig. 5a.

Remarks: The genus *Cribrohantkenina* is regarded as a monotypic genus. Blow (1969), Toumarkine and Luterbacher (1985), Anan (1995, 2018), Coxall and Pearson (2006), and Pearson and Wade (2015) consider this genus to have evolved from the genus *Hantkenina* Cushman (1924). The Late Eocene species *C. inflata* is distinguished from all other hantkeninids by the presence of one or more areal secondary circular apertures with lips in the final adult chamber. It was recorded in the low-mid latitudes: the Atlantic Ocean, the Northern Tethys (Spain, Italy), and also the Southern Tethys (Egypt, UAE, India, Indian Ocean). Anan (1995) presented a map (Fig. 6) showing the distribution of *C. inflata* in six localities in the world (between 40º N-20ºS): the Atlantic Ocean, the Northern Tethys (Spain, Italy, Caucasus), the Southern Tethys (UAE, Oman, and India).

Genus *Hantkenina* Cushman, 1924
Type species *Hantkenina alabamensis* Cushman, 1924

***Hantkenina alabamensis* Cushman, 1924**
(Pl. 2, fig. 11)
1924 *Hantkenina alabamensis* Cushman, p. 3, pl. 1, figs. 1-6.
1968 *Hantkenina alabamensis*; Srinivasan, p. 145, pl. 13, figs. 5, 6, 9.
1970 *Hantkenina alabamensis*; Samanta, p. 37, pl. 7, fig. 8.
1975 *Hantkenina alabamensis*; Toumarkine and Bolli, p. 174, pl. 1, figs. 10-13.
1975 *Hantkenina alabamensis*; Martinez-Gallego and Molina, p. 180.
1985 *Hantkenina alabamensis*; Keller, p. 886, fig. 3. 9,10.
1988 *Hantkenina alabamensis*; Coccioni, p. 85, pl. 1, figs. 1-9.
1990 *Hantkenina alabamensis*; Premoli Silva and Spezzaferri, p. 311, pl. 1, figs. 4-6.
1992 *Hantkenina alabamensis*; Anan et al., p. 239, fig. 8.6.
1992 *Hantkenina alabamensis*; Haggag, p. 106, pl. 2, fig. 3.
1995 *Hantkenina alabamensis*; Anan, p. 8, pl. 1, fig. 16.

1997 *Hantkenina alabamensis*; Pearson and Chaisson, p. 61, pl. 1, fig. 8.
2000 *Hantkenina alabamensis*; Sztràkos, p. 143.
2006 *Hantkenina alabamensis*; Coxall and Pearson, p. 230, pl. 8.4, figs. 1-14.
2015 *Hantkenina alabamensis*; Pearson and Wade, p. 22, fig. 24.1-6.
2015 *Hantkenina alabamensis*; Molina, p. 172, fig. 5.
2018 *Hantkenina alabamensis*; Anan, p. 125, fig. 5b.
2020 *Hantkenina alabamensis*; Anan, p. 499, pl. 1, fig. 11.

Remarks: Coxall et al. (2003) revealed that the Middle-Late genus *Hantkenina* was evolved gradually from the clavata species *Clavigerinella eocenica* (Nuttall), and contrary to the long-held view it is related to the genus *Pseudohastigerina* (Banner and Blow). The genus *Hantkenina* Cushman (1924) is characterized by having tubulospine on some or all of the chambers in the adult whorls. The cosmopolitan Middle-Late Eocene species *H. alabamensis* is the most advanced representative of the genus. It was recorded in the low-mid latitudes: the Atlantic Ocean, the Northern Tethys (Spain, France, Italy, Caucasus) and also the Southern Tethys (Tanzania, Libya, Egypt, Syria, UAE, India, Indian Ocean, and New Zealand).

***Hantkenina compressa* Parr, 1947**
(Pl. 2, fig. 12)
1947 *Hantkenina compressa* Parr, p. 46, text-figs. 1-7.
2006 *Hantkenina compressa*; Coxall and Pearson, p. 233, pl. 8.6, figs. 1-21.
2015 *Hantkenina compressa*; Molina, p. 173, fig. 6.
2018 *Hantkenina compressa*; Anan, p. 127, fig. 5d.
2020 *Hantkenina compressa*; Anan, p. 499.

Remarks: The *Hantkenina compressa* Middle-Late Eocene species is characterized by its more laterally compressed chambers than *H. alabamensis*. The final 2-3 chambers are in contact with the posterior wall of the adjacent chambers. Coxall and Pearson (2006) noted that this species is intermediate in morphology between Middle Eocene *H. dumblei* and Middle-Late Eocene *H. alabamensis* and overlaps stratigraphically with them both, and the morphospecies of the latter species and *H. compressa* seem to be linked by a continuous gradation of morphology. It was recorded in the Atlantic Ocean, the Northern Tethys (Spain, Italy) and also the Southern Tethys (Tanzania, Egypt, UAE and Australia).

***Hantkenina primitiva* Cushman and Jarvis, 1929**
(Pl. 2, fig. 13)
1929 *Hantkenina alabamensis* Cushman var. *primitiva* Cushman and Jarvis, p. 16, pl. 3, figs. 2, 3.
1969 *Hantkenina primitiva*; Samanta, p. 340, pl. 1, fig. 9.
1992 *Hantkenina primitiva*; Anan et al., p. 236, fig. 8.7.
2006 *Hantkenina primitiva*; Coxall and Pearson, p. 250, pl. 8.12, figs. 1-20.
2015 *Hantkenina primitiva*; Molina, p. 173, fig. 6.
2015 *Hantkenina primitiva*; Pearson and Wade, p. 23, fig. 25. 5-9.
2018 *Hantkenina primitiva*; Anan, p. 127, fig. 5f.

Remarks: *Hantkenina primitiva* Middle-Late Eocene species has 5-6 compressed polygonal chambers extending into hollow tubulospine and increasing steadily in size as added. Coxall and Pearson (2006) noted that this species might have evolved from *H. compressa* at the base of Middle Eocene E13 (*Morozovella crassata* Zone). It was recorded in the Atlantic Ocean, the Northern Tethys (Spain, Italy) and the Southern Tethys (Tanzania, Libya, Egypt, UAE and India).

Family Globoquadrinidae Blow, 1979
Genus *Dentoglobigerina* Blow, 1979
Type species *Globigerina galavisi* Bermúdez, 1961

***Dentoglobigerina galavisi* (Bermúdez, 1961)**
(Pl. 2, fig. 14)
1961 *Globigerina galavisi* Bermúdez, p. 1183, pl. 4, fig. 3.
1975 *Globigerina galavisi*; Toumarkine and Bolli, p. 72.
2006 *Dentoglobigerina galavisi*; Olsson et al., p. 403, pl. 13.1, figs. 1-16.
2006 *Dentoglobigerina galavisi*; Hernitz Kučenjak et al., p. 30, pl. 1, fig. 11.
2015 *Dentoglobigerina galavisi*; Molina, p. 172, fig. 5.
2015 *Dentoglobigerina galavisi*; Pearson and Wade, p. 17, fig. 15.1-8.
2021 *Dentoglobigerina galavisi*; Salama et al., p. 12, fig. 7. N.

Remarks: *Dentoglobigerina galavisi* Middle-Late Eocene species is characterized by 3½ nearly globular chambers in the final whorl with a small umbilicus enclosed by surrounding chambers. It is recorded and illustrated in the study section, for the first time, in UAE. It was recorded in the Atlantic Ocean, the Northern Tethys (Spain, Italy, Caucasus) and also the Southern Tethys (Tanzania, Libya, Egypt, Syria, UAE, Indian Ocean and Pacific Ocean).

***Dentoglobigerina pseudovenezuelana* (Blow and Banner, 1962)**
(Pl. 2, fig. 15)
1962 *Globigerina yeguaensis pseudovenezuelana* Blow and Banner, p. 100, pl. 11, figs. J-L.
1992 *Globigerina pseudovenezuelana*; Anan et al., p. 239, fig. 11.1.
2006 *Dentoglobigerina pseudovenezuelana*; Olsson et al., p. 404, pl. 13.2, figs. 1-16.
2008 *Dentoglobigerina pseudovenezuelana*; Wade and Pearson, p. 249, fig. 5.
2015 *Dentoglobigerina pseudovenezuelana*; Molina, p. 172, fig. 5.
2015 *Dentoglobigerina pseudovenezuelana*; Pearson and Wade, p. 18, fig. 17.1-6.
2021 *Dentoglobigerina pseudovenezuelana*; Salama et al., p. 12, fig. 7. O.

Remarks: *Dentoglobigerina pseudovenezuelana* Late Eocene species is characterized by its embracing 3¼ chambers in the last whorl, which led to a compact subcircular test. Olsson et al. (2006) regarded that this species evolved from *D. galavisi.* It was recorded in the Northern Tethys (Spain, Caucasus) and also the Southern Tethys (Tanzania, Egypt and UAE).

***Dentoglobigerina tripartita* (Koch, 1926)**
(Pl. 2, fig. 16)
1926 *Globigerina bulloides* var. *tripartita* Koch, p. 742, fig. 21.
1975 *Globigerina tripartita*; Toumarkine and Bolli, p. 180, pl. 4, figs. 3,4.

1992 *Globigerina tripartita*; Anan et al., p. 239, fig. 11. 5.
1992 *Globigerina tripartita*; Haggag, p. 104, pl. 1, fig. 16.
2000 *Subbotina tripartita*; Sztràkos, p. 143.
2006 *Globigerina tripartita*; Hernitz Kučenjak et al., p. 36, pl. 4, fig. 4.
2006 *Dentoglobigerina tripartita*; Olsson et al., p. 408, pl. 13.3, figs. 1-16.
2015 *Dentoglobigerina tripartita*; Molina, p. 172, fig. 5.
2021 *Dentoglobigerina tripartita*; Salama et al., p. 12, fig. 7. Q.

Remarks: *Dentoglobigerina tripartita* Middle-Late Eocene species is characterized by its compact test with 3 chambers increasing rapidly in size in the last whorl, the final chamber hangs over the umbilicus. Olsson et al. (2006) regarded that this species evolved from *D. galavisi*. It was recorded in the Northern Tethys (Spain, France, Italy, Caucasus) and also Southern Tethys (Tanzania, Libya, Egypt, Syria, UAE, India, Indian and Pacific Oceans).

Family Hedbergellidae Loeblich and Tappan, 1961
Genus *Pseudohastigerina* Banner and Blow, 1959
Type species *Nonion micrus* Cole, 1927

***Pseudohastigerina micra* (Cole, 1927)**

1927 *Nonion micrus* Cole, p. 22, pl. 5, fig. 12.
1957 *Hastigerina micra*; Bolli, p. 161, pl. 35, fig. 2.
1959 *Pseudohastigerina micrus*; Banner and Blow, p. 19, fig. 4.1-9.
1969 *Pseudohastigerina micrus*; Samanta, p. 342, pl. 1, fig. 6.
1975 *Pseudohastigerina micrus*; Toumarkine and Bolli, p. 174, pl. 1, figs. 1, 2.
1975 *Pseudohastigerina micrus*; Martinez-Gallego and Molina, p. 181, pl. 2, fig. 1.
1985 *Pseudohastigerina micrus*; Keller, p. 886, fig. 3.3,4.
1988 *Pseudohastigerina micrus*; Coccioni et al., p. 75, pl. 1, figs. 14, 15.
1992 *Pseudohastigerina micrus*; Anan et al., p. 242, fig. 8,9.
1992 *Pseudohastigerina micrus*; Haggag, p. 106, pl. 2, figs. 1,2 .
2000 *Pseudohastigerina micrus*; Sztràkos, p. 143.
2002 *Pseudohastigerina micrus*; Abdelghany, p. 214. pl. 2, figs. 1,2.
2006 *Pseudohastigerina micrus*; Hernitz Kučenjak et al., p. 30, pl. 1, fig. 5.
2008 *Pseudohastigerina micrus*; Olsson and Hemleben, p. 422, pl. 14.3, figs. 11-24.
2008 *Pseudohastigerina micrus*; Wade and Pearson, p. 249, fig. 5.
2015 *Pseudohastigerina micrus*; Molina, p. 172, fig. 5, p. 173, fig. 6.4.
2015 *Pseudohastigerina micra*; Pearson and Wade, p. 23, fig. 26. 1-7.
2020 *Pseudohastigerina micra*; Anan, p. 500.
2021 *Pseudohastigerina micra*; Salama et al., p. 12, fig. 7. Z2.

Remarks: This Eocene species is characterized by its planispiral compressed test with 6-7 globular chambers, an equatorial symmetrical circular aperture bordered by a narrow lip. Olsson and Hemleben (2006) considered it evolved from Early-Middle Eocene *P. wilcoxensis* (Cushman and Ponton). This cosmopolitan species was recorded in the many Tethyan localities, i.e.. USA, Mexico, Trinidad, Spain, France, Italy, Egypt, Syria, UAE and India.

Genus *Turborotalia* Cushman and Bermúdez, 1949
Type species *Globorotalia centralis* Cushman and Bermúdez, 1937

***Turbrotalia ampliapertura* (Bolli, 1957)**

(Pl. 2, fig. 17)
1957 *Globigerina ampliapertura* Bolli, p. 108, pl. 22, figs. 4-6.
1968 *Globigerina ampliapertura*; Srinivasan, p. 147, pl. 16, figs. 5, 6.
1970 *Globigerina ampliapertura*; Samanta, p. 31, pl. 6, figs. 9,10, pl.7, figs. 1, 2.
1975 *Globigerina ampliapertura*; Toumarkine and Bolli, p. 180, pl. 4, figs. 17, 18.
1985 *Globigerina ampliapertura*; Keller, p. 886, fig. 3. 14,15.
1992 *Globigerina ampliapertura*; Cherif et al., p. 46, pl. 1, fig. 34.
1992 *Globigerina ampliapertura*; Anan et al., p. 239, fig. 11. 9.
1990 *"Globigerina" ampliapertura*; Premoli Silva and Spezzaferri, p. 312, pl. 2, fig. 1.
2006 *Turbrotalia ampliapertura*; Pearson et al., p. 441, pl. 15.2, figs. 1-20.
2006 *Turbrotalia ampliapertura*; Hernitz Kučenjak et al., p. 32, pl. 2, figs. 10.
2008 *Turbrotalia ampliapertura*; Wade and Pearson, p. 249, fig. 5.
2015 *Turbrotalia ampliapertura*; Pearson and Wade, p. 23, fig. 27. 1-6.
2021 *Turbrotalia ampliapertura*; Salama et al., p. 10, fig. 6. M, p. 14, fig. 8. B.

Remarks: This *Turbrotalia ampliapertura* Late Eocene species is characterized by its high trochospiral test with normally four globular chambers in the last whorl, with a high arched wide umbilical-extraumbilical aperture. Pearson et al. (2006) regarded this species evolved from Middle-Late Eocene *T. increbescens* (Bandy). It was recorded in the Atlantic Ocean, the Northern Tethys (Italy, Caucasus) and the Southern Tethys (Tanzania, Libya, Egypt, Syria, UAE, India, Indian Ocean, New Zealand and Pacific Ocean).

***Turbrotalia cerroazulensis* (Cole, 1928)**

(Pl. 2, fig. 18)
1928 *Globigerina cerro-azulensis* Cole, p. 217, pl. 32, figs. 11-13.
1970 *Globigerina cerro-azulensis*; Samanta, p. 36, pl. 6, figs. 24,25.
1970 *Globorotalia c. cerroazulensis*; Toumarkine and Bolli, p. 144, pl. 1, figs. 19-24.
1979 *Globorotalia (Turborotalia) cerroazulensis*; Blow, p. 1054, pl. 242, figs. 1-7.
1985 *Globorotalia c. cerroazulensis*; Toumarkine and Luterbacher, p. 137, figs. 34.3-4.
1985 *Globorotalia cerroazulensis*; Keller, p. 886, fig. 9-11.
1992 *Globorotalia c. cerroazulensis*; Anan et al., p. 236, fig. 9.6.
1992 *Turbrotalia c. cerroazulensis*; Haggag, p. 106, pl. 2,

fig. 12.
1995 *Turbrotalia c. cerroazulensis*; Anan, p. 8, pl. 1, fig. 7.
2000 *Turbrotalia c. cerroazulensis*; Sztràkos, p. 142.
2006 *Turbrotalia cerroazulensis*; Pearson et al., p. 442, pl. 15.3, figs. 1-20.
2006 *Turbrotalia cerroazulensis*; Hernitz Kučenjak et al., p. 32, pl. 2, figs. 4,5.
2008 *Turbrotalia cerroazulensis*; Wade and Pearson, p. 249, fig. 5.
2015 *Turbrotalia cerroazulensis*; Molina, p. 172, fig. 5.
2013 *Turbrotalia cerroazulensis*; Strougo et al., p. 128, fig. 12. D.
2015 *Turbrotalia cerroazulensis*; Pearson and Wade, p. 24, fig. 28. 1-4.
2020 *Turbrotalia cerroazulensis*; Anan, p. 500, pl. 2, fig. 20.
2021 *Turbrotalia cerroazulensis*; Salama et al., p. 10, fig. 6. H1, H2.

Remarks: Toumarkine and Bolli (1970) introduced a Middle-Late Eocene *Turbrotalia cerroazulensis* lineage to include a series of six subspecies, and four of them are recorded in the Late Eocene: *T. pomeroli*, *T. cerroazulensis*, *T. cocoaensis* and *T. cunialensis*, while the other two subspecies *T. frontosa* and *T. possagnoensis* normally exist at a lower stratigraphic level than Late Eocene. The Middle-Late Eocene *T. cerroazulensis* species is characterized by its moderate trochospiral test, conical shape in side view, flat spiral side, and a broad arched aperture. Pearson et al. (2006) considered this species evolved from the Middle-Late Eocene *T. pomeroli*. It was recorded in the Atlantic Ocean, the Northern Tethys (Spain, France, Italy, Caucasus) and also the Southern Tethys (Tanzania, Libya, Egypt, Syria, UAE, India, Indian Ocean, New Zealand and Pacific Ocean).

***Turbrotalia cocoaensis* (Cushman, 1928)**
(Pl. 3, fig. 19)
1928 *Globorotalia cocoaensis* Cushman, p. 75, pl. 10, fig. 3.
1975 *Globorotalia cerroazulensis cocoaensis*; Toumarkine and Bolli, p. 176, pl. 2, figs. 16-18.
1985 *Globorotalia cerroazulensis cocoaensis*; Keller, p. 886, fig. 4.5-7.
1992 *Turbrotalia cerroazulensis cocoaensis*; Anan et al., p. 236, fig. 9.7.
1995 *Turbrotalia cerroazulensis cocoaensis*; Anan, p. 8, pl. 1, fig. 2.
1997 *Turbrotalia cocoaensis*; Pearson and Chaisson, p. 65.
2000 *Turbrotalia cerroazulensis cocoaensis*; Sztràkos, p. 142.
2002 *Turbrotalia cocoaensis*; Abdelghany, p. 214, pl. 1, figs. 1, 2.
2006 *Turbrotalia cocoaensis*; Hernitz Kučenjak et al., p. 32, pl. 2, figs. 1, 2.
2006 *Turbrotalia cocoaensis*; Pearson et al., p. 446, pl. 15.4, figs. 1-12.
2008 *Turbrotalia cocoaensis*; Wade and Pearson, p. 249, fig. 5.
2015 *Turbrotalia cocoaensis*; Molina, p. 172, fig. 5, p. 173, fig. 6.3.
2015 *Turbrotalia cocoaensis*; Pearson and Wade, p. 24, fig. 28. 5-13.
2021 *Turbrotalia cocoaensis*; Salama et al., p. 10, fig. 6. I1, I2.g

Remarks: This *Turbrotalia cocoaensis* Middle-Late Eocene species is characterized by its low to moderate trochospiral biconvex test with 4-5 chambers in the last whorl. It distinguished from *T. cerroazulensis* by having a distinctly acute periphery to the final chamber as seen in the side view and evolved from it. It was recorded in the Atlantic Ocean, the Northern Tethys (Spain, France, Italy, Caucasus) and also the Southern Tethys (Tanzania, Libya, Egypt, Syria, UAE, India, Indian and Pacific Oceans).

***Turbrotalia* sp.**
(Pl. 3, fig. 20)
Transition specimen between *Turbrotalia cocoaensis* (Cushman) and *Turbrotalia cunialensis* (Toumarkine and Bolli), *Globigerinatheka index* Zone (E15), Late Eocene, J. Hafit, UAE.

Remarks: The Late Eocene *Turbrotalia* sp. resembles *T. cocoaensis* with acute periphery in the last final chamber but without a keel, on one hand, and resemble *T. cunialensis* in having weak raised keel in the first two chambers, on the other hand. It is recorded and illustrated, for the first time, in the current study.

***Turbrotalia cunialensis* (Toumarkine and Bolli, 1970)**
(Pl. 3, fig. 21)
1970 *Globorotalia cerroazulensis cunialensis* Toumarkine and Bolli, p. 144, pl. 1, figs. 37-39.
1985 *Globorotalia cerroazulensis cunialensis*; Keller, p. 886, fig. 4.1-4.
1988 *Turbrotalia cunialensis*; Coccioni et al., p. 75, pl. 1, figs. 7-9.
1992 *Turbrotalia cerroazulensis cunialensis*; Anan et al., p. 236, fig. 9. 8.
1995 *Turbrotalia cerroazulensis cunialensis*; Anan, p. 8, pl. 1, fig. 1.
2000 *Turbrotalia cerroazulensis cunialensis*; Sztràkos, p. 142.
2002 *Turbrotalia cunialensis*; Abdelghany, p. 214, pl. 1, figs. 3, 4.
2006 *Turbrotalia cunialensis*; Pearson et al., p. 450, pl. 15.4, figs. 13-17.
2015 *Turbrotalia cunialensis*; Molina, p. 173, fig. 6.
2015 *Turbrotalia cunialensis*; Pearson and Wade, p. 25, fig. 29. 1-11.
2021 *Turbrotalia cunialensis*; Salama et al., p. 10, fig. 6. J.

Remarks: *Turbrotalia cunialensis* Late Eocene species is characterized by its strongly compressed biconvex test with keel around periphery. It distinguished from *T. cocoaensis* by having a distinctly keel around periphery, and evolved from it. It was recorded in the Atlantic Ocean, the Northern Tethys (France, Italy) and also the Southern Tethys (Tanzania, Egypt, UAE, Oman, India and Indian Ocean).

***Turbrotalia increbescens* (Bandy, 1949)**
(Pl. 3, fig. 22)
1949 *Globigerina increbescens* Bandy, p. 120, pl. 23, fig. 3.
1962 *Globorotalia (Turborotalia) increbescens*; Blow and Banner, p. 118, pl. 13, figs. T-V. 1968 *Turbrotalia increbescens*; Srinivasan, p. 146, pl. 14, figs. 5-7.

1970 *Globorotalia (Turborotalia) increbescens*; Samanta, p. 36, pl. 6, fig. 26, 27.
1985 *Globorotalia increbescens*; Keller, p. 886, fig. 3. 16.
1992 *Globorotalia (Turborotalia) increbescens*; Cherif et al., p. 50, pl. 3, fig. 2.
2000 *Turbrotalia increbescens*; Sztràkos, p. 142.
2006 *Turbrotalia increbescens*; Pearson et al., p. 453, pl. 15.6, figs. 1-15.
2006 *Turbrotalia increbescens*; Hernitz Kučenjak et al., p. 32, pl. 2, figs. 11.
2015 *Turbrotalia increbescens*; Pearson and Wade, p. 25, fig. 27. 7-8.
2021 *Turbrotalia increbescens*; Salama et al., p. 10, fig. 6. L.

Remarks: *Turbrotalia increbescens* Middle-Late Eocene species is characterized by its highly trochospiral test including 4 globular chambers in the last whorl with a rounded periphery, a broad arched aperture in an intra-extraumbilical position. It differs from *T. cerroazulensis* by having a round periphery, fewer and fewer chambers, and more globular test shape. Pearson et al. (2006) regarded that this species is intermediate in morphology between *T. pomeroli* and *T. ampliapertura* and evolved from *T. pomeroli* in the Middle Eocene. It was recorded in the Atlantic Ocean, the Northern Tethys (Spain, France, Caucasus), and the Southern Tethys (Tanzania, Libya, Egypt, Syria, UAE, India, Indian Ocean, New Zealand and Pacific Ocean).

***Turborotalia pomeroli* (Toumarkine and Bolli, 1970)**
(Plate 3, figure 23)
1970 *Globorotalia cerroazulensis pomeroli* Toumarkine and Bolli, p. 140, pl. 1, figs. 10-18.
1988 *Turborotalia pomeroli*; Coccioni et al., p. 75, pl. 1, figs. 1-3.
1992 *Globorotalia (Turborotalia) cerroazulensis pomeroli*; Cherif et al., p. 50, pl. 3, fig. 1.
1992 *Turborotalia cerroazulensis pomeroli*; Haggag, p. 106, pl. 2, fig. 12.
1995 *Turborotalia cerroazulensis pomeroli*; Anan, p. 8, pl. 1, fig. 8.
2000 *Turborotalia cerroazulensis pomeroli*; Sztràkos, p. 142, pl. 23, fig. 14.
2006 *Turborotalia cerroazulensis pomeroli*; Pearson et al., p. 454, pl. 15.7, figs. 10-20.
2006 *Turborotalia cerroazulensis pomeroli*; Hernitz Kučenjak et al., p. 32, pl. 2, fig. 8.
2013 *Turborotalia cerroazulensis pomeroli;* Strougo et al., p. 128, fig. 12. C.
2015 *Turborotalia cerroazulensis pomeroli*; Molina, p. 172, fig. 5.
2020 *Turborotalia pomeroli*; Anan, p. 500, pl. 2, fig. 21.
2021 *Turbrotalia pomeroli*; Salama et al., p. 10, fig. 6. K.

Remarks: The *Turbrotalia pomeroli* Middle-Late Eocene species is characterized by its moderate trochospiral test with 4 globular chambers increasing moderately in size, a broad arched aperture in umbilical-extraumbilical position. Pearson et al. (2006) regarded that this species evolved from *T. frontosa* in the Middle Eocene and was ancestral to *T. cerroazulensis* and *T. increbescens*. It was recorded in the Northern Tethys (Spain, France, Italy) and the Southern Tethys (Tanzania, Libya, Egypt, Syria, UAE, India and Pacific Ocean).

***Turborotalia pseudoampliapertura* (Blow and Banner, 1962)**
(Pl. 3, fig. 24)
1962 *Globigerina pseudoampliapertura* Blow and Banner, p. 95, pl. 12, figs. A-C.
1968 *Globigerina ampliapertura pseudoampliapertura*; Srinivasan, p. 147, pl. 17, figs. 4-6.
1969 *Globigerina pseudoampliapertura*; Samanta, p. 331, pl. 1, fig. 13.
1990 *Turborotalia pseudoampliapertura*; Premoli Silva and Spezzaferri, p. 312, pl. 2, figs. 3,5.
1992 *Turborotalia pseudoampliapertura*; Anan et al., p. 236, fig. 9.10.
1995 *Turborotalia p. pseudoampliapertura*; Haggag and Luterbacher, p. 41, pl. 3, figs. 5-8.
1995 *Turborotalia pseudoampliapertura*; Anan, p. 8, pl. 1, fig. 6.
2013 *Turborotalia pseudoampliapertura*; Strougo et al., p. 128, fig. 12. F-G.

Remarks: *Turborotalia pseudoampliapertura* Middle-Late Eocene species is characterized by its moderate trochospiral test with 4 globular chambers increasing moderately in size, a broader arched aperture in umbilical-extraumbilical position than *T. pomeroli*. Haggag and Luterbacher (1991) introduced in a younger part of the Middle –Late Eocene a *Turborotalia pseudoampliapertura* lineage, which includes *T. pomeroli, T. nukhulensis*, *T. pseudoampliapertura*, *T. sinaiensis.* The members of *T. pseudoampliapertura* lineage flourish those of *T. cerroazulensis* lineage become rare or disappear. Haggag and Luterbacher (1995) regarded that this species evolved from their *T. nukhulensis* in the late Middle Eocene and was ancestral to their *T. sinaiensis*. Two only members of *T. pseudoampliapertura* lineage are recorded in the study section: *T. pseudoampliapertura T. sinaiensis,* while *T. nukhulensis* was recorded in Jabal Malaqet section, Al Ain area, UAE (Anan, 1995). *T. pseudoampliapertura* was used by Haggag (1992) as a zonal marker for her '*T. pseudoampliapertura* Zone', which she considered as to be located between the *Truncorotaloides rohri* Zone (P14=E13) and *Globigerinatheka semiinvoluta* Zone (P15=E14). *T. pseudoampliapertura* was recorded, so far, in the Southern Tethys (Libya, Egypt, UAE, India, Indian Ocean and New Zealand).

***Turborotalia sinaiensis* Haggag and Luterbacher, 1995**
(Pl. 3, fig. 25)
1995 *Turborotalia pseudoampliapertura sinaiensis* Haggag and Luterbacher, p. 41, pl. 3, figs. 1-4.
2013 *Turborotalia sinaiensis*; Strougo et al., p. 128, fig. 12. H.

Remarks: *Turborotalia sinaiensis* Middle-Late Eocene species is characterized by its moderate trochospiral test with 4 globular chambers increasing moderately in size, a more broad arched aperture in umbilical-extraumbilical position than *T. pseudoampliapertura.* Haggag and Luterbacher (1995) regarded that this species evolved from *T. pseudoampliapertura* in the late Middle Eocene. *T.*

sinaiensis is recorded and illustrated, for the first time, in the study section, after its occurrence in Sinai of Egypt.

Family Chiloguembelinidae Reiss, 1963

Genus *Chiloguembelina* Loeblich and Tappan, 1956

Type species *Guembelina midwayensis* Cushman, 1940

***Chiloguembelina cubensis* (Palmer, 1934)**

1934 *Guembelina cubensis* Palmer, p. 74, figs. 1-6.

1957 *Chiloguembelina cubensis*; Beckmann, p. 89, pl. 21, fig. 21.

1968 *Chiloguembelina cubensis*; Srinivasan, p. 142, pl. 13, fig. 1.

1985 *Chiloguembelina cubensis*; Keller, p. 886, fig. 3.8.

1992 *Chiloguembelina cubensis*; Anan et al., p. 236, fig. 8.1.

1992 *Chiloguembelina cubensis*; Cherif et al., p. 46, pl. 1, fig. 32.

2006 *Chiloguembelina cubensis*; Hernitz Kučenjak et al., p. 36, pl. 4, fig. 11.

2015 *Chiloguembelina cubensis*; Molina, p. 172, fig. 5.

2015 *Chiloguembelina cubensis*; Pearson and Wade, p. 25, fig. 30. 3.

2021 *Chiloguembelina cubensis*; Salama et al., p. 10, fig. 6. B.

Remarks: The *Chiloguembelina cubensis* Middle-Late Eocene species is characterized by its biserial elongate test, surface texture distinctly costate in rows or striae aligned with the long axis of the test. It was recorded in the Northern Tethys (Spain) and the Southern Tethys (Tanzania, Egypt, Syria, UAE, India, New Zealand and Pacific Ocean).

The biozone *Gt. semiinvoluta* (E14) has yielded: *Catapsydrax dissimilis*, *C. unicavus*, *Subbotina angiporoides*, *S. corpulenta*, *S. eocaena*, *S. gortanii*, *S. jacksonensis*, *S. linaperta*, *S. utilisindex*, *S. yeguaensis*, *Globigerinatheka index*, *Gt. luterbacheri*, *Gt. semiinvoluta*, *Gt. tropicalis*, *Hantkenina alabamensis*, *H. compressa*, *Dentoglobigerina galavisi*, *D. pseudovenezuelana*, *D. tripartita*, *Turborotalia ampliapertura*, *T. cerroazulensis*, *T. cocoaensis*, *T. pomeroli*, *T. increbescens*, *T. pseudoampliapertura*, *T. sinaiensis*, *Pseudohastigerina micra.* The biozone *G. index* Zone (E15) has yielded all the previous species, except *Globigerinatheka semiinvoluta*, *G. luterbacheri*, *G. tropicalis* and *Subbotina corpulenta*, but added *Hantkenina primitiva*, *Cribrohantkenina inflata* and *Chiloguembelina cubensis.* The biozone *H. alabamensis* Zone (E16) has yielded: *Catapsydrax dissimilis*, *C. unicavus*, *Pseudohastigerina micra*, *T. pseudoampliapertura*, *T. cunialensis* and *Hantkenina alabamensis.*

4. Paleogeography

Based on the paleogeographic distribution of the Late Eocene faunal content of the study section, a brief account is given: Twenty-five of thirty two identified planktic foraminiferal species have wide geographic distribution around the world (Fig. 5). Some of them have been recorded in five or more localities, i.e. *Catapsydrax dissimilis, C. unicavus*, *Subbotina angiporoides*, *S. corpulenta*, *S. eocaena*, *S. gortanii*, *S. linaperta*, *S. yeguaensis*, *Globigerinatheka index*, *G. semiinvoluta*, *G. tropicalis*, *Cribrohantkenina inflata*, *Hantkenina alabamensis*, *H. primitiva*, *Dentoglobigerina galavisi, D. tripartita*, *Turborotalia ampliapertura*, *T. cerroazulensis*, *T. cocoaensis*, *T. cunialensis*, *T. increbescens*, *T. pomeroli*, *T. pseudoampliapertura*, *Pseudohastigerina micra,* and *Chiloguembelina cubensis*. Haq and Aubry (1980) noted that North Africa and the Middle East formed important parts of the Tethyan link between the Atlantic and the Pacific Ocean during the Early Cenozoic. The paleogeographic map of Mintz (1981) shows that the ancestral Tethyan Ocean in the Paleogene time is connected with the ancestral Indian, Atlantic, and Pacific Oceans (Fig. 5). Adams et al. (1983) noted that the continuous marine Paleogene connection between the area occupied by the present-day Mediterranean and the Indian Ocean had been lost by mid-Burdigalian (early Oligocene) times when a land bridge connected S.W. Asia to Arabia. Anan (1994) presented a map showing the paleogeographic distribution of some diagnostic Late Eocene planktic foraminiferal species from their original description, i.e.. *Cribrohantkenina inflata* and *Turborotalia cunialensis* (Fig. 6), which are restricted in the tropical-subtropical provinces (Lat. 45º N- 30º S). Anan (1995) noted that the almost identical planktic foraminifera are barren in the cross-bedded nummulitic limestones succession, which represents the topmost Eocene rocks of both J. Hafit and J, Malaqet in Al Ain area, UAE. These rocks overlie a succession of gypsiferous calcareous marls (with limestone intercalations) with abundant planktic foraminifera, among them *Globigerinatheka index*, *Cribrohantkenina inflata*, *Turborotalia cunialensis,* and *Hantkenina alabamensis.* Rögl (1999) noted that by the end of the Eocene the Tethyan Ocean had already vanished (the new Indian Ocean was born), and the western end of the Tethys was reduced to the Mediterranean Sea. The existence of marked differences between the number of recorded planktic foraminiferal species in the closest or farest localities concerning Jabal Hafit may be due to one or more of these parameters: the differences in the paleoenvironment conditions (depth, temperature, salinity, nutrients, dissolved oxygen), scarce of detailed or documented studies, the deficiency of available works of literature, and/or due to less homogeneity in the species concept between different authors.

5. Paleoenvironment

The planktic foraminiferal Late Eocene species in the current study are rich and diversified in the marly samples of the study section of Jabal Hafit, and represent a middle-upper neritic environment. The following is a brief account of the relevant paleoenvironment and interpretation of the study area: Anan (1995) noted that in the Late Eocene in the UAE and surrounding areas had been located in the tropical and warm temperature region based on many faunal environmental elements, i.e. tubular spines in the hantkeninids and accessory apertures in the *Globigerinatheka* spp. The current study yields many Hantkeninids (*H. alabamensis*, *H. compressa*, *H. primitiva*) and *Globigerinatheka* species (*G. index, G. luterbacheri*, *G. semiinvoluta*), and also *Cribrohantkenina inflata* with its accessory apertures and tubular spines (Plates 1, 2). These elements proved that J. Hafit had been located in the tropical and warm temperature region in the Late Eocene time. Bodiselitsch et al. (2004) noted that the Late Eocene

is a period of major changes, with a sharp temperature drop of about 2 °C near the Eocene/Oligocene boundary. Anan (2009) noted that an intraformational conglomeratic bed separates P15 and P16 (= E14 and E15) at Mazyad Member of the Dammam Formation within the Late Eocene (Fig. 3), which represents sea level lowering (about 39 Ma), which had not been presented in the Vail et al (1977), but in Keller et al. (1987) (Fig. 7). Anan (2018) noted that the presence of accessory apertures and tubulospine in the Hantkeninids planktic foraminiferal species are suggested by many authors (i.e. Coccioni 1988; Anan, 1994; Coxall and Pearson, 2006) to be restricted in the mid to low latitude, in the open ocean and shelf paleoenvironments and tropical-subtropical warm-temperate regions. Anan (2020) noted that the two intraformational conglomeratic beds in the Middle and Late Eocene of Jabal Hafit, UAE (Fig. 8), were documented by Keller et al. (1987) as (PHe and PHd, respectively), and represented a minimal reworking and accumulating in the low-energy environment in a short distance of transportation on a slight steepening paleoslope from a positive localized source area during the time of a marked fall in the eustatic sea level lowering with active tectonics.

6. Discussion and Conclusions

More than two decades have been dedicated to the Late Eocene planktic foraminiferal species content in various parts of Al Ain outcrops: Jabal Hafit, J. Malaqet (UAE), and J. Qatar (Oman). Several facts regarding the temporal and spatial distribution of the species have emerged.

- Many attempts were done on the biozonation of the Late Eocene: two zones (Bipartite) by some authors (i. e. Stainforth et al, 1975): the lower *Globigerinatheka semiinvoluta* Zone (P15) and the upper *Turborotalia cerroazulensis* Zone (P16), while it is subdivided to three zones (Tripartite) by others (i. e. Berggren and Miller, 1988): the lower *Globigerinatheka semiinvoluta* Zone (P15), the middle *Cribrohantkenina inflata* Zone (P16), and the upper *Turborotalia cerroazulensis* Zone (P17). Three planktic foraminiferal biozones (Tripartite), but with another planktic foraminiferal species, are recognized in the current study, according to the modern biozonation (after Berggren and Pearson, 2005; Pearson et al., 2006 and Wade et al., 2011), from base to top: *Globigerinatheka semiinvoluta* Zone (E14), *G. index* Zone (E15), and *Hantkenina alabamensis* Zone (E16).

- The recognized taxa have been correlated with those in Al Ain area: J. Malaqet, UAE, and J. Qatar, Oman (24 km northeast of Al Ain city) (Fig. 1), as well as other Late Eocene succession in some of the Northern and the Southern Tethys localities (i.e. the Atlantic Ocean, Spain, France, Italy, Carpathica, Caucasus, Tanzania, Libya, Egypt, Syria, India, Indian Ocean, New Zealand, Pacific Ocean, Fig. 5).

- The number of the Late Eocene planktic foraminifera species in the current study yields a higher number (32 species) than others in or outside Al Ain area, UAE: 31 species in Egypt, 26 species in each of the Atlantic Ocean and Spain, 23 species in the Indian Ocean, 21 species in India, 20 species in Italy (Table 1). The existence of marked differences between the numbers of recorded species in different localities is most probably indicated by the differences in the paleoenvironmental conditions, land barriers, deficiency of the available literature, or misidentifying the species.

- The uncloses number of the Late Eocene faunal assemblages between J. Malaqet (18 species) and J. Qatar (8 species) and J. Hafit (32 species), in spit that all sections are located in the same basin at Al Jaw Plain (Fig. 1) may due to not detailed study for those sections by different authors.

- Some species are recorded in more than 15 localities in the world: *Subbotina linaperta*, *S. eocaena*, *Pseudohastigerina micra*, *Hantkenina alabamensis*, *Dentoglobigerina tripartita*, *Turborotalia cerroazulensis*, *T. cocoaensis*, while the lowest record is *T. sinaensis* and *T.* sp. in J. Hafit. The record of some species in a wide localities emphasizes the interpretations that were presented by different authors (e.g. Mintz, 1981; Adams et al., 1983) about the extended realms of Tethys Indo-Pacific with the Atlantic during the Late Eocene time.

- The presence of keels, accessory apertures, and tubular spines in some identified species reflect some aspect of the paleoenvironment, which suggests that the Late Eocene time in the Al Ain area, UAE had been in the subtropical-tropical belt during that period, in the open ocean and shelf paleoenvironments.

- The intraformational conglomeratic bed within the Late Eocene of Jabal Hafit, looks-like a “head-like “ rock (Fig. 9) caused by minimal reworking and accumulation in a low-energy environment associated with a short distance of transportation on a slight steepening paleoslope from a positive localized source area during that time accompanied with a marked fall in the eustatic sea level and active tectonics (Fig. 7, PHd).

Acknowledgement

The author is greatly indebted to Prof. Hanspeter Luterbacher (Tübingen University, Germany) for permission to photograph some of the fauna using SEM; to colleague Prof. Mona A. Haggag (Ain Shams University, Cairo, Egypt) for her valuable comments; for colleague Prof. Abdul Rahim Hamdan (former Prof. of the United Arab Emirates University, and former Vice President of Hashemite University, Jordan) for improving the English language of the manuscript and fruitful comments. The author would like to thank the editor of JJEES and the reviewers for critical reviewing the manuscript and making useful comments. I am also indebted to my daughter Dr. Huda Anan for her assistance in the development of the figures and plates.

References

Abdelghany, O. (2002). Biostratigraphy (Turborotalia cunialensis / Cribrohantkenina inflata Concurrent-Range Zone, P16) of the Late Eocene Dammam Formation, west of the Northern Oman Mountains. Micropaleontology 48 (3): 209-221.

Abdel-Kireem, M.R. (1983). Planktonic foraminifera of Mokattam Formation (Eocene) of Gebel Mokattam, Cairo, Egypt. Revue de Micropaléontologie 28 (2): 77-96.

Adams, C.G., Gentry, A.W. and Whybrow, P.J. (1983). Dating the terminal Tethys event. Utrecht Micropaleontological Bulletin 30: 273-298.

Anan, H.S. (1994). Contribution to the stratigraphy and paleobiogeography of some diagnostic Upper Cretaceous and Paleogene Foraminifera. Neues Jahrbuch für Geologie und Paläontologie, H.5: 257-266.

Anan, H.S. (1995). Late Eocene biostratigraphy of Jabals Malaqet and Mundassa of Al Ain region, United Arab Emirates. Revue de Micropaléontologie 38 (1): 3-14.

Anan, H.S. (2005). Agglutinated Middle-Upper Eocene foraminifera in Jabal Hafit, Al Ain area, United Arab Emirates. Revue de Paléobiologie 24 (1): 17-27.

Anan, H.S. (2009). paleontology and stratigraphical distribution of suborder Lagenina (benthic foraminifera) from the Middle-Late Eocene Mazyad Member of the Dammam Formation in Jabal Hafit, Al Ain area, United Arab Emirates, Northern Oman Mountains. Revue de Paléobiologie 28 (1): 1-18.

Anan, H.S. (2018). Hantkeninidae (planktonic foraminifera) from the Middle-Upper Eocene of Jabal Hafit, United Arab Emirates. Earth Sciences India 11 (2): 122-132.

Anan, H.S. (2020). Taxonomical considerations, phylogeny, paleogeography and paleoclimatology of the Middle Eocene (Bartonian) planktic foraminifera from Jabal Hafit, Al Ain area, United Arab Emirates. Earth Sciences Pakistan (ESP) 4 (1): 10-20.

Anan, H.S., Bahr, S.A., Bassiouni, M.A., Boukhary, M.A. and Hamdan, A.R. (1992). Contribution to Early Eocene-Oligocene biostratigraphy of Jabal Hafit succession, United Arab Emirates. Middle East Research Center, Ain Shams University, Earth Science Series, Cairo 6: 225-247.

Bandy O.L. (1949). Eocene and Oligocene foraminifera from Little Stave Creek, Clarke County, Alabama. Bulletin of American Paleontology 42: 210 p.

Banner, F.T. and Blow, W.H. (1959). The classification and stratigraphical distribution of the Globigerinacea. Paleontology 2: 1-27.

Beckmann, J.P. (1957). Chiloguembelina Loeblich and Tappan and related foraminifera from the Lower Tertiary of Trinidad, B.W.I. United States Natural Museum Bulletin 215: 83-96.

Berggren, W.A. and Miller, K.G. (1988). Paleogene tropical planktonic foraminiferal biostratigraphy and magnetobiochronology. Micropaleontology 34 (4): 362-380.

Berggren, W.A. and Pearson, P.N. (2005). A revised tropical to subtropical Paleogene planktonic foraminiferal zonation. Journal of Foraminiferal Research 35 (4): 279-298.

Bermúdez, P.J. (1961). Contribucion al studio de las Globigerindea de la region Caribe-Antillana (Paleoceno-Reciente). Boletino Geologia (Venezuela), Special Publicacion 3 (Congres Geologia Venezolano, 3ed Caracas, Memoria 3: 1119-1393.

Blow, W.H. (1969). Late Middle Eocene to Recent planktonic foraminiferal biostratigraphy. 1st International Conference of Planktonic Microfossils (Geneva 1967) 1: 199-422.

Blow, W.H. (1979). The Cainozoic Globigerinida. E.J. Brill, Leiden: 753-1413.

Blow, W.H. and Banner, F.T. (1962). The Mid-Tertiary (Upper Eocene to Aquitanian) Globigerinacea, in Eames, F.T. and others (eds.), Fundamentals of Mid-Tertiary Stratigraphical Correlation: Cambridge University Press, Cambridge: 61-151.

Bodiselitsch, B., Montanari, A., Koeberl, C., and Coccioni, R. (2004). Benthic foraminifers from DSDP site 219 (Eocene-Pleistocene, Arabian Sea). Revista Española de Micropaleontologia 25 (1): 127-156.

Bolli, H.M. (1957). Planktonic foraminifera from the Oligocene-Miocene Cipero and Lengua formations of Trinidad, B.W.I. United States National Museum Bulletin 215: 97-121.

Bolli, H.M. (1957). Planktonic foraminifera from the Eocene Navet and San Fernando formations of Trinidad, B.W.I. United States National Museum Bulletin 215: 155-172.

Bolli, H.M. (1972). The genus *Globigerinatheka* Brönnimann. Journal of Foraminiferal Research 2: 109-136.

Bolli, H.M., Loeblich, A.R. and Tappan, H. (1957). Planktonic foraminiferal families Hantkeninidae, Orbulinidae, Globorotaliidae and Globotruncanidae. United States Natural Museum Bulletin, Studies in foraminifera 215: 3-50.

Bolli, H.M. and Saunders, J.B. (1985). Oligocene to Holocene low latitude planktonic foraminifera. In Bolli et al. (Eds.): Plankton stratigraphy. Cambridge Earth Science Series: 155-262.

Borsetti, A.M. (1959). Tre nuovi foraminiferi planctonici dell' Oligocene piacentino. Giornale di Geologia 27: 205-212.

Brönnimann, P. (1952). Trinidad Paleocene and Lower Eocene Globigerinidae. Bulletin of American Paleontology 34: 1-34.

Brotzen, F. and Pozaryska, K. (1961). Foraminifères du Paléocène et de l'Eocène inférieur en Pologne septentrionale; remarques paléogéographiques. Revue de Micropaléontologie 4: 155-166.

Cherif, O.H., Al-Rifaiy, I.A. and El Deeb, W.Z. (1992). "Post-Nappes" early Tertiary foraminiferal paleoecology of the northern Hafit area, south of Al Ain City (United Arab Emirates). Micropaleontology 38 (1): 37-56.

Cherif, O.H. and El Deeb, W.Z. (1984). The Middle Eocene–Oligocene of the Northern Hafit Area, south of Al Ain City (United Arab Emirates). Geologie Méditerranéenne 11 (2): 207-217.

Coccioni, R. (1988). The genera *Hantkenina* and *Cribrohantkenina* (Foraminifera) in Massignano section (Ancona, Italy). International Subcommision of the Paleogene Stratigraphy, E/O Meeting, Ancona, Special Publication 2 (2): 81-96.

Coccioni, R., Monaco, P., Monechi, S. and Parisi, G. (1988). Biostratigraphy of the Eocene-Oligocene boundary at Massignano (Ancona, Italy). International Subcommision of the Paleogene Stratigraphy, E/O Meeting, Ancona, Special Publication 2 (1): 59-80.

Cole, W.S. (1927). A foraminiferal fauna from the Guayabal Formation in Mexico. Bulletins of American Paleontology 14: 1-46.

Cole, W.S. (1928). A foraminiferal fauna from the Chapapote Formation in Mexico. Bulletins of American Paleontology 14: 1-32.

Coxall, H.K. and Pearson, P.N. (2006). Taxonomy, biostratigraphy of the Hantkeninidae (Clavigerinella, Hantkenina and Cribrohantkenina). Atlas of Eocene Planktonic Foraminifera. Cushman Foundation Special Publication 41: 213- 256.

Cushman, J.A. (1924). A new genus of Eocene foraminifera. Proceeding of the U.S. National Museum 66: 1-4.

Cushman, J.A. (1925). New foraminifera from the Upper Eocene of Mexico. Contributions from the Cushman Laboratory for foraminiferal Research 1: 4-8.

Cushman, J.A. (1928). Foraminifera their classification and economic use. Special Publication Cushman Laboratory for Foraminiferal Research 1: 1-401.

Cushman, J.A. and Bermudez, P.J. (1937). Further new species of foraminifera from the Eocene of Cuba. Contributions from the Cushman Laboratory for Foraminiferal Research 13: 1-29.

Cushman, J.A. and Jarvis, P.W. (1929). New foraminifera from Trinidad. Contributions from the Cushman Laboratory for foraminiferal Research 5: 6-17.

Coxall, H.K., Huber, B.T. and Pearson, P.N. (2003). Origin and morphology of the Eocene planktonic foraminifer Hantkenina. Journal of Foraminiferal Research 33 (3): 237-261.

Coxall, H.K. and Pearson, P.N. (2006). Taxonomy, biostratigraphy of the Hantkeninidae (Clavigerinella, Hantkenina and Cribrohantkenina). Atlas of Eocene Planktonic Foraminifera. Cushman Foundation Special Publication 41: 213- 256.

El Khoudary, R.H. and Helmdach, F.F. (1981). Biostratigraphic studies on the Upper Eocene Apolonia Formation of N.W. Jabal Al Akhdar, N.E. Libya. Revista Espaňola de Micropaleontología 15 (1): 5-23.

Finlay, H.J. (1939). New Zealand foraminifera: Key species in stratigraphy, 3. Transactions of the Royal Society of New Zealand 69: 309-329.

Gümbel, C.W. (1868). Beiträge zur Foraminiferenfauna der nordalpinen Eocängebilde. Abhandlungen der K. Bayerische Akademie der Wissenschaften Cl. II, 10 (2): 579-730.

Haggag, M.A. (1990) *Globigerina pseudoampliapertura* Zone, a new Late Eocene planktonic foraminiferal zone (Fayoum area, Egypt). Neues Jahrbuch für Geologie und Paläontologie Mh., H. 5: 295-307.

Haggag, M.A. (1992). Planktonic foraminiferal groups and zonation of the Paleocene/Eocene of the South Galala and environs. Egyptian Journal of Geology 35, 1-2: 37-50.

Haggag, M.A. and Bolli, H.M. (1996). The origin of *Globigerinatheka semiinvoluta* (Keijzer), Upper Eocene, Fayoum area, Egypt. Neues Jahrbuch für Geologie und Paläontologie Mh., H. 6: 365-374.

Haggag, M.A. and Luterbacher, H. (1991). Middle Eocene planktonic foraminiferal groups and biostratigraphy of the Wadi Nukhul section, Sinai, Egypt. Neues Jahrbuch für Geologie und Paläontologie Mh. 6: 319-334.

Haggag, M.A., Luterbacher, H. (1995). The *Turborotalia pseudoampliapertura* lineage in the Eocene of the Wadi Nukhul section, Sinai, Egypt. Revue de Micropaléontologie 38 (1): 37-47.

Hamdan, A.R. and Bahr, S.A. (1992). Lithostratigraphy of Paleogene succession of northern Jabal Hafit, Al Ain area, United Arab Emirates. Middle East Research Center, Ain Shams University, Earth Science Series, Cairo 6: 201-224.

.Haq, B.U. and Aubry, M.-P. (1980). Early Cenozoic calcareous nannoplankton biostratigraphy and palaeobiogeography of North Africa and the Middle East and Trans-Tethyan correlations. The Geology of Libya (1). 2nd Symposium on the Geology of Libya, Tripoli: 271-304.

Haque, A.F.M.M. (1956). The foraminifera of the Ranikot and the Laki of the Nammal Gorge, Salt Range, Pakistan. Pakistan Geological Survey Memoir, Palaeontologica Pakistanica 1: 1-229.

Hernitz Kučenjak, M., Premec Fućek, V., Slavković, R. and Mesić, I.A. (2006). Planktonic Foraminiferal Biostratigraphy of the Late Eocene and Oligocene in the Palmyride Area, Syria. Geologic Croatica 59 (1): 19-39.

Hornibrook, N. De. B. (1965). New Zealand foraminifera: key species in stratigraphy. New Zealand Journal of Geology and Geophysics 1: 635-676.

Howe, H. (1928). An observation on the range of the genus *Hantkenina*. Journal of Paleontology 2: 13, 14.

Hunting Geology and Geophysics Ltd. (1979). Report on a Mineral Survey of the United Arab Emirates, Al Ain area. Ministry of Petroleum and Mineral Resources, Abu Dhabi 9: 1-29 (unpublished).

Imam, M.M. (1999). Lithostratigraphy and planktonic foraminiferal biostratigraphy of the Late Eocene-Middle Miocene sequence in the area between Wadi Al Zeitun and Wadi Rahib, Al Bardia area, Northeast Libya. Journal of African Earth Science 28 (3): 619-639.

Jenkins, D.G. (1971). New Zealand Cenozoic Planktonic Foraminifera. New Zealand Geological Survey Paleontological Bulletin 42: 278p.

Jenkins, D.G. and Orr, W.N. (1973). *Globigerina utilisindex* n. sp. from the upper Eocene-Oligocene of the eastern equatorial Pacific. Journal of Foraminiferal Research 3: 133-135.

Keijzer, F.G. (1945). Outline of the Eastern part of the province of Oriente, Cuba. Publicaties uit het Geographisch en uit het Mineralogisch-Geologisch Instituut der Rijksuniversiteit te Utrecht, Physiographisch-Geologische Reeks 2 (6): 1-216.

Keller, G. (1983). Paleoclimatic analysis of Middle Eocene through Oligocene planktic foraminiferal faunas. Palaeogeography, Palaeoclimatology, Palaeoecology 43: 73-94.

Keller, G. (1985). Eocene and Oligocene stratigraphy and Erosional unconformities in the Gulf of Mexico and Gulf Coast. Journal of Paleontology 59 (4): 882-903.

Keller, G., Herbert, T., Dorsey, R., d'Hondt, S., Johnsson, M. and Chi, W.R. (1987). Global distribution of late Paleogene hiatus. Geology 15: 199-203.

Koch, R. (1926). Mitteltertiäre Foraminiferen aus Bulongan, Ost-Borneo. Ecologae Geologicae Helvetiae 19: 722-751.

Loeblich, A. R. and Tappan, H. (1988). Foraminiferal genera and their classification. Van Nostrand Reinhold (VNR), New York, Part 1: 970 p., part 2: 847 p.

Martinez-Gallego, J. and Molina, E. (1975). Estudio del transito Eoceno-Oligoceno con foraminiferos planctonicos al sur de Torre Cardela (Provincia de Granada, Zona Subbetica). Cuad. Geol. Universidad de Granada 6: 177-195

Mintz, L.W. (1981). Historical Geology, the Science of a Dynamic Earth, 3rd Edition. Merrill Publication Company, USA, 611p.

Molina, E. (2015). Evidence and causes of the main extinction events in the Paleogene based on extinction and survival patterns of foraminifera. Earth-Science Reviews 140: 166-181.

Molina, E., Gonzalvo, C., Ortiz, S. and Cruz, L.E. (2006). Foraminiferal turnover across the Eocene-Oligocene transition at Fuente caldera, southern Spain: no cause-effect relationship between meteoric impacts and extinctions. Marine Micropaleontology 58: 270-286.

Mukhopadhyay, S.K. (2005). *Turborotalia cerroazulensis* group in the Paleogene sequence of Cambay Basin, India with a note on the evolution of *Turborotalia cunialensis* (Toumarkine and Bolli). Revue de Paléobiologie 24 (1): 29-50.

Olsson, R.K., Hemleben, C., Huber, B.H. and Berggren, W.A. (2006). Taxonomy, biostratigraphy and phylogeny of Eocene

Globigerina, Globoturborotalia, Subbotina and *Turborotalia.* Atlas of Eocene Planktonic Foraminifera, Cushman Foundation Special Publication 41: 111-168.

Olsson, R.K. and Hemleben, C. (2006). Taxonomy, biostratigraphy and phylogeny of Eocene *Globanomalina, Planoglobanomalina* n. gen. and *Pseudohastigerina*. Atlas of Eocene Planktonic Foraminifera, Cushman Foundation Special Publication 41: 413- 432.

Palmer, D.K. (1934). The foraminiferal genus Gümbelina in the Tertiary of Cuba. Mémoire Société Cubana Histoire Naturelle 8: 73-76.

Parr, W.J. (1947). An Australian record of the foraminiferal genus *Hantkenina*. Proceedings of the Royal Society of Victoria, Melbourne 58, 45-47.

Pearson, P.N. and Berggren, W.A. (2006). Taxonomy, biostratigraphy and phylogeny of *Morozovelloides* n. gen. (in Atlas of Eocene planktonic foraminifera). Cushman Foundation Special Publication 41: 327-342.

Pearson, P.N. and Chaisson, W.P. (1997). Late Paleocene to Middle Miocene foraminifer biostratigraphy of the Ceara Rise. Proceeding of the Ocean Drilling Program, Scientific Results 154: 33-68.

Pearson P.N., Olsson, R.K., Huber, B.T., Hemleben, C. and Berggren, W.A. (2006). Atlas of Eocene Planktonic Foraminifera, Cushman Foundation Special Publication 41:1–513.

Pearson, P.N. and Wade, B.S. (2015). Systematic taxonomy of exceptionally well-preserved planktonic foraminifera from the Eocene/Oligocene boundary of Tanzania. Cushman Foundation Special Publication 45:1–85.

Premoli Silva, I. and Spezzaferri, S. (1990). Paleogene planktonic foraminifer biostratigraphy and paleoenvironmental remarks on Paleogene sediments from Indian Ocean sites, Leg 115. Proceeding of the Ocean Drilling Program, Scientific Results 115: 277-314.

Premoli Silva, I., Wade, B.S. and Pearson, P.N. (2006). Taxonomy, Biostratigraphy and Phylogeny of *Globigerinatheca* and *Orbulinoides*. Atlas of Eocene planktonic foraminifera. Cushman Foundation Special Publication 41: 169-212.

Plummer, H.J. (1926). Foraminifera of the Midway Formation in Texas. Bulletin University of Texas 2644: 3-206.

Rögl, F. (1999). Mediterranean and Paratethys. Facts and hypotheses of an Oligocene to Miocene paleogeography (short overview). Geologica Carpathica 50 (4): 339-349.

Samanta, B.K. (1969). Eocene planktonic foraminifera from the Garo Hills, Assam, India. Micropaleontology 15: 325-350.

Samanta, B.K. (1970). Upper Eocene planktonic foraminifera from the Kopili Formation, Mikir Hills, Assam, India. Contribution from the Cushman Foundation for Foraminiferal Research 21 (1): 28-39.

Salama Y., Sayed M., Saber S., and Abd El-Gaied I. (2021). Eocene planktonic foraminifera from the north Eastern Desert, Egypt: Biostratigraphic, paleoenvironmental and sequence stratigraphy implications. Palaeontologia Electronica 24 (1): 1-29.

Samuel, O. (1972). New species of planktonic foraminifera from the Paleogene of the west Carpathian in Slovakia (Czechoslovakia). Zbornik Geologick" ck. Vied Západné Karpaty 17: 165-221.

Shahin, A. (1998). Tertiary planktonic foraminiferal biostratigraphy and paleobathymetry at Gebel Withr, southwestern Sinai, Egypt. Neues Jahrbuch für Geologie und Paläontologie, Abh. 209 (3): 323-348.

Srinivasan, M.S. (1968). Late Eocene and Early Oligocene planktonic foraminifera from Port Elizabeth and Cape Foulwind, New Zealand. Contributions from the Cushman Foundation for foraminiferal research 19 (4): 142-157.

Stainforth, R.M., Lamb, J.L., Luterbacher, H.P., Beard, J.H. and Jeffords, R.M. (1975). Cenozoic planktonic foraminiferal zonation and characteristics of index forms. Paleontological Contribution, University of Kansas 62: 163-425.

Subbotina, N.N. (1953). Iskopaeme foraminifery SSSR, Globigerinidy, Khantkeninidy i Globorotaliidy [Fossil foraminifers of the USSR, Globigeriniidae, Hantkeninidae and Globorotaliidae]. Trudy Vsesoyuznogo Neftyanogo Naucho-issledovatel'skogo Geologorazvedochnogo Instituta (VNIGRI), 76: 1-296 (in Russian, translated into English by E. Lees, 1971).

Sztrákos, K. (2000). Eocene foraminifers in the Adour Basin (Aquitaine, France): biostratigraphy and taxonomy. Revue de Micropaléontologie 43 (1-2): 71-172.

Toumarkine, M. (1978). Planktonic foraminiferal biostratigraphy of the Paleogene of Sites 360 to 364 and the Neogene of Sites 362A, 363 and 364 Leg 40, *In* Bolli et al. (Eds.). Initial Reports of the Deep Sea Drilling Projects: U.S. Government Printing Office, Washington, D.C. 40: 679-721.

Toumarkine, M. and Bolli, H.M. (1970). Evolution de *Globorotalia cerroazulensis* (Cole) dans l'Eocene Moyan et Supérieur de Possagno (Italie). Revue de Micropaléontologie 13: 131-145.

Toumarkine, M. and Bolli, H.M. (1975). Foraminifères Planctoniques de l'Eocene Moyan et Supérieur de la Coupe de Possagno. Schweizerische Paläontologische Abhandlungen 97: 69-185.

Toumarkine, M. and Luterbacher, H.P. (1985). Paleocene and Eocene plaktonic foraminifera. *In*: Bolli, H.M. et al. (Eds.): Plankton Stratigraphy. Cambridge Earth 97: 69-83.

Vail, P.R., Mitchum, R.M. and Thompson III, S. (1977). Seismic stratigraphy and global changes of sea level. *In*: Payton, C.E. (Ed.), Stratigraphic Interpretation of Seismic Data. The American Association of Petroleum Geologists Memoir 26: 83-97.

Wade. B.S. and Pearson P.N. (2008). Planktonic foraminiferal turnover, diversity fluctuations and geochemical signals across the Eocene/Oligocene boundary in Tanzania. Marine Micropaleontology 68: 244–255.

Wade, B.S., Pearson, P.N., Berggren, W.A. and Pälike, H. (2011). Review and revision of Cenozoic tropical planktonic foraminiferal biostratigraphy and calibration to the geomagnetic polarity and astronomical time scale. Earth-Science Reviews 104, 111–142.

Warraich, M.Y. and Ogasawara, K. (2001). Tethyan Paleocene-Eocene planktic foraminifera from the Rakhi Nala and Zinda Pir land sections of the Sulaiman Range, Pakistan. Science Reports of the Institute of Geoscience University of Tsukuba, section B 22: 1-59.

Warraich, M.Y., Ogasawara, K. and Nishi, H. (2000). Late Paleocene to Early Eocene planktonic foraminiferal biostratigraphy of the Dungan Formation, Sulaiman Range, Central Pakistan. Paleontological Research 4: 275-301.

Weinzierl, L.L. and Applin, E.R. (1929). The Claiborne formation on the coastal domes. Journal of Paleontology 7. 384-410.

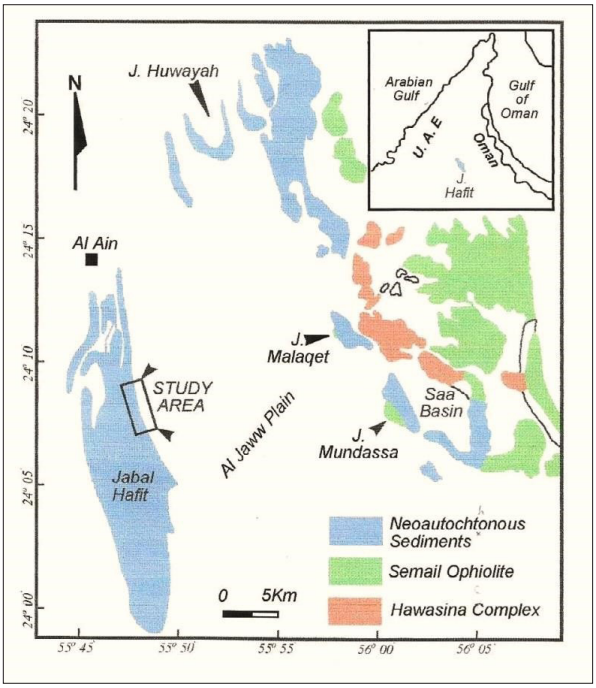

Figure 1. Location map of the study area at the eastern limb of Jabal Hafit, and also J. Malaqet and J. Mundassa, Al Ain area, UAE.

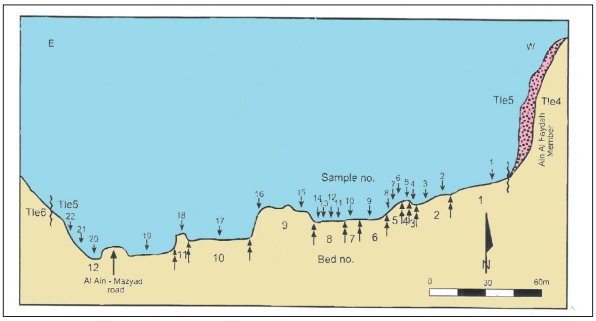

Figure 2. The schematic diagram of the upper part of Tle5 of Hunting, 1979 (= Mazyad Member of the Dammam Formation, after Hamdan and Bahr, 1992), which represents the Late Eocene succession of the studied section, sample nos. 17-22 (bed nos. 10-12), around Al Ain-Mazyad road, Al Ain area, UAE.

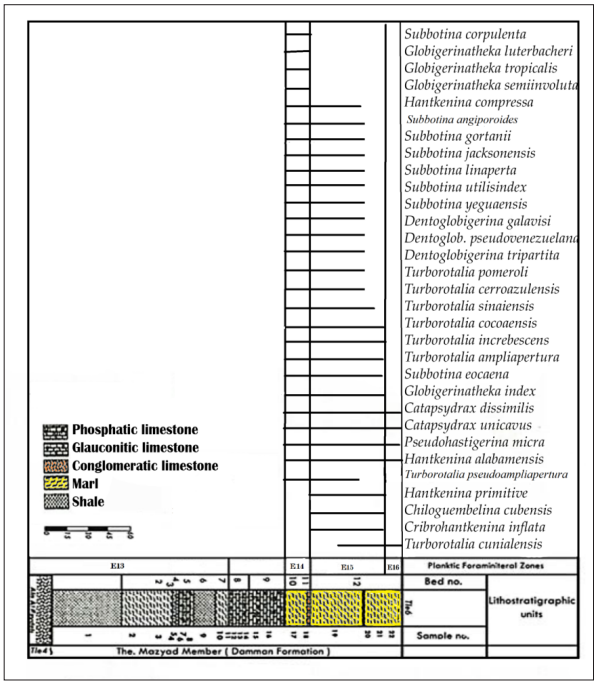

Figure 3. Stratigraphic ranges of the recorded Late Eocene planktonic foraminiferal species (E14-E16) of the upper Mazyad Member succession in the eastern limb of Jabal Hafit, Al Ain area, UAE.

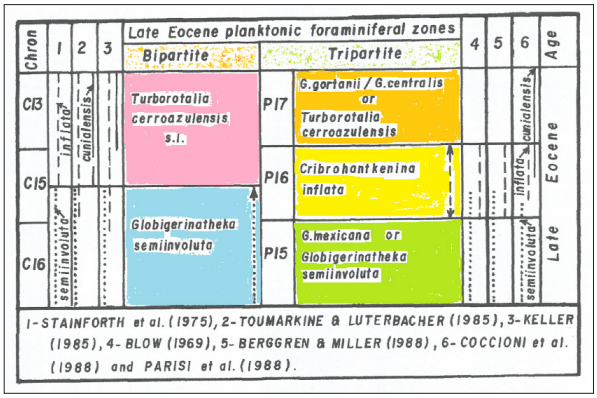

Figure 4. Stratigraphic ranges of the Late Eocene taxa: *Globigerinatheka semiinvoluta* (…. points), *Cribrohantkenina inflata* (- - - dashed line), and *Turborotalia cerroazulensis cunialensis* (----- solid line) as recorded by some authors (after Anan, 1995).

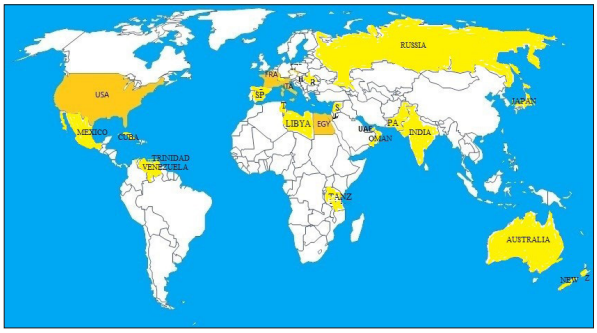

Figure 5. The geographic distribution of the identified planktic foraminiferal species in the study section (North and South America, Atlantic Ocean), Northern Tethys (Europe), Southern Tethys (North Africa, South Asia, Australia, New Zealand).

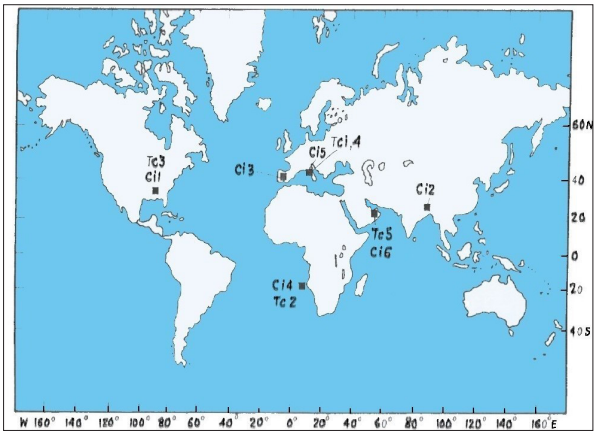

Figure 6. Geographic distribution of the occurrence of some diagnostic Late Eocene planktic foraminiferal species: *Ci=Cribrohantkenina inflata, Tc=Turborotalia cunialensis. Ci* 1: Cushman (1925), *Ci* 2: Samanta (1969), *Ci* 3: Martinez-Gallego and Molina (1975), *Ci* 4: Toumarkine (1978), *Ci* 5: Coccioni (1988), *Ci* 6 (Anan et al., 1992), *Tc* 1: Toumarkine and Bolli (1970), *Tc* 2: Toumarkine (1978), *Tc* 3: Keller (1985), *Tc* 4: Coccioni et al. (1988), *Tc* 5: Anan et al. (1992).

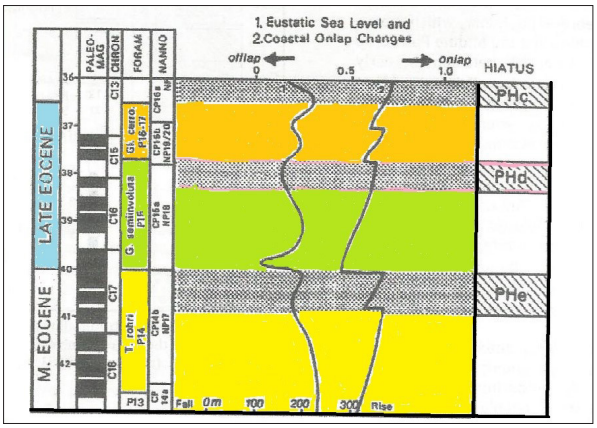

Figure 7. Global Paleogene hiatuses: PHc (the Eocene/Oligocene boundary), PHd (within the Late Eocene, between early (E14) and middle Late Eocene (E15) (after Keller et al., 1987).

Figure 8. The thick intraformational conglomeratic bed (arrows, nearly vertical) at the top part of Ain Al Faydha Member (Tle4), followed by the Mazyad Member (Tle5) of the Dammam Formation (nearly at the Middle/Late Eocene boundary) in the eastern limb of Jabal Hafit (at the ground).

Figure 9. A diagnostic "head-like" rock consistutes a part of an intraformational conglomeratic limestone bed, which located between E14 and E15 in the studied section of J. Hafit, UAE (besides Al Ain-Mazyad asphalted road).

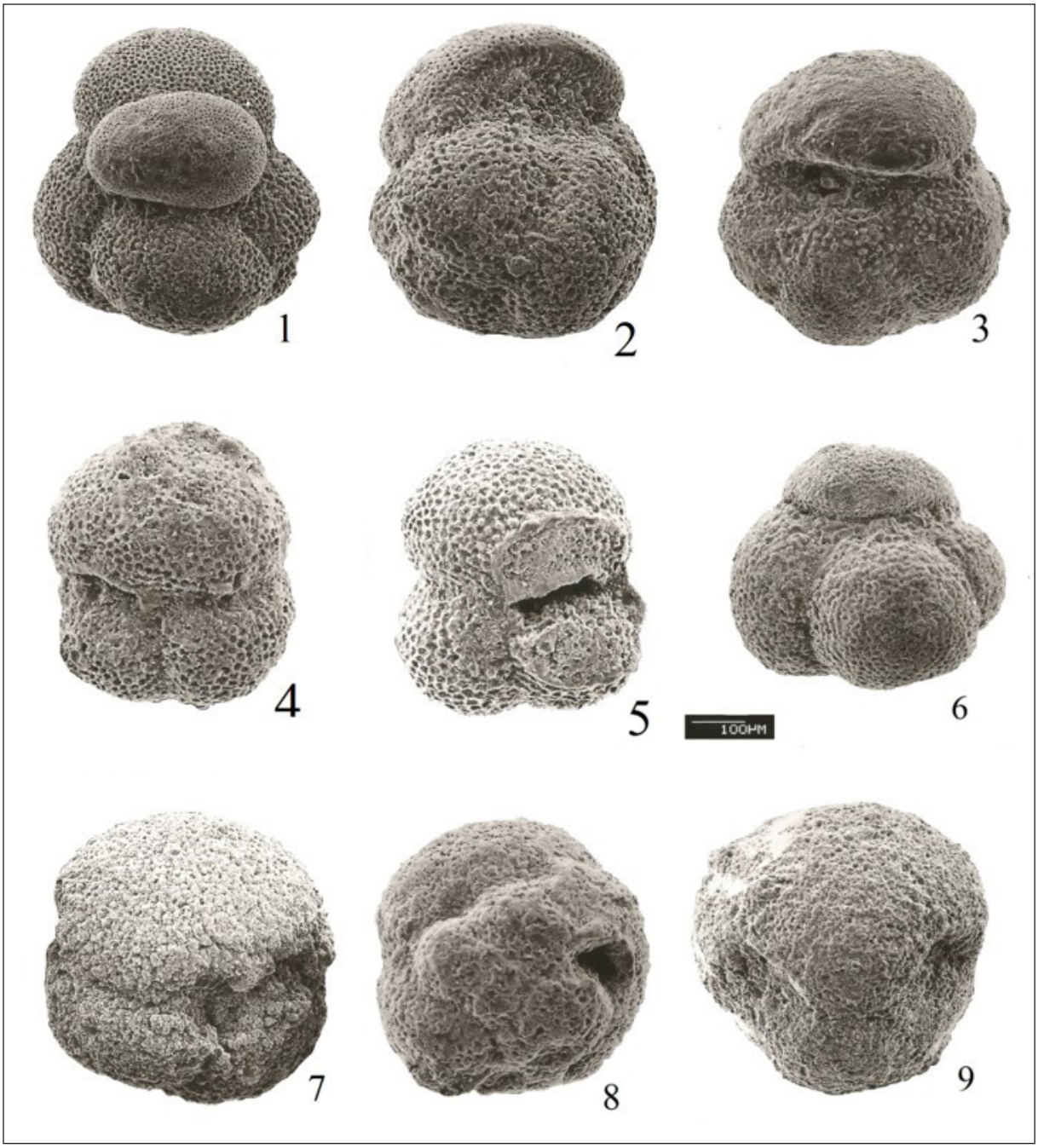

Plate 1. Fig. **1**. *Catapsydrax unicavus* Bolli, Loeblich and Tappan, 1957, sample 19; **2**. *Subbotina gortanii* (Borsetti, 1959), s. 19; **3**. *Subbotina jacksonensis* (Bandy, 1949), s. 19; **4.** *S. linaperta* (Finlay, 1939), s. 20; **5.** *S. utilisindex* (Jenkins and Orr, 1973), s. 20; **6**. *S. yeguaensis* (Weinzierl and Applin, 1929), s. 19; **7**. *Globigerinatheka index* (Finlay, 1939), s. 21; **8**. *G. luterbacheri* Bolli, 1972, s. 17; **9**. *G. semiinvoluta* (Keijzer, 1945), s. 17.

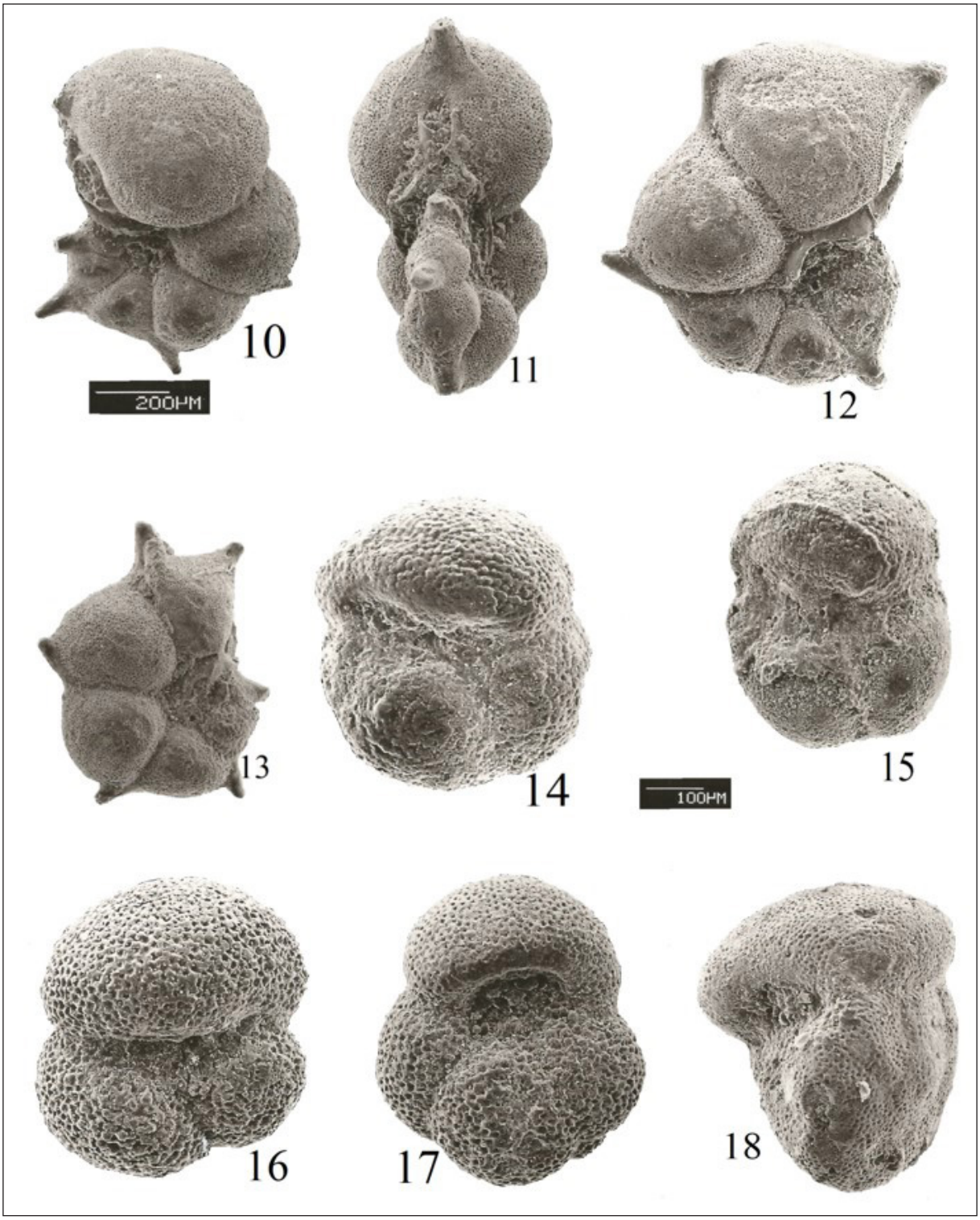

Plate 2. Fig. **10**. *Cribrohantkenina inflata* (Howe, 1928), s. 20; **11.** *Hantkenina alabamensis* Cushman, 1924, s. 20; **12**. *H. compressa* Parr, 1947, s. 19; **13**. *H. primitive* Cushman and Jarvis, 1929, s. 20; **14**. *Dentoglobigerina galavisi* (Bermúdez, 1961), s. 17; **15**. *D. pseudovenezuelana* (Blow and Banner, 1962), s. 19; **16**. *D. tripartita* (Koch, 1926), s. 20; **17**. *Turbrotalia ampliapertura* (Bolli, 1957), s. 19; **18**. *T. cerroazulensis* (Cole, 1928), s. s. 19.

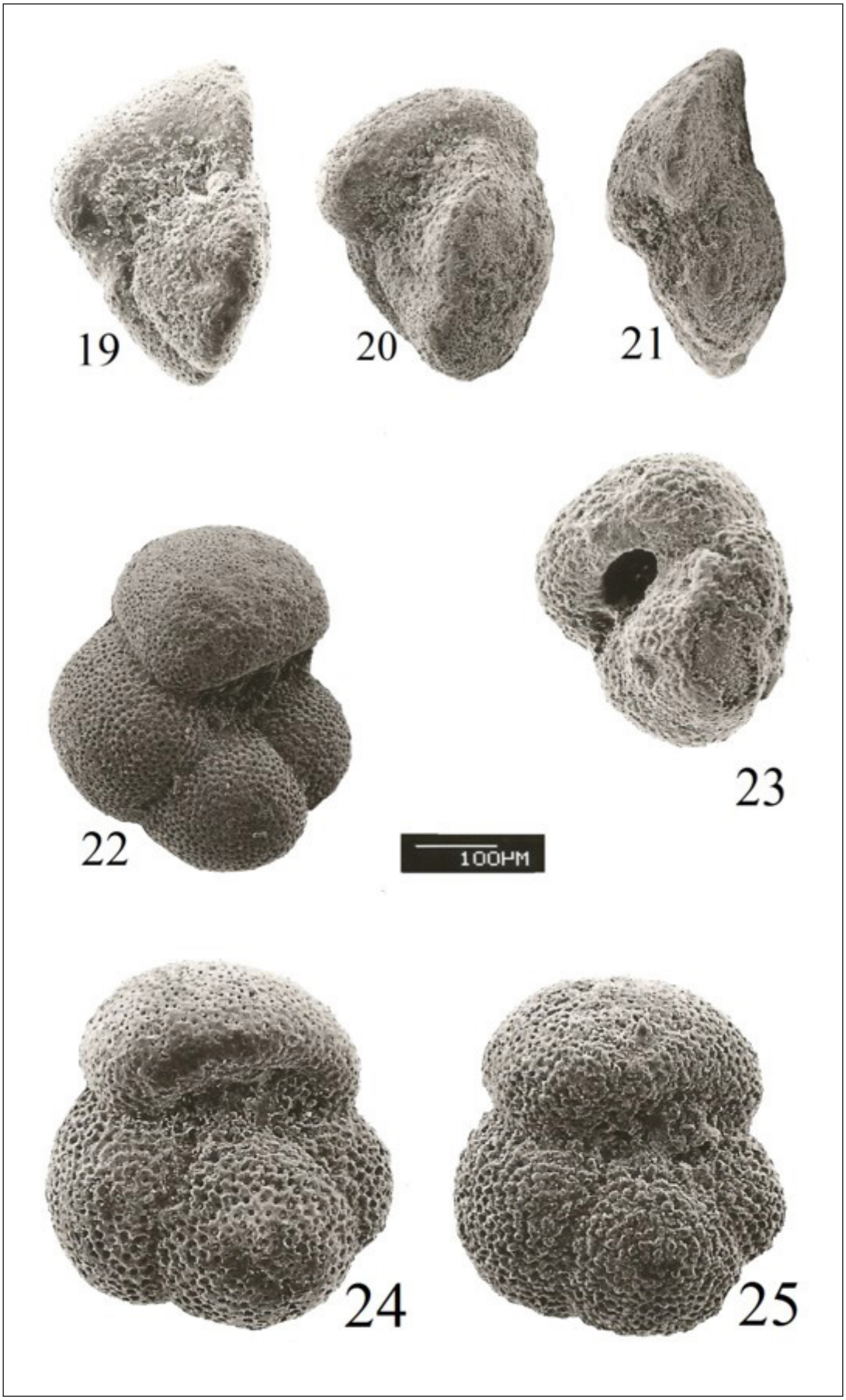

Plate 3. Fig. **19.** *Turbrotalia cocoaensis* (Cushman, 1928), s. 20; **20**. *T.* sp., Transitional specimen between *Turbrotalia cocoaensis* and *T. cunialensis,* s. 20; **21**. *T. cunialensis* (Toumarkine and Bolli, 1970), s. 22; **22**. *T. increbescens* (Bandy, 1949), s. s.19; **23**. *T. pomeroli* (Toumarkine and Bolli, 1970), s. 19; **24**. *T. pseudoampliapertura* (Blow and Banner, 1962), s. s.20; **25**. *T. sinaiensis* Haggag and Luterbacher, 1995, s. 17.

Table 1. Paleogeographic distribution of the Late Eocene planktic foraminifera in the United Arab Emirates (UAE): Jabal Hafit: H1 (The current study), H2 (Anan et al., 1992), H3 (Cherif et al., 1992), Malaqet, M (Anan, 1995); Oman, Q=Qatar section (Abdelghany, 2002), and other Northern and Southern Tethyan localities: **A**= Atlantic Ocean (Cushman, 1925; Brönnimann, 1952; Stainforth et al, 1975; Keller, 1985; Pearson et al., 2006), Northern Tethys: **S**= Spain (Molina et al., 2006, Molina, 2015), **F**= France (Sztràkos, 2000), Y= Italy (Toumarkine and Bolli, 1975; Coccioni, 1988; Coccioni et al., 1988); **CC**= Carpathica, Caucasus (Samuel, 1972) Southern Tethys: **T**= Tanzania (Wade and Pearson, 2008); **L**= Libya (El Khoudary and Helmdach, 1981; Imam, 1999); **E**= Egypt (Abdel-Kireem, 1983; Haggag, 1992; Haggag and Luterbacher, 1995; Haggag and Bolli, 1996; Shahin, 1998); R= Syria (Hernitz Kučenjak et al., 2006), **UAE**=United Arab Emirates (H1. The current study, H2. Anan et al., 1992, H3. Cherif et al., 1992, M=Malaqet), O= Oman, Jabal Qatar (Abdelghany, 2002); P= Pakistan (Haque, 1956; Warraich et al., 2000; Warraich and Ogasawara, 2001); I= India (Samanta, 1969, 1970, Mukhopadhyay, 2005); IO= Indian Ocean (Premoli Silva and Spezzaferri, 1990), NA= New Zealand (Srinivasan, 1968, Jenkins, 1971) and Australia (Parr, 1947), PO= Pacific Ocean (Pearson et al., 2006). **Θ** = illustrated species, x = recorded species, - = not recorded species.

Sp. No.	Late Eocene planktic foraminiferal species		AO	S	F	Y	CC	T	L	E	R	UAE				O	P	I	IO	NA	PO
												H1	H2	H3	M	Q					
1	*Catapsydrax*	*dissimilis*	x	x	x	-	-	x	x	x	-	x	x	-	-	-	x	x	x	-	x
2		*unicavus*	x	x	-	-	-	x	x	x	x	**Θ**	-	-	-	-	-	x	-	x	x
3	*Subbotina*	*angiporoides*	x	x	-	x	x	-	-	x	-	x	x	-	x	-	-	-	x	x	-
4		*corpulenta*	x	x	x	-	-	x	-	x	-	x	x	-	x	x	-	x	x	-	x
5		*eocaena*	x	x	x	x	x	x	x	x	-	x	x	x	x	x	-	x	-	x	-
6		*gortanii*	x	x	x	x	x	x	x	x	-	**Θ**	x	-	x	x	-	x	x	-	-
7		*jacksonensis*	x	x	-	-	-	-	-	x	-	**Θ**	-	-	-	-	-	-	-	-	-
8		*linaperta*	x	x	x	x	x	x	x	x	-	**Θ**	x	x	x	x	x	x	x	x	x
9		*utilisindex*	-	-	x	-	-	-	-	x	-	**Θ**	-	-	-	-	-	-	x	-	x
10		*yeguaensis*	x	x	-	-	x	x	x	x	-	**Θ**	x	-	x	-	x	x	x	x	x
11	*Globigerinatheka*	*index*	x	x	x	x	x	x	x	x	-	**Θ**	-	-	x	-	-	x	x	x	x
12		*luterbacheri*	x	x	-	x		-	-	x	-	**Θ**	x	-	-	-	-	-	x	-	x
13		*semiinvoluta*	x	x	x	x	x	x	x	x	-	**Θ**	x	-	-	-	-	-	x	-	x
14		*tropicalis*	x	x	x	x	x	x	x	x	-	x	x	-	-	-	-	x	x	x	x
15	*Cribrohantkenina*	*inflata*	x	x	-	x	x	x	-	x	x	**Θ**	x	x	x	-	-	x	x	-	-
16	*Hantkenina*	*alabamensis*	x	x	x	x	x	x	x	x	x	**Θ**	x	x	x	-	-	x	x	x	-
17		*compressa*	x	x	-	x	-	x	-	x	-	**Θ**	-	-	-	-	-	-	-	x	-
18		*primitiva*	x	x	-	x	x	x	x	x	-	**Θ**	x	-	-	-	-	x	-	-	-
19	*Dentoglobigerina*	*galavisi*	x	x	-	x	x	x	x	x	x	**Θ**	-	-	-	-	-	-	x	-	x
20		*pseudovenezuelana*	-	x	-	-	x	x	-	x	-	**Θ**	x	-	-	-	-	-	-	-	-
21		*tripartita*	x	x	x	x	x	x	x	x	x	**Θ**	x	x	x	-	-	x	x	-	x
22	*Pseudohastigerina*	*micra*	x	x	x	x	x	x	x	x	x	x	x	x	x	-	x	x	x	x	x
23	*Turborotalia*	*ampliapertura*	x	-	-	x	x	x	x	x	-	**Θ**	x	-	x	-	-	x	x	x	x
24		*cerroazulensis*	x	x	x	x	x	x	x	x	x	**Θ**	x	x	x	-	-	x	x	x	x
25		*cocoaensis*	x	x	x	x	x	x	x	x	x	**Θ**	x	x	x	x	-	x	x	-	x
26		.sp	-	-	-	-	-	-	-	-	-	**Θ**	-	-	-	-	-	-	-	-	-
27		*cunialensis*	x	-	x	x	-	x	-	x	-	**Θ**	x	-	x	x	-	x	x	-	-
28		*increbescens*	x	x	x	-	x	x	x	x	x	**Θ**	-	x	-	-	-	x	x	x	x
29		*pomeroli*	-	x	x	x	-	x	x	x	x	**Θ**	x	x	x	-	-	-	x	-	x
30		*pseudoampliapertura*	-	-	-	-	-	-	x	x	-	**Θ**	x	-	x	-	-	x	x	x	-
31		*sinaiensis*	-	-	-	-	-	-	-	x	-	**Θ**	-	-	-	-	-	-	-	-	-
32	*Chiloguembelina*	*cubensis*	x	x	-	-	-	-	-	x	x	x	x	x	x	-	-	x	-	x	x

JJEES

JJEES (2023) 14 (1): 50-63
ISSN 1995-6681

Jordan Journal of Earth and Environmental Sciences

Anoxic Marine Conditions Recorded from the Middle Paleozoic Black Shales (Kaista and Ora formations), Northern Iraq: A multi-Proxy Approach

Ali I. Al-Juboury[1*], Rahma S. Al-Auqadi[2], Safwan H. Al-Lhaebi[3], Harold D. Rowe[4] and Salim H. Hussein[3]

[1]Department of Petroleum Engineering, College of Engineering, Al-Kitab University, Kirkuk, Iraq
[2]College of Petroleum and Mining Engineering, University of Mosul, Iraq
[3]Geology Department, University of Mosul, Iraq
[4]Premier Oilfield Laboratories, Houston, TX 77041, USA

Received 14th February 2022; Accepted 12th June 2022

Abstract

The shale units of the Late Devonian to Early Carboniferous successions of the Kaista and Ora formations from extreme northern Iraq have been studied for their geochemical and mineralogical features to reconstruct paleoenvironmental conditions. The Chemical Index of Alteration (CIA; high values ~93-99), high, Plagioclase Index of Alteration (PIA ~92– 98), and the A-CN-K plot indicate the studied shales have undergone intense weathering at the source area. Also, high kaolinite content and predominance of kaolinite over illite in the studied shale support this conclusion. The Rb/K and Sr/Ba ratios of the Kaista and Ora formations indicate freshwater to brackish water during deposition. Geochemical investigations, using redox-sensitive trace elements ratios such as V/ (V + Ni), Th/U, and U index suggest deposition of the Ora black shales under anoxic marine conditions, thus recording an ocean anoxic event in the region. Geochemical variations in the concentrations of some major and trace elements and their elemental ratios such as an increase in the Rb, K_2O, Th, K/Al, and TOC values and a decrease in the Zr/Al, Ti/Al, Mo, P, Zn, and Zr, from the Kiasta upward to the Ora Formation indicate the transgressive systems tract (TST) of the Kaista-Ora sequence. Paleo-productivity indicators (P content, P/Ti, and P/Al ratios) suggest lower productivity and the paleoredox conditions in the Ora shales play an important role in the preservation of organic matter. The ternary diagram of Co–Zn–Ni, Co/Zn, U/Th, and Ba/Sr ratios indicates that there was hydrothermal activity in the basin during the deposition.

Keywords: *Geochemistry, Northern Iraq, Kaista and Ora shales, Late Devonian-Early Carboniferous, Paleoenvironmental conditions, Anoxic event.*

1. Introduction

Shale (mostly calcareous) represents one of the main lithofacies in the succession of Devonian-early Carboniferous Kaista and Ora formations from extreme northern Iraq intercalated with sandstones, siltstones, and limestone (dominantly dolomitic). The studied succession is hydrocarbon-promising in the northern part of Iraq (Al-Hadidy, 2007; Aqrawi et al., 2010; Abdula et al., 2020) and prospective in the western desert near Jordan, Saudi Arabia, and Syria.

A combination of the mineralogical and chemical composition of siliciclastic rocks (sandstones and shales) commonly is used as a tool to determine the paleoenvironmental conditions and provenance history of these rocks (Armstrong-Altrin et al., 2004; Jafarzadeh and Hosseini-Barzi, 2008; Dostal and Keppie, 2009; Armstrong-Altrin, 2009; Armstrong-Altrin et al., 2015, Khazaei et al., 2018, Akkoca et al., 2019) and to evaluate weathering processes and paleogeography (Absar et al., 2009; Ranjan and Banerjee, 2009; Zimmermann and Spalletti, 2009; Armstrong-Altrin et al., 2013; Tobia and Mustafa, 2019; Akkoca and Karatas, 2019).

The middle Paleozoic shale of the Kaista and Ora formations did not get enough attention in the geologic studies of the study area. Most of the studies were focused on the middle Paleozoic sequence in terms of sequence stratigraphy (Al-Juboury et al, 2012), facies and depositional environment (Al-Juboury and Al-Hadidy, 2008), palynostratigraphy (Sherwani et al., 2010), oil and gas generation based on palynology (Abdula et al., 2020).

The present work aims to address the paleoenvironmental conditions, including paleoclimate, paleosalinity, paleoredox conditions, transgressive system tract, paleoproductivity, and hydrothermal activity of the middle Paleozoic (Devonian-Carboniferous) shales in the Kaista and Ora formations.

2. Materials and Methods

Shale samples were collected from the Middle Paleozoic Kaista and Ora formations of the Ora type section, northernmost Iraq, representing various mineralogical and geochemical characteristics to achieve the goals of the present study.

These samples were studied as follows:

2.1. X-ray diffraction (XRD)

Twenty-one samples from the Kaista (5 samples) and

* Corresponding author e-mail: alialjubory@yahoo.com

Ora (16 samples) were selected and analyzed by XRD to identify the mineralogical composition. The investigation was carried out on bulk rock samples at the Premier Laboratory in Houston, Texas, USA., using a Bruker D8 Advance XRD instrument. Quantification of mineral phases in the bulk diffraction pattern is accomplished using the TOPAS software package.

2.2. Scanning electron microscopy (SEM)

Eight samples were selected for SEM analysis to identify the clay minerals' main detrital and diagenetic elements, as well as mica, feldspar, quartz, and carbonate minerals. The analysis was conducted using a Camscan MV 2300 SEM with a calibrated energy dispersive X-ray analysis system on gold-coated samples at the Institut für Geowissenschaften-Geologie, University of Bonn, Germany.

2.3. X-ray fluorescence (XRF)

The Geochemical analysis of major and trace elements for 21 shale samples (5 and 16 from the Kaista and Ora formations respectively) was done using the portable Bruker Tracer 5i Energy-Dispersive X-Ray Fluorescence (ED-XRF) instrument. Analyses were performed at the Premier Laboratory in Houston, Texas, USA.

2.4. Total organic carbon (TOC) content

Twenty-one samples of shales from the Kaista (5 samples) and Ora (16 samples) were analyzed for their Total Organic Carbon using the LECO C230 instrument, which requires decarbonization of the rock sample by treatment with hydrochloric acid (HCl). This is accomplished by soaking weighted samples for two hours in concentrated HCl. The acid is then removed by rinsing the samples with water and flushing them through filtration equipment. The filter is then removed, placed into a LECO crucible, and dried in a low-temperature oven (110^{o}C) for 4 hours. Samples were weighed after this process to obtain a percent carbonate value based on weight loss. The Leco instrument is calibrated with a standard of known carbon values. Furthermore, the standard is analyzed as an unknown for every 10 samples to check the variation and calibration of the analysis. Random and selected reruns are done to verify the data. The acceptable standard deviation for TOC is a 3% variation from the established value.

3. Geological Setting and Paleogeography

Iraq lies in the border area between the major Phanerozoic units of the Middle East, i.e., between the Arabian part of the African Platform (Nubio-Arabian) and the Asian branches of the Alpine tectonic belt. The platform part of the Iraqi territory is divided into two basic units, i.e., a stable and an unstable shelf (Fig. 1). The stable shelf is characterized by a relatively thin sedimentary cover and a lack of significant folding. The unstable shelf has a thick and folded sedimentary cover and the intensity of the folding increases toward the northeast (Buday,1980).

The Devonian-Early Carboniferous time was interpreted as a period of extension and compression that resulted from the Hercynian orogeny and development of the intracratonic basin (Tectonic Megasequence AP4; Sharland et al., 2001). At that time, widespread marine shales and limestones were deposited in intracratonic basins throughout the central part of the Arabian Plate in Iraq, Syria, and Turkey (Jassim and Goff, 2006). The wide shelf sea of this basin was located between tropical and subtropical regions of the southern hemisphere and their areal extent changed in response to succeeding transgressions and regressions (Beydoun, 1991).

The middle Paleozoic (Late Devonian-Early Carboniferous) sedimentary succession of Iraq is represented by the Kaista, Ora, and Harur formations. They extend from the western part of Iraq to the Ora area of northernmost Iraq (Fig. 1). This succession is composed of siliciclastic-carbonate facies and was considered to be deposited in a subsiding basin with a wide geographic distribution reflecting epicontinental or epeiric seas setting in a homoclinic ramp in a transgressive system tract (TST) (Al-Hadidy, 2007; Al-Juboury and Al-Hadidy; 2008, 2009; Al-Juboury et al., 2012).

The Kaista Formation is about 70 m thick (Fig. 2). It consists of heterogeneous clastics of sandstones intercalated with siltstones and calcareous shale and represents the transition between the continental-fluvial deposition of Pirispiki Formation and those of shallow-marine deposits of the Ora Formation. The depositional environment of the Kaista Formation is interpreted to be a mixed fluvial-marine system (Al-Juboury and Al-Hadidy, 2008).

The Ora Formation is more than 220 m thick and characterized by its shale lithofacies that intercalate with subordinate sandstones, siltstones, and dolomitic units (Fig. 2). It represents the transition between the mixed (fluvial-marine) clastics of the Kaista Formation and the carbonates of the Harur Formation. The black micaceous and calcareous shales of the Ora Formation were deposited in a subtidal shelf environment Sharland et al. (2001). The Harur Formation represents the termination of the overall transgressive Late Devonian-Early Carboniferous sequence, in which the facies are dominantly carbonates, alternated with dolomitic shale and thin sandstones. These carbonates are commonly dolomitized and are similar to other Paleozoic carbonates in the geologic record (Wilson, 1975). The Harur Formation was deposited in a shallow-marine environment and is a continuation of the ramp setting of the Ora Formation.

The studied formations are recorded in wells Akkas- 1, Key Hole KH 5/1, and Khleisia-1 with a thickness ranging from 45-104 m for the Kaista Formation and from 100–300 m for the Ora Formation (Al-Hadidy, 2001; Gaddo and Parker, 1959; Al-Haba et al. 1991, 1994). These formations crop out in the Kaista and Harur areas, near the Khabour Valley, and in the Geli Sinat and Derashish areas northwest of Shiranish, Amadia district of extreme northern Iraq (Fig. 1).

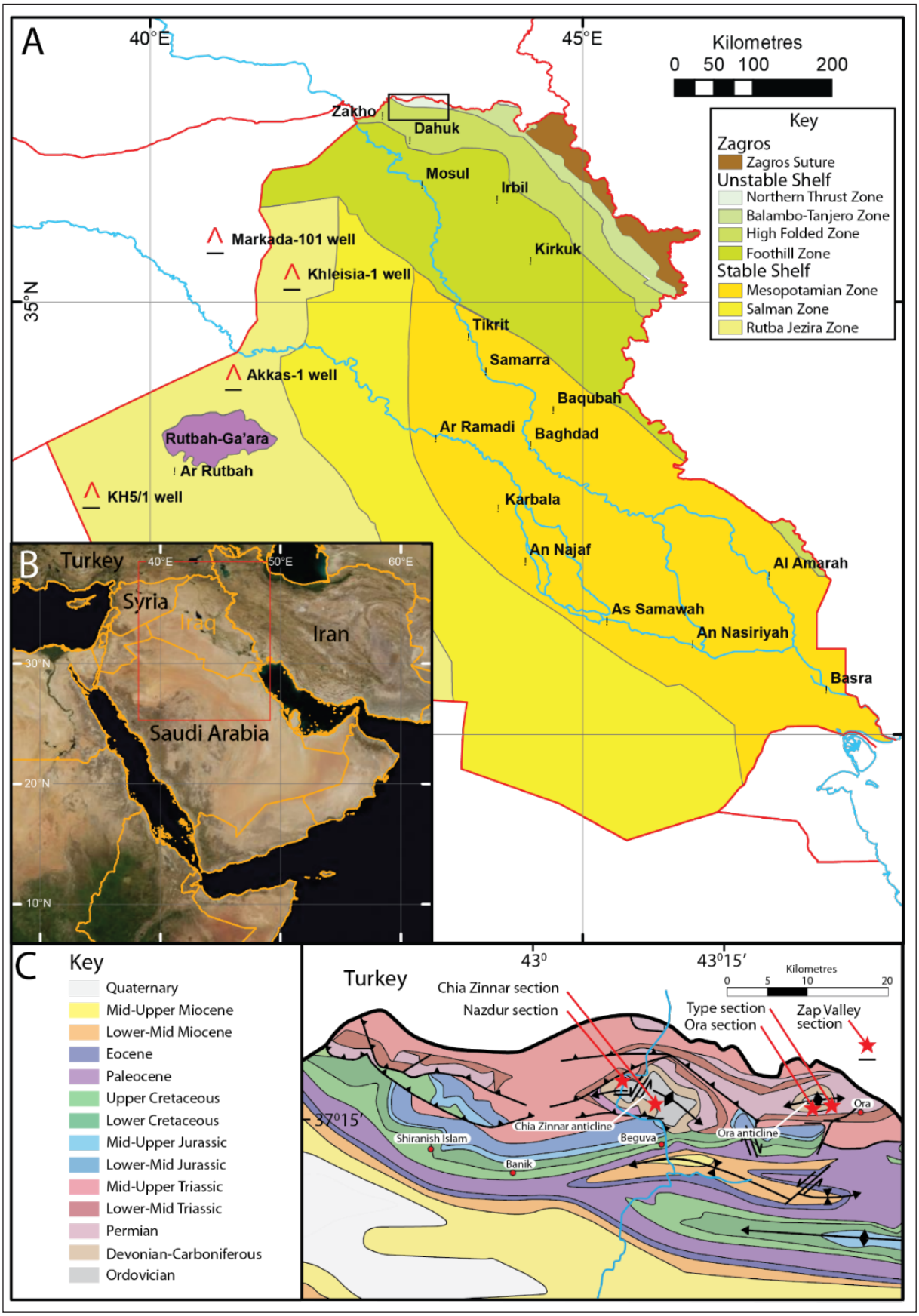

Figure 1. A- Structural provinces of Iraq modified after Jassim and Goff (2006) showing the location of wells referred to in the text. The location of map C- is indicated by the black box. B- Inset map shows countries neighboring Iraq; the location of map A is indicated by the red box. C- Geological map of northern Iraq modified after Sissakian (2000) showing the location of the Ora type section.

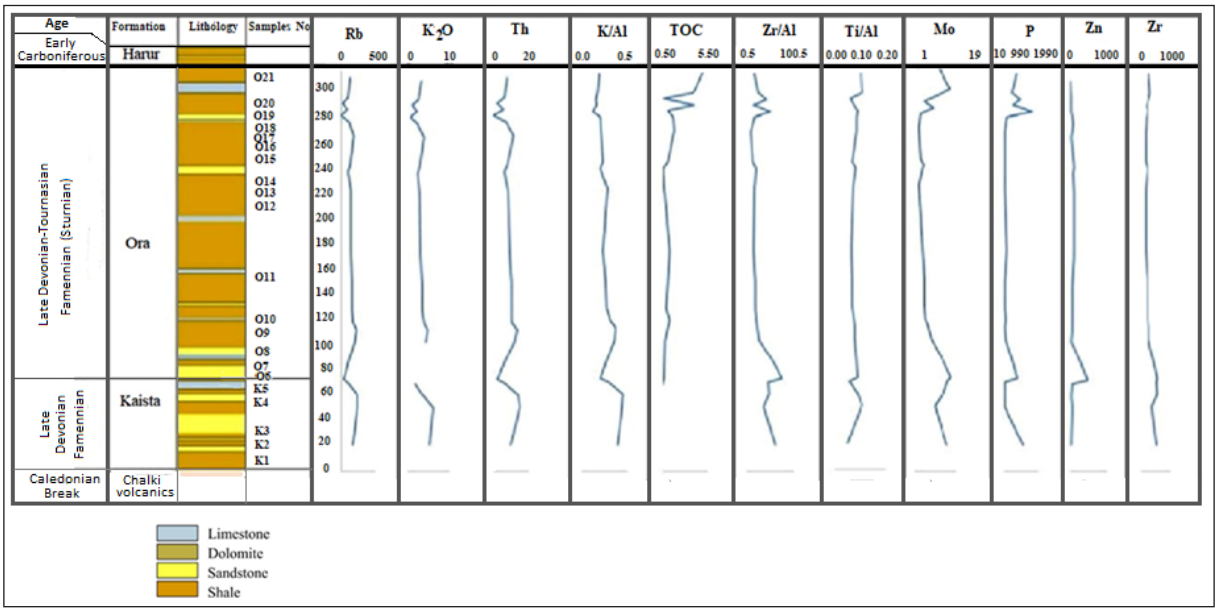

Figure 2. Lithological section of the studied formations at Ora type section of northernmost Iraq with sample locations and geochemical parameters indicative of transgressive system tract (TST), see Tables 2 and 3 for values and ratios.

4. Results

4.1. Mineralogical study

4.1.1. XRD analysis

Mineral compositions of the shale samples from XRD analyses have revealed that they consist mainly of clay minerals represented by mixed layered Illlite/smectite (I/S), followed by varying amounts of illite/mica (I/M), pyrophyllite, kaolinite, and chlorite (Fig. 3). Other non-clay minerals include quartz, feldspars (k-feldspar and plagioclase), calcite, Fe-dolomite (ankerite), goethite, rutile, and a few pyrite (Table 1).

The main carbonate mineral phases are calcite and a few Fe-rich dolomites (ankerite). In general, the studied shales are carbonate-rich. $CaCO_3$ ranged from 1.5-16.8 wt% in the Kaista shale, and 5.8-34.8 wt% in the Ora shale (Table 2).

4.1.2. SEM study

SEM study shows that shale is composed mainly of hexagonal degraded kaolinite plates (Fig. 4A-B). Illite is commonly found in the form of fibers or platy illite as intergrown on kaolinite grains and mica (Fig. 4A-B). Illite/smectite (I/S) is present in the form of interlocked fibers (Fig. 4C). Fractures and vugs/pores are commonly present in the studied samples (Fig. 4A-D). Carbonates are dominated by calcite and/or dolomite and occur as fine grains and/or lumps either filling fractures and pore space or distributed randomly throughout the matrix (Fig. 4B).

4.2. Elemental Geochemistry

The major and trace element analysis results of the shale from the middle Paleozoic (Kaista and Ora) formations are presented in Tables 2 and 3 respectively.

4.2. 1. Major elements

The average concentration of major element oxides of shale samples from Kiasta is enriched in the absolute abundances of SiO_2 (53.02%), Al_2O_3 (18.18%), Fe_2O_3 (7.06 %), K_2O (4.216%), CaO (2.69%), MgO (2.25%), TiO_2 (1.21%), Na_2O (0.17), P_2O_5 (0.11%) and MnO (0.05%). In contrast, the major element oxide concentrations of shales from Ora are characterized by narrow compositional variations and are enriched in the absolute abundances of SiO_2 (52.01%), Al_2O_3 (20.36%), Fe_2O_3 (8.45 %), K_2O (2.98%), MgO (1.59 %), CaO (1.39 %), TiO_2 (1.39%), Na_2O (0.77%), P_2O_5 (0.12%) and MnO (0.05%).

The EFs (enrichment factors) averages of the major elements relative to the average shale (AS), K, Ca, Mg, and Na in the Kaista shale and are more enriched than those of the Ora shale, while Fe, A, and Na are more enriched in the Ora shale (Fig. 5A).

4.2. 2. Trace elements

The concentrations of the trace elements are presented in table-2. On average, the elemental content of shale from Kaista, is phosphorus (P: 596), barium (Ba: 552 ppm), and sulfur (S: 1439. ppm. In contrast, their corresponding average values in Ora shale are 493 ppm, 509 ppm, and 6959 ppm respectively. The concentrations of these elements are significantly higher than Mo, Co, and Zn, whose average concentration values from the Kaista and Ora shale are 21, 7, 128 ppm, and 7, ~3, 51 ppm, respectively.

Based on the enrichment factor averages, the Ora shales are enriched in Pb, Ga, V, Cr, and Ni, compared with Kaista shales, which are relatively enriched in U, Th Mo, Zr, Ba, Rb, Sr, Zn, Cu, and Co (Fig. 5B).

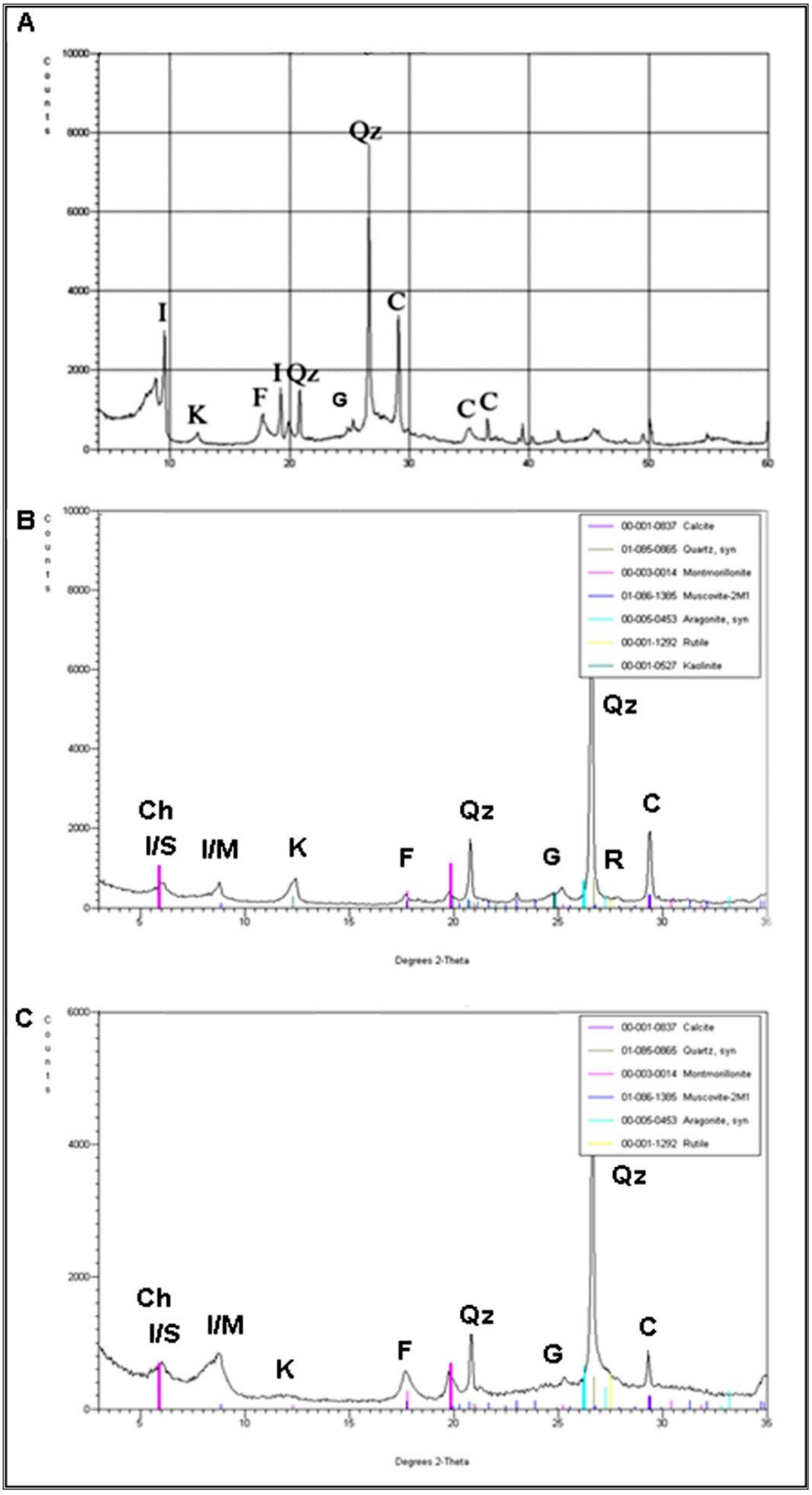

Figure 3. Representative X-ray diffractograms of the main clay and non-clay minerals components in the studied shales. K=Kaolinite; I/S= Illite/Smectite; I=Illite; I/M=Illite/Mica; Ch=Chlorite, Qz= Quartz; C= Calcite; F= Feldspar; R=Rutile; G=Goethite.

Table 1. Mineralogical composition (percent) of the studied selected samples from the Kaista and Ora formations.

Sample No.	Mixed I/S	Illite/Mica	Pyrophyllite	Kaolinite	Chlorite	Quartz	Feldspars	Calcite	Dolomite	Goethite	Rutile	Pyrite
Ora 21	28.9	22.5	2.4	0.0	1.7	28.2	7.6	2.4	1.7	5.7	0.7	0.0
Ora 20	28.6	31.1	0.4	02	1.3	24.6	2.6	1.8	0.8	5.1	1.0	0.0
Ora 19	30.0	21.1	1.6	1.1	5.8	15.8	3.1	15.3	0.0	2.9	0.7	0.0
Ora 18	34.6	12.6	0.5	0.9	5.6	12.8	8.2	11.4	0.0	6.7	0.7	0.0
Ora 17	34.3	4.2	2.0	1.0	2.1	27.9	8.1	9.4	0.6	2.0	0.9	0.0
Ora 16	34.0	18.1	5.1	0.0	5.7	29.1	0.7	28.9	0.0	0.0	0.0	0.0
Ora 15	33.7	12.3	0.0	0.0	4.8	24.4	5.1	26.4	0.5	5.9	0.5	0.0
Ora 14	10.0	16.0	1.7	2.9	2.9	24.4	1.8	0.6	0.0	8.2	1.0	0.0
Ora 13	33.3	24.4	3.0	2.1	0.0	33.0	3.3	0.6	0.6	7.5	0.8	0.0
Ora 12	22.6	23.3	12.4	10.1	0.0	8.9	4.1	2.1	0.7	3.0	1.2	0.0
Ora 11	23.7	26.2	9.9	8.5	4.9	28.6	9.8	0.0	0.0	3.9	1.1	0.0
Ora 10	24.5	18.4	3.8	1.7	2.4	57.7	6.2	0.0	0.0	2.5	0.6	8.7
Ora 9	17.8	14.7	13.0	13.0	0.0	20.9	1.6	0.0	0.0	3.3	0.8	0.0
Ora 8	28.7	8.8	5.0	0.0	0.0	72.7	3.1	0.0	0.0	1.4	0.0	0.0
Ora 7	4.9	13.7	12.2	7.9	0.0	25.3	5.8	1.5	0.0	0.9	0.7	4.2
Ora 6	32.0	17.6	12.1	8.0	0.0	19.6	6.7	1.5	0.0	0.6	0.8	0.0
Kaista 5	32.9	19.3	0.0	0.0	2.3	44.2	2.5	15.2	0.5	0.0	0.5	0.0
Kaista 4	25.7	25.8	0.0	0.0	2.5	33.3	4.1	1.8	1.3	4.6	0.8	0.0
Kaista 3	23.4	27.1	0.0	0.0	0.0	42.2	3.1	0.9	1.2	1.3	0.5	0.0
Kaista 2	22.1	25.2	0.0	5.8	0.0	36.6	0.0	0.0	0.9	6.7	0.7	0.0
Kaista 1	5.0	9.9	0.0	2.5	3.5	65.4	0.2	0.7	0.0	6.5	1.0	0.0

Table 2. Major-element oxides (in wt%) and the chemical index of alteration (CIA), plagioclase index of alteration (PIA), and index of chemical variability (ICV) from the Kaista and Ora formations.

Sample No.	TOC	SiO_2	Al_2O_3	TiO_2	Fe_2O_3	MnO	MgO	CaO	K_2O	Na_2O	P_2O_5	Sum	CIA	PIA	ICV	K/AL	$CaCO_3$
Ora 21	5.00	61.12	28.59	2.56	1.78	0.03	0.50	0.11	3.40	0.49	0.15	98.73	98.30	98.07		0.19	5.80
Ora 20	3.86	60.66	24.31	2.21	3.69	0.03	0.64	0.28	2.58	0.78	0.10	95.28	96.84	96.47		0.17	6.62
Ora 19	0.52	64.53	10.92	0.57	5.08	0.01	0.21	0.61	1.01	0.80	0.20	83.49	93.07	92.41	0.70	0.15	11.15
Ora 18	3.95	52.50	23.33	1.51	8.55	0.05	1.15	0.50	2.29	1.08	0.11	91.07	95.51	95.05	0.63	0.15	10.63
Ora 17	1	44.80	8.22	0.62	12.04	0.02	0.77	1.27	0.61	0.61	0.38	69.43	92.97	92.45	1.79	0.12	15.23
Ora 16	1.62	49.19	19.84	1.48	10.39	0.07	1.54	1.72	2.39	1.06	0.02	87.07	94.79	94.12	0.86	0.19	16.88
Ora 15	1.7	54.27	30.29	2.23	6.16	0.05	0.95	0.47	4.00	0.93	0.10	99.45	96.97	96.52	0.47	0.21	10.28
Ora 14	0.9	52.16	19.53	1.11	9.30	0.05	1.85	1.06	2.81	0.93	0.10	88.90	95.43	94.70	0.82	0.23	14.48
Ora13	0.39	48.72	20.59	1.47	10.98	0.07	2.34	0.63	2.52	1.30	0.10	88.72	93.97	93.19	0.91	0.19	11.08
Ora 12	0.58	52.78	16.59	0.98	9.39	0.07	2.04	0.79	2.85	0.46	0.10	86.05	97.23	96.67	0.95	0.27	13.06
Ora 11	1.19	43.31	20.77	1.14	10.83	0.07	2.54	6.70	2.99	0.90	0.02	89.27	95.31	94.56	0.89	0.23	34.8
Ora 10	0.93	46.71	20.91	1.19	11.32	0.07	1.83	1.55	3.43	0.77	0.10	87.88	96.35	95.66	0.89	0.26	15.30
Ora 9	0.71	46.76	20.72	1.18	11.29	0.07	1.98	1.53	3.43	1.06	0.10	88.12	95.03	94.11	0.92	0.26	15.01
Ora 8	1.16	48.65	20.89	1.36	9.52	0.05	1.86	2.36	4.05	0.47	0.01	89.22	97.59	97.03	0.83	0.30	22.3
Ora 7	0.93	53.22	21.17	1.41	7.37	0.05	2.49	0.77	4.86	0.29	0.10	91.73	98.60	98.20	0.78	0.36	12.0
Ora 6	0.63	52.83	19.15	1.27	7.53	0.05	2.65	1.94	4.37	0.45	0.01	90.25	97.51	96.80	0.85	0.36	21.94
Average	1.57	52.01	20.36	1.39	8.45	0.05	1.58	1.39	2.98	0.77	0.11	89.94	95.97	95.38	0.88	0.23	14.78
.Max	5.00	64.53	30.29	2.56	12.04	0.07	2.65	6.70	4.86	1.30	0.38	99.20	98.60	98.20	1.79	0.36	34.8
.Min	0.39	43.31	8.22	0.57	1.78	0.01	0.21	0.11	0.61	0.29	0.01	80.76	92.97	92.41	0.47	0.12	5.8
Kaista 5	0.19	51.73	13.60	1.02	9.93	0.06	2.63	2.29	1.68	0.42	0.17	82.95	96.74	96.29	1.16	0.19	8.36
Kaista 4	0.29	47.46	20.92	1.00	11.25	0.06	1.49	0.91	3.80	0.18	0.10	86.27	99.07	98.86	0.85	0.28	3.36
Kaista 3		60.83	21.16	1.61	3.01	0.02	2.33	0.10	6.19	0.10	0.00	95.17	99.52	99.32	0.63	0.46	1.49
Kaista 2	5.00	54.18	18.73	1.71	6.82	0.04	2.79	0.70	5.26	0.10	0.10	89.87	98.89	98.46	0.90	0.44	2.06
Kaista 1	3.86	50.90	16.50	0.71	4.26	0.04	1.98	9.43	4.15	0.07	0.24	88.22	98.62	98.16	0.69	0.39	16.78
Average	2.3	53.02	18.18	1.21	7.05	0.05	2.25	2.69	4.22	0.17	0.12	88.50	98.57	98.22	0.85	0.35	6.42
max	5.0	60.83	21.16	1.71	11.25	0.06	2.79	9.43	6.19	0.42	0.24	95.17	99.52	99.32	1.16	0.46	16.78
Min	0.19	47.46	13.60	0.71	3.01	0.02	1.49	0.10	1.68	0.07	0.00	82.95	96.74	96.29	0.63	0.19	1.49

Table 3. Trace elements (in ppm) and elemental ratios sensitive to environmental conditions for the Kaista and Ora formations

Sample No.	Co	Ni	Cu	Zn	Ga	As	Pb	Se	Th	Rb	Sr	Y	Zr	Nb	Mo	U-	Cr	Mn	V	Ba	V/ (V+Ni)	Ni/ Co	V/ Cr	Ga/ Rb	Sr/ Cu	U/ Th	Th/U	U index (δU)	P/Ti	P/Al	Zr/Al	Ti/ Al	Sr/ Ba	Rb/K	Ba/ Sr
Ora 21	3	22	4	6	33	12	15	0	8	124	67	40	251	21	17	18	283	205	0	0		7.3		0.27	18.92	2.29	0.44	1.75	0.04	44.63	16.56	0.10		0.003	0.00
Ora20	5	26	9	17	33	15	16	2	6	96	53	51	309	24	25	17	232	223	0	0		5.2		0.35	5.91	2.73	0.37	1.78	0.03	34.09	24.00	0.10		0.005	0.00
Ora 19	3	30	10	33	12	12	15	4	2	23	22	121	243	20	16	7	87	115	155	513	0.84	10.0	1.78	0.54	2.23	3.58	0.28	1.83	0.26	152.40	42.01	0.06	0.04	0.000	23.44
Ora18	0	29	12	22	34	19	18	0	6	94	19	52	177	16	6	12	173	354	112	585	0.80		0.65	0.37	1.64	1.99	0.50	1.71	0.05	39.69	14.37	0.07	0.03	0.006	30.88
Ora 17	0	39	28	54	17	21	20	0	0	2	30	103	215	17	12	8	76	189	240	1038	0.86		3.15	9.55	1.07			2.00	0.45	383.04	49.36	0.09	0.03	0.005	35.01
Ora 16	0	45	44	78	35	16	16	0	7	117	41	42	184	16	2	13	144	566	154	181	0.77		1.07	0.30	0.94	1.74	0.57	1.68	0.01	10.30	17.57	0.08	0.23	0.005	4.41
Ora15	3	26	25	12	44	14	16	0	11	179	131	25	142	13	1	23	224	372	0	0		8.6	0.00	0.24	5.32	2.06	0.48	1.72	0.00		8.84	0.08		0.005	0.00
Ora 14	0	43	27	96	29	9	12	0	8	124	65	22	140	13	3	9	133	421	219	509	0.84		1.64	0.24	2.41	1.13	0.88	1.54	0.00		13.52	0.06	0.13	0.006	7.78
Ora13	0	48	61	74	33	6	10	0	6	101	43	46	221	18	5	20	138	558	202	82	0.81		1.46	0.33	0.70	3.18	0.31	1.81	0.00		20.25	0.08	0.53	0.006	1.90
Ora12	0	37	18	97	28	13	15	0	8	135	44	23	139	13	1	5	114	506	224	613	0.86		1.96	0.20	2.51	0.59	1.69	1.28	0.00		15.88	0.07	0.07	0.006	13.92
Ora 11	0	48	31	103	36	11	13	0	9	145	106	33	160	14	4	9	133	578	312	273	0.87		2.35	0.25	3.38	0.94	1.06	1.48	0.01	8.77	14.56	0.06	0.39	0.006	2.59
Ora10	0	45	26	53	34	12	14	0	10	158	120	33	208	17	5	12	130	545	235	890	0.84		1.80	0.22	4.66	1.13	0.89	1.54	0.00		18.81	0.06	0.13	0.005	7.41
Ora9	0	46	31	52	36	13	14	0	11	157	141	34	205	17	5	13	128	546	251	921	0.85		1.97	0.23	4.50	1.24	0.80	1.58	0.00		18.68	0.06	0.15	0.005	6.55
Ora8	0	38	28	57	34	11	13	0	10	161	64	39	218	18	6	12	156	422	245	158	0.87		1.57	0.21	2.28	1.20	0.83	1.57	0.01	4.80	19.76	0.07	0.40	0.005	2.47
Ora7	2	38	16	40	35	9	13	0	14	216	0	32	252	20	8	6	156	365	148	354	0.79	19.0	0.95	0.16		0.47	2.13	1.17	0.00		22.54	0.08	0.53	0.005	
Ora 6	0	38	21	28	30	14	16	0	12	191	0	27	258	20	10	9	144	377	197	0	0.84		1.37	0.16		0.73	1.37	1.37	0.00	3.08	25.42	0.08		0.006	
Avg	3	37	24	51	32	13	15	3.08	9	127	67	45	208	17	7	12	153	396	207	510	0.84	7.7	1.67	0.85	4.03	1.67	0.84	1.61	0.10	75.64	21.38	0.08	0.22	0.005	11.17
Max	5	48	61	103	44	21	20	4.25	14	216	141	121	309	24	25	23	283	578	312	1038	0.90	19.0	3.15	9.55	18.92	3.58	2.13	2.00	0.45	383.04	49.36	0.10	0.53	0.006	35.01
Min	2	22	4	6	12	6	10	1.92	2	2	19	22	139	13	1	5	76	115	112	82	0.78	5.2	0.65	0.16	0.70	0.47	0.28	1.17	0.00	3.08	8.84	0.06	0.03	0.000	1.90
Kaista5	0	36	20	478	20	17	15	4	2	35	102	59	554	37	26	11	124	457	187	183	0.84		1.50	0.59	5.20	5.82	0.17	1.89	0.12	100.98	76.91	0.08	0.56	0.004	1.79
Kaista 4	0	53	10	60	32	3	9	1	6	100	118	54	511	36	23	10	116	482	285	781	0.84		2.46	0.32	11.44	1.67	0.60	1.67			46.17	0.05	0.15	0.005	6.61
Kaista3	6	29	5	28	27	2	9	9	14	231	24	24	541	38	19	21	189	192		639		5.15		0.12	4.73	1.52	0.66	1.64	0.00	0.66	48.31	0.09	0.04	0.005	27.11
Kaista2	0	39	121	51	27	27	24	2	15	234		28	363	27	14	18	156	341	73		0.65		0.47	0.12		1.20	0.83	1.57			36.61	0.10		0.004	
Kaista1	10	25	27	23	20	8	13	5	10	165	172	26	529	35	23	10	142	304	250	608	0.91	2.64	1.77	0.12	6.28	0.98	1.02	1.49	0.25	120.90	60.59	0.05	0.28	0.005	3.54
Avg	8	37	37	128	25	12	14	4	9	153	104	38	499	35	21	14	145	355	199	552.73	0.81	3.89	1.55	0.25	6.91	2.24	0.66	1.65	0.12	74.18	53.72	0.08	0.26	0.004	9.76
Max	10	53	121	478	32	27	24	9	15	234	172	59	554	38	26	21	189	482	285	781.10	0.91	5.15	2.46	0.59	11.44	5.82	1.02	1.89	0.25	120.90	76.91	0.10	0.56	0.005	27.11
Min	6	25	5	23	20	2	9	1	2	35	24	24	363	27	14	10	116	192	73	183.06	0.65	2.64	0.47	0.12	4.73	0.98	0.17	1.49	0.00	0.66	36.61	0.05	0.04	0.003	1.79

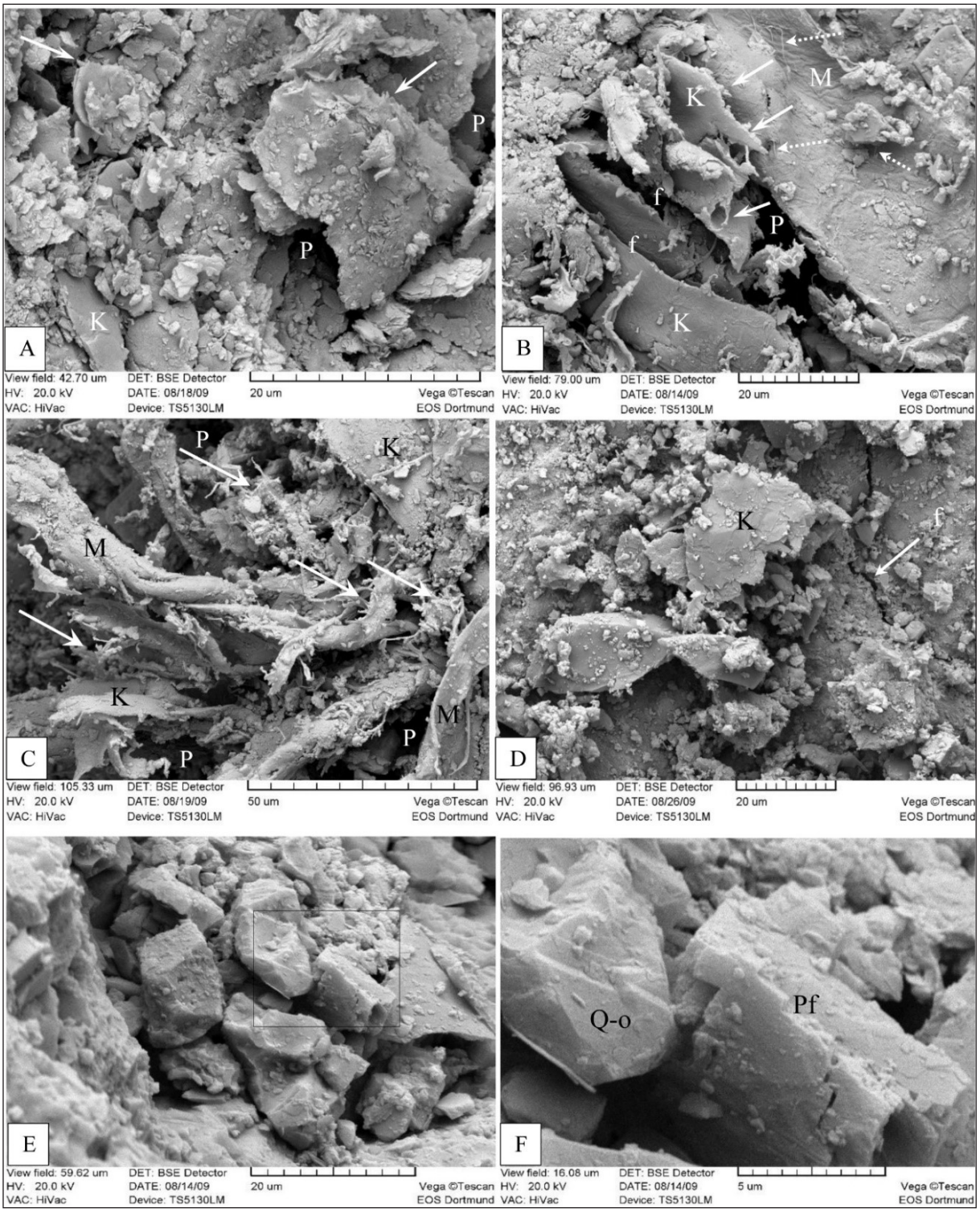

Figure 4. Scanning electron microscopic (SEM) images of the Kaista and Ora shales illustrate; (A and B) Degraded kaolinite plates (K), the fine illite fibers growing up from kaolinite (illitization of kaolinite "white arrows"), common pores (p) and fracture (f) in between kaolinite plates. Note the authigenic illite fibers (dashed white arrows) attached to the surface of detrital mica flake and scattered carbonate grains and/or lumps in the upper right side of image A. A- image is from the Ora shale (sample Ora 6) and B image from the Kaista shale (sample Kaista 3). C- Mixed layers I/S interlocked fibers (arrows) are present in between kaolinite plates (K) and mica flakes (M), note also fine carbonate grains distributed throughout the image. Image C is from the Kaista shale (sample Kaista 4). D- Degraded kaolinite plates (K) and common carbonate grains distributed throughout the image. This image is from the Kaista shale (sample Kaista 3). E- Cabonate grains, quartz and plagioclase fill the pore space of clayey matrix. F- Enlarged view of area outline in E showing quartz overgrowths (Q-o) associated with plagioclase-feldspar (Pf). E image is from the Kaista shale (sample Kaista 5).

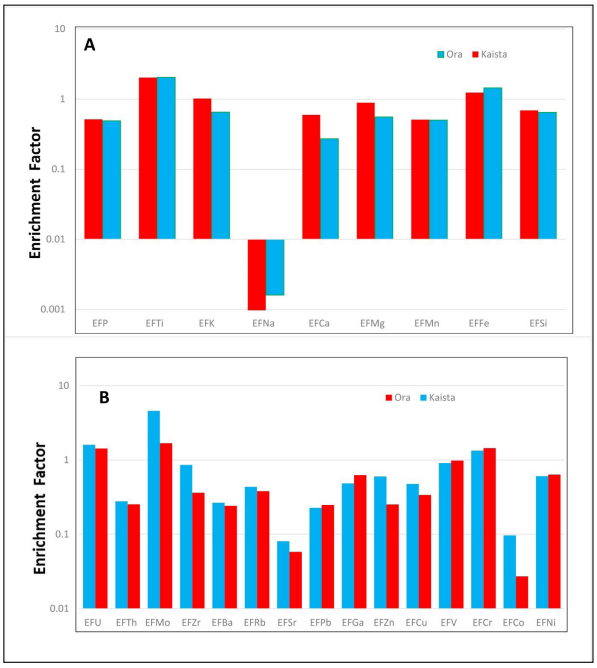

Figure 5. EFs diagram of the selected major (A) and trace (B) elements in the Kaista and Ora formations. A horizontal line (EF = 1) denotes an element enrichment or depletion.

4.3. TOC content

The TOC values in the studied shale samples of the Kaista and Ora formations ranged from 0.10 to 0.57 (avg. = 0.320) and 0.39 to 5.00 (avg. = 1.57), respectively (Table 2).

It's worth noting that the Ora shale has a higher TOC concentration than the Kaista shale.

5. Discussion

5.1. Paleoenvironmental condition

5.1.1. Paleoclimate and paleosalinity

The chemical index of alteration (CIA= [Al_2O_3/(Al_2O_3 + CaO* + Na_2O + K_2O)] × 100) proposed by Nesbitt and Young (1982) is widely used as a proxy for paleoclimate change as well as to assess the degree of weathering of the parent rock (Wang et al., 2020).

Generally, CIA ranges from 50 to 100, reflecting different climatic conditions: cold and dry climate (CIA = 50–60), warm and humid climate (CIA = 60–80), and hot and humid climate (CIA = 80–100) (Nesbitt and Young, 1982, 1989). The CIA values of the Ora and Kaista formations range from 92.9 to 99.5, and from 96.74 to 99.5, respectively (Table 2), indicating a hot and humid climate during their deposition. The CIA values of the present study are higher than the average NASC (North American Shale Composite) value of 57 (Gromet et al., 1984) and typical shale values (PAAS: 70 – 75; Taylor and McLennan, 1985), indicating intense chemical weathering at the source rocks.

The degree of chemical weathering of sediments and sedimentary rocks can also be estimated using the Plagioclase Index of Alteration [PIA: Fedo et al., 1995; PIA = [(Al_2O_3 - K_2O)/ (Al_2O_3+Na_2O+CaO*-K_2O)] × 100 (molecular proportions)]. The PIA values of Ora and Kaista shale (PIA: 92.4 – 99.3 and 96.2 -99.3 respectively) are consistent with CIA values, which further supports that these shales have undergone intense weathering at the source area.

In the A-CN-K diagram (Fedo et al., 1996; Fig. 6), all the studied samples fall above the K-feldspar-plagioclase line, and most of them are parallel to the A–K join and close to the muscovite point. This weathering trend indicates a high loss of Ca, Na, and K in the shale samples, as they tend to plot close to the A apex, suggesting that most feldspars have converted to clay minerals. This could be reflected by the type of clay minerals, whereas intense chemical weathering under humid conditions results in a kaolinite-rich composition of sediments (Chamley, 1989). Thus, the high content of degraded kaolinite (Fig. 4) and the predominance of kaolinite over illite in the studied shale samples are likely a result of intense chemical weathering and may correlate with the Hangenberg climatic event at the Devonian/Tournaisian boundary (Misch et al., 2018).

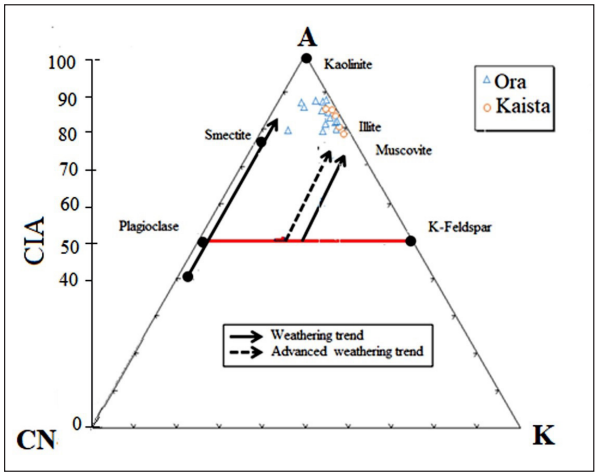

Figure 6. A-CN-K [Al_2O_3 – (CaO*+Na_2O) – K_2O; all in molar proportions] ternary plot for the Kaista and Ora shales (After Nesbitt and Young, 1982; Fedo et al., 1996)

The paleosalinity levels during the deposition of sediments were measured by ratios of Rb/K (Campbell and Williams,1965) and Sr/Ba (Zhen et al., 2020, Li et al., 2020). Ratios of Rb/K ≤ 0.004 infer freshwater column, 0.004 ≤ 0.006 designates a fresh to the brackish water environment, and >0.006 values suggest fully marine water conditions. According to (Li et al. 2020, and Zhen et al., 2020), ratios of Sr/Ba more than 1 show saline water conditions, from 1.0 to 0.6 represent brackish environments, and less than 0.6 indicates freshwater conditions. In addition, the Sr/Ba ratio can be used to distinguish between marine and lake environments, in lake deposits less than 0.6, and ranging from 0.8 to 1.0 in marine sediment conditions. The Rb/K ratios of the Kaista and Ora formations shale (0.003 to 0.005; average: 0.004) and (0.000 to 0.006; average: 0.005), respectively are characteristic of freshwater to brackish water conditions, while the Sr/Ba ratios of the samples from the Kaista and Ora formations vary from (0.04 to 0.56), with an average of 0.26 and from (0.03 to 0.53) with an average of 0.22 respectively, indicating a freshwater environment during deposition. The relatively moderate TOC content of the Ora shale may be attributed to water stratification, resulting from the freshwater influx, which diminishes oxygen exchange with the atmosphere and further intensifies reducing conditions favorable for organic matter preservation (Li et al., 2017).

5.1.2. Paleoredox Conditions

Redox-sensitive trace elements such as V, Ni, U, and Mo in the sediments have been used extensively to infer paleo-redox conditions of water because these elements are insoluble in reducing environments and are enriched under anoxic conditions more than oxic conditions (Hatch and Leventhal, 1992; Jones and Manning, 1994; Algeo and Maynard, 2004; Tribovillard et al., 2006). The V/(V+Ni) ratio is also widely used for paleo-redox reconstruction and tends to indicate consistently lower oxygen regimes than other paleo-redox indicators (Rimmer, 2004). Hatch and Leventhal (1992) suggested that V/(V+Ni) ratios are between 0.46–0.60 for dysoxic environments, 0.54–0.82 for anoxic environments, and up to 0.84 for euxinic environments. In this study, the V/(V+Ni) ratios of Kaista and Ora shale vary from 0.64-0.91 (avg. = 0.80), and 0.77-0.90 (avg. = 0.83) respectively (Table 3). These values coherently indicate deposition under anoxic conditions.

Another elemental value such as the Th/U ratio is also used to evaluate paleo-redox conditions. The geochemical properties of Th and U are quite different in oxidizing environments but are similar in reducing environments (Wignall and Twitchett, 1996). These researchers recommended that Th/U ratios between 0 and 2 indicate a reducing environment, from 2 to 7 in the oxic environment and > 8 implies a strongly oxidizing environment. Th/U ratios of Kaista and Ora shale are 0.17–1.02 (avg. = 0.66) and 0.00 –2.13 (avg. = 0.84), (Table 3), respectively also suggesting anoxic conditions. Similarly, some researchers used the U index [δU = U/−0.5 × (Th/3 + U)] to reconstruct the depositional condition, where its value is more than 1 refers to a reducing environment and less than 1 indicates an oxidizing environment (Steiner et al2001 .). The δU values of the Kaista and Ora shale range from 1.49 to 1.89 (avg. = 1.65) and from 1.17 to 2 (avg. = 1.61) respectively also suggesting an anoxic condition.

5.1.3. Transgressive system tracts

The transgressive and highstand system tracts are defined by different characteristics and can be related to many variables, such as anoxic conditions, low detrital input index, strong paleo-productivity, and condensed sections. Generally, it should be noted that the top of the section of a transgressive system tract is due to the existence of a condensed section (Hou et al., 2022).

Transgressive systems tracts (TST) are characterized by relatively higher levels of organic richness as compared to other tracts, so the higher amount of organic matter in shales might be due to paleosalinity, dilution, paleoproductivity, and redox conditions (Katz, 1995). During the transgressive period, the organic matter may increase due to the contribution of terrigenous organic matter supplies from the neighboring continent and highly productive marine sources by active circulation (Hyun et al., 2006).

The transgressive system tracts can be reflected by the variations in the concentrations of major and minor elements and their ratios. In the present study, it was observed that there is an increase in the Rb, K_2O, Th, K/Al, and TOC values of the major and trace elements and the elemental ratios from the Kaista upward to the Ora Formation. Conversely, there is a decrease in the same trend of Zr/Al, Ti/Al, Mo, P, Zn, and Zr (Fig. 2). This variation of elemental ratios at the transitional area from the Kiasta to Ora shale could be related to TST, which has been confirmed by Al-Juboury et al. (2012). Furthermore, Sharland et al. (2001) considered the Ora shale in Northern Iraq to have the maximum flooding surface of D30, deposited in a sub-tidal shelf environment.

5.1.4. Paleo-productivity proxies

The organic matter accumulation of the marine shale has been influenced by several factors, such as primary productivity, redox condition, palaeoclimate, palaeosalinity, and paleogeography (Fu et al., 2009; Wang et al, 2010; Zeng et al., 2015).

Fu et al. (2007) proposed that the organic carbon preservation in the shale may be influenced dominantly by anoxic conditions rather than high primary productivity, and such a factor cannot be ruled out.

Phosphorus (P) is an important nutritional element, which can greatly control the paleo-productivity of marine and lacustrine shales (Tyrrell, 1999). Therefore, P_2O_5 concentrations are widely used to analyze variations in paleo-productivity (Latimer and Filippelli, 2002). To decrease the influence of authigenic minerals and organic matter on the P dilution effect from terrigenous detritus, other indicators, including P/Ti and P/Al, are more effective for assessing paleo-productivity conditions (Latimer and Filippelli, 2002; Algeo et al., 2011). P_2O_5 content, P/Ti, and P/Al ratios determined are shown in Tables (2 and 3). Similar change curves are found for each of these indicators, and the maximum values of P_2O_5, P/Ti, and P/Al ratios are found in samples 17, 19, and 21 for Ora shale (Table 3)

The average values of P_2O_5 content, P/Ti, and P/Al ratios of the Ora shale are 0.11%, 0.1 and 75.64, and those of the Kaista shales are 0.12%, 0.12, and 74.18, respectively. However, the average value of P/Ti is less than 0.34, which indicates lower productivity, whereas values greater than 0.79 refer to higher productivity, and values between 0.34 and 0.79 indicate a moderate level of primary productivity (Algeo et al., 2011). The P/Ti values are low in Ora shales (<0.34; Table 3). In addition, the correlations of P/Ti versus TOC in the Ora Formation (r = -0.098) and P/Al versus TOC (r = -0.064) exhibit a very weak negative correlation, respectively (Table 3), suggesting low primary productivity and that the paleoredox conditions in Ora shales play a significant role in the preservation of organic matter.

5.1.5. Hydrothermal activity

Large amounts of organic material and various types of metals were transported from the deep oceanic basin and accumulated in the sedimentary environments along the continental shelf, resulting in the enrichment of these metals in the black shales (Wu et al., 2017). Trace elements and rare earth elements are important in the study of ancient hydrothermal systems (Choi and Hariya., 1992; Hatch and Leventhal, 1992). Submarine hydrothermal activities can be identified by using several geochemical indices such as Co–Zn–Ni, U/Th, and Ba/Sr ratios.

The ternary diagram of Co–Zn–Ni can be used to

discriminate between hydrogenous and hydrothermal deposits (Choi and Hariya,1992). In this diagram, the studied samples of Kaista and Ora shale generally fall into the hydrothermal field (Fig. 7). The U/Th ratio can also be used to estimate the influence of hydrothermal fluids (Dickson. and Scott, 1997). Uranium–thorium ratios larger than 1 indicate that hydrothermal activity was present during the depositional period, whereas U/Th <1 indicates normal seawater depositional conditions. In the studied samples of the Kaista and Ora formations shale, U/Th values range from 0.98 to 5.82 (avg.= 2.24) and 0.47 to 3.58 (avg.= 1.67) respectively, suggesting input from deep hydrothermal sources.

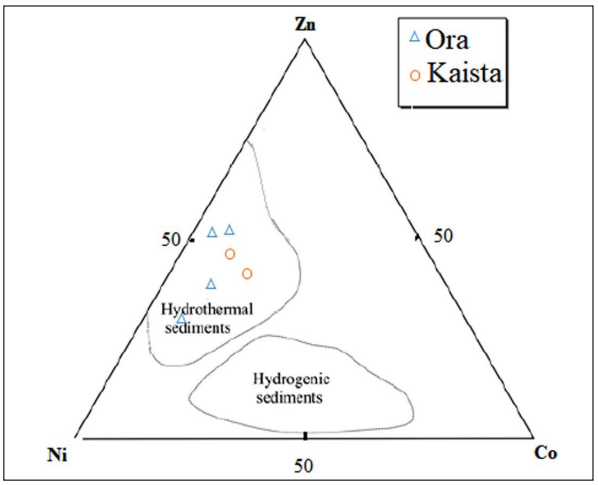

Figure 7. Ni-Zn-Co ternary plot for the Kaista and Ora shales, distinguishing hydrothermal and hydrogenic sediments (Chen et al., 2019).

The Ba/Sr ratios are also used by many researchers to indicate hydrothermal activity (Smith and Cronan, 1983; Peter and Scott, 1988). Where its ratios range from 5.0 to 20, with an average of 11, indicating the influence of submarine hydrothermal fluids (Liu et al., 2021). Ba/Sr ratios of the Kaista and Ora formations shale range from 1.79 to 27.11 (avg.= 9.76) and from 1.89 to 35.01 (avg.= 12.4) (Table 3) respectively, depicting that depositional area was affected by hydrothermal activity. In addition, the petrographic study indicates the presence of quartz overgrowth associated with plagioclase (Fig. 4 E-F), which suggests that solutions rich in silica were probably derived from hydrothermal activity (Zaghloul et al., 2010). Additionally, the presence of pyrophyllite in the Ora shales (Table 1) may suggest the effect of hydrothermal origin (Swindale and Hughes, 1968). All the data sets above might suggest that there was hydrothermal activity in the basin during the deposition.

The Late Devonian-Early Carboniferous was interpreted as a period of extension and compression with Hercynian back-arc rifting, inversion, and uplift formed by subduction of the southern margin of Paleo-Tethys (Sharland et al., 2001). This is supported by the presence of Devonian-Carboniferous volcanic and metamorphics in the Kuh-Sefid area of the Sanandaj-Sirjan Zone (Davoudzadeh and Weber-Diefenbach, 1987). The study area was not so far distance from the Sanandaj-Sirjan Zone which suggests that the hydrothermal activity in the study area was probably affected by this subduction.

6. Conclusion

The Late Devonian–Early Carboniferous succession of the Kaista and Ora formations from northern Iraq is composed mainly of calcareous shales intercalated with sandstones, siltstones, and limestone (dominantly dolomitic). Geochemical and mineralogical investigations of the shale units were carried out to constrain paleoclimate, paleosalinity, paleo redox conditions, transgressive system tract, paleoproductivity, and hydrothermal activity. In addition to the kaolinite-rich composition of the studied shale samples, chemical indices such as the chemical index of alteration (CIA), the plagioclase index of alteration (PIA), and the A–CN–K plot indicate intense chemical weathering in the source area under humid climate conditions. The Rb/K and Ba/Sr ratios suggest that the depositional area experiences freshwater to brackish water conditions. Paleo redox trace elements proxies such as V/(V+Ni), Th/U ratios, and U index indicates deposition under anoxic conditions. The variation of some major and trace elements and their elemental ratios (Rb, K_2O, Th, Mo, P, Zn, Zr, Zr/Al, Ti/Al, and K/Al) in the transitional area from Kiasta to Ora shale could be related to transgressive systems tracts (TST). The reduced primary productivity and paleoredox conditions are responsible for the preservation of organic matter in the Ora Formation. The ternary plot of Co–Zn–Ni, U/Th, and Ba/Sr ratios indicate that the depositional setting was affected by hydrothermal activity probably due to the subduction of the southern margin of Paleo-Tethys.

References

Abdula, R.A., Akram, R., Jabbar, W.J., Albeyati, F. (2020). The efficiency of oil and gas generation of Palaeozoic formations outcrops in Nazdur area, Kurdistan region, Northern Iraq: insights from palynological study. Iraqi Geological Journal 53(1A): 16–35.

Absar, N., Raza, M., Roy, M., Naqvi, S. M., Roy, A. K. (2009). Composition and weathering conditions of the Paleoproterozoic upper crust of Bundelkhand craton, Central India: records from the geochemistry of clastic sediments of 1.9 Ga Gwalior Group. Precambrian Research 168: 313–329.

Al-Haba, Y.K., Khalaf, F.H., Al-Rubaii, M., Michal, A. (1991). Regional geology studies for Paleozoic section, west Iraq. EOC unpublished report, Baghdad. 97 p.

Al-Haba, Y., Al-Sammarai, A., Al-Jubori, F., Georgis, N.N., Ahmed, I.M. (1994). Exploration for the Paleozoic Prospects in Western Iraq, Part 1, Exploration of the Paleozoic system in Western Iraq. In: Proceedings of the Second Seminar on Hydrocarbon Potential of Deep Formations in the Arab Countries (OAPEC), Cairo.

Al-Hadidy, A.H. (2001). Facies and sedimentary environment of Late Paleozoic successions (Devonian–Permian) of Iraq. Ph.D. Thesis, Mosul University, Iraq.

Al-Hadidy, A.H.,(2007). Paleozoic stratigraphic lexicon and hydrocarbon habitat of Iraq. GeoArabia 12(1): 63-130.

Al-Juboury, A.I., Al-Hadidy, A.H. (2008). Facies and depositional environments of the Devonian–Carboniferous succession of Iraq. Geological Journal 43: 383-396.

Al-Juboury, A.I., Al-Hadidy, A.H. (2009). Petrology and depositional evolution of the Paleozoic rocks of Iraq. Marine and Petroleum Geology 26(2): 208-231.

Al-Juboury, A.I., Al-Banna, N.Y., Barzinjy, D.N. (2012). Sequence Stratigraphy of the late Devonian-early Carboniferous

(Kaista and Ora formations), North Iraq. Stratigraphy and Sedimentology of Oil-Gas Basins 9: 18-36.

Akkoca, D.B., Karatas, M.A. (2019). The geochemical composition of the Palu Formation from the Palu-Uluova basin, Elaziğ, Eastern Anatolia (Turkey): implication of source area, weathering, and tectonic setting. Journal of African Earth Sciences 151: 472-489.

Akkoca, B. D., Eriş, K. K., Çağatay, M. N., Biltekin, D.(2019). The mineralogical and geochemical composition of Holocene sediments from Lake Hazar, Elazığ, Eastern Turkey: Implications for weathering, paleoclimate, redox conditions, provenance, and tectonic setting. Turkish Journal of Earth Sciences 28: 760-785.

Algeo, T.J., Kuwahara, K., Sano, H., Bates, S., Lyons, T., Elswick, E., Maynard, J.B. (2011). Spatial variation in sediment fluxes, redox conditions, and productivity in the Permian–Triassic Panthalassic Ocean. Paleogeography Palaeoclimatology Palaeoecology 308 (1–2): 65–83.

Algeo, T.J., Maynard, J.B. (2004). Trace-element behavior and redox facies in core shales of Upper Pennsylvanian Kansas-type cyclothems. Chemical Geology 206 (3–4): 289-318.

Aqrawi, A. A., Goff, J.C., Horbury, A.D., Sadooni, F. N. (2010). The Petroleum Geology of Iraq. pp. 1-424, Scientific Press, UK.

Armstrong-Altrin, J.S. (2009). Provenance of Sands from Cazones, Acapulco, and Bahia Kino Beaches, Mexico. Mexican Geosciences Journal 26: 764-782.

Armstrong-Altrin, J.S., Lee, Y.I., Verma, S.P., Ramasamy, S. (2004). Geochemistry of sandstones from the upper Miocene Kudankulam Formation, southern India: implications for provenance, weathering, and tectonic setting. Journal of Sedimentary Research 74(2): 285-297.

Armstrong-Altrin J.S., Nagarajan R., Madhavaraju J., Rosalez-Hoz L., Lee Y.I., Balaram V., Cruz-Martínez A., Avila-Ramírez G. (2013). Geochemistry of the Jurassic and Upper Cretaceous shales from the Molango Region, Hidalgo, eastern Mexico: implications for source-area weathering, provenance, and tectonic setting. Comptes Rendus Geoscience 345: 185-202.

Armstrong-Altrin, J.S., Nagarajan, R., Balaram, V., Natalhy-Pineda, O. (2015). Petrography and geochemistry of sands from the Chachalacas and Veracruz beach areas, western Gulf of Mexico, Mexico: constraints on provenance and tectonic setting. Journal of South American Earth Sciences 64: 199-216.

Beydoun, Z.R. (1991). Arabian plate hydrocarbon, geology and potential: a plate tectonic approach. AAPG Studies in Geology 33, 77 p.

Buday, T. (1980). The Regional of Iraq. Stratigraphy and Palaeogeography. Dar Al-Kutub Publishing House, University of Mosul, Mosul, Iraq 445 p.

Campbell, F.A., Williams, G.D. (1965). Chemical composition of shales of Mannville group (lower Cretaceous) of central Alberta, Canada. American Association of Petroleum Geologists Bulletin 49: 81-87.

Chamley, H. (1989). Clay sedimentology. Springer, Berlin 623 p.

Chen, Z., Cui, J., Ren, Z., Jiang, S., Liang, X., Wang, G., Zou, C. (2019). Geochemistry, paleoenvironment and mechanism of organic-matter enrichment in the lower Silurian Longmaxi Formation shale in the Sichuan basin, China. Acta Geologica Sinicia 93 (1): 505-519. DOI: 10.1111/1755-6724.13868

Choi, J.H., and Hariya, Y. (1992). Geochemistry and depositional environment of Mn oxide deposits in the Tokoro Belt, northeastern Hokkaido, Japan. Economic Geology 87(5): 1265-1274.

Davoudzadeh, M., Weber-Diefenbach, K. (1987). Contribution to the paleogeography, stratigraphy, and tectonic of the Upper Paleozoic of Iran. Neues Jahrbuch für Geologie und Paläontologie. Abhandlungen 175 (2): 121-146.

Dickson, B.L., Scott, K.M. (1997). Interpretation of aerial gamma-ray surveys – Adding the geochemical factors, AGSO. Journal of Australian Geology and Geophysics 17 (2): 187-200.

Dostal, J., Keppie, J. (2009). Geochemistry of low-grade clastic rocks in the Acatlán Complex of southern Mexico: Evidence for local provenance in felsic–intermediate igneous rocks. Sedimentary Geology 222 (3): 241-253.

Fedo, C.M., Eriksson, K.A., Krogstad, E.J. (1996). Geochemistry of shales from the Archean (~3.0 Ga) Buhwa Greenstone Belt, Zimbabwe: implications for provenance and source-area weathering. Geochimica et Cosmochimica Acta 60: 1751-1763.

Fedo, C.M., Nesbitt, H.W., Young, G.M. (1995). Unraveling the effect of potassium metasomatism in sedimentary rocks and paleosols, with implications for paleoweathering conditions and provenance. Geology 23: 921-924.

Fu, X. G., Wang, J., Tan, F. W., Zeng, Y. H. (2009). Sedimentological investigations of the Shengli River–Changshe Mountain oil shale (China): Relationships with oil shale formation. Oil Shale 26 (3): 373-381.

Fu, X. G., Wang, J., Wang, Z. J., Chen, W.X. (2007). Marine oil shale depositional environment of Qiangtang Basin in northern Tibet. Xinjiang. Petroleum Geology 28 (5): 529-533.

Gaddo, J., Parker, D.M. (1959). Final report on well Khleisia-1", MPC Report, Iraq, 102 p.

Gromet, L.P., Haskin, L.A., Korotev, R.L., Dymek, R.F. (1984). The "North American shale composite": Its compilation, major and trace element characteristics. Geochimica et Cosmochimica Acta 48 (12): 2469-2482.

Hatch, J.R., Leventhal, J.S. (1992). Relationship between inferred redox potential of the depositional environment and geochemistry of the Upper Pennsylvanian (Missourian) Stark Shale Member of the Dennis Limestone, Wabaunsee County, Kansas, USA. Chemical Geology 99 (1-3): 65-82.

Hou, H., Shao, L., Li, Y., Liu, L., Liang, G., Zhang, W., Wang, X., Wang, W. (2022). Effect of paleoclimate and paleoenvironment on organic matter accumulation in lacustrine shale: Constraints from lithofacies and element geochemistry in the northern Qaidam Basin, NW China. Journal of Petroleum Science and Engineering 208 (A), 109350.

Hyun, S., Lim, D. I., Yoo, H. S. (2006). Transgressive geochemical records in the East China Sea: A perspective with Holocene paleoceanography. Economic and Environmental Geology 39 (1): 53-61.

Jafarzadeh, M., Hosseini-Barzi, M. (2008). Petrography and Geochemistry of Ahwaz Sandstone Member of Asmari Formation, Zagros, Iran: Implications on Provenance and Tectonic Setting. Revista Mexicana De Ciencias Geologicas 25: 247-260.

Jassim, S. Z., Goff, J. C. (2006). Phanerozoic development of the northern Arabian Plate. In: Geology of Iraq, edited by Jassim, S.Z., Goff, J. C., Dolin, Prague and Moravian Museum, Czech Republic pp. 32-44.

Jones, B., Manning, D.A.C. (1994). Comparison of geochemical indices used for the interpretation of palaeoredox conditions in ancient mudstone. Chemical Geology 111: 111–129.

Katz, B. J. (1995). Factors controlling the development of lacustrine petroleum source rocks-An Update. In: Paleogeography, Paleoclimate, and Source Rocks, edited by Huc, A. Y., AAPG Studies in Geology, 40, Tulsa, Oklahoma, USA, 79.

Khazaei, E., Mahmoudy-Gharaie, M.H., Mahboubi, A., Moussavi-Harami, R., Taheri, J. (2018). Petrography, major

and trace elemental geochemistry of the ordovician-silurian siliciclastics in North of tabas block, central Iran: Implications for provenance and paleogeography. Journal of Sciences, Islamic Republic of Iran 29 (2): 129-142.

Latimer, J.C., Filippelli, G.M. (2002). Eocene to Miocene terrigenous inputs and export production: geochemical evidence from ODP Leg 177, Site 1090. Paleogeography. Paleoclimatology. Paleoecology 182: 151-164.

Li, L., Liu, Z., Sun, P., Li, Y., George, S.C. (2020). Sedimentary basin evolution, gravity flows, volcanism, and their impacts on the formation of the Lower Cretaceous oil shales in the Chaoyang Basin, northeastern China. Marine and Petroleum Geology 119: 1-21.

Li, Y., Zhang, T., Ellis, G. S., Shao, D. (2017). Depositional environment and organic matter accumulation of Upper Ordovician–Lower Silurian marine shale in the Upper Yangtze Platform, South China. Palaeogeography Palaeoclimatology Palaeoecology 466: 252-264.

Liu, H., Wang, C., Li, Y., Deng, J., Deng, B., Feng, Y., Zhao, S. (2021). Geochemistry of the black rock series of lower Cambrian Qiongzhusi Formation, SW Yangtze Block, China: Reconstruction of sedimentary and tectonic environments. Open Geosciences 13 (1): 166-187.

Misch, D., Wegerer, E., Gross, D., Sachsenhofer, R.F., Rachetti, A., Gratzer, R. (2018). Mineralogy and facies variations of Devonian and Carboniferous shales in the Ukrainian Dnieper-Donets Basin. Austrian Journal of Earth Sciences 111: 5-25.

Nesbitt, H.W., Young, G.M. (1989). Formation and diagenesis of weathering profiles. Journal of Geology 97: 129-147.

Nesbitt, H.W., Young, G.M. (1982). Early Proterozoic climates and plate motions inferred from major element chemistry of lutites. Nature 199: 715-717.

Peter, J.M., Scott, S. (1988). Mineralogy, composition, and fluid–inclusion microthermometry of seafloor hydrothermal deposits in the southern trough of Guaymas basin, Gulf of California. Canadian Mineralogist 26: 567-587.

Ranjan, N., Banerjee, D.M. (2009). Central Himalayan crystallines as the primary source for the sandstone-mudstone suites of the Siwalik Group: new geochemical Evidence. Gondwana Research 16: 687-696.

Rimmer, S.M. (2004). Geochemical paleoredox indicators in devonian–mississippian black shales, central appalachian basin (USA). Chemical Geology 206 (3-4): 373-391.

Sissakian, V.K. (2000). Geological map of Iraq, Sheets No. 1, Scale: 1: 1000000, Baghdad.

Smith, P.A., Cronan, D.S. (1983). The geochemistry of metalliferous sediments and waters associated with shallow submarine hydrothermal activity (Santorini, Aegean Sea). Chemical Geology 39: 241-262.

Sharland, P.R., Archer, R., Casey, D.M., Davies, R.B., Hall, S.H., Heward, A.P., Horbury, A.D., Simmons, M.D. (2001). Arabian Plate Sequence Stratigraphy. GeoArabia Special Publication, volume 2, Gulf PetroLink, Manama, Bahrain 371 p.

Sherwani, G., Naqishbandi S.F., Redha, D. (2010). Palynological Study of Ora and Upper part of Kaista Formations in Zakho area, Iraqi Kurdistan Region. Kirkuk University Journal 5 (1): 50-73.

Steiner, M., Wallis, E., Erdtmann, B.-D., Zhao, Y., Yang, R. (2001). Submarine-hydrothermal exhalative ore layers in black shales from south China and associated fossils-insights into a Lower Cambrian facies and bio-evolution: Palaeogeography, Palaeoclimatology, Palaeoecology 169:165–191.

Swindale, L.D., Hughes, I.R. (1968). Hydrothermal association of pyrophyllite, kaolinite, diaspore, dickite, and quartz in the Coromandel Area, New Zealand. New Zealand Journal of Geology and Geophysics 1195: 1163-1183.

Taylor, S.R., McLennan, S.M. (1985). The Continental Crust: Its Composition and Evolution. Blackwell Scientific, Oxford 328 p.

Tobia, F.H., Mustafa, B.H. (2019). Provenance and depositional environment of the carbonates from the Baluti formation (Late Triassic), Kurdistan region, Iraq. Iraqi Geological Journal 52 (2): 18-35.

Tribovillard, N., Algeo, T.J., Lyons, T., Riboulleau, A. (2006). Trace metals as paleoredox and paleoproductivity proxies: an update. Chemical Geology 232 (1-2): 12-32.

Tyrrell, T. (1999). The relative influences of nitrogen and phosphorus on oceanic primary production. Nature 400: 525–531.

Wang, J., Fu, X. G., Li, Z. X. (2010). Formation and significance of the oil shales from the north Qiangtang Basin. Sedimentary Geology and Tethyan Geology 30 (3): 11-17.

Wang, P., Du, Y., Yu, W., Algeo, T. J., Zhou, Q., Xu, Y., Qi, L., Yuan, L., Pan, W. (2020). The chemical index of alteration (CIA) as a proxy for climate change during glacial-interglacial transitions in Earth history. Earth Science Review 201, 103032.

Wignall, P.B., Twitchett, R.J. (1996). Oceanic anoxia and the end Permian mass extinction. Science 272: 1155-1158.

Wilson, J.L. (1975). Carbonate Facies in Geologic History. Springer, Berlin 471 p.

Wu, C., Tuo, J., Zhang, M., Liu, Y., Xing, L., Gong, J., Qiu, J. (2017). Multiple controlling factors of lower Palaeozoic organic-rich marine shales in the Sichuan Basin, China: Evidence from minerals and trace elements. Energy Exploration and Exploitation 35 (5): 627-644.

Zaghloul, M.N., Critelli, S., Perri, F., Mongelli, G., Perrons, V., Sonnino, M., Tuker, M., Aiello, M., Ventimiglia, C. (2010). Depositional systems, composition, and geochemistry of Triassic rifted-continental margin redbeds of the Internal Rif Chain", Morocco. Sedimentology 57: 312-350.

Zeng, S. Q., Wang, J., Fu, X. G., Chen, W. B., Feng, X. L., Wang, D, Wang, Z. W. (2015). Geochemical characteristics, redox conditions, and organic matter accumulation of marine oil shale from the Changliang Mountain area, northern Tibet, China. Marine and Petroleum Geology 64: 203–221. https://doi.org/10.1016/j.marpetgeo.2015.02.031

Zhen, Z., Li, W., Xu, L., Wang, C., Zhao, L. (2020). Characteristics of palaeosalinity and palaeoredox records in sediment from Dali Lake: Climate change in North China from 0 to 2100 cal BP. Quaternary Geochronology 60, 101104.

Zimmermann, U., Spalletti, L.A. (2009). Provenance of the lower Paleozoic Balcarce formation (Tandilia system, Buenos Aires Province, Argentina): implications for paleogeograpic reconstructions of SW Gondwana. Sedimentary Geology 219 (1–4): 7-23.

JJEES

JJEES (2023) 14 (1): 64-69
ISSN 1995-6681

Jordan Journal of Earth and Environmental Sciences

2D Seismic Stratigraphic Analysis of Harthaand Kifl Formations in Balad Area– Center of Iraq

Ali M. Abed[1], Jassim M. Al-Halboosi[2], Amer S. Al-Jibouri[1*], Salam O. Al-Hetty[1]

[1]Department of Applied Geology, College of Science, University of Anbar, Ramadi, Iraq
[2]Department of Geology, College of Science, University of Baghdad, Baghdad, Iraq

Received 2nd February 2022; Accepted 22nd June 2022

Abstract

An interpretive study of the two-dimensional seismic data of the Balad area was carried out. The study area is important due to its location within the oil field zone and still without exploration wells. A synthetic seismogram with good matching with the seismic section was done, to ensure the identification of reflectors and reflectivity type: peak or trough following each one through the whole area. Top Al-Hartha and Al-Kifil formation reflectors were picked using the composite line to link the seismic sections with each other after enhancing the tie between seismic lines. Time and depth maps were made using velocity maps created from the velocity model. The seismic interpretation showed the existence of certain stratigraphic features in the studied reflector. Some distribution grabens in the study area are continuous in more two-dimensional seismic lines. By calculating the difference in depth values between the Al-Hartha and Al-Kifl formations, an isopach map of the Al-Haritha Formation was obtained. The minimum thickness of the Hartha formation is approximately 250 m in the center, While the highest thickness of the formation was 650 m in the southwest of the study area. These activity elements provide a reasonable explanation for the distribution of hydrocarbons in the area of study.

Keywords: *Seismic stratigraphy, Hydrocarbon indicators, Al-Kifl Formation, Seismic reflection.*

1. Introduction

Stratigraphical interpretations of seismic data require clarification of the seismic sections and give them the geological marker of the component of the earth's content within the known geological basis and principles, including good information and the expected geological changes in the area. Seismic Stratigraphy is divided into seismic-sequence (facies) analysis and reflection-character analysis. It determines the nature of sedimentary rocks and their fluid content from the analysis of seismic data.

In seismic-sequence analysis, the first step is to separate seismic-sequence units, which are also called seismic-facies units (Lessenger, 1988). From seismic sections processing and identifying the sedimentation situations in the region and the available petrophysical studies, we can pick up the seismic reflectors as well as the characteristics of rocks and fluids in general (Haq et al., 1987). For the first time, an interpretation was attempted in terms of seismic stratigraphy (not yet formalized at the time) by examining the lateral and vertical variations of the reflections and units consisting of several reflections in a homogeneous sequence (Ravenne, 2002). The geophysical studies history regarding hydrocarbon accumulations began in the last century when the seismic reflection method was used to detect the accumulations of hydrocarbons (Berg, 1982).

The seismic method can be looked the most important geophysical technique in cost and number of geophysicists obligated. The spread of This method compared with other geophysical methods is due to many factors such as the accuracy results, great resolution, high penetration, and considered as an over wide used in petroleum exploration (Hart, 2004).

Several authors have studied seismic attributes derived from seismic data that can be used in seismic-stratigraphic interpretation [Taner et al. 1979; Marfurt, 2005; Ali and Kadhim, 2019; Nassir et al. 2021; Ali et al. 2021].

Numerous studies have been focusing on the Cretaceous succession in Iraq because it is the largest productive reservoir which contains about 80% of Iraq's oil reserves. One of the most important carbonate reservoirs in the southeast of Iraq is the Zubair Formation which contains oil in structures of more nearest oilfields (Khorshid and Kadhim, 2015)

Albeyati et al., 2021interpreted the 3D seismic reflection data for the Kifl oil field to detect the Zubair Formation and how the oil is trapped in it. Fadhil (2010) analyzed the 3D seismic reflection data for the Kifl oil field to delineate the seismic stratigraphy of the Lower Cretaceous Formations. In the study area and the regions to its east, a seismic reflection survey was conducted by the Iraqi Petroleum Exploration Company several times during the years 1979-1984.

Abdul-Rahman, 1997 studied some of the seismic sections of the southern Hamrin region, preparing depth maps for each of the Fatha, Injana, and Al-Juraibiformations.In 1990, a reinterpretation of previous seismic data was carried out, and the Balad structure at the intra-Hartha reflector is an anticline (faulted traps) located southeast of the study area where the Ba-2, 5, 6, and 7 wells were drilled. Also, two small closures

* Corresponding author e-mail: sc.aalgibouri@uoanbar.edu.iq

(faulted traps) located northwest of an Anticline, separated by two saddles where Ba-3well was drilled in the second saddles. The presence of the main graben consists of small structural faulted traps on both sides of the graben, where the Ba-1, 4, and 8 wells were drilled (figure 1-13). All these structural features extend in the NW-SE trend.

The current study aims to build the seismic depositional models of the Hartha and Kifl Formations in the Balad area. Reflection patterns and reflection amplitudes are interpreted to determine bed thicknesses and depositional environment.

2. Materials and methods

2.1. Description of site and stratigraphy

Based on the geological map of Iraq issued by the General Organization for Geological Survey and Mining in 1990, the study area is flat land with some simple elevations ranging from (48-58 m)and increases in height towards the northeast. This area is characterized by agriculture, many orchards, irrigation projects, marshes, and swamps, as well as the presence of residential areas, and civil and military facilities. Recent and Pleistocene sediments represented by alluvial deposits and river terraces covered all the studied areas as shown in Figure (1). The rocks of these formations generally consist of muddy muddy deposits with sand and gravel (Abdul-Rhaman, 1997). Balad field is one of the Iraqi oil fields where 9 oil wells were drilled according to two-dimensional seismic surveys. Figure (2) shows the generalized stratigraphic column of the Balad oil field and adjacent area (JAPEX Company, 2006). In general, the formations of Pliocene to late Jurassic are characterized by increased thickness towards the east of the region and the Mesopotamia foredeep, while the thickness of older formations (late Jurassic to the early Triassic) is decreasing towards the northwest part of the region.

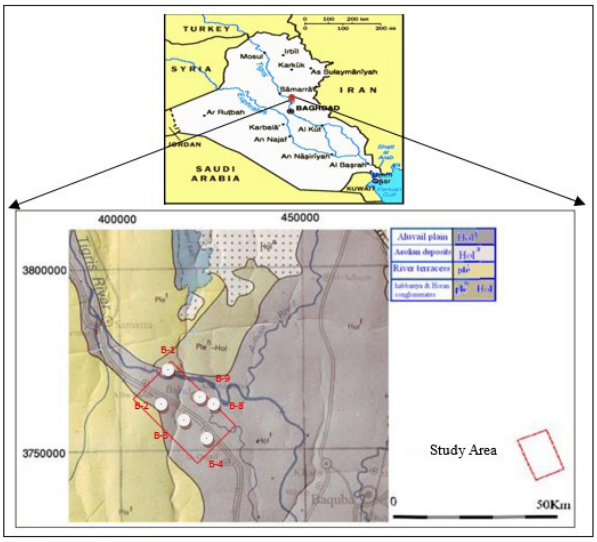

Figure 1. Surface geology map of the study area and surroundings, after (the State Establishment of Geological Survey and mining)

Structurally Balad field is divided into two sectors: • The first sector is located within the major graben area, which includes the wells Ba-1, 3, 4, and 8. • The second sector is located outside the major graben area (east shoulder, which includes the wells Ba-2, 5, 6, 7 and 9.

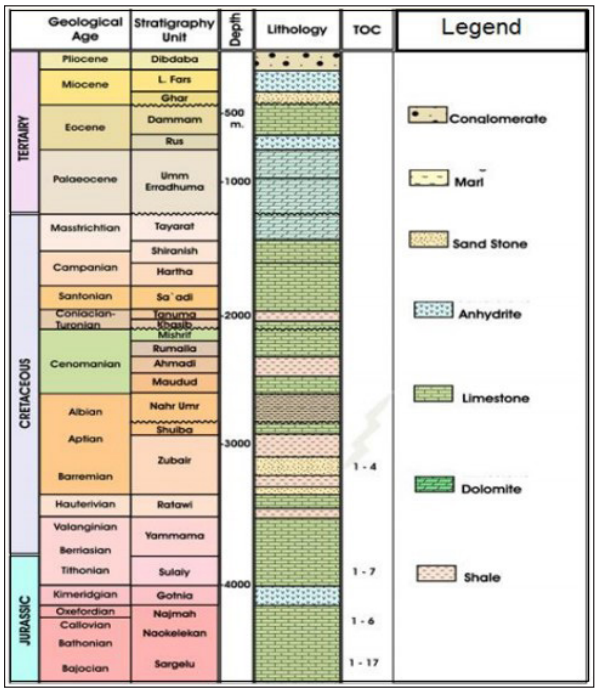

Figure 2. Generalized stratigraphic column in Balad and adjacent area, after (JAPEX Company, 2006).

2.2. Processing of seismic data

The selection of field techniques before implementing the seismic reflection surveys leads to improved field recordings, in other words, to improve the signal-to-noise ratio. These options which are decided by the geophysicist contribute to determining the number of controls including the length of the seismic trace, the fold of coverage, the distance between the traces, and others. It is worth noting that the study area is within the survey areas of Baquba– Samarra (BS) and west of Tikrit–Makhoul (WTM). The main objective of processing seismic information is to convert the recorded seismic information into a picture that greatly facilitates the process of geological interpretation. A large number of researchers have addressed the processing steps [Telford, et al. 1970; Dobrin, 1976; McQuillin, et al. 1984; Yilmaz,1987; Al-Sadi, 2017].

Several processing steps were applied to the seismic sections studied in the present paper, these steps are True Amplitude Recovery (TAR), Common Depth Point gathering (CDP Gather), Data Editing, Time-Variant De-convolution (TVD), Time-Variant Scaling (TVS), Static Correction, Velocity Analyses, Normal-Move-Out (NMO) Correction, Mute, CDP Stack and Time-Variant-Filtering (TVF). Additional processing was done for each seismic section namely, Residual Static Correction, Coherence, Migration in tilted areas, Wavelet Process, and 3D-Processing.

3. Results and Discussions

3.1.Two-Way-Time (2To) maps

Quantity two reflectors were picked in this study which represent the Upper Cretaceous age and they are:

- the First reflector represents the top Hartha Formation.
- the Second reflector represents the top Kifl Formation.

Hartha was picked to understand the type of faults and their effect on Balad field construction to get the final structural and geological models image of traps in the Balad field. The continuity of the picked reflector can be described as top of Hartha reflector has moderate continuity and Kifl reflector has good continuity. Seismic sections show the concordance of reflectors to be good, especially at the Tertiary Formations. While at the Upper Cretaceous Formations, the seismic sections with geophysical and geological models show that there is a variation of reflector thicknesses, especially in the graben areas, this is due to the presence of the structuralandstratigraphicfeatures.

The TWT maps can be described as a major graben area (faulted syncline) over the area and have variable widths (4-4.5km) in the southern part and the east and west shoulders of the major graben. The major graben and its shoulders are separated to the north and south parts by a Strike-Slip fault-dominated E-W trend. Thus, the study area is divided into the following regions: • The north and south graben areas (faulted Synclines) dominated with NW – SE trend. This area contains small secondary normal faults formed by elongated narrow traps at the right side of the major graben area.

The east shoulder of the major graben is divided into two parts (south and north). The south part is a faulted nose confined by the south major graben fault, which represents the Balad field trap. The north part is a horst area confined by north major graben and other local graben faults. The time maps show that the Balad field trap and the horst have one axis dominated by NW – SE trend and shifted by the strike-slip fault. The west shoulder of the major graben represents an open nose dominated by the NW – SE trend and located in the northwest part of the area. Figures (3 and 4) represent the TWT maps with contour intervals (10ms) for the studied reflectors.

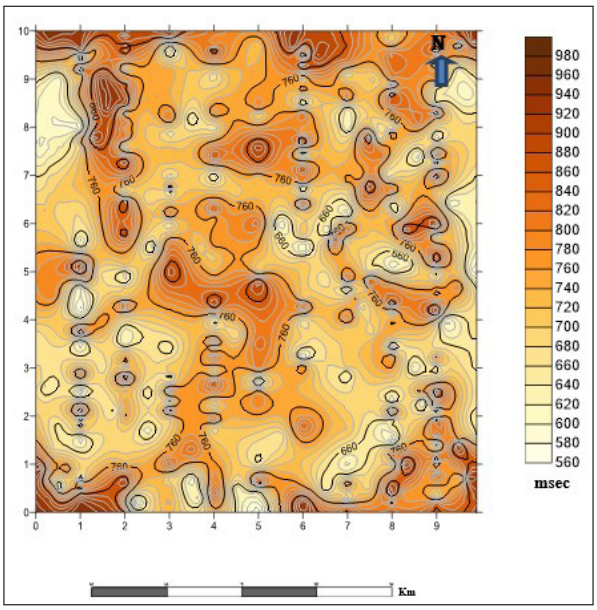

Figure 3. Two way time map of top Hartha Formation.

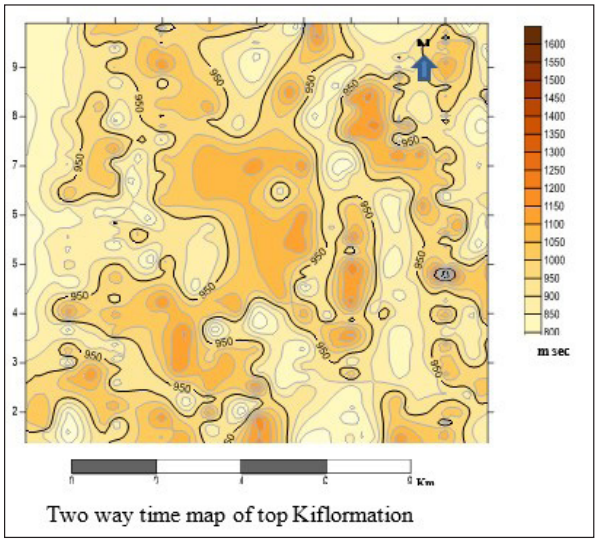

Figure 4. Two-way time map of the top Kifl Formation.

3.2. Velocity maps

The average velocity is the suitable velocity that is used to convert the TWT maps to depth maps. It is considered the more accurate velocity type used in seismic methods and can be computed directly from a good velocity survey (check shot) (McQuilline, et, al 1984). In the study area, there are 6 wells (Ba-1, 2, 3, 4, 8, and 9) with average velocity values from check shot logs which are used, but (Bd-5, 6, and 7) wells don't have check shot logs, therefore, the TWT time values at well locations and depth values from good markers are used to obtain average velocity values of the studied reflectors; but it's not enough velocity values to cover all the study area. Thus, the stack velocity values provided by the processing department and printed on 2D seismic paper sections were used.

First, the average velocity maps are drawn from the good data for all studied reflectors. Stack velocity values were computed along with the studied reflectors from the velocity boxes. The average values of the velocity of each neighbor's group of stack velocities values were taken. Thus, the stack velocity maps were drawn and smoothed to all studied reflectors, because the stack velocity has values more than the average velocity values, the differences in velocity values between them were calculated and removed from the stack velocities map to get the final velocity maps for studied reflectors in the studied area.

This method offers a good distribution of velocity points in the study area. The velocity maps of studied reflectors show the following: •The top Hartha velocity values increase in the south and there is local closure in the middle of the area representing an increase in velocity values. The magnitude of velocity values ranges in the top Hartha velocity map from (2680 to 2920 m/sec) (figure5). • The top kifl velocity values increase in the south and there is local closure in the middle of the area representing an increase in velocity values. The range velocity values range in Kifl velocity map from (2800-3040 m/sec) (figure 6).

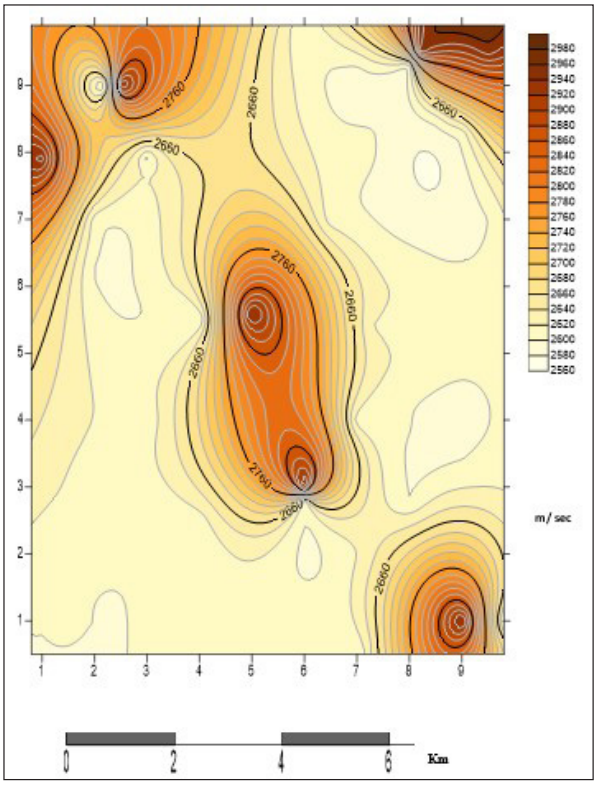

Figure 5. Average velocity map of top Hartha Formation.

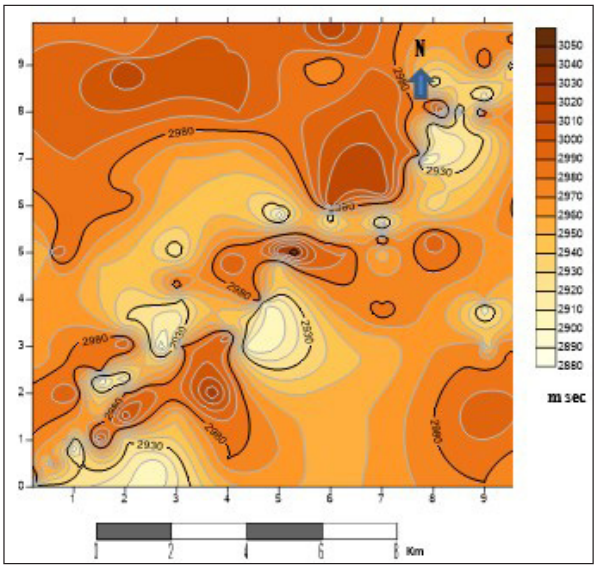

Figure 6. Average velocity map of top Kifl Formation.

3.3. Depth maps

In seismic methods, the depth map is established by using the time map of a given reflector with its velocity map, as follows:

Depth at any point = (velocity × time) at this point.

In the seismic reflection method, a map of the top of a geologic formation reflects the geologic image below the surface. Thus, the depth maps also show the same picture of the studied formations, but the difference lies in the closures dimensions, number of contour intervals between these maps, faults displacements, and difference in the number of minor faults located in major graben areas. The structural picture can be described as a major graben area (faulted syncline) along the study area with the east and west shoulders of major graben.

The major graben has variable dimensions (4-4.5km) in width, large displacements of about 400m, large throw of about 300m, and heave of about 265m in the left side of the south graben at the top Kifl Formation. Figures (7), and (8) represent the depth maps with contour intervals (10m) for studied formations.

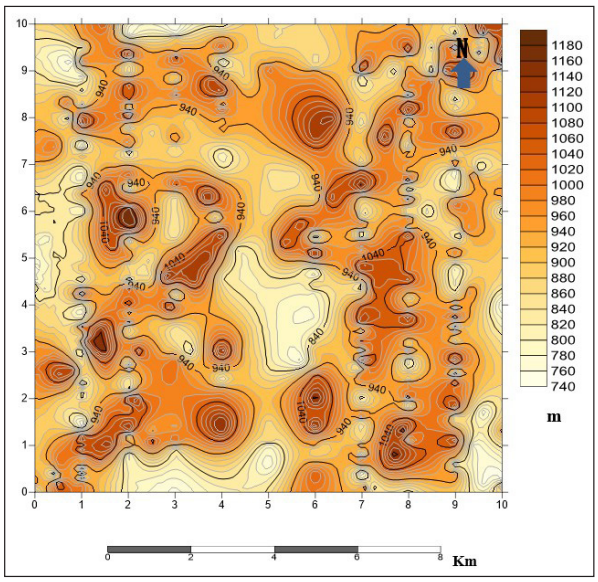

Figure 7. Depth map of top Hartha Formation.

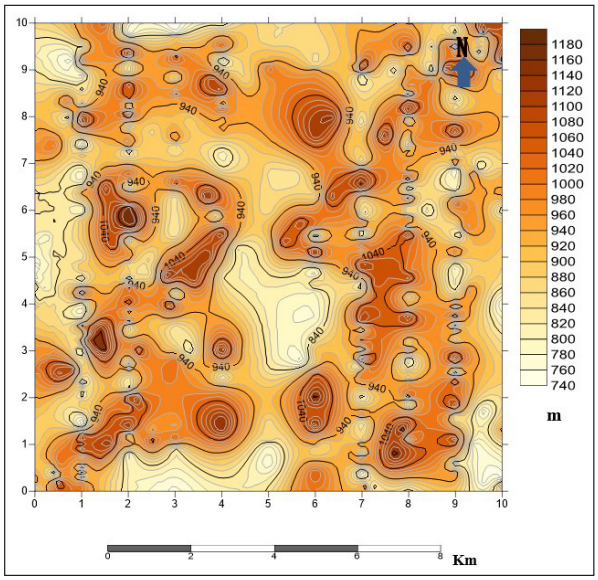

Figure 8. Depth map of top kifl Formation.

3.4.Isopach map

By calculating the difference in depth values between the Al-Haritha and Al-Kifl formations, an isopach map of the Al-Haritha Formation was obtained (Fig. 8).

The minimum thickness of the Hartha formation is approximately 250 m in the center, While the highest thickness was 650 m in the southwest of the study area. The average thickness value of the formation is approximately 450 m for most of the study area.

When a comparison is made between the depth map of the Hartha Formation and the isopach map of the formation, it becomes clear that the depression in the depth map is accepted by the lowest thickness values. the depth of the formation in

the center of the map has the lowest values of about 250 m, while the depth values for the same area range from 990 m to 1040 m. Since this formation represents a reservoir, we expect that the presence of oil in the northern, southern, and western sections will be more quantitative compared to the central and eastern settlements of the study area. This is based on the heterogeneity of formation thickness values between the different parts of the area. This is based on the heterogeneity of formation thickness values between different parts of the region. On this basis, the southwestern part can be considered more abundant for oil, as the formation thickness reaches more than 650 m.

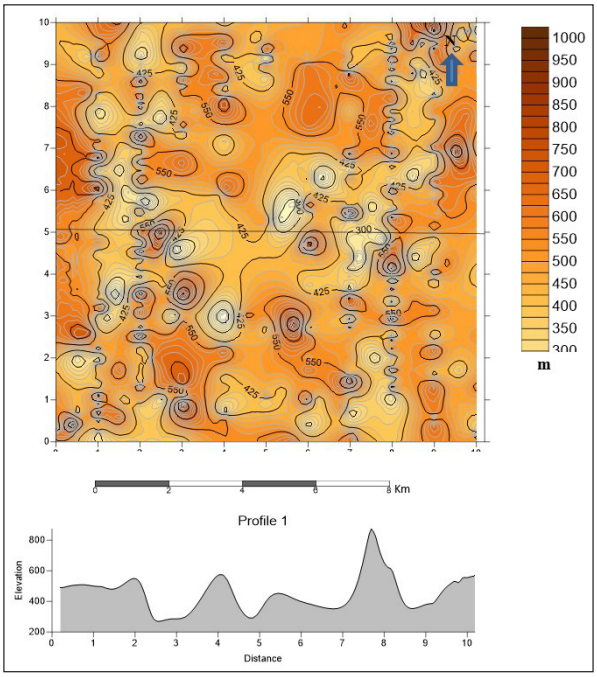

Figure 9. Isopach map of Hartha Formation.

4. Conclusions

The time and depth maps show many nose structures located at NW and SW the studied reflectors bearing E-W, NE-SW, SE-NW with a general slope towards the southeast. These monoclonal structures are a result of the compressional tectonic phase in the Middle Cretaceous-Tertiary time. This is because of the convergence between Arabian Plate (AP) and adjacent plates; however; subduction of AP beneath the Eurasian plate event has occurred. Velocity maps show an irregular increase in depth due to the inhomogeneity of the sedimentary layers as a result of different facies and depositional environments.

The study area was affected by three faults, and only one of them, which is a normal fault with a small offset reached the studied reflectors. Its trend (NW-SE) was shown to be parallel to the collision stretching between the Arab and Iranian plates, which formed due to tension stresses maybe belongs to either the Najd fault system (Precambrian faults) or Abo-jir fault which is located to the west of the studied area .This is because of the convergence between Arabian Plate (AP) and adjacent plates; however, subduction of AP beneath the Eurasian plate event has occurred. Velocity maps show an irregular increase in depth due to the inhomogeneity of the sedimentary layers as a result of different facies and depositional environments.

As further future work the following recommendations are important:

Re-interpretation of the northwest and southwest part of the studied area, and outside the studied area by using available 3D seismic data. Structurally, the area is considered a promising hydrocarbon area; therefore, re-interpretation gives more details about apparent structural phenomena which are maybe closed outside the studied area to the northwest and define faults systems more precisely.

3D interpretation of seismic data to obtain high-resolution power for recognition of a stratigraphic feature on the time sections and attributes section.

References

Albeyati1, F.M., Abdula, R. A., Othman, R.S. (2021) Organic geochemistry of the Middle to Upper Jurassic source rocks succession in Balad-1 Well, Balad Oil Field, Central Iraq. Bulletin of the Geological Society of Malaysia 71:125–138

Abdul-Rahman, A. (1997). Estimation geological study of the Hartha, Sadi and Khasib reservoirs in the Balad Field, (O.E.C. doc.). 89 p.

Ali, K. K., and Kadhim, F. G. (2019). 3D seismic attributes interpretation of Zubair Formation in AlAkhadeir area, southwestern Karbala, Iraqi Journal of Science 56 (4C):3613-3524.

Ali, K. K., Wanas A. A., Mahdi M. E. (2021). Application of Velocity Analysis Picking for 2D Seismic Data Processing in West An-Najaf Area. Iraqi Journal of Science 62(2): 555-564

Al-Sadi, H. N. (2017). Seismic hydrocarbon exploration: 2D and 3D Techniques, springer international publishing, Switzerland. 331 P.

Berg, O. (1982). Seismic Detection and Evaluation of Detta and Turbidite sequences: Their Application to exploration for The Subtle trap, American Association of Petroleum Geologists 66 (9):1271-1288.

Dobrin, M. (1976). Introduction to Geophysical Prospecting, 3rd ed., McGraw Hill. Into., International Student Edition. 386 p.

Fadhil, M. (2010). Seismic Reflection Study of Lower Cretaceous Rocks in Kifl Oil Field, Iraq, Thesis of Master of Science in Geophysics, Geology Department, Baghdad University. 142 p.

Haq, B. U., Hardenbol, J., Vail, P.R. (1987). Chronology of fluctuating sea levels since the Triassic. Science 235: 1156-66.

Hart, B. S. (2004). Principle of 2D and 3D seismic interpretation, McGill University. 443p.

JAPEX Company. (2006). Japan Petroleum Exploration, The G & G Study of the East Baghdad Field, Central Iraq, O.E.C. documents. 560 p.

Khorshid, S. Z. and Kadhm, A.D. (2015). Subsurface Investigation of Oligocene Geologic Formations Age, East Baghdad Oil Field.Iraqi Journal of Science 56(4C): 3441-3451.

Lessenger, A. (1988). Seismic stratigraphy. Annual Review of Earth and Planetary Sciences, 16: 319-15

Marfurt, K. J. (2005). Robust estimates of 3D reflector dip and azimuth. Geophysics71(4): 29-40

McQuillin, r., Bacon, M., Barclay, W. (1984). An Introduction to Seismic Interpretation, Graham and Trotman. 287 p.

Nassir N. A., AL- Banna, A. S., Al-Sharaa, G. H. (2021). The Use of Seismic Reflection Data Inversion Technique to Evaluate the Petro- Physical Properties of NahrUmr Formation at Kuwait and Dujaila Oil Fields – Southern Iraq. Iraqi Journal of Science 62 (2): 565-577

Ravenne, Ch. (2002). Stratigraphy and Oil. Oil E & Gas Science

and Technology-Review IFP. 57(3): 211-250

Taner, M.T., Kohler, F., Sheriff, R.E. (1979). Complex trace analysis, Geophysics, 44(6): 1041-1063.

Telford, W.M., Geldart, L.P., Sheriff, R.E., Keys, D.A. (1970). Applied Geophysics, Cambridge University Press 860 p.

Yilmaz, O. (1987). Seismic data processing, SEG series: Investigation Geophysics V.2, 526 p.

JJEES

JJEES (2023) 14 (1): 70-74
ISSN 1995-6681

Jordan Journal of Earth and Environmental Sciences

Chemical Effect on Soil Strength by adding Lime and Natural Pozzolana

Dr. Maiasa Mlhem

Geotechnical Engineering Department – Civil engineering College – Damascus University

Received 31th January 2022; Accepted 24th June 2022

Abstract

Mostly, clay soil is a common problem encountered by civil engineers on site, because of its complicated structure and different geotechnical properties. Therefore, it was necessary to find useful and applicable solutions to solve problems that may be found upon designing and constructing. One of the most widespread solutions for soil improvement is soil stabilization by different types of additives, which achieves high efficiency and economical results. Many additives were used, including cement, lime, silica, fly ash, and others. A lot of natural resources of lime and pozzolana exist in Syria, however, it needs investment plans, and due to the lack of studies that discuss using these additives under foundations and then detecting the changing of bearing capacity of the soil. In this research, experimental and analytical methods are followed by conducting loading experiments on a foundation model located on clay soil, after adding lime to clay soil with percentage 2% up to 8%, which cause a decrease in the water content and increases the strength of soil where the maximum was at 4% lime. Then 10% up to 30% of natural pozzolana were added alongside 4% of lime, which caused decreasing in both the water content and the strength.

Keywords: *Lime, Pozzolana, Additive, Soil improvement.*

1. Introduction

The soil under different construction, such as roads, residential and industrial buildings, irrigation facilities, and airports; may not satisfy the engineering requirements. So, engineers always try to modify the engineering design such as: increasing the thickness of the pavement layers or increasing the dimensions of the footing, or changing the type of footing from shallow to deep, and this causes a significant increase in the cost of the structure as a whole. Recently, engineers and researchers concentrate on finding new methods to improve the soil properties and approaching the standards values which minimize the cost of any other modifying. Therefore, soil stabilization science and its applications have attractive research and studies. It provides economic solutions for many soil problems. There are the main group of improving methods: mechanical methods (soil reinforcement and soil mixing), and chemical (soil injection with chemical additives: cement, lime, fly ash, silicates, and polymers). Using lime and natural pozzolana as additives were main concept for many types of research since natural pozzolans used in normal proportions typically improve concrete performance and durability [Ekolu, et al., 2006], however, a few of research investigates the changing of soil properties by using both lime and pozzolana under loads. Moreover, the availability of natural lime and pozzolana in Syria encourages searching and detecting the effect of these additives on soil under foundations.

[Tran, et al., 2014] investigated the effects of lime treatment on the microstructure and hydraulic conductivity of compacted expansive clays that result in increasing hydraulic conductivity in lime-treated soil. [Abbasi & Mahdieh, 2018] studied Adding lime or pozzolan or both of them to a silty sand soil causes an increase in optimum moisture content and a decrease in the maximum dry density.

[Khan, et al., 2020] studied different types of stabilizers to improve the strength of soil, and [Harichane, et al., 2011] and [Harichane, et al., 2017] studied adding lime (0-4-8)% and pozzolana (0-10-20)% on two types of clay soils, they found that pozzolana enhances the effect of lime on decreasing the plasticity index the classification of soil change from CH to MH for both types. [Haas & Ritter, 2018] clarified in their research the effect of time on the degree of reaction of quicklime and hence the increase of compressive strength. [Alrubaye, et al., 2016] studied kaolin clay and mixed (3-5-7-9)% lime and 4% silica dust. the result was a decrease in the maximum density and an increase in shear strength and internal friction angle. [Türköz, et al., 2018] concentrated on silica dust (1-3-5-10-15-20) % and lime (3%) and found decreasing in the plasticity Index of a clay soil from Turkey and an increase in maximum dry density. [Kalyane & Patil, 2020] tried to stabilize black cotton soil from India by using lime (5%) and fly ash (5-10-15)%, which reach to increasing plasticity limit and unconfined strength and decreasing in maximum dry density. Many types of research expressed the increasing of bearing capacity with a module (BCR) bearing capacity ratio which expresses the proportion between bearing capacity after improvement and virgin bearing capacity (before improvement or stabilization). All researchers used a laboratory model to define this ratio. [Maharaj, et al., 2019] studied the bearing capacity ratio of soil after reinforcement with geotextile, and concluded that the maximal increase in ultimate bearing capacity is ascertained by placing the reinforcement at a depth of half the width of footing (B). [Keskin & Laman, 2012] investigated the bearing capacity of a strip footing resting on sand slopes, and found that the bearing capacity of strip footing on a sand slope is significantly

* Corresponding author e-mail: rooyagroupsy@gmail.com

dependent on the slope angle, and increases with an increase in the relative density of sand. In other research, [Gabr, et al. 1998] studied the stress distribution for reinforcement soil under square footing (0.33m*0.33m) loaded in a metal box (1.37m*1.52m*1.52m). [Tsukada, et al., 2006] used circle footing with a diameter (of 40mm) on reinforcement soil and studied BCR for spread footing. [Hwang, et al., 2016] researched the effect of Micropile on increasing the bearing capacity of the soil. Therefore, the goal of this research was to study the effect of lime and natural pozzolana on soil strength. The research was done experimentally in a physical laboratory model.

2. Materials & Methods:

2.1 Materials:

The soil in the area of Dara'a (locating in the south of Syria) causes many problems under foundations for different types of buildings where most researchers suggested that the reason is due to its high plasticity. Therefore, according to the previous papers and research, this paper focuses on detecting the changing in the soil properties after adding two types of available additives lime and natural pozzolana in Syria. Limestone quarry spread in different locations in Syria and the expected geological reserve is $8*10^9$ m^3, just the investment quantity is approximately $200*10^6$ m^3 [General Establishment]. In addition, Pozzolana spreads in the south area, east-south area, and east-north area in Syria, the expected geological reserve is $600*10^6$ m^3 [14].

2.2 Methods:

2.2.1 Soil Samples Tests:

Basically, all soil samples have been tested in the soil mechanics laboratory to be classified and specified. Fig.1 illustrates the grain size distribution of soil samples according to ASTM D6913 and D7928. Fig. 2 presents the proctor tests results to define the maximum dry density according to ASTM D698, and fig.3 shows the unconfined compressive strength (UCS) results for these types of samples. In addition, Atterberg limits have been determined as clarified in Table 1.

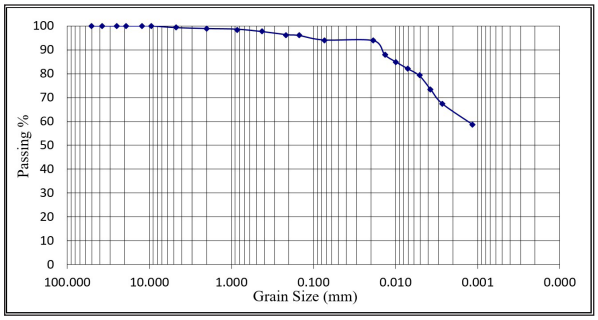

Figure 1. Grain Distribution.

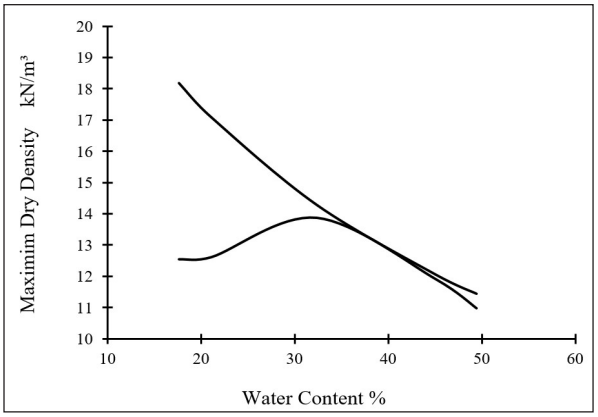

Figure 2. Compaction Test.

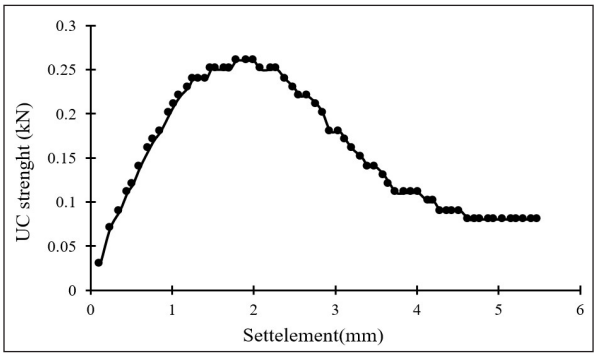

Figure 3. Unconfined Compressive Strength.

Table 1. Physical properties of clay soil

Test	ASTM code	Result
Moisture (water content)	D 2216	10%
Specific Gravity (Gs)	D 854	2.753
Grain Size Distribution: Sieve Hydrometer	 D 6913 D 7928	Gravel (0.73) %, Sand (5.17)%, Silt (29.50)%, Clay (64.60)%
Atterberg Limits	D 4318	LL=74.09%, PL=38.10%, Class - CH
Compaction Test	D 698	Fig.2
Unconfined Compressive Strength	D 2166	Fig.3

2.2.2 Additive Tests:

Then, both additive lime and natural pozzaolana have testes chemically. The lime additive contains 90.2% (CaO). Blaine fineness test according to (ASM-C204) shows fineness (4500±100) cm^2/gr of natural pozzolana that was used in this research. Syrian standards (1998/1887) recommend that active silica should not be less than 25% in pozzolana to assure the activity of pozzolana as an additive. Chemical analysis for pozzolana is as follows in table2:

Table 2. Chemical Analysis of Pozzolana.

Oxide	SO_3	K_2O	MgO	CaO	Fe_2O_3	Al_2O_3	SiO_2 (active)	SiO_2 (all)
%	0.32	7.47	8.02	8.29	16.04	12.57	44.31	47.29

2.2.3 Laboratory Model:

The laboratory model is a plexiglass box with dimensions (30cm*35cm*50cm). It was filled with soil and the model of footing is a metal plate, its dimensions: (30cm*8cm). The settlement gauge was placed at the top of the plate as shown in fig. 4. The loading device was a hydraulic press with a velocity of 0.5mm/sec and the maximum settlement was calculated as 20% of the footing width (for our case = 16mm) [Das, 2011].

Figure 4. Laboratory Model.

2.2.4 Laboratory Methodology:

- Prepare the laboratory model.
- Adding lime with a percentage **of 2%-4%-6%-8%** then find the best additive percentage of lime.
- Adding Pozzolana with percentages **10%-20%-30%** with the optimum percentage of lime and applying load tests until failure.
- Choose the best mixing percentage.

2.2.5 Loading Test Procedures:

The samples were disturbed, so an approximate unit weight and water content were determined: γ=15kN/m^3, w=40%. Big Samples were crushed and then water was added to the soil sample and kept it 24 hours. Then, quick lime was crushed and sieved on sieve No. 40. When samples get their water content, the lime, and pozzolana are added to the sample and mixed for not less than half an hour until reached homogenous, then forming the soil layers inside the box and leaving the soil for 24 hours to be as homogenous as much, and then begin with loading steps. After finalizing the loading, the box is emptied, and repeat the steps to do a new experiment are. In each experiment, 80kg of soil was used, and 22kg of water to reach the required water content, in addition to lime and pozzolana after grinding. The loading process could be divided into three main stages:

1) Virgin soil without any additions:

After the loading test the maximum load for settlement 20% of footing width, was Q=4.8kN.

2) Soil with Lime:

Lime was added to the soil with percentages (of 2%, 4%, 6%, and 8%). Fig. 5 shows the results of loading where the maximum load for 2% lime additive was 8.45kN, for 4% lime additive was 13.5kN, for 6% lime additive was 12.4kN and for 8% lime additive was 11kN.

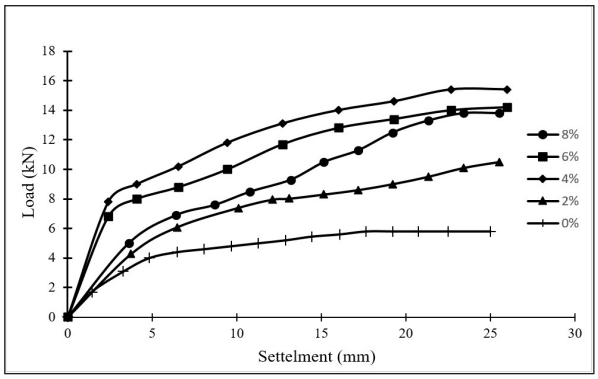

Figure 5. Loading Test Curves for stabilized samples with lime additives.

To study the effect of lime additives, it is obvious that maximum load increase by increasing lime additives until 4% then begin to decrease as shown in fig. 6.

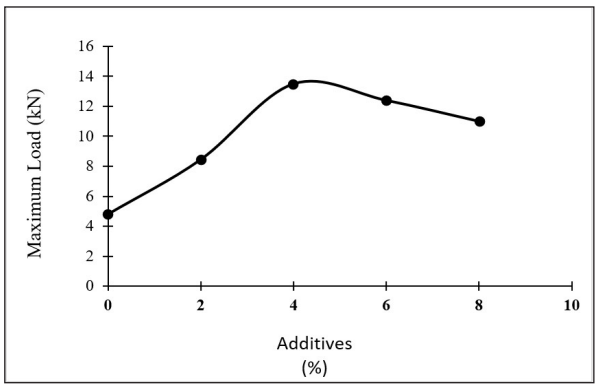

Figure 6. Maximum Load vs Lime additive percentages.

Moreover, fig. illustrates the relation between water content and lime additives. Lime additives cause decreasing in water content.

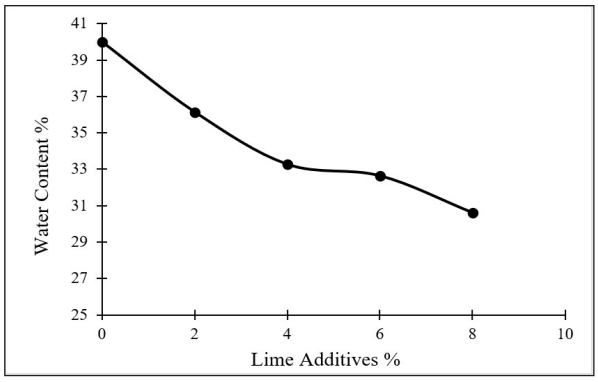

Figure 7. Water Content vs additive percentages.

Fig. 8 shows the results of the unconfined compressive strength (UCS) test and it is clear that the best additive ratio is 4%, which increases the strength of the sample significantly. It is the same trend in fig. 9, which presents the stress-strain behavior.

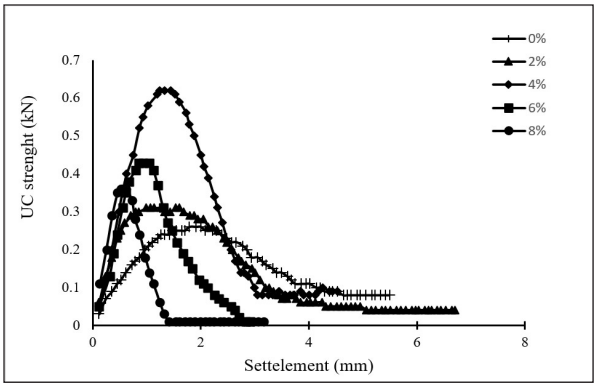

Figure 8. Unconfined Compression Strength.

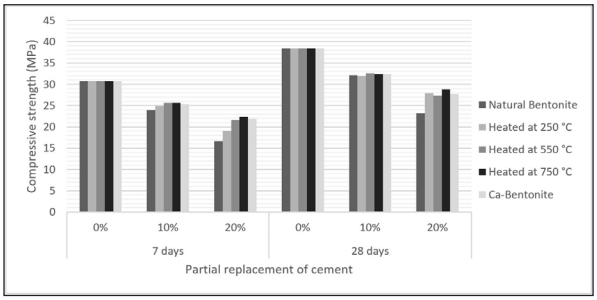

Figure 9. Stress-Strain Curves.

2) Soil with Lime & Pozzolana:

After we define the optimum ratio for lime additive as 4%, we fixed this ratio and begin to add pozzolana with a percentage of 10%-20%-30% to explore the effect of lime and pozzolana together in changing the soil properties. Fig. 10 shows the loading results and Fig.11 shows the effect of pozzolana additives on the water content in a soil sample. Moreover, Fig. 12 shows the results of the UCS test where adding pozzolana caused decreasing in UCS compared with a mixture of soil and lime only. We notice the same trend in Fig. 13, which present the stress-strain behavior.

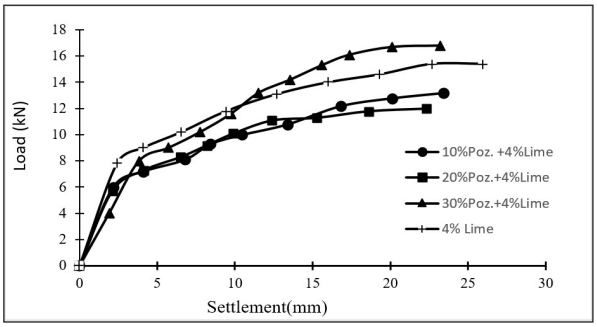

Figure 10. Loading Test Curves.

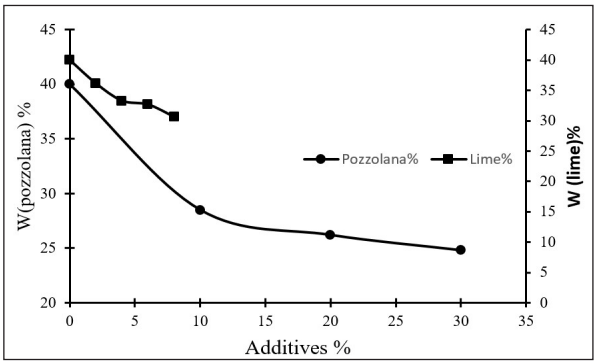

Figure 11. Water Content vs. Additives Percentages.

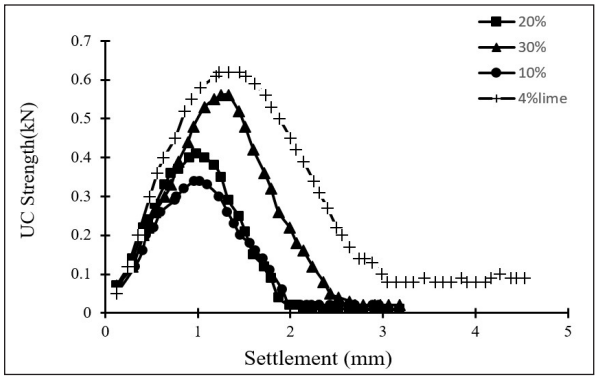

Figure 12. Unconfined Compression Strength.

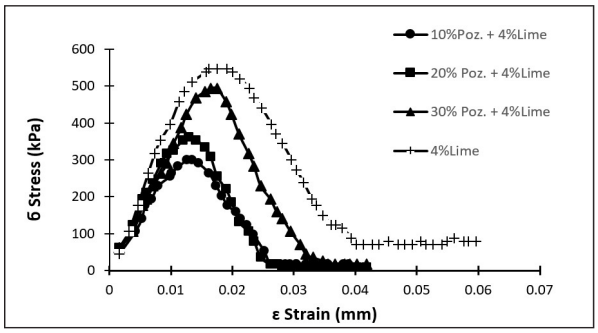

Figure 13. Stress–Strain Curves.

3. Discussion:

According to the results as shown in Fig. 8, we notice that UCS tests for soil samples after mixing with different ratios of lime match the load test results (Fig.5) and together give that the best ratio of additives is 4%. Moreover, Fig.9 presents, at the same strain percentage that the maximum value of stress increase from 220kPa up to 546kPa when the lime additive is 0% and 4% respectively, which confirms the great effect of lime on increasing the strength of the soil. Upon using natural pozzolana it is obvious from Fig.10 to Fig. 13 a decrease in the strength of soil samples compared to the strength value for soil samples without pozzolana and with lime additives only. Table 3 clarifies the differences in maximum loads according to pozzolana percentages. pozzolana may replace soil particles and works with lime to improve the soil in case the pozzolana additive percentage is more than 30%. We could explain this by the lime reaction.

Table 3. Maximum loads after adding Pozzolana

Maximum Load (kN)	Soil with Additives
4.8	Virgin Soil
13.5	Soil+4% Lime
11.7	Soil+4% Lime+10%Pozzolana
11.8	Soil+4% Lime+20%Pozzolana
14.3	Soil+4% Lime+30%Pozzolana

3.1 Lime reaction:

Calcium Oxide reacts with existing water in the voids of soil and release heat during and after the reaction so the water content of the soil decreases as shown in Fig. 11. The reaction occurs according to the following equation:

$$CaO + H_2O \rightarrow Ca(OH)_2 + Heat$$

The previous reaction could continue for many years and create a chemical bond between soil particles as cement bonds that result from cement hydration. Calcium additives

increase soil pH, which causes dissolution of soil components (silicates and alumina), after the dissolution, silicates, and alumina react with calcium and result hydrate calcium alumina CAH and hydrate calcium silicate CSH according to following equations:

$$2\ Ca_3SiO_5 + 7\ H_2O \rightarrow 3\ CaO \cdot 2\ SiO_2 \cdot 4\ H_2O + 3\ Ca(OH)_2 + 173.6\ kJ$$

$$8Ca^{++} + 16(OH) + Al_2O_3 \rightarrow 8CaO \cdot Al_2O_3 \cdot 8\ H2O$$

The compounds that result from the previous equation are hard crystal materials and do not dissolve in water so it provides soil with strength. A practical consequence of the pozzolanic reaction is the gradual hardening of pastes containing pozzolanic materials and lime. Strength increases as the number of combined lime increases. However, may be pozzolana responsible for low early strength, and as much as pozzolana quantity increases as much as strength increases [McCarthy & Dyer, 2019].

4. Conclusion:

Results could be summarized as follows:

- Lime affects decreasing the water content and this effect increases directly with the percentage of lime. On the other hand, the water content decreases by approximately 25% of its initial value at the highest ratio of additives e.g. lime 8%.
- Lime additive increases UCS of soil and there is always an optimum ratio of additives, in our case, it was 4%.
- Lime additives enhance the bearing of soil by increasing the maximum load of soil. In our research, the maximum load increase is 2.8 fold from the initial one.
- Pozzolana additives enhance decreasing water content.
- Pozzolana decreases the strength compared with the effect of lime additives alone.
- The best percentage of Pozzolana additives is 30% for our soil samples.
- Moreover, it could be recommended to:
- Studying pozzolana additives ratio greater than 30% along with 4% of lime additives.
- Studying pozzolana additives with a lime ratio greater than 4%.
- Studying the effect of pozzolana fineness on strength of soil with pozzolana and lime.

Declaration: Not applicable.

Funding: “This research received no external funding”

Conflicts of Interest:

“The authors declare no conflict of interest.”

References

Abbasi, N., Mahdieh, M., (2018), Improvement of geotechnical properties of silty sand soils using natural pozzolan and lime, International Journal of Geo-Engieering, Springer open.

Alrubaye, A.J., Hasan, M., Fattah, M.Y. (2016), Improving Geotechnical Characteristics Of Kaolin Soil Using Silica Fume And Lime, An International Journal, 7 (1): 77–85 (2016).

Das, B., (2011), Shallow Foundations: Ultimate Bearing Capacity, Principles of foundation engineering seventh edition, p.133-137.

Ekolu, S.O., Thomas, M.D.A., and Hooton, R.D, (2006), Studies on Ugandan Volcanic ash and Tuff, Proceedings from the International Conference on Advances in Engineering and Technology, Elsevier, doi.org/10.1016/B978-008045312-5/50009-1

Gabr, M.A., Dodson, R., & Collin, J.G. (1998). A Study Of Stress Distribution In Geogrid-Reinforced Sand. Proceedings of geosynthetics in foundation reinforcement and erosion control systems, ASCE Geotechnical Special Publication, 76, Pp.62-67.

General Establishment for Geology & Minerals (GEGM), Syria, 2019.

Haas, S., Ritter, H., (2018) Soil improvement with quicklime – long-time behaviour and carbonation, Road Materials and Pavement Design Journal, https://doi.org/10.1080/14680629.2018.1474793

Harichane, K., Ghrici, I. M., & Missoum . H. (2011) Influence Of Natural Pozzolana And Lime Additives On The Temporal Variation Of Soil Compaction And Shear Strength, Front. Earth Sci., 5(2): 162–169

Harichane, K., Ghrici, I. M., & Kenai, S. (2017), Stabilization of Algerian Clayey Soils

with Natural Pozzolana and Lime, Periodica Polytechnica

Civil Engineering, paper 9229.

Hwang, T., Kim, K., Shin, J. (2016). Effective Installation Of Micropiles To Enhance Bearing Capacity Of Micropile Raft. Soils and Foundations 57 (2017) 36–49.

Kalyane, A., & Patil, R.J. (2020), Experimental Investigation Of Black Cotton Soil By Lime And Fly-Ash Stabilization, ACTA TECHNICA CORVINIENSIS – Bulletin of Engineering [e-ISSN: 2067-3809] TOME XIII [2020] | FASCICULE 2 [April – June]’.

Keskin, M.S., and Laman, M., (2012), Model Studies of Bearing Capacity of Strip Footing on Sand Slope, KSCE Journal of Civil Engineering (2013) 17(4):699-711.

Khan, A. N., Yakub, A., Mahvi, S., Junaid, M., Iqbal, k., (2020), Different Soil Stabilization Techniques, International Journal of Advanced Science and Technology, Vol. 29, No. 9s, pp. 7778-7791

Maharaj, D.K., Resham, Gupta, V., (2019), Improvement in Bearing Capacity of Soil, MNK Publication.

McCarthy, M.J., Dyer, T.D., (2019), Pozzolanas and Pozzolanic Materials, Lea’s Chemistry of Cement & Concrete, p. 363-467, doi.org/10.1016/B978-0-08-100773-0.00009-5

Tran, T.D., Cui, Y.-J., Tang, A.M., Audiguier, M. and Cojean, R. (2014), Effects of lime treatment on the microstructure and hydraulic conductivity of Héricourt clay, Journal of Rock Mechanics and Geotechnical Engineering, pp. 399-404.

Tsukada, Y., Miura, K,. Tsubolkawa, Y., Otani, Y., & You, L.,(2006) Mechanism Of Bearing Capacity Of Spread Footings Reinforced With Micropiles. Soils and Foundations Vol.46, No.3,367-367.

Türköz, M., Savaş, H., & Tasci, G. (2018), The effect of silica fume and lime on geotechnical properties of a clay soil showing both swelling and dispersive features, Arabian Journal of Geosciences (2018) 11:735.

JJEES

JJEES (2023) 14 (1): 75-82
ISSN 1995-6681

Jordan Journal of Earth and Environmental Sciences

Kinematic Analysis of Amman-Hallabat Structure, Northeast Dead Sea, Jordan

Masdouq Al-Taj

Department of Earth Sciences and Environment, Prince El Hassan Bin Talal Faculty for Natural Resources and Environment, The Hashemite University, P.O. Box 330127, Zarqa 13133, Jordan.

Received 4th April 2022; Accepted 3rd July 2022

Abstract

In this study, a new collection of kinematic data sets relating to the Amman-Hallabat Structure (AHS) is presented. Measurements of fault slip were taken over the near field of a structure that was thirty kilometers long and located northeast of the Dead Sea. The kinematic study that was carried out as a consequence reveals that strike-slip faulting predominates, along with minor episodes of oblique-slip and reverse faulting. Overall, there is a regional coherence in the orientations of the extensional and shortening axes associated with both types of faulting over the whole research area. This coherence can be seen in the orientations of the extensional and shortening axes. It is suggested that the data set be interpreted as the result of sinistrally transpressive kinematics that are more or less continuous, with shortening axes mainly oriented NW–SE to NNW–SSE and minor NE-SW and extensional axes predominately oriented NE–SW and minor NW–SE. These kinematic axes result from the two stress fields that affect the area, the earlier Syrian Arc Stress and the later Dead Sea Stress. The multistage kinematic history of the AHS indicates that the stress fields that generates AHS are kinematically incompatible.

Keywords: *Kinematic analysis, Amman-Hallabat Structure, Dead Sea Transform, Syrian Arc, Strain axis.*

1. Introduction

The development of the Syrian Arc Fold System (SAFS) in the Upper Cretaceous and the movement of the Arabian Plate in the Miocene-Recent define the structural deformation of Jordan (Abed, 2017). The Syrian Arc Fold System is an "S" shape and consists of a sequence of asymmetric anticlines and synclines that extend from Egypt's Sinai Peninsula to the Palmyrides in Syria (Fig. 1) (Moustafa, 2013). The general trend of the whole folded belt varies from NE (Sinai and Naqab) to NNE (central part) and then back to NE (Palmyrides in Syria). The entire SAFS started folding in the late Turonian when the early Mesozoic extensional stress field changed to a compressional stress field with maximum shortening oriented WNW-ESE. (Eyal, 2011; Guiraud and Bosworth, 1997).

The Dead Sea Transform Fault (DST) is 1100 km long and separates the Arabian and Sinai-Palestine plates (Fig. 2) (Lu et al., 2020; Hempton, 1987; Garfunkel, 1981). It accommodated about 105 km of left-lateral displacement (Garfunkel, 1981; Freund et al., 1970; Quennell, 1958). The DST connects the Gulf of Aqaba in the south with the Karasu Valley in southeast Turkey in the north (Mahmoud et al., 2012). Several Pliocene-Quaternary basins are conjoined as the Dead Sea Basin and the Ghab Basin (Brew et al., 2001). The beginning age of the DST is the Early Miocene (Freund et al., 1970), or the Early-Middle Miocene with increasing displacement in the Pliocene-Quaternary (Steckler and Ten Brink, 1986). Several regional models estimated relative motion along the DST at 5 to 10 mm/yr (Meghraoui, 2015; Ferry et al., 2011; Chu and Gordon, 1998; Joffe and Garfunkel, 1987; Garfunkel, 1981). According to space geodetic techniques, the current slip rate across the DST is 4.9 + 0.4 mm/yr (Hamiel et al., 2018; Al Tarazi et al., 2011). The maximum horizontal axis of compression near the DST is NNW-SSE (e.g., Diabat, 2009; Zain Eldeen et al., 2002) (Fig. 2). Many inherited structures, such as the Syrian Arc, accommodate this stress (Alchalbi et al., 2010; Abou Romieh et al., 2009; Badawy and Horváth, 1999; Chaimov et al., 1990). The southern part of the DST has two structures; the Wadi Araba Fault (WAF) and the Jordan Valley Fault (JVF) (Fig. 2) (i.e Beon et al., 2010; Ferry et al., 2007). The WAF, with 250 km in length, is a sinistral strike-slip fault composed of several segments connected by either small-scale thrust edges or pull-apart basins (Ferry et al., 2011; Le Beon et al., 2010, 2008; Hofstetter et al., 2007; Klinger et al., 2000; Atallah, 1992; Garfunkel, 1981). At the northeast corner of the Dead Sea, WAF shows a change in direction to the northeast, forming a restraining bend with the sinistral sense of movement and merging with two geological structures: the Amman Hallabat Structure (AHS) and the Shueib Structure (SHS) (Fig. 1) (Al Hseinat et al., 2020; Mikbel and Zacher, 1981). The two structures were formed in an NW-SE compressive framework, producing NE-SW folds and reverse faults in the upper Cretaceous and superimposed on the Syrian Arc (Al-Awabdeh et al., 2016; Diabat, 2009).

* Corresponding author e-mail: maltaj@hu.edu.jo

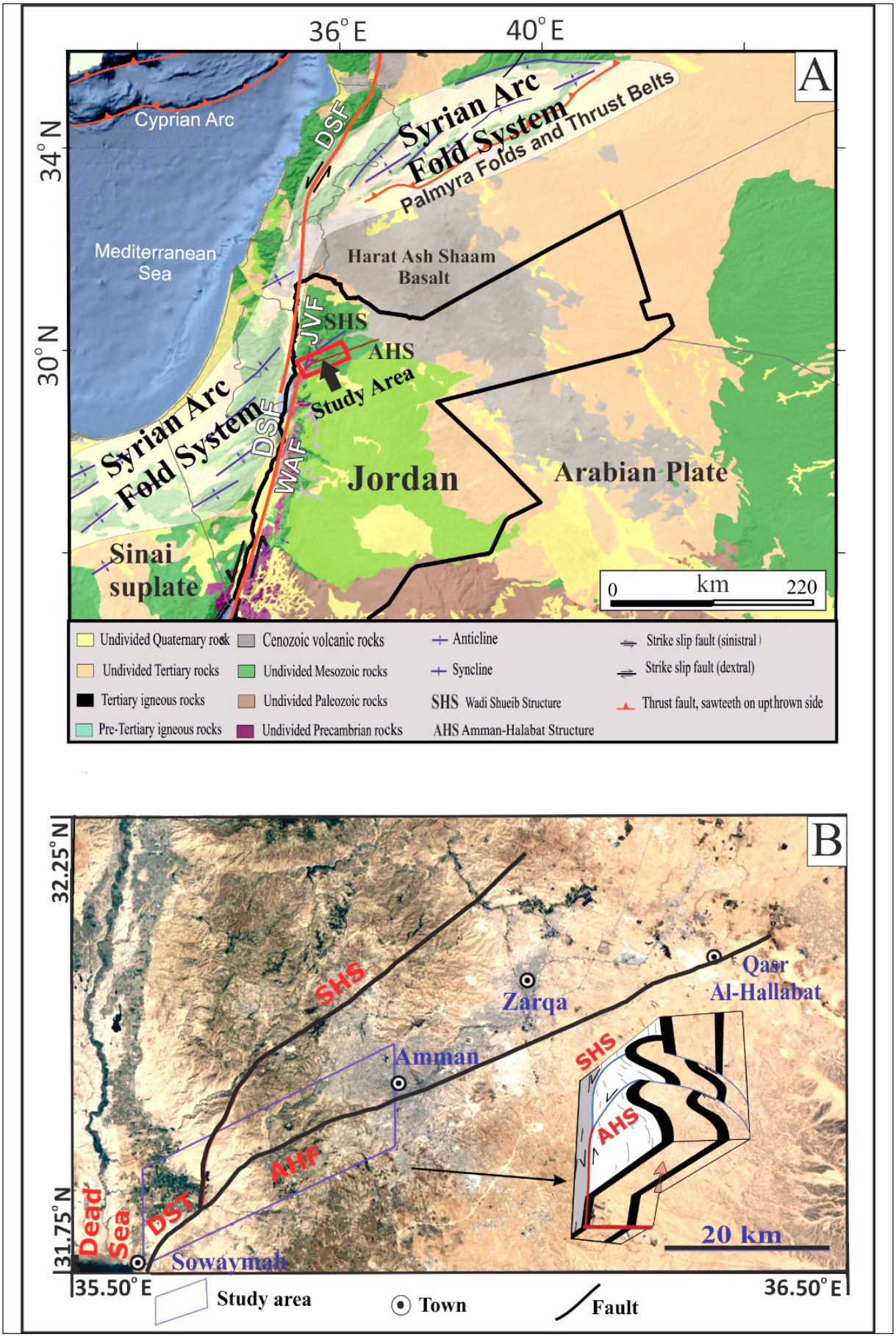

Figure 1. The Syrian Arc fold system and main structures in Jordan (A). The inset shows the location of the study area, (B) Amman -Hallabat Fault (AHF), Shuaib Structure (SHS), and a simplified model shows 3D of AHS and SHS (Modified from Al Hseinat et al., 2020).

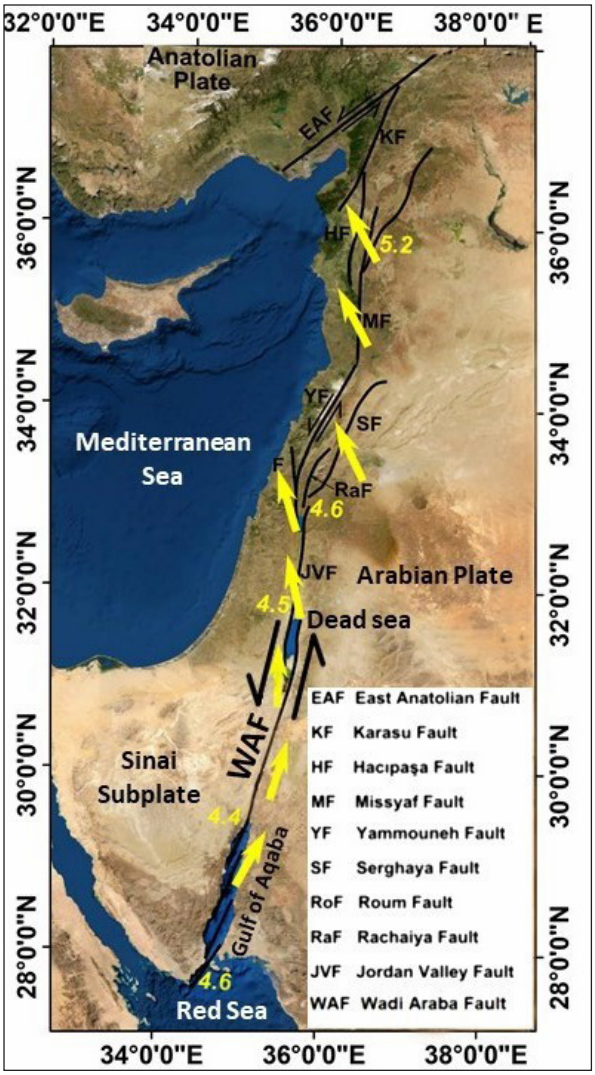

Figure 2. Dead Sea Transform fault (DST). Yellow arrows and numbers show the direction and amount of movement of the Arabian Plate concerning the Africa Plate in mm per year (Modified from Gomez et al., 2007).

2. Geological Setting

2. 1 Stratigraphy of the area

The Triassic Zarqa Ma'in Group is the oldest rock unit in the study area (Fig. 3). It is composed mainly of sandstone, sandy limestone, and dolomite (Makhlouf, 2003). The Azab Jurassic Group was sub-divided into 7 formations (Abed, 2017; Andrews, 1992): Hihi claystone, Nimir limestone, Silal sandstone, Dahab limestone, Ramla sandstone, Hamam sandstone, and Mughanyya limestone. The early Cretaceous, Kurnub Sandstone Group, overlies unconformably Triassic and Jurassic sediments in the southern and northern areas, respectively. It consists of braided-rivers sand deposits (Andrews, 1992). The late Cretaceous to the early Paleogene, Ajlun, and Belqa groups, consist predominantly of limestone, chalk, marls, chert, and phosphate. Ajlun Group was divided into five formations; they are from older to younger: Na'ur, Fuhies, Hummar, Shueib, and Wadi As Sir formations (Masri, 1963; Powell, 1989; Abed, 2017). Whereas Belqa Group was divided into five formations, they are from older to younger: Wadi Umm Ghudran, Amman Silicified, Al Hisa Phosphorite, Muwaqqar Chalk-Marl and Umm Rijam Chert-Limestone formations (Powell, 1989). The lower three formations are exposed in the study area whereas the upper two formations are exposed to the east of the area. The Neogene is largely eroded; Lisan and Damya formations represent the late Quaternary sediments in the study area (Fig. 3).

2.2 Tectonic setting of the area

According to Bender (1968), the study area is located within the highlands east of the DST and the Amman plateau (East Jordanian Plateau). Two main structures represent the Syrian arc in Jordan: The AHS is about 80 km long and extends from WAF in the west to Qasr Al Hallabat in the east of Jordan (Fig. 1) (Al Hseinat et al., 2020; Diabat, 2009; Mikbel and Zacher, 1981). The SHS represents a NE-SW oblique reverse fault with sub-parallel folds. This Structure was active in the late Cretaceous period. The study of Al-Awabdeh et al., (2016) proposed a Neogene reactivation of local faults in this structure as linked to the transpression activity of the DST. AHF is a NE–SW to ENE–WSW strike-slip fault and sub-parallel to anticlines and synclines (Mikbel and Zacher, 1986). In the eastern part of the studied area, the Amman Formation (Santonian-Campanian) on the northwestern side of the AHS is downfaulted against Wadi As Sir Formation (Turonian) on the southeastern side of the AHS. The downthrow of this fault is in the NNW direction (Diabat, 2009). Both the late Cretaceous (AHF and faults of SHS) are associated with ESE-WNW maximum compressive stress. Those structures were inactive during the Neogene (Sahawneh and Atallah, 2002; Mikbel and Zacher, 1981). Diabat (2009) proposed that they have a Quaternary activity and showed a significant similarity between the stress field orientation related to the DST. Recently, Al Hseinat et al. (2020) supposed that the DSF has combined with the main faults of the AHS. They further supposed that these faults were reactivated as a restraining bend formed from the DSF branches that developed due to the NNW-SSE-trending Dead Sea transpressional stress field. Thrust components are present on faults with horsetail geometry depending on the interaction between the direction of the AHS strands and the regional tectonic displacement along the DST. These movements are followed by folding and uplifting. Consequently, the main faults in the AHS have a horsetail structure, with folds and thrusting deformation.

3. Methodology

The current research focused on the kinematics of the AHS, where the structures are spatially continuous and bound by the DST and SHS (Fig. 1). Seven stations (S1-S7) were selected to perform the required measurements over a 30-kilometer length between the WAF in the west and the Amman area in the east (Fig. 3). The majority of the measurements were taken at Cretaceous outcrops. The study focuses on carbonate rocks that indicate reliable lineations or growth fibers on the fault planes. Due to the nature of the outcrop in the region, a relatively small number of observations were collected. All data acquired for this investigation consist of fault plane-striation pair measurements. The sense of movement on the plane was

determined by shear sense indicators, namely striations, and fibers on fault planes, which were observed to be highly developed in carbonate rocks (Fig. 4). To eliminate bias in the data set, one measurement per fault plane-striation was acquired, and only fault planes exhibiting shear indicators have been included in the kinematic analysis. To justify the relatively small set of data we have gathered, it is important to note that the fault-slip data from the quarries analyzed in this study are the only coherent data sets identified in the carbonate strata of the investigated sites.

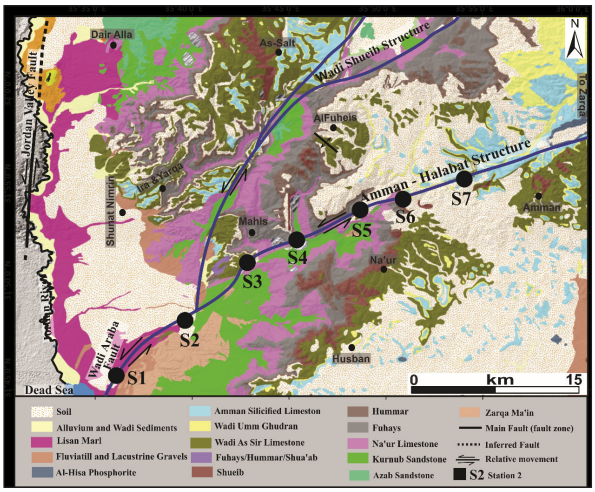

Figure 3. Geological Map and Locations of the measurement stations. The stations are marked by black circles and numbered from S1 to S7. (Geological map modified from Al Hseinat et al., 2020).

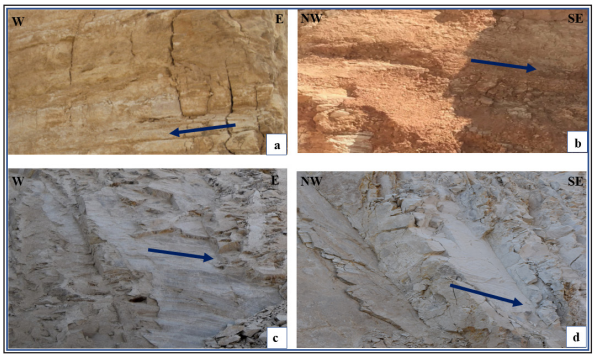

Figure 4. Fault-plane kinematic indicators. (a) Slickenlines on dextral strike-slip fault. (b) grooves on oblique-slip fault. (c) and (d) calcite mineral growth fiber on sinistral strike-slip faults. In (a) and (b) the arrow indicates the movement of the lost wall.

The Multiple Slip Method (MSM) (Zalohar and Vrabec, 2008) was used to calculate the common extension, intermediate, and shortening axes of a population of fault slip data. The MSM is an updated and modified version of the moment tensor summation (MTS) method developed by Kostrov (1974), Molnar (1983), and Marrett and Allmendinger (1991, 1990) and the finite strain and rotation from the fault slip method of Cladouhos and Allmendinger (1993). The MSM method is based on the theory of Linear Elastic Fracture Mechanics (LEFM) and the theory of scaling of fracture and fault systems. The main goal of the MSM method is to give an alternative way to figure out the weighting factors in the infinitesimal method of summing the moment tensor.

In general, the MSM method allows for calculating the macro-strain and relative micro-rotation tensors. This method allows constraining the fields P (shortening axis) and T (extension axis) delimited by each fault. The vectors of this tensor are parallel to the kinematic axes P, B (middle axis), and T of the fault. In this case, each fault's P and T fields are approximately similar to the corresponding fields (P and T) defined by the common macro-strain tensor. The axes determined for extension and shortening were examined for agreement with the results obtained using the P-T axes method (Jena and Pradhan, 2020). T-Tecto Studio X5 software (Zalohar, 2020) was used to perform the MSM method calculations.

4. Results of kinematic analysis

The number of fault-slip field measurements is 91 (Figs. 5 and 6), but the data used in the analysis is 77 (Fig. 7); the 14 field measurements were discarded since they are incompatible with slip deviations and provide inaccurate results. So. This research was confined to planes having reliable shear indicators, resulting in a somewhat small but significant data set. Measurements were taken at quarries near the AHS. The NE-SW oriented major direction of all fault planes, as shown in the rose diagram at the top of Fig. 6, agrees with AHS. This direction is well presented in the rose diagram of all reverse faults measured in the stations (Fig. 5c and Fig. 6) and less illustrated in the rose diagram of dextral and sinistral strike-slip faults measured in the stations (Figs. 5a and b). The strike-slip faults are sub-verticals with striations pitched between 0° and more than 30° (Fig. 6). The large values of striations pitch are due to later deformation episodes. The dextral and sinistral faults are largely similar in directions (Figs. 5a and b) which suggest the existence of many compressive episodes, with NW-SE and NE-SW shortening axes or faults reactivation, or strength anisotropy, providing cause for the generation of the dextral and sinistral faults.

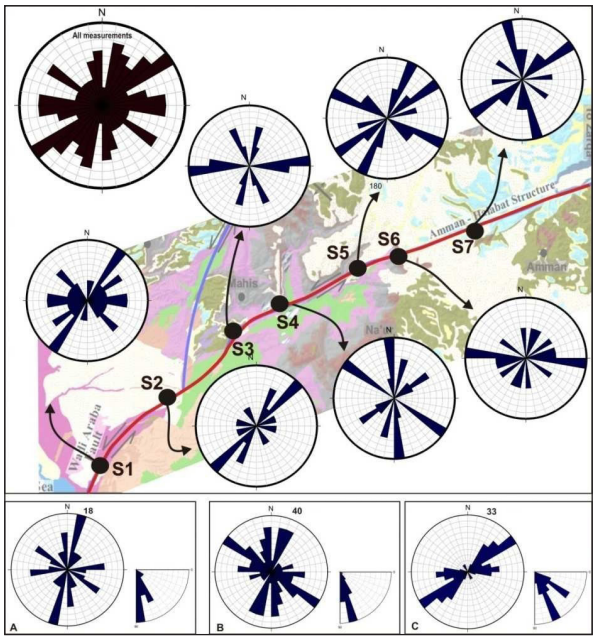

Figure 5. Fault geometries: Rose diagram of fault orientations measured at every station.

Rose diagram of all: a-Dextral strike-slip, b- Sinistral strike-slip, and c- Reverse faults measured in the whole stations. The Rose diagram at the top of the figure presents the direction of all fault types in all stations. (Base map from Al Hseinat et al. 2020)).

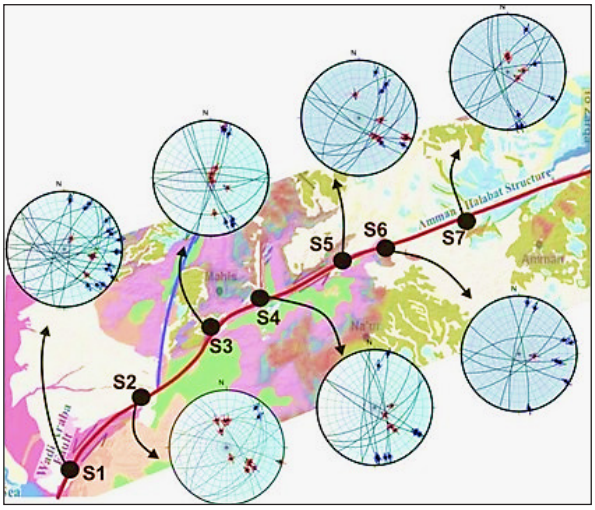

Figure 6. Lower hemisphere projections show measured fault plane-striation for each station. Red points with arrowheads on striation plunge symbols indicate the sense of displacement of hanging wall blocks of reverse faults, and blue points with arrows indicate the sense of displacement on strike-slip faults. (Base map from Al Hseinat et al., 2020).).

The MSM method was applied to the obtained station data. Results are documented in Table 1 and shown in Fig. 7. The best-determined solutions were obtained from those sites where the measurements were divided into fault sets (S1, S2, S4, and S5). However, some sites with few data measurements (S3, S6, and S7) also give reasonable results. The majority of the sites have strike-slip solutions with axes of shortening in the NW–SE to NNW–SSE and the NE–SW orientations (Fig. 7). Reverse faults present an NNW–SSE shortening direction of some of the sites (S2 and S5, Fig. 7). Rotation along the faults is likely to be caused by the tilting of the beds at some locations. The oblique-slip solutions at several sites demonstrate the deviations from kinematic calculations. Normal faulting was not obtained in the studied area.

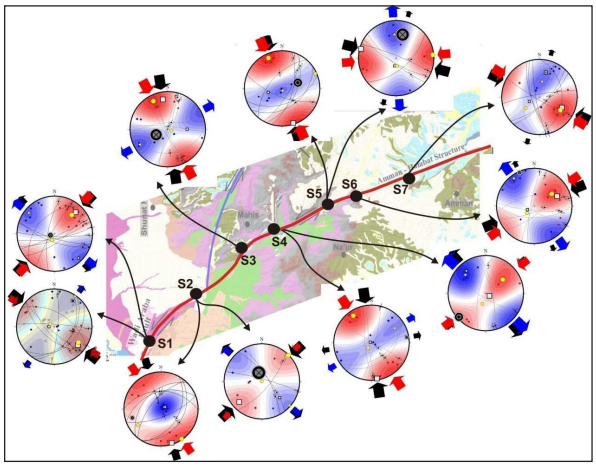

Figure 7. P- and T-axes for the measured faults as calculated by using the MSM method. Mean orientations for the P (horizontal shortening=red arrow), T (horizontal extension=blue arrow), and rotation axes (black arrows). The coinciding of black arrows and Kinematic axes means pure shear. Otherwise, it means simple shear and strain axes rotation with incremental strain. (Base map from Al Hseinat et al., 2020).

The positions of the calculated shortening axes are horizontal or close to horizontal (Fig. 8). Analyzing kinematic measurements present several shortening axes trends within the AHS. The main direction of the shortening axis is presented in the rose diagram attached at the top of Fig. 8. The dominant direction is NNW-SSE to NW-SE. The less important direction of shortening is NE-SW. Analyzing both reverse and strike-slip faults present NNW-SSE to NW-SE direction of shortening, whereas the NE-SW direction is a result of only strike-slip fault analysis.

Table 1. Results of kinematic analysis (trend and plunge) of the principal axes of strain obtained from SMS calculations. N: number of fault measurements.

Location and Number		Axis 1		Axis 2	Axis 3	
Station	N	Shortening		Intermediate	Extension	
S1 -a	9	123/14	(NW-SE)	304/76	035/0	(NE-SW)
S1 -b	10	042/21	(NE-SW)	204/68	309/6	(NW-SE)
S2 -a	7	145/0	(NW-SE)	235/14	065/76	(NE-SW)
S2 -b	4	046/0	(NE-SW)	304/90	131/0	(NW-SE)
S3	9	333/9	(NNW-SSE)	109/77	241/9	(NE-SW)
S4 -a	7	326/7	(NW-SE)	213/72	058/17	(NE-SW)
S4 -b	4	051/29	(NE-SW)	196/56	312/17	(NW-SE)
S5 -a	7	336/6	(NW-SE)	066/1	162/83	(NNW-SSE)
S5 -b	4	085/0	(E-W)	175/66	356/24	(N-S)
S6	8	055/30	(NE-SW)	226/59	323/4	(NW-SE)
S7	8	122/22	(NW-SE)	231/38	010/44	(NNE-SSW)

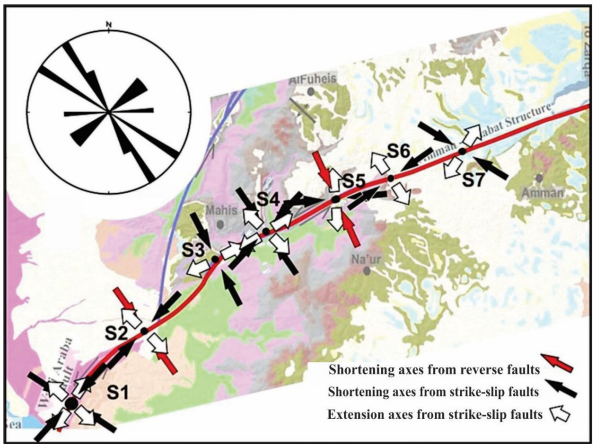

Figure 8. Shortening (black and red) and stretching axes (white) from MSM calculations in the AHS (Table 1). The Rose diagram at the top of the figure presents the main directions of the shortening axes for all stations. (Base map from Al Hseinat et al., 2020).

5. Discussion

The geometry of the measured fault in the different stations along the AHS should already be a reflection of its kinematics. Then, we have to agree that the AHS must have originated as a reverse fault with an important strike-slip component and has been found in this manner since its formation, and it has developed in different stages (Al-Awabdeh et al., 2016; Diabat, 2009). Zoback (1992) showed that mechanical anisotropies at a large-scale fault zone could modify the stress axes' orientation. Therefore, the origin of principal strain deviation from fault populations of known kinematics mustn't be considered problematic. The MSM method shows a combined NW–SE and NE–SW shortening axes and NE–SW stretching axes with local deviations (Fig. 8). Most of the shear indicators measured in the stations agree with this kinematics (Fig. 4). The kinematic structures in the studied area are strike-slip and reverse movements. Strike-slip and dip-slip kinematic indicators on the fault planes suggest that the faults were reactivated later.

The AHS accommodates the NE–SW trending reverse faults and the NE–SW faults with sinistral movement. These latter fault trends are due to the inherited structure of the Syrian Arc in the AHS which resulted from the E-W to ENE-WSW stress field. These transpressive structures are probably operated since the upper Cretaceous. The Senonian shortening in the western Syrian Arc was NNW-SSE directed and changed progressively to NW-SE and nearly WNW-ESE in Palestine (Sehim, 1993; Letouzey and Tremolibres, 1980). However, the cause of these transpressive structures may be a local response to anticlockwise rotation of the horizontal NNW–SSE shortening at restraining bends near WAF and AHS (Al-Taj et al., 2007).

The calculated kinematic axes correspond to many phases of tectonic development that control the AHS's deformations (Fig. 8). The geometry of the reverse faults measured in the AHS and adjoining NE-SW folds agrees with the NW-SE shortening axis. The NNW-SSE shortening axis accommodated the DST deformation and affected the geometry of the AHS at a later stage of its initial formation. It is suggested that the strain field of the NNW-SSE shortening axes in the AHS zone is consistent with sinistral movement on the fault. The NW-SE shortening field related to sinistral strike-slip faults is presented in the studied area (Fig. 8). As has been shown in previous works (Al Hseinat et al., 2020; Eyal and Eyal, 2015; Hofstetter et al., 2007; Badawy and Horváth, 1999; Eyal, 1996; Chaimov et al., 1990), it agrees with the present-day kinematics field of the DST. The results of kinematic axes indicate that the Dead Sea stress and the Syrian Arc Stress fields are kinematically incompatible.

The acquired observations in the area are in agreement with a change in the strain field of the AHS from thrust deformation during the Cretaceous to strike-slip and oblique reverse faulting in the Neogene. Diabat (2009) proposed a possible Quaternary reactivation in the northernmost part of AHS.

The stress field based on seismological studies (Palano et al., 2013; Hofstetter et al., 2007) showed sinistral movement that drives the deformation in the DST. It is compatible with strain tensors with the NNW–SSE shortening axis. It is suggested that NNW–SSE shortening drives the Quaternary reactivation tectonics in AHS.

6. Conclusions

For the AHS, a small but reliable set of fault slip data has been acquired. Almost all data can be explained by oblique strike-slip and reverse movement dominating the majority of the investigated stations near the AHS. With the notable exception of an extension in the NW–SE direction, there is remarkable coherence in the orientation of the NE–SW extension along the investigated strike length of the AHS. The majority of calculated shortening axes have subhorizontal NW–SE to NW–SE orientations. The kinematic axes indicate that the E-W compressional Syrian Arc stress field and NW-SE Dead Sea stress field with about anticlockwise rotation. The current findings indicate that AHS is produced in more or less continuous, sinistrally transpressional kinematics in space and time.

References

Abed, A. (2017). Geology of Jordan, its water and environment. 2nd Edition (In Arabic), Dar Wael, Amman.

Abou Romieh, M., Westaway, R., Doud, M., Radwan, Y., Yasminh, R., Khalil, A., Al-Ashkar, A., Loughlin, S., Arrell, K., Bridgland, D. (2009). Active crustal shortening in NE Syria revealed by deformed terraces of the River Euphrates. Terra Nova 21: 427-437.

Al Hseinat, M., Al-Rawabdeh, A., Al-Zidaneen, M., Ghanem, H., Al-Taj, M., Diabat, A., Jarrar, G., Atallah, M. (2020). New Insights for Understanding the Structural Deformation Style of the Strike-Slip Regime along the Wadi Shueib and Amman-Hallabat Structures in Jordan Basedbased on Remote Sensing Data Analysis. Geosciences 10, 253.

Al Tarazi, E., Abu Rajab, J., Gomez, F., Cochran, W., Jaafar, R., Ferry, M. (2011). GPS measurements of near-field deformation along the southern Dead Sea Fault System. Geochemistry, Geophysics, Geosystems 12(12). Q12021. doi:10.1029/2011GC003736 https://doi.org/10.1029/2011GC003736

Al-Awabdeh, M., Perez-Pena, J., Azanon, J., Booth-Rea, G., Abed, A., Atallah, M., Galve, J. (2016). Quaternary tectonic activity in NW Jordan: Insights for a new model of transpression–transmission along the southern Dead Sea

Transform Fault. Tectonophysics 693: 465-473.

Alchalbi, A., Daoud, M., Gomez, F., McClusky, S., Reilinger, R., Abu Romeyeh, M., Alsouod, A., Yasmin R., Ballani, B., Darawcheh, R., Sbeinati, R., Radwan, Y., Al Masri, R., Bayerly, M., Al Ghazzi, R., Barazangi, M. (2010). Crustal deformation in northwestern Arabica from GPS measurements in Syria: slow slip rate along the northern Dead Sea Fault. Geophys J Int 180:125–135.

Al-Taj, M., Shaqour, F., Atallah, M. (2007). Morphotectonic indices of the Dead Sea transform, Jordan. Geografia Fisica e Dinamica Quaternaria 30(1): 5-12.

Andrews, I. (1992). Permian, Triassic, and Jurassic Lithostratigraphy in the Subsurface of Jordan. Ministry of Energy and Mineral Resources. Amman, Jordan. https://books.google.jo/books?id=_EbrPgAACAAJ

Atallah, M. (1992). Tectonic evolution of northern Wadi Araba, Jordan. Tectonophysics 204:17–26.

Badawy, A., Horváth, F. (1992). The Sinai subplate and tectonic evolution of the northern Red Sea region. J Geodyn 27:433-450.

Bender, F. (1968). Geologie von Jordanien—Beiträge zur Regionalen Geologie der Erde. Gebruder Borntraeger. Stuttgart, Germany.

Brew, G., Lupa, J., Barazangi M., Sawaf, T., Al-Imam, A., Zaza, T. (2001). Structure and tectonic development of the Dead Sea Fault System and Ghab Basin in Syria. Journal of the Geological Society 158: 665-647.

Cardozo, L., Behrmann, J. (2006). Kinematic analysis of the Upper Rhine Graben boundary fault system, Journal of Structural Geology 28: 1028-1039.

Chaimov, T., Barazangi, M., Al-Saad, D., Sawaf, T., Gebran, A. (1990). Crustal shortening in the Palmyride fold belt, Syria, and implication for movement along the Dead Sea Fault system. Tectonics 9(6): 1369-1386.

Chu, D., Gordon, R. (1998). Current plate motions across the Red Sea. Geophys J Int 135: 313–328.

Cladouhos, T., Allmendinger, R. (1993). Finite strain and rotation from fault slip data. Journal of Structural Geology 15: 771-784.

Diabat, A. (2009). Structural and stress analysis based on fault-slip data in the Amman area, Jordan. J Afr Earth Sci 54:155–162.

Eyal Y. (2011). The Syrian Arc Fold system: Age and rate of folding. Geophysical Research 13, EGU2011-7401, EGU General Assembly.

Eyal, Y. (1996). Stress fluctuations along the Dead Sea rift since the Middle Miocene. Tectonics 15: 157-170.

Eyal, Y., Eyal, M. (2015). Nature of slip transfer between strike-slip faults: The Eastern Sinai (Egypt) shear zone, Dead Sea Transform, Journal of Structural Geology 76: 52-60. https://doi.org/10.1016/j.jsg.2015.03.014.

Ferry, M., Meghraoui, M., Abou Karaki, N., Al-Taj, M., Amoush, H., Al-Dhaisat, S., Barjous, M. (2007). A 48-Kyr-long slip rate history for the Jordan Valley segment of the Dead Sea fault. Earth Planet Sci Lett 260: 394-406.

Ferry, M., Meghraoui, M., Abou Karaki, N., Al-Taj, M., and Khalil, L. (2011). Episodic Behavior of the Jordan Valley Section of the Dead Sea Fault Inferred from a 14-ka-Long Integrated Catalog of Large Earthquakes. Seismol. Soc. Am., Bull 101(1): 39-67.

Freund, R., Garfunkel, Z., Zak, I., Goldberg, M., Weissbrod, T., Derin, B. (1970). The shear along the Dead Sea rift. Philosophical Transactions of the Royal Society, London 267:107–130.

Garfunkel, Z. (1981). Internal structure of the Dead Sea leaky transform (rift) in relation to plate kinematics. Tectonophysics 80: 80–108.

Gomez, F., Karam, G., Khawalie, M., McClusky, S., Vernant, P., Reilinger, R., Jaffar, R., Tabet, C., Khair, K., Barazangi, M. (2007). Global positioning system measurements of strain accumulation and slip transfer through the restraining bend along the Dead Sea fault system in Lebanon. Geophys J Int 168:1021–1028.

Guiraud, R., Bosworth, W. (1997). Senonian basin inversion and rejuvenation of rifting in Africa and Arabia: synthesis and implications to plate-scale tectonics. Tectonophysics 282: 39-82.

Hamiel, Y., Piatibratova, O., Mizrahi, Y., Nahmias, Y., Amir Sagy, A. (2018). Crustal Deformation across the Jericho Valley Section of the Dead Sea Fault as Resolved by Detailed Field and Geodetic Observations. Geophysical Research Letters 45 (7): 3043-3050. https://doi.org/10.1002/2018GL077547

Hempton M. R. (1987). Constraints on Arabian plate motion and extensional history of the Red Sea. Tectonics: 687-705.

Hofstetter, R., Klinger, Y., Amrat, A., Rivera, L., Dorbath, L. (2007). Stress tensor and focal mechanisms along the Dead Sea fault and related elements based on seismological data. Tectonophysics 429:165–181.

Jena, R., Pradhan, B. (2020). A model for visual assessment of fault plane solutions and active tectonics analysis using the global centroid moment tensor catalog. Earth Syst Environ 4: 197–211. https://doi.org/10.1007/s41748-019-00142-9

Joffe, S., Garfunkel, Z. (1987). Plate kinematics of the circum Red Sea. A re-evaluation. Tectonophysics 141: 5-22.

Klinger, Y., Avouac, J., Abou Karaki, N., Dorbath, L., Bourles, D., Reyss, J. (2000). Slip- rate on the Dead Sea transform fault in northern Araba valley. Geophys. J. Int 142: 755-768.

Kostrov, V.V. (1974). Seismic moment and energy of earthquakes, and seismic flow of rocks. Physics of Solid Earth 1: 23-40.

Le Beon, M., Klinger, Y., Al-Qaryouti, M., Mériaux, A., Finkel, R., Elias, A., Mayyas, O., Ryerson, F., Tapponnier, P. (2010). Early Holocene and late Pleistocene slip rates of the southern Dead Sea fault determined from 10Be cosmogenic dating of offset alluvial deposits. J Geophys Int 115: B11414.

Le Beon, M., Klinger, Y., Amrat, A., Agnon, A., Dorbath, L., Baer, G., Ruegg, J., Charade, O., Mayyas, O. (2008). Slip rate and locking depth from GPS profiles across the southern Dead Sea transform. J Geophys Res 113: B11403.

Letouzey, J., and Tremolieres, P. (1980). Palaeostress field around the Mediterranean derived from microtectonics: Comparison with plate tectonic data, Rock Mechanics 9: 173–192.

Lu, Y., Wetzler, N., Waldmann, N., Agnon, A., and Marco, S. (2020). A 220,000-Year-Long Continuous Large Earthquake Record on a Slow-Slipping Plate Boundary. Sci. Adv. 6 (48). doi:10.1126/sciadv.aba4170

Mahmoud, Y., Masson, F., Meghraoui, M., Cakir, Z., Alchalbi, A., Yavaoglu,H., Yönlü, O., Daoud, M., Ergintav, S., Inan, S. (2012). Kinematic study at the junction of the East Anatolian fault and the Dead Sea fault from GPS measurements. Journal of Geodynamics 67: 30-39. doi:10.1016/j.jog.2012.05.006

Makhlouf, I. (2003). Fluvial/tidal interaction at the southern Tethyan strandline during Triassic Mukheiris times in central Jordan. J Asian Earth Sci 21:377-385.

Marrett, R., Allmendinger, R. (1990). Kinematic analysis of fault-slip data. Journal of Structural Geology 12: 973-986.

Marrett, R., Allmendinger, R. (1991). Estimates of strain due to brittle faulting: sampling of fault populations. Journal of Structural Geology 13: 735-738.

Masri, M. (1963) Unpublished report on the geology of the

Amman-Zerqa Area. Central Water Authority, Amman, Jordan.

Mikbel, S., Zacher, W. (1981). Fold structures in northern Jordan. Neues Jahrbuch für Geologie und Paläontologie. Monatshefte 4: 248–256.

Mikbel, S., Zacher, W. (1986). The Wadi Shueib Structure in Jordan: Neues Jahrbuch für Geologie und Paläontologie. Monatshefte 9: 571–576.

Molnar, P. (1983). Average regional strain due to slip on numerous faults of different orientations. Journal of Geophysical Research 88: 6430-6432.

Moustafa, A. (2013). Fold-related faults in the Syrian Arc belt of Northern Egypt. Marine and Petroleum Geology 48: 441-454. 10.1016/j.marpetgeo.2013.08.007

Mustapha Meghraoui, M. (2015). Paleoseismic History of the Dead Sea Fault Zone. Encyclopedia of Earthquake Engineering. 10.1007/978-3-642-36197-5_40-1

Palano, M., González P., Fernández, J. (2013). Strain and stress fields along the Gibraltar Orogenic Arc: constraints on active geodynamics. Gondwana Res 23(3):1071–1088. https://doi.org/10.1016/j.gr.2012.05.021

Powell, J.H. (1989). Stratigraphy and sedimentation of the Phanerozoic rocks in Central and South Jordan, Natural Resources Authority, Jordan, Geology Bulletin, No. 11, Part A, Ram & Khreim Groups, 130p., Part B Kurnub, Ajlun & Belqa Groups, 72p.

Quennell, A.M. (1958). The structural and geomorphic evolution of the Dead Sea Rift. Q. J. Geol. Soc 114: 1-24.

Sahawneh, J., Atallah, M. (2002). Tectonic evolution of the north-eastern corner of the Dead Sea, Jordan. Abhath Al Yarmouk 11: 581–598.

Sehim, A. (1993). Cretaceous tectonic in Egypt. Egyptian Journal of Geology, 37(1):335-372.

Steckler, M. S. & Ten Brink, U. S. (1986). Lithospheric strength variations as a control on new plate boundaries: examples from the northern Red Sea region. Earth and Planetary Science Letters 79: 120–132.

Zain Eldeen, U., Delvaux, D., Jacobs, P. (2002). Tectonic evolution in the Wadi Araba Segment of the Dead Sea Rift, Southwest Jordan. EGU Stephan Mueller Spec. Publ. Ser 2: 63–81.

Zalohar J. (2020). T-TECTO Studio X5, Omega Architect Integrated Software for Structural Analysis of Earthquake Focal-Mechanisms and Fault-Slip Data. file:///C:/Users/Admin/Downloads/T-TECTO%20Studio%20X5%20-%20Introductory%20Tutorial.pdf

Žalohar, J., Vrabec, M. (2008). Combined kinematic and paleostress analysis of fault-slip data: The Multiple-slip method. Journal of Structural Geology 30(12): 1603-1613. 10.1016/j. jsg.

Zoback, M. (1992). First- and second-order patterns of stress in the lithosphere: The World Stress Map project, J. Geophys. Res., 97(B8) 11: 703-728. doi:10.1029/92JB00132

المملكة الأردنية الهاشمية

صندوق دعم البحث العلمي

الجامعة الهاشمية

المجلة الأردنية
لعلوم الأرض والبيئة

JJEES

مجلة علمية عالمية محكمة

المجلد (١٤) العدد (١)

http:// jjees.hu.edu.jo/

ISSN 1995-6681

المجلة الأردنية لعلوم الأرض والبيئة

مجلة علمية عالمية محكمة

المجلة الأردنية لعلوم الأرض والبيئة: مجلة علمية عالمية محكمة ومفهرسة ومصنفة، تصدر عن عمادة البحث العلمي في الجامعة الهاشمية وبدعم من صندوق البحث العلمي - وزارة التعليم العالي والبحث العلمي، الأردن.

ترسل البحوث إلكترونيا إلى البريد الإلكتروني التالي:

رئيس تحرير المجلة الأردنية لعلوم الأرض والبيئة

jjees@hu.edu.jo

لمزيد من المعلومات والأعداد السابقة يرجى زيارة موقع المجلة على شبكة الانترنت على الرابط التالي:

www.jjees.hu.edu.jo

المملكة الأردنية الهاشمية صندوق دعم البحث العلمي الجامعة الهاشمية

Indexed by Scopus ELSEVIER

JJEES

المجلة الأردنية لعلوم الأرض والبيئة

المجلد (14) العدد (1)

مجلة علمية عالمية محكمة تصدر بدعم من صندوق دعم البحث العلمي

ISSN 1995-6681 jjees.hu.edu.jo آذار 2023